APPLIED COMPUTATIONAL ELECTROMAGNETICS SOCIETY JOURNAL

July 2026
Vol. 41 No. 07
ISSN 1054-4887

The ACES Journal is abstracted in INSPEC, in Engineering Index, DTIC, Science Citation Index Expanded, the Research Alert, and to Current Contents/Engineering, Computing & Technology.

The illustrations on the front cover have been obtained from the ARC research group at the Department of Electrical Engineering, Colorado School of Mines

Published, sold and distributed by: River Publishers, Broagervej 10, 9260 Gistrup, Denmark

THE APPLIED COMPUTATIONAL ELECTROMAGNETICS SOCIETY
http://aces-society.org

EDITORS-IN-CHIEF

Sami Barmada
University of Pisa, ESE Dept.
56122 Pisa, Italy

Atef Elsherbeni
Colorado School of Mines, EE Dept.
Golden, CO 80401, USA

ASSOCIATE EDITORS

Giulio Antonini
Università degli Studi dell'Aquila
Italy

Marco Arjona
La Laguna Institute of Technology
Coahuila 27266, Mexico

Abd A. Arkadan
Colorado School of Mines, Golden
CO 80401, USA

Alireza Baghai-Wadji
University of Cape Town
Cape Town, 7701, South Africa

Santanu Behera
National Institute of Technology
Rourkela-769008, India

Rui Chen
Nanjing University of Science
and Technology
China

Vinh Dang
Sandia National Laboratories
USA

Sounik Kiran Kumar Dash
SRM Institute of Science and Technology
Chennai, India

Alessandro Formisano
Seconda Universita di Napoli
81031 CE, Italy

Nunzia Fontana
University of Pisa
56122 Pisa, Italy

Fatih Kaburcuk
Sivas Cumhuriyet University
Sivas, Turkey

Piotr Gas
AGH University of Kraków
30-059 Krakow, Poland

Mona El Helbawy
University of Colorado
Boulder, CO 80302, USA

Zhixiang Huang
Anhui University
China

Qiuhua Huang
Colorado School of Mines
USA

Long Li
Xidian University
Shaanxi 710071, China

Yingsong Li
Harbin Engineering University
Harbin 150001, China

Wenxing Li
Harbin Engineering University
Harbin 150001, China

Ibrahim Mahariq
Gulf University for Science and Technology
Kuwait

Riyadh Mansoor
Al-Muthanna University
Samawa, Al-Muthanna, Iraq

Maria Evelina Mognaschi
University of Pavia
Italy

Antonino Musolino
University of Pisa
56123 Pisa, Italy

Sima Noghanian
Wafer LLC
Beverly, MA 01915, USA

Mauro Parise
University Campus Bio-Medico of Rome
00128 Rome, Italy

Luca Di Rienzo
Politecnico di Milano
20133 Milano, Italy

Daniele Romano
Università degli Studi dell'Aquila
Italy

Huseyin Savci
Istanbul Medipol University
Turkey

Stefano Selleri
DINFO – University of Florence
0139 Florence, Italy

Sihua Shao
Colorado School of Mines
USA

Jiming Song
Iowa State University
IA 50011, USA

Sheng Sun
University of Electronic Science
and Technology of China
China

Francesca Venneri
DIMES, Università della Calabria
Italy

Steven Weiss
US Army Research Laboratory
USA

Wei-Chung Weng
National Chi Nan University
Puli, Nantou 54561, Taiwan

Kaikai Xu
University of Electronic Science
and Technology of China
China

Lei Zhao
China University of Mining
and Technology, Jiangsu 221116
China

EDITORIAL ASSISTANTS

Matthew J. Inman
University of Mississippi, EE Dept.
University, MS 38677, USA

Shanell Lopez
Colorado School of Mines, EE Dept.
Golden, CO 80401, USA

EMERITUS EDITORS-IN-CHIEF

Duncan C. Baker
EE Dept. U. of Pretoria
0002 Pretoria, South Africa

Allen Glisson
University of Mississippi, EE Dept.
University, MS 38677, USA

Ahmed Kishk
Concordia University, ECS Dept.
Montreal, QC H3G 1M8, Canada

Robert M. Bevensee
Box 812
Alamo, CA 94507-0516

Ozlem Kilic
Catholic University of America
Washington, DC 20064, USA

David E. Stein
USAF Scientific Advisory Board
Washington, DC 20330, USA

EMERITUS ASSOCIATE EDITORS

Yasushi Kanai
Niigata Inst. of Technology
Kashiwazaki, Japan

Mohamed Abouzahra
MIT Lincoln Laboratory
Lexington, MA, USA

Alexander Yakovlev
University of Mississippi, EE Dept.
University, MS 38677, USA

Levent Gurel
Bilkent University
Ankara, Turkey

Sami Barmada
University of Pisa, ESE Dept.
56122 Pisa, Italy

Ozlem Kilic
Catholic University of America
Washington, DC 20064, USA

Erdem Topsakal
Mississippi State University, EE Dept.
Mississippi State, MS 39762, USA

Alistair Duffy
De Montfort University
Leicester, UK

Fan Yang
Tsinghua University, EE Dept.
Beijing 100084, China

Rocco Rizzo
University of Pisa
56123 Pisa, Italy

Atif Shamim
King Abdullah University of Science and Technology (KAUST)
Thuwal 23955, Saudi Arabia

William O'Keefe Coburn
US Army Research Laboratory
Adelphi, MD 20783, USA

Mohammed Hadi
Kuwait University, EE Dept.
Safat, Kuwait

Amedeo Capozzoli
Univerita di Naoli Federico II, DIETI
I-80125 Napoli, Italy

Maokun Li
Tsinghua University
Beijing 100084, China

Lijun Jiang
University of Hong Kong, EEE Dept.
Hong, Kong

Shinishiro Ohnuki
Nihon University
Tokyo, Japan

Kubilay Sertel
The Ohio State University
Columbus, OH 43210, USA

Salvatore Campione
Sandia National Laboratories
Albuquerque, NM 87185, USA

Toni Bjorninen
Tampere University
Tampere, 33100, Finland

Paolo Mezzanotte
University of Perugia
I-06125 Perugia, Italy

Yu Mao Wu
Fudan University
Shanghai 200433, China

Amin Kargar Behbahani
Florida International University
Miami, FL 33174, USA

Laila Marzall
University of Colorado, Boulder
Boulder, CO 80309, USA

Qiang Ren
Beihang University
Beijing 100191, China

EMERITUS EDITORIAL ASSISTANTS

Khaleb ElMaghoub
Trimble Navigation/MIT
Boston, MA 02125, USA

Kyle Patel
Colorado School of Mines, EE Dept.
Golden, CO 80401, USA

Christina Bonnigton
University of Mississippi, EE Dept.
University, MS 38677, USA

Anne Graham
University of Mississippi, EE Dept.
University, MS 38677, USA

Madison Lee
Colorado School of Mines, EE Dept.
Golen, CO 80401, USA

Allison Tanner
Colorado School of Mines, EE Dept.
Golden, CO 80401, USA

Mohamed Al Sharkawy
Arab Academby for Science and Technology, ECE Dept.
Alexandria, Egypt

JULY 2026 REVIEWERS

Intan Sorfina Zainal Abidin
Jawad K. Ali
Giovanni Angiulli
Yogesh Kumar Coukiker
Vinh Dang
Arkaprovo Das
Tanmaya Kumar Das
Javad Ebadi
Jun Fan
Amir Jafargholi
Ulrich Jakobus
Haolin Jiang
Bhanutheja Nagabhushana Reddy Kasinayakanahally
Mikko Kokkonen
Matteo Bruno Lodi
Bojana Petkovic
Shi Pu
Kannadhasan S.
Natarajamani S.
Cheng-An Sun
Lingasamy Veluchamy

THE APPLIED COMPUTATIONAL ELECTROMAGNETICS SOCIETY JOURNAL

Vol. 41 No. 07 July 2026

TABLE OF CONTENTS

Digital Twin Assisted Self-Interference Cancellation for Wideband Full Duplex Radios
Md Rakibur Rahman, Satheesh Bojja Venkatakrishnan, and John L. Volakis 603

Three-Port Common Aperture Metasurface Antenna Designed Using Characteristic Mode Analysis
Z. N. Jiang, L. Wu, B. Z. Sun, and L. L. Yu 614

A Bear-Shaped UWB MIMO Antenna Based on Characteristic Mode Analysis
Xiaoyan Wei, Zhonggen Wang, Wenyan Nie, Chenlu Li, and Zhengting Zhang 621

A Deep Learning and NSGA-II Based Multi-Objective Optimization Framework for SAR-Aware AMC-Backed Wearable Antenna Design
Muthukumaravel K and Suganthi Santhanam 635

Deep Learning Enhanced Hybrid BEM-rMLNCA Method for Efficient Power Cable Crosstalk Prediction
Abdul Mueed, Weiqiang Tang, and Rui Ma 650

An Efficient Multi-GPU Accelerated IEDG-CBFM-SMWA Method for Electromagnetic Scattering Analysis
Ziang Shen, Xinlei Chen, and Zhuo Li 657

Ant Colony Algorithm Optimized Method for Electromagnetic Interference Suppression of Power Line Inspection UAVs
Jian Chen, Yuxuan Huang, and Ziheng Wan 665

A Hybrid Triangle-Voxel Model with Local Voxelization for Resolving Diffraction Edge Deficiency in Ray Tracing
Baolai Zhang, Dan Shi, Jinyu Song, Xiaoyong Liu, Hongbo Tao, Huichun Yang, Zhonghua Xin, and Yuhao Jia 678

Numerical Modeling and Uncertainty Analysis of Downhole Low-Frequency Electromagnetic Transmission
Dongxiao Pang, Huiyan Hou, Jinjun Bai, and Xiong Han 687

Frequency-Selective Polarization Converter with Ultra-Wideband Linear-to-Circular Conversion and High Selectivity Based on Stair-Case Shape
Kun Liao, Jie Shu, Ruquan Wen, Renxia Ning, and Zhiming Liu 697

© 2026, The Applied Computational Electromagnetics Society

Digital Twin Assisted Self-Interference Cancellation for Wideband Full Duplex Radios

Md Rakibur Rahman, Satheesh Bojja Venkatakrishnan, and John L. Volakis

Department of Electrical and Computer Engineering
Florida International University, Miami, FL – 33174, USA
mrahm080@fiu.edu, sbojjave@fiu.edu, jvolakis@fiu.edu

Abstract – Achieving high self-interference cancellation (SIC) in broadband in-band full-duplex (IBFD) radios requires a multi-stage passive architecture using real-world components. A fundamental challenge in such systems is that practical components (cables, connectors, splitters) deviate from their ideal behavior due to fabrication tolerances and parasitic effects. As such, they introduce phase and amplitude mismatches that severely degrade isolation performance. Even deviations of a few degrees in phase or a fraction of a dB in amplitude can reduce achievable cancellation by 10 dB or more. To bridge this gap, we develop a digital twin framework that models the idealized system behavior and enables compensation through de-embedding of the fabricated hardware. Experimental results demonstrate that the proposed method improves the average isolation by 15 dB across a 1 GHz bandwidth within the X-band. Overall, a peak IBFD isolation of 65 dB is achieved, thus validating the effectiveness of the digital twin framework.

Index Terms – De-embedding, digital twin, high isolation, in-band full-duplex (IBFD), self-interference cancellation (SIC), wideband.

I. INTRODUCTION

In-band full-duplex (IBFD) radios enable simultaneous transmission and reception over the same frequency band, offering up to a twofold improvement in spectral efficiency as compared to conventional half-duplex architectures [1–3]. Achieving practical IBFD operation requires the suppression of high-power self-interference signals that leak into the co-located receiver. Often, these exceed 100 dB, necessitating a multi-stage approach [4, 5] (see Fig. 2). This multi-stage SI cancellation strategy employs various high-performance RF components and circuitry to ensure robust isolation for broadband IBFD performance [2].

IBFD radios enhance spectral efficiency and throughput by simultaneously transmitting and receiving across the same frequency band [1–3]. Achieving practical IBFD operation requires the suppression of high-power self-interference (SI), especially across large bandwidths [4, 6]. This suppression often requires more than 100 dB of interference mitigation [4, 5] and necessitates a multi-stage approach (see Fig. 2). This multi-stage SI cancellation strategy employs various high-performance RF components and circuitry to ensure robust isolation for broadband IBFD performance [2]. However, practical components such as splitters, cables, and connectors often deviate from ideal behavior due to broadband non-uniformity, fabrication flaws, and parasitic effects, leading to phase and amplitude mismatches. Compensating for these inconsistencies using de-embedding is crucial for effective IBFD operation across broadband frequencies.

Existing SIC strategies can be broadly classified into four stages. The first and most cost-effective approach exploits the antenna stage for propagation-domain isolation. This stage leveraged polarization diversity or spatial separation between transmit and receive elements [7–9]. As noted in [7–9], these passive antenna-based methods can achieve up to 40 dB of isolation but are fundamentally limited due to the antenna geometry and cross-polarization purity [7].

The second stage involves passive or active RF-domain filters, where a reference copy of the transmitted signal is weighted and subtracted from the leakage signal at the receiver. Passive implementations using cascaded stub-loaded microstrip architectures offer cost advantages but are sensitive to fabrication tolerances and component impairments [10, 11]. Active RF cancellers using multi-tap delay lines can improve cancellation depth but introduce noise, nonlinearity, and increased power consumption [5, 12].

The last two stages, mixed-signal and digital-assisted approaches, combine analog RF cancellation with baseband processing [13–15]. While flexible and adaptive, these methods require high-speed analog-to-digital and digital-to-analog converters (ADCs/DACs), resulting in higher hardware complexity, cost, and susceptibility to saturation from residual high-power

Submitted On: June 17, 2025
Accepted On: July 15, 2026

1054-4887 © ACES

https://doi.org/10.13052/2026.ACES.J.410701

self-interference. Notably, photonic-assisted topologies can also support very wideband SIC [16–18], but require specialized hardware incompatible with standard low-cost RF microstrip integration.

Despite the aforementioned advances, a persistent and underexplored challenge in passive multi-stage SIC systems is the degradation in isolation caused by phase and amplitude mismatches introduced by non-ideal passive components. These include cables, connectors, splitters, etc used to interconnect the cancellation stages. As illustrated in Fig. 3, even deviations of a few degrees in phase or a fraction of a dB in amplitude can reduce achievable isolation by 10 dB or more. Existing approaches do not systematically compensate for these hardware-level impairments. This paper addresses this gap through a digital twin-assisted de-embedding framework.

It is instructive to distinguish the proposed approach from other compensation strategies in the literature. Among them, adaptive filter-based SIC methods dynamically update cancellation tap weights using real-time digital signal processing [15, 19]. They operate in the digital domain and require ADC/DAC hardware. That is, they are not instantaneous, and require LookUp tables (LUT) to pre-characterize the system under a discrete set of conditions. Further, such approaches do not generalize to hardware that drift, ages, and/or are reconfigured. By contrast, the proposed digital twin, provides a physics-based, measurement-driven model that can be updated incrementally whenever a component is re-characterized. Thereby, they are more robust and extensible.

We further enhance the de-embedding process by introducing a digital twin-assisted framework that extends beyond static modeling. A digital twin, as defined in recent literature [20], is dynamic, intelligent, and incorporates an evolving virtual model that mirrors its physical counterpart using integrated measurements, historical data and optimization. By embedding this concept into the cancellation process, we enable a closed-loop calibration mechanism that actively compensates for physical deviations and refines RF filter design. Specifically, we identify and correct hardware impairments through targeted measurements, simulation, and optimization, and integrate these insights into a digital twin environment. This virtual counterpart allows us to model practical components minimizing the accuracy gap between the actual hardware and their ideal counterpart. This integration enhances the accuracy of the amplitude and phase cancellation, leading to high isolation across wide bandwidths.

This paper describes a two-stage self-interference cancellation strategy (Stages 1 and 2), highlighted in Fig. 2. We propose a de-embedding strategy, assisted by the digital twin framework. The goal is to counter fabrication imperfections as well as distortions due to connectors, cables, and device tolerances. The two stages of self-interference cancellation incorporate a typical 4-arm spiral antenna and an RF self-interference cancellation (SIC) filter. Integrating these stages with cables and connectors presents challenges due to their dispersive behavior, resulting in reduced transmitter-receiver isolation. Consequently, this passive canceller requires careful pre-design and integration to avoid use of active tuning components. To address these unavoidable distortions, in this paper, we characterize and de-embed each component and optimize the RF-SIC filter design to enhance second-stage cancellation. The goal of digital twin is to simulate and predict the impact of component deviations, facilitating optimization of the filter response. Indeed, by compensating for phase and amplitude deviations in the filter design, we significantly enhance isolation.

The key contributions and novelty of this paper are as follows. First, we introduce a digital twin-assisted de-embedding framework for broadband IBFD radio design. Unlike prior work that assumes idealized component models, our framework builds a measurement-driven virtual replica of the physical signal chain and derives a compensating filter design target that accounts for all practical deviations. Second, we employ transmission matrix (T-matrix) cascading to precisely characterize the cumulative effect of all interconnecting components including cables, connectors, splitters, and attenuators. Using this an inverse compensation is computed which is directly embedded into the RF-SIC filter design. Third, we experimentally demonstrate that this methodology yields an average improvement of 10–20 dB in combined antenna-plus-filter isolation across a 1 GHz bandwidth in the X-band (9.6–10.6 GHz), reaching a peak combined isolation of 65 dB with a fabricated prototype.

This paper is structured as follows. Section II outlines the implementation of digital twin models in a real world RF system. Section III details the combined two-stage cancellation for IBFD radios, focusing on the antenna and filter stages of cancellation. Section IV explains the de-embedding process. This involves the RF-SIC filter design and outlines deviations between practical and ideal components. Also, this section also highlights how to establish design rules and optimize practical RF-SIC filter designs. In section V, the effectiveness of the de-embedding process is assessed. Section VI provides concluding remarks.

II. DIGITAL-TWIN MODEL

The concept of a digital twin has emerged as a transformative approach in engineering, enabling dynamic

virtual models of physical systems. In the context of RF transceivers—particularly in complex, wideband in-band full-duplex (IBFD) radios, physical prototypes often suffer from non-idealities introduced by practical components, such as connectors, splitters, and cables. These elements introduce phase and amplitude mismatches that undermine the accuracy of practical system behavior versus their simulated counterparts. This discrepancy, known as the behavioral divergence, limit the effective self-interference cancellation (SIC), necessitating iterative physical prototyping. To bridge this gap, we adopt a digital twin framework that builds on traditional model-driven design principles. It incorporates measurement data, de-embedding techniques, and component-level characterization.

Unlike abstract or purely mathematical models, the digital twin creates a virtual representation that closely reflects the physical system. It identifies and de-embeds deviations between the physical prototype and the ideal model. This allows the system to compensate for component impairments during the design process, ensuring optimal performance. Fig. 1 outlines a de-embedding approach that reduces the behavioral gap between the digital model and its physical counterpart. It uses simulation and optimization to refine a digital prototype, which is validated through trial benchmarks. By comparing the practical prototype with a reference model, behavioral deviations are identified. These deviations guide parameter updates, enabling the digital prototype to better match real-world performance and minimize the accuracy gap.

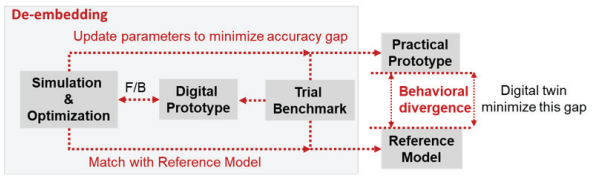


Fig. 1. A digital twin model to improve system performance in the real world.

In this paper, the digital twin enables high-fidelity modeling of the RF front end by embedding measurement-driven data into the design. That is, the design leverages S-parameter measurements, simulation feedback, and hardware characterization to build a closed-loop calibration model. This allows for predictive optimization of the RF-SIC filter response, aligning realistic information from signal propagation paths and interconnects. In particular, referring to Fig. 2, the digital twin supports:

- Precision modeling of the antenna-coupled and filter-coupled paths using measured scattering parameters,
- Dynamic compensation for component-induced phase and amplitude deviations via de-embedding,
- Iterative refinement of the filter parameters and architecture using updated transmission matrices derived from empirical data.

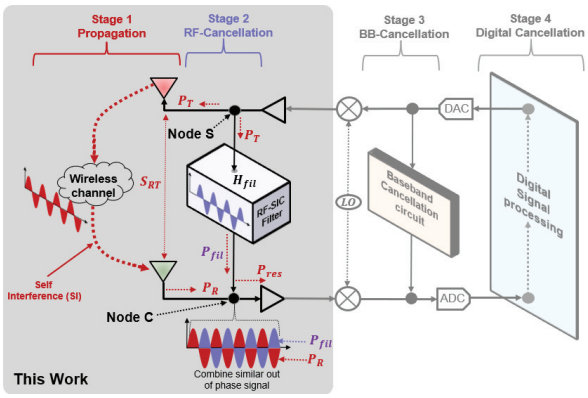


Fig. 2. IBFD radio schematic with self-interference cancellation circuitry.

Through a virtual-to-physical convergence, the digital twin model enables proactive tuning of the cancellation circuitry before fabrication. By doing so, there is significant improvement in matching the simulated measured system behavior. This approach not only enhances cancellation accuracy across a wide bandwidth, but also reduces the design cycle time and cost.

In this paper, we implemented the digital twin concept in developing an antenna plus filter package to enhance RF performance. The digital twin framework implemented herewith is feedback-driven to ensure that component mismatches are accurately represented and compensated for. By closely integrating measurements with virtual modeling, a robust and scalable RF cancellation strategy suitable for next-generation IBFD systems is achieved.

The computational implementation of the digital twin framework is straightforward and practical. The T-matrix cascade for N interconnecting components involves $\mathcal{O}(N)$ multiplications of 2×2 complex matrices. This operation is completed in milliseconds on standard computing hardware. Each component's S-parameters are measured once using a calibrated vector network analyzer (VNA), and the resulting T-matrices are cascaded to compute the equivalent mismatch matrix ΔT as defined in (6).

The filter optimization uses a Genetic Algorithm (GA) with a population of 100 individuals and a maximum of 500 generations for global search, followed by a Gradient Descent algorithm for local refinement. Notably, the combined optimization converges in approximately 10–15 minutes on a standard laptop

across the 1 GHz operating bandwidth. The digital twin model is then updated on-demand. This is done whenever: 1) a physical component is replaced or re-characterized, 2) its measured S-parameters are updated in the cascade, and when the filter design is redone. In the current implementation, two to three such iterations were sufficient to achieve the target isolation level.

An important practical concern was a potential divergence between the digital twin model and the physical hardware. This arises from unaccounted parasitic effects or measurement noise.

After each fabrication cycle, the measured combined isolation is compared against the de-embedded filter target prediction (Fig. 7). If a significant discrepancy is observed, the process is iterated and the affected components are re-measured, the T-matrix cascade is updated, and the filter design is refined. This measurement-grounded iterative loop ensures that the digital twin remains anchored to physical reality and prevents unchecked model drift.

III. TWO-STAGE CANCELLATION IN IBFD RADIOS

A typical IBFD radio is depicted in Fig 2. The first two stages of this multi-stage SIC begin with the antenna (Stage 1), followed by the RF filter (Stage 2). This paper focuses on designing/combining the first two stages of IBFD radio. Implementing this architecture requires the cancellation of the transmitted signals that leak into the receiver [21]. Past work [7] has shown that a 4-arm spiral antenna can achieve up to 40 dB of isolation using polarization diversity. One pair of this 4-arm spiral is used for transmission, and the other pair is used for reception. The RF-SIC filter behind the spiral provides for additional cancellation of the transmitted leakage signal. As much as 25 to 30 dB of SIC from the RF-SIC filter [22] (Stage 2) is expected. To achieve this, the filter must replicate the leaked antenna-coupled signal into the receiver [10].

To ensure high isolation, it is important to align the phase of the cancellation signal and to concurrently account for component impairments, added cables, and connectors. Due to the very low level of signals being processed, any amplitude and phase mismatches can lead to ineffective cancellation. Figure 3 shows the achievable 2nd stage RF-SIC cancellation with respect to phase and amplitude deviations. As depicted, even a few degrees in phase or a fraction of a dB mismatch between the antenna and cancellation circuitry can cause significant performance variations.

Assuming that the RF-SIC filter response is H_{fil} and the Tx-Rx antenna coupling is S_{RT} (see Fig. 2), the cancellation conditions are satisfied by

$$H_{fil}(j\omega) = -S_{RT}. \tag{1}$$

Alternatively, (1) can be stated as

$$|H_{fil}(j\omega)| = |S_{RT}|$$

and

$$\angle H_{fil}(j\omega) = \angle S_{RT} + (2n+1)\pi. \tag{2}$$

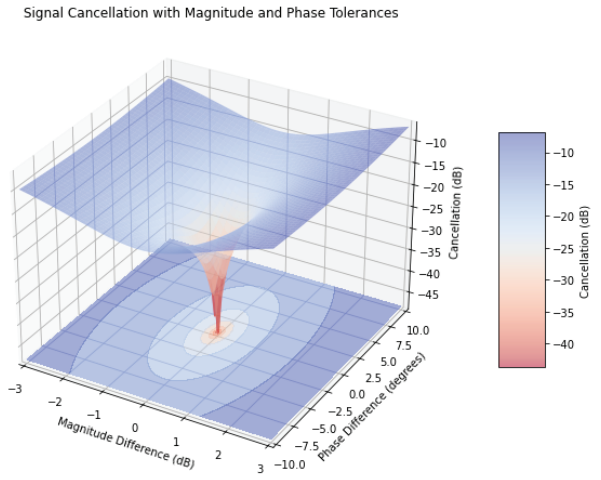


Fig. 3. Achievable cancellation in dB as a function of phase and amplitude mismatches.

Furthermore, for the sake of simplicity, we only consider analyzing the self-interference (SI) signal, ignoring the desired one. From Fig. 2, the second stage of signal cancellation occurs at node C. At this node, the coupled signal from node S is weighted (filtered) and used to cancel the incoming leakage SI signal P_R, which indeed is the coupled transmitted signal P_T after antenna stage cancellation. Figure 4 illustrates the first two stages of cancellation, where node S and node C are represented as splitter and combiner respectively. Following Fig. 4, the combined two-stage cancellation, SIC_{total} can be represented as

$$\begin{aligned} SIC_{total} &= -(S_{RT} + SIC_{RF}) \\ &= \underbrace{-20\left[log(S_{RT})}_{\textit{antenna isolation}} \underbrace{-20log\frac{P_T(S_{RT}-H_{fil})}{P_R}\right]}_{\textit{RF cancellation}} \\ &= -20\left[log(S_{RT}) - 20log\frac{S_{RT}-H_{fil}}{S_{RT}}\right]. \end{aligned} \tag{3}$$

The above equation corresponds to the total achievable cancellation for stages 1 and 2. All the parameters used in (3) are described in Fig. 4. And as noted, fabrication flaws, frequency-dependence, and the presence of parasitic effects in practical components impact the achievable cancellation in practice. To enhance the overall cancellation in the 2nd stage, the next section will describe a de-embedding process. Our goal is to account for any design deviations in the practical components.

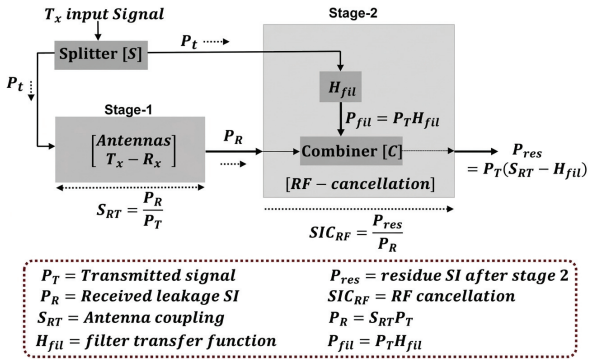


Fig. 4. Combined two-stage cancellation.

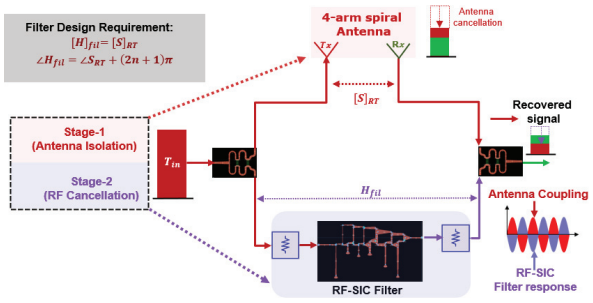


Fig. 5. Implementation of IBFD radio using practical components requires de-embedding.

IV. DE-EMBEDDING PROCESS

A. Implementing Stage 1 and 2

Past work has shown that a 4-arm spiral antenna (Stage 1) can achieve up to 40 dB of transmit/receive isolation [7]. As usual, the 4-arm spiral used one pair of arms for transmission and the other pair for reception. Subsequently, the RF-SIC filter is used to cancel the leakage P_R that is not canceled in the antenna stage.

Stage 2 is a RF filter constructed with a set of microstrip stubs load cascaded with specific delays to form the RF-SIC filter. Each RF filter stub was terminated with a radial section for broadband operation. Notably, each stub's impedance and length are key design parameters. Further, we used two attenuators on both sides of the filter to reduce power levels and counteract large signal mismatches. Unlike previous designs [10], our filter leverages the impedance and delay properties of the microstrip stubs, reducing the number of discrete components and avoiding bandwidth limitations. A filter order of 6 (using polynomial fit) achieved a desired 1 GHz bandwidth. Design optimizations led to a 6th order filter that was fabricated. The details of the periodic stub are given in [21]. However, when stages 1 and 2 were combined, even the addition of simple cables, splitters, or connectors between the antenna and the filter resulted in a severe impact in terms of RF cancellation. Below, we discuss a de-embedding approach to overcome the challenge.

B. Update filter design using de-embedding

The combined two-stage cancellation architecture (Stages 1 and 2) using practical components is depicted in Fig. 5. As noted, combining the antenna and filter stages requires additional components such as splitters, combiners, cables, connectors, and attenuators. Additionally, connecting cables between the antenna and filter stages introduces further phase delays. Therefore, the filter design must be updated to account for these practical effects.

Assuming n number of components present in stages 1 and 2 (see Fig. 5), we follow the de-embedding process shown in Fig. 6. To remove component impairments, we convert the corresponding scattering matrix (S-parameters) into a T-matrix for each component, comprising antenna and filter. This T-matrix is also called T-parameters or ABCD-Matrix [23]. This conversion requires measuring the S-parameters of each component and then converting them to the corresponding T-matrices. To do that, the first step involves converting the antenna coupling S_{ant} into a T-matrix (ABCD). S_{ant} can be expressed as

$$S_{ant} = \begin{bmatrix} S_{TT} & S_{TR} \\ S_{RT} & S_{RR} \end{bmatrix}. \tag{4}$$

By converting S_{ant} into T-matrix, we have

$$T_{ant} = \frac{1}{S_{RT}} \begin{bmatrix} det(S_{ant}) & S_{TT} \\ -S_{RR} & 1 \end{bmatrix} = \begin{bmatrix} A_{RT} & B_{RT} \\ C_{RT} & D_{RT} \end{bmatrix}, \tag{5}$$

where $det(S_{ant}) = S_{TT}S_{RR} - S_{TR}S_{RT}$. The next step (see Fig. 6) is to take out the effect of combined component impairment. To do that, first we need to estimate the equivalent compensating T-matrix, ΔT which corresponds to the total deviations of all practical components from their ideal counterparts. Later, we used its inverse matrix for de-embedding component impairment as follows

$$\begin{aligned} T_{ant,dmb} &= T_{ant}(\Delta T)^{-1} \\ &= \begin{bmatrix} A_{RT} & B_{RT} \\ C_{RT} & D_{RT} \end{bmatrix} \cdot \begin{bmatrix} A_\Delta & B_\Delta \\ C_\Delta & D_\Delta \end{bmatrix}^{-1} \\ &= \begin{bmatrix} A_{dmb} & B_{dmb} \\ C_{dmb} & D_{dmb} \end{bmatrix}, \end{aligned} \tag{6}$$

where,

$$\Delta T = T_{eq}^{true}(T_{eq}^{ideal})^{-1} = \prod_{i=1}^{n} T_i^{true}(T_i^{ideal})^{-1}.$$

Providing the equivalent practical and ideal T-matrices as

$$T_{eq}^{true} = \prod_{i=1}^{n} T_i^{true} \quad and \quad T_{eq}^{ideal} = \prod_{i=1}^{n} T_i^{ideal}.$$

Furthermore, following step 4 in Fig. 6 and converting (6) back into S-matrix gives $S_{RT,dmb}$ as

$$S_{RT,dmb} = \frac{2}{A_{dmb} + B_{dmb} + C_{dmb} + D_{dmb}}. \tag{7}$$

Using (7), we can update (1) to satisfy the new filter design requirements as

$$H_{fil}(j\omega) = -S_{RT,dmb}, \tag{8}$$

which implies

$$|H_{fil}(j\omega)| = |S_{RT,dmb}|$$

and

$$\angle H_{fil}(j\omega) = \angle S_{RT,dmb} + (2n+1)\pi. \tag{9}$$

To assess the robustness of the de-embedding procedure, we considered measurement uncertainties through the T-matrix cascade. Each component's S-parameters were measured using a calibrated VNA with a typical uncertainty of ± 0.1 dB in magnitude and $\pm 1^\circ$ in phase. This was done after SOLT (Short-Open-Load-Through) calibration within the 9.6–10.6 GHz band. For the six cascaded components used in this work (antenna, splitter, two cables, attenuator, and combiner), the root-sum-square (RSS) estimate of cumulative phase uncertainty was approximately $\pm 2.5^\circ$. Referring to the sensitivity analysis in Fig. 3, a $\pm 2.5^\circ$ phase deviation corresponds to a reduction in achievable RF cancellation of less than 2 dB. This confirms that the de-embedding procedure is robust to address the VNA measurement uncertainty.

A notable advantage of the proposed architecture is that it introduces no additional DC power consumption. This is because the RF-SIC filter, attenuators, splitters, and phase trimmer are all passive components. The primary power-related cost is the insertion loss of the combined filter and coupling network. This insertion loss is approximately 4–6 dB across the 9.6–10.6 GHz operating band. Therefore, it must be accounted for in the overall link budget. It is offset by the significant improvement in receiver isolation achieved through de-embedding. Notably, active RF cancellation approaches achieve similar isolation levels, and typically require several hundred milliwatts of DC power for amplifiers, DACs, and control logic.

Figure 6 illustrates the de-embedding process to compensate for practical deviations from ideal components. Figure 7 shows the filter design algorithm

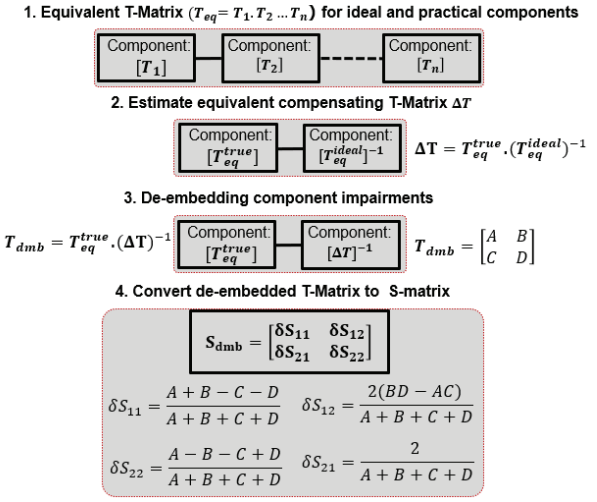


Fig. 6. De-embedding ideal vs. practical component mismatch and compensation.

incorporating de-embedding. This approach restores the expected output by compensating for component impairments in filter design. This strategy ensures accurate modeling and optimization of filter to enhance practical isolation in the RF cancellation stage.

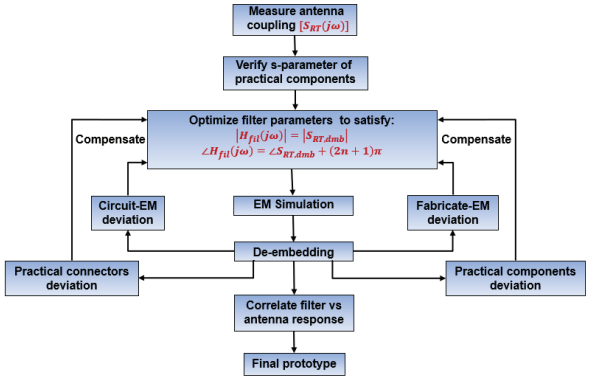


Fig. 7. Filter design algorithm.

V. MEASUREMENT RESULTS AND DISCUSSION

The experimental validation was carried out using a calibrated two-port VNA. Prior to full system integration, the S-parameters of each individual component including the SMA cables, broadband splitter/combiner pair, attenuators, and the 4-arm spiral antenna, were measured separately following SOLT calibration at the measurement reference planes. These measured S-parameters were used to populate the T-matrix cascade in the de-embedding process described in section IV. The fabricated 4-arm spiral antenna and RF-SIC filter board (Fig. 9) were stacked vertically

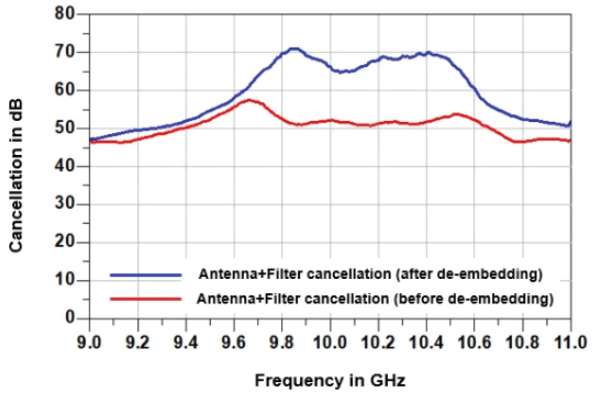


Fig. 8. Combined two stages with and without de-embedding.

and connected using phase-matched cables. Combined isolation measurements (S_{21} from Tx port to Rx port), were taken across the 9.0–11.0 GHz range, with the target band being 9.6–10.6 GHz. All measurements were performed under controlled bench conditions to minimize parasitic reflections.

To illustrate the effectiveness of the combined two-stage isolation of the IBFD front end, we conducted measurements of combined antenna and filter cancellation both before and after de-embedding. As seen in Fig. 9, a phase trimmer was used to compensate for phase impairments to enhance isolation. As shown in Fig. 8, the combined isolation is initially constrained within 50 dB due to the effects of non-ideal components. However, after de-embedding and taking out the effect in filter design, combined isolation was increased up to 65 dB across 1 GHz bandwidth, as depicted in Fig. 8. Using de-embedding, a significant improvement of 10–20 dB of isolation can be seen in Fig. 10 across the entire 1 GHz bandwidth from 9.6 GHz to 10.6 GHz.

To better understand the physical mechanism behind the isolation improvement, it is important to trace the source of degradation before de-embedding. When stages 1 and 2 are combined using practical components, each element introduces a small but non-trivial phase delay with amplitude modification that deviates from its idealized model. These individual deviations accumulate across the full signal chain, resulting in a composite phase and amplitude mismatch between the RF-SIC filter output and the antenna-coupled leakage signal arriving at the combiner node (Node C in Fig. 2). As illustrated in Fig. 3, even a 3–5° phase error can reduce achievable cancellation by 10 dB or more.

Before de-embedding, the RF-SIC filter was designed to satisfy the ideal condition $H_{fil}(j\omega) = -S_{RT}(j\omega)$, without accounting for the intervening practical components. As a result, the combined system isolation was constrained to approximately 50 dB across the 1 GHz band (Fig. 8).

The de-embedding process corrects this by: (1) individually measuring the S-parameters of each component in the chain; (2) converting them to T-matrices and computing the overall equivalent mismatch matrix ΔT (from 6); and (3) deriving an updated filter design target $S_{RT,dmb}$ that incorporates the inverse of ΔT. When the RF-SIC filter is redesigned to satisfy $H_{fil}(j\omega) = -S_{RT,dmb}(j\omega)$, the filter response at the combiner node is effectively pre-distorted to cancel the adverse effects of all practical components. The result is a 10–20 dB improvement in isolation across the entire 1 GHz band. This is a direct consequence of restoring phase and amplitude alignment at the combiner node after accounting for all hardware impairments.

This demonstration can verify that careful consideration of hardware impairments and the effectiveness of the de-embedding process can enhance overall IBFD performance.

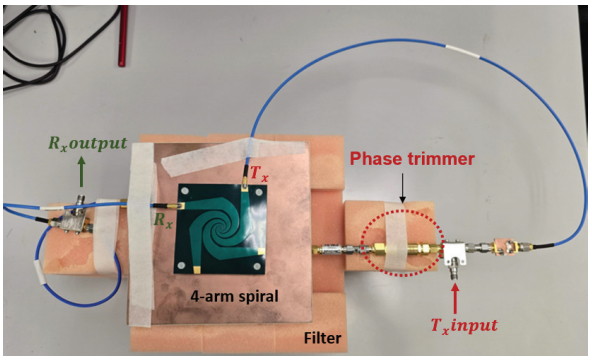


Fig. 9. Fabricated IBFD antenna and filter prototype.

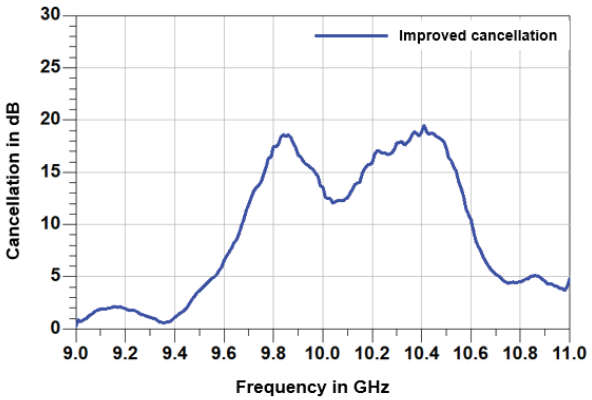


Fig. 10. Improved isolation after de-embedding.

Table 1 compares the proposed digital twin-assisted de-embedding approach against a representative set of recently published IBFD and STAR system implementations. Among passive microstrip designs, prior works

Table 1: Comparison of performance with existing state-of-the-art STAR/IBFD system implementations

Ref.	Technology/Design	Bandwidth	Isolation	Circuit	Stages	Process
[8]	Antenna + Resonator	520 MHz	30 dB	Passive	1	Microstrip
[5]	Multi-tap delay line	200 MHz	45 dB	Active	1	Switch cap.
[11]	Antenna + SIC Filter	500 MHz	44 dB	Passive	2	Microstrip
[24]	LNA + EBD	500 MHz	44 dB	Passive	2	Microstrip
[18]	Photonic mixers	1 GHz	28 dB	Photonic	2	Photonic
[25]	Co-polarized antenna	100 MHz	25 dB	Passive	1	MS (defected gnd.)
[26]	Antenna + circulator	400 MHz	40 dB	Active	2	Microstrip
[27]	Hybrid metamaterial-TL	500 MHz	39 dB	Active	1	Microstrip
[12]	Tapped delay line	120 MHz	50 dB	Passive	2	Microstrip
[28]	Cavity-like structure	400 MHz	43 dB	Passive	1	Cavity slot
[29]	Co-horiz. pol. antennas	520 MHz	37 dB	Passive	1	Multi-layer MS
[30]	Dual polarized + rat race	280 MHz	50 dB	Active	2	Microstrip
[31]	Dual polarized antenna	100 MHz	47 dB	Passive	1	Microstrip
[15]	Multi-tap SIC	20 MHz	30 dB	Passive	1	Microstrip
***This Work**	**DT-Assisted RF-SIC + 4-arm Spiral**	**1 GHz**	**$>$65 dB**	**Passive**	**2**	**Microstrip**

*DT = Digital Twin; MS = Microstrip; EBD = Electrical Balance Duplexer.

have demonstrated bandwidths ranging from 20 MHz to 520 MHz, with combined isolation levels of 25–50 dB. The proposed approach achieves a combined isolation exceeding 65 dB across a contiguous 1 GHz bandwidth in the X-band, representing a 10–20 dB improvement over the best comparable passive implementations. Unlike active or mixed-signal approaches that require digital converters or external tuning hardware, our architecture relies entirely on passive components characterized through the digital twin-assisted de-embedding workflow. This is a cost-effective and scalable method, and is directly applicable to next-generation IBFD radio platforms.

The proposed digital twin-assisted de-embedding framework offers several practical advantages. First, it is entirely passive and requires no active components, ADCs, or tuning circuits, making it inherently low-cost and power-efficient. Second, the methodology is modular. That is, each component is individually characterized from standard VNA measurements, making it straightforward to apply to new hardware configurations. Third, the iterative closed-loop structure allows the digital twin to be refined as prototypes are fabricated, reducing design cycle time.

The primary applications of this work include: (1) next-generation 5G/6G base stations requiring simultaneous transmit and receive over wide bandwidths; (2) cognitive radio architectures exploiting IBFD for dynamic spectrum access; (3) radar-communications coexistence systems where transmitter-receiver isolation is critical; and (4) tactical military communication systems requiring compact, passive, wideband IBFD front ends.

In closing, it is important to note some limitations. The de-embedding procedure is hardware-specific. That is, when a physical component is replaced or the system topology changes, re-characterization and filter re-optimization are required. The achievable isolation is also bounded by the accuracy of the phase trimmer and the SNR of the VNA measurement setup. Furthermore, in highly dynamic wireless channels where the self-interference channel may vary rapidly, this passive approach may require supplemental digital cancellation at the baseband stage.

VI. CONCLUSION

Our study presents a novel de-embedding approach to enhance the isolation in broadband IBFD radios through a strategic combination of advanced antenna design and RF-SIC filter realization. The successful implementation of our digital-twin aided de-embedding strategy not only enhances isolation but also ensures the robust performance of IBFD systems across a wide bandwidth in the X-band. Our proven de-embedding method increased cancellation by up to 15 dB on average across the whole 1 GHz bandwidth, reaching a maximum of 65 dB when the first two stages were combined. This work paves the way for more efficient and low-cost IBFD radio designs in future communications systems.

Looking ahead, several directions merit further investigation. First, the digital twin framework given here can be extended to reconfigurable and electronically tunable RF-SIC filter architectures, enabling real-time adaptation to changes in hardware state or operating frequency. Second, integration of the proposed analog-domain cancellation with subsequent baseband and digital cancellation stages (Stages 3 and 4 in Fig. 2) would allow a full-system evaluation of the combined isolation chain. Third, the de-embedding methodology

is not limited to the X-band and can be applied to sub-6 GHz and mmWave IBFD systems with appropriate component characterization. Finally, further study into automated, sensor-embedded digital twin calibration for tracking component drift with near real-time compensation represents a promising avenue toward fully self-calibrating IBFD radios.

ACKNOWLEDGMENT

This work was partially funded by NSF IUCRC, NSF SWIFT, and NSF ENG-ADVWIRE:CCSS under the grant numbers 2052764, 2128628, and 2430828, respectively.

REFERENCES

[1] G. R. B. Injila, "In band full duplex (IBFD) technology for next generation wireless networks: A survey in cellular networks," *China Communications*, vol. 20, no. 5, pp. 20–39, 2023.

[2] M. R. Rahman, S. Bojja Venkatakrishnan, T. Nakatani, and J. L. Volakis, "Wideband Self Interference Cancellation (SIC) RF front end for Simultaneous Transmit and Receive (STAR) radios," in *2022 IEEE International Symposium on Antennas and Propagation and USNC-URSI Radio Science Meeting (AP-S/URSI)*, pp. 948–949, 2022.

[3] M. R. Rahman, S. Bojja-Venkatakrishnan, and J. L. Volakis, "Ultra-wideband RF Self interference cancellation filter for STAR radios," in *2021 IEEE International Symposium on Antennas and Propagation and USNC-URSI Radio Science Meeting (APS/URSI)*, pp. 523–524, 2021.

[4] K. E. Kolodziej, B. T. Perry, and J. S. Herd, "In-band full-duplex technology: Techniques and systems survey," *IEEE Transactions on Microwave Theory and Techniques*, vol. 67, no. 7, pp. 3025–3041, 2019.

[5] C. W. Morgenstern, Y. Rong, A. Herschfelt, A. C. Molnar, A. B. Apsel, D. G. Landon, and D. W. Bliss, "Analog-domain self-interference cancellation for practical multi-tap full-duplex system: Theory, modeling, and algorithm," *IEEE Journal on Selected Areas in Communications*, vol. 41, no. 9, pp. 2796–2807, 2023.

[6] B. Debaillie, D.-J. van den Broek, C. Lavín, B. van Liempd, E. A. M. Klumperink, C. Palacios, J. Craninckx, B. Nauta, and A. Pärssinen, "Analog/RF solutions enabling compact full-duplex radios," *IEEE Journal on Selected Areas in Communications*, vol. 32, no. 9, pp. 1662–1673, 2014.

[7] A. Hovsepian, E. A. Alwan, and J. L. Volakis, "A wideband, scanning array of four-arm spiral elements for simultaneous transmit and receive," *IEEE Antennas and Wireless Propagation Letters*, vol. 19, no. 4, pp. 537–541, 2020.

[8] X.-K. Zhang, Y.-H. Ke, X.-Y. Wang, S.-C. Tang, and J.-X. Chen, "Broadband dual-polarized dielectric patch antenna with high isolation for full-duplex communication," *IEEE Antennas and Wireless Propagation Letters*, vol. 22, no. 4, pp. 878–882, 2023.

[9] K. J. Tang, L. H. Ye, W. J. Zhu, J.-F. Li, and D.-L. Wu, "Broadband dual-polarized magnetoelectric dipole antenna for in-band full-duplex application," *IEEE Antennas and Wireless Propagation Letters*, vol. 22, no. 9, pp. 2210–2214, 2023.

[10] S. Bojja Venkatakrishnan, E. A. Alwan, and J. L. Volakis, "Wideband RF self-interference cancellation circuit for phased array simultaneous transmit and receive systems," *IEEE Access*, vol. 6, pp. 3425–3432, 2018.

[11] M. N. A. Tarek and E. A. Alwan, "Wideband, low profile coupling suppression circuit for simultaneous transmit and receive system based on hybrid finite impulse response and resonator topology," *IEEE Access*, vol. 10, pp. 126508–126515, 2022.

[12] K. E. Kolodziej, J. G. McMichael, and B. T. Perry, "Multitap RF canceller for in-band full-duplex wireless communications," *IEEE Transactions on Wireless Communications*, vol. 15, no. 6, pp. 4321–4334, 2016.

[13] H. Li, J. Van Kerrebrouck, O. Caytan, H. Rogier, J. Bauwelinck, P. Demeester, and G. Torfs, "Self-interference cancellation enabling high-throughput short-reach wireless full-duplex communication," *IEEE Transactions on Wireless Communications*, vol. 17, no. 10, pp. 6475–6486, 2018.

[14] A. Kiayani, M. Z. Waheed, L. Anttila, M. Abdelaziz, D. Korpi, V. Syrjälä, M. Kosunen, K. Stadius, J. Ryynänen, and M. Valkama, "Adaptive nonlinear RF cancellation for improved isolation in simultaneous transmit–receive systems," *IEEE Transactions on Microwave Theory and Techniques*, vol. 66, no. 5, pp. 2299–2312, 2018.

[15] Y. Liu, X. Quan, W. Pan, and Y. Tang, "Digitally assisted analog interference cancellation for in-band full-duplex radios," *IEEE Communications Letters*, vol. 21, no. 5, pp. 1079–1082, 2017.

[16] X. Yu, J. Ye, L. Yan, T. Zhou, X. Zou, and W. Pan, "Photonic-assisted multipath self-interference cancellation for wideband MIMO radio-over-fiber transmission," *Journal of Lightwave Technology*, vol. 40, no. 2, pp. 462–469, 2022.

[17] Y. Xing, S. Li, X. Xue, and X. Zheng, "Photonic-assisted RF self-interference cancellation based on optical spectrum processing," *Journal of Lightwave Technology*, vol. 40, no. 7, pp. 2015–2022, 2022.

[18] X. Hu, D. Zhu, S. Liu, H. Xiao, and S. Pan, "Photonics-assisted simultaneous RF channelization and self-interference cancellation," *Journal of Lightwave Technology*, vol. 41, no. 18, pp. 5902–5910, 2023.

[19] C. W. Morgenstern, Y. Rong, A. Herschfelt, A. C. Molnar, A. B. Apsel, D. G. Landon, and D. W. Bliss, "Analog-domain self-interference cancellation for practical multi-tap full-duplex system: Theory, modeling, and algorithm," *IEEE Journal on Selected Areas in Communications*, vol. 41, no. 9, pp. 2796–2807, 2023.

[20] B. R. Barricelli, E. Casiraghi, and D. Fogli, "A survey on digital twin: Definitions, characteristics, applications, and design implications," *IEEE Access*, vol. 7, pp. 167653–167671, 2019.

[21] M. R. Rahman, S. Bojja-Venkatakrishnan, and J. L. Volakis, "Miniature footprint of multi-stage self interference cancellation in a STAR radio," in *2023 IEEE International Symposium on Antennas and Propagation and USNC-URSI Radio Science Meeting (USNC-URSI)*, pp. 77–78, 2023.

[22] M. R. Rahman, S. Bojja-Venkatakrishnan, M. Pulugurtha, and J. L. Volakis, "Miniaturization of RF SIC filter on high-K ceramic substrate for STAR application," in *2024 United States National Committee of URSI National Radio Science Meeting (USNC-URSI NRSM)*, p. 105, 2024.

[23] D. M. Pozar, *Microwave Engineering*, 3rd ed. Hoboken, NJ: Wiley, 2005.

[24] J.-T. Lim, H.-W. Choi, J.-H. Song, and C.-Y. Kim, "An in-band full-duplex low noise amplifier integrated with an electrical balance duplexer without explicit matching," *IEEE Microwave and Wireless Technology Letters*, vol. 33, no. 8, pp. 1175–1178, 2023.

[25] M. Abedian, M. Khalily, P. Xiao, F. Wang, R. Tafazolli, and A. A. Kishk, "MM-wave high isolated dual polarized dielectric resonator antenna for in-band full-duplex systems," *IEEE Access*, vol. 11, pp. 38218–38225, 2023.

[26] M. N. A. Tarek, M. R. Guerra, A. Nunez, M. N. Uddin, and E. A. Alwan, "Improving isolation in monostatic simultaneous transmit and receive systems using a quasi-symmetrical self-interference cancellation architecture," *IEEE Journal of Microwaves*, vol. 3, no. 2, pp. 655–664, 2023.

[27] K. Y. Yang, W. J. Zhu, L. H. Ye, J.-F. Li, and D.-L. Wu, "Metamaterial-based low-profile broadband in-band full-duplex antenna," *IEEE Antennas and Wireless Propagation Letters*, vol. 22, no. 8, pp. 1942–1946, 2023.

[28] C. J. Ma, S. Y. Zheng, and Y. M. Pan, "Millimeter-wave co-polarized in-band full-duplex antenna based on a mode superposition method," *IEEE Transactions on Antennas and Propagation*, vol. 71, no. 6, pp. 4675–4685, 2023.

[29] D. Wu, Y.-X. Sun, R. Lian, B. Xiao, M. Li, and K.-D. Xu, "Metasurface antenna with cocircularly polarized radiation characteristics for wideband monostatic simultaneous transmit and receive applications," *IEEE Transactions on Antennas and Propagation*, vol. 71, no. 4, pp. 3304–3313, 2023.

[30] Y.-N. Chen, C. Ding, H. Zhu, and Y. Liu, "A $\pm 45^{\circ}$-polarized antenna system with four isolated channels for In-Band Full-Duplex (IBFD)," *IEEE Transactions on Antennas and Propagation*, vol. 71, no. 4, pp. 3000–3010, 2023.

[31] Q. Tan and K.-M. Luk, "Wideband co-linearly polarized magneto-electric dipole antenna for in-band full-duplex applications," *IEEE Transactions on Antennas and Propagation*, vol. 71, no. 2, pp. 1907–1912, 2023.

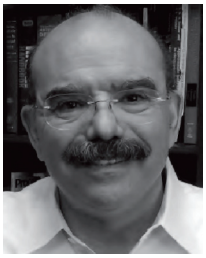


Md Rakibur Rahman (Member, IEEE) received his Bachelor's and Master's degrees in Applied Physics, Electronics, and Communication Engineering from the University of Dhaka, Bangladesh, in 2010 and 2012, respectively. From 2012 to 2017, he worked as a telecommunications engineer in Bangladesh. He later pursued a second Master's degree (2022) and a Ph.D. (2024) in Electrical Engineering at Florida International University (FIU), Miami, FL, USA. Following his Ph.D., he worked as a Postdoctoral Associate at the RFCOM Lab at FIU until April 2025. He is currently working as a Wireless Systems Engineer at Apple. Since 2018, his research has focused on developing simultaneous transmit and receive (STAR) radio and secure wireless communication links. His research interests include spectral-efficient radio communication, in-band full-duplex radio (IBFD), interference mitigation in wireless links, ultra-wideband wireless communication, software-defined radio (SDR), high-speed wireless communication system benchmarks, RF transceiver design, and the modeling and design of high-performance RF components using advanced circuit-EM simulation tools.



Satheesh Bojja Venkatakrishnan (Senior Member, IEEE) was born in Tiruchirappalli, India, in 1987. He received the bachelor's degree in electronics and communication engineering from the National Institute of Technology Tiruchirappalli, in 2009, and the M.S. and Ph.D. degrees in electrical engineering from The Ohio State University (OSU), Columbus, OH, USA, in 2017. He was a Scientist at DRDO, India, from 2009 to 2013, working on the development and implementation of active electronic steerable antennas. He is currently a Research Assistant Professor of electrical and computer engineering at Florida International University.

His current research interests include receiver design for communication circuits, RF systems, and digital signal processing using FPGAs. He is also working on simultaneous transmit and receive systems (STAR), to improve the spectral efficiency. He has been a Phi Kappa Phi Member, since 2015, and is also an Associate Member of USNC–URSI. He was a recipient of the IEEE Electromagnetic Theory Symposium (EMTS2019) Young Scientist Award. He won the 2nd prize in International Union of Radio Science General Assembly and Scientific Symposium (URSI-GASS) Student Paper Competition held at Montreal, Canada, in August 2017. He also received the Honorable Mention in the Student Paper Competition at the IEEE Antenna and Propagation Symposium (AP-S/URSI), in 2015 and 2016, and the Student Fellowship Travel Grant Award at the U.S. National Committee for the International Union of Radio Science (USNC–URSI), in 2016 and 2017.



John L. Volakis (S'77-M'82-SM'89-F96) obtained his B.E. Degree, summa cum laude, in 1978 from Youngstown State Univ., Youngstown, Ohio, M.Sc. in 1979 from The Ohio State Univ., Columbus, Ohio and the Ph.D. degree in 1982, also from the Ohio State Univ.

Prof. Volakis started his career at Rockwell International North American Aircraft Operations (1982–84), now Boeing. In 1984, he was appointed Assistant Professor at the University of Michigan, Ann Arbor, MI, becoming a full Professor in 1994. He also served as the Director of the Radiation Laboratory from 1998 to 2000. From January 2003 to Aug. 2017 he was the Roy and Lois Chope Chair Professor of Engineering at the Ohio State University, Columbus, Ohio and served as the Director of the ElectroScience Laboratory from 2003 to 2016. From 2017–2023 he was the Dean of the College of Engineering and Computing. Since 2023, he is a Professor in the Electrical and Computer Engineering at Florida International University (FIU).

Over the years, he carried out research in computational methods, antennas, wireless communications and propagation, electromagnetic compatibility and interference, design optimization, RF materials, multi-physics engineering, millimeter waves, terahertz and medical sensing. His publications include 9 books, over 450 journal papers and 950 conference papers, 33 book chapters and 32 patents/disclosures. Among his co-authored books are: *Approximate Boundary Conditions in Electromagnetics*, 1995; *Finite Element Methods for Electromagnetics*, 1998; 4th and 5th ed. *Antenna Engineering Handbook*, 2007 and 2019; *Small Antennas*, 2010; *Integral Equation Methods for Electromagnetics*, 2011; and *Wearable Antennas and Electronics*, Artech House, 2022. He has graduated/mentored over 100 doctoral students/post-docs with 44 of them receiving best paper awards at conferences. His service to Professional Societies include: 2004 President of the IEEE Antennas and Propagation Society (2004), Chair of USNC/URSI Commission B (2015–2017), Chair and Vice Chair of the International Radio Science Union (URSI) Commission B (2017–23), twice the general Chair of the IEEE Antennas and Propagation Symposium, IEEE APS Distinguished Lecturer, IEEE APS Fellows Committee Chair, IEEE-wide Fellows committee member & Associate Editor of several journals. He was listed by ISI among the top 250 most referenced authors (2004). Among his awards are: The Univ. of Michigan College of Engineering Research Excellence award (1993), Scott award from The Ohio State Univ. College of Engineering for Outstanding Academic Achievement (2011), IEEE AP Society C-T. Tai Teaching Excellence award (2011), IEEE Henning Mentoring award (2013), IEEE Antennas & Propagation Distinguished Achievement award (2014), The Ohio State University Distinguished Scholar Award (2016), The Ohio State Univ. ElectroScience Lab. George Sinclair Award (2017), URSI Booker Gold Medal (2020), Advanced Computational Electromagnetics Society Fellow, American Association for the Advancement of Science Fellow, and National Academy of Inventors Fellow (2021).

Three-Port Common Aperture Metasurface Antenna Designed Using Characteristic Mode Analysis

Z. N. Jiang[1,2], L. Wu[1], B. Z. Sun[1], and L. L. Yu[1]

[1]School of Computer and Information
Hefei University of Technology, Hefei, China
jiangzhaoneng@hfut.edu.cn, 2916956457@qq.com, 2909503223@qq.com, yll@hfut.edu.cn

[2]National Mobile Communications Research Laboratory
Southeast University, Jiangsu, China

Abstract – In this paper, a three-port common aperture antenna based on metasurface (MTS) is presented. The omnidirectional radiation pattern of the two frequency bands is excited through the coupling of the central coaxial cable and the slit feed, respectively. The annular microstrip structure is introduced into the multi-layer structure design to generate wide-beam radiation along the +Z-axis. Characteristic modal analysis (CMA) is used to adjust the shape and size of the MTS patch to increase the bandwidth of the omnidirectional mode. The optimized antenna size is $1.25\lambda \times 1.25\lambda \times 0.1\lambda_{\min}$. Simulation and measurement results show that the omnidirectional radiation characteristics can be realized in dual-band impedance bandwidths of 2.92–3.08 GHz and 4.11–4.69 GHz, respectively. In the 1.74–1.87 GHz band, the half-power beamwidth (HPBW) of the E and H planes is at least 100° and 80°, respectively. The antenna achieves the performance of multi-band and wide-angle radiation while saving space volume as much as possible.

Index Terms – CMA, metasurface (MTS), omnidirectional, three-port, wide-beam.

I. INTRODUCTION

With the continuous development of wireless communication technology in various communication applications, common aperture antennas have been widely concerned because of their multi-function integration, such as multi-frequency band and multi-radiation direction, which can effectively reduce the cost and volume of the system. At present, common-aperture antennas are widely used in military, commercial, and medical fields [1–6], also synthetic aperture radar [2], low Earth orbit satellites [3, 4], and mobile communications [5].

Metasurface (MTS) can increase bandwidth and reduce antenna size [7–10], and is often viewed as a 2D metamaterial [11]. In [12], the three modes of the MTS are combined with the mode of the slot to achieve an impedance bandwidth of more than 79% under multi-mode resonance. The MTS antenna in [13] is miniaturized by reducing the side gap and expanding the center gap to achieve good bandwidth. In [14], wideband impedance matching is achieved by loading non-uniform MTS onto a stair-shape aperture.

Characteristic modal analysis (CMA) is a suitable antenna design method that mainly analyzes the radiation behavior of the antenna from a physical perspective by studying the current distribution of the characteristic mode [15, 16]. In particular, there are some examples based on CMA in the optimized design of MTS structures. In [17], a method is proposed for designing an anisotropic complementary metantenna that combines low sidelobe levels and low in-band co-polarized scattering for wide-side radiation. An example is provided in reference [18] of loading a 3×3 square MTS cell array to help the antenna achieve dual-band operation, where four cells are cut at the corners to suppress unwanted patterns.

In this paper, a three-port share-aperture antenna based on MTS is designed by using the merit adaptability of the share-aperture structure to the scarce space resources and the complex space structure, and by using the CMA. Two radiation effects of omnidirectional radiation and wide-beam radiation are realized by feeding excitation at different positions of the upper microstrip patch. Simulation and measurement results show that the proposed three-port common aperture antenna achieves an omnidirectional radiation effect in the dual-band impedance bandwidths of 2.92–3.08 GHz and 4.1–4.69 GHz, respectively, and a wide-beam radiation effect in the band of 1.74–1.87 GHz.

Submitted On: September 03, 2025
Accepted On: July 07, 2026

1054-4887 © ACES

https://doi.org/10.13052/2026.ACES.J.410702

II. ANTENNA DESIGN AND ANALYSIS

A. Steps of antenna design and analysis

In wide-beam antenna design, 3-dB beamwidth is critical. A 360° beamwidth on a plane defines an omnidirectional antenna. For MTS-based antennas, a rectangular MTS with central capacitive coupling excitation (CCE) is commonly used for omnidirectional radiation. However, the CCE structure introduces a deviation in the resonant frequency predicted by characteristic mode theory by altering the field distribution on the microstrip patch. To systematically address this issue, CMA is adopted here as a design tool. CMA provides a physical basis for selecting modes that are close to resonance and exhibit desired radiation patterns. By comparing rectangular and circular MTS layouts (Fig. 1), modes with omnidirectional or wide-beam potential are identified based on their characteristic currents and 3D patterns. The following subsections detail the CMA-guided design process.

Figure 1 shows the 4×4 rectangular MTS (MTS1) and circular MTS (MTS2) structures with their modal significance (MS) curves, where MS indicates how close a mode is to resonance (MS $=$ 1 for ideal resonance). The mode currents and radiation patterns for MTS1 and MTS2 are also presented. The modal solutions of the MTS structures are analyzed using CST. The MS curve of MTS1 shows good matching potential in the 4–6 GHz band. Modes 1, 2, and 10 with potential omnidirectional radiation potential are selected. However, considering the limitations of the antenna feed structure, the current distribution should be in a state of uniform divergence around to form a good vertical polarization characteristic. Mode 10 conforming to the feed structure is selected, but its antenna pattern roundness on the E plane is higher than 4 dB, and the radiation beamwidth on the H plane still needs to be further optimized.

To improve the omnidirectional pattern roundness, the rectangular MTS is replaced by a circular one (MTS2 in Fig. 1). Modes with modal significance MS $>$ 0.5 (meaning the mode is sufficiently close to resonance and can be effectively excited) and regular 3D patterns are displayed to analyze the required radiation modes. Eight modes are thus selected.

Modes 3, 4, 5, and 11 of MTS2 all have the potential of omnidirectional radiation. By analyzing the surface current, mode 11 is selected as the omnidirectional radiation mode. In addition, although modes 9 and 10 do not have omnidirectional radiation characteristics, they have broad beam radiation characteristics along the X- and Y-axis. The current distribution of mode 9 and mode 10 is basically the same, except that mode 9 is polarized along the X -axis and mode 10 is polarized along the Y-axis, so mode 9 and mode 10 are a pair of merging modes. In the two modes, the feed position of capacitive coupling excitation is inconsistent with that of omnidirectional radiation excitation, so a circular microstrip patch can be used to stimulate dual-polarized radiation to achieve a wide-beam common aperture structure design. At the same time, the capacitive patch structure directly connected with the inner conductor of the coaxial line was optimized, and the final microstrip patch structure design is shown in Fig. 2 (a). The surface current distribution of optimized modes 11, 9, and 10 at 4 GHz is shown in Fig. 2 (b). In addition, considering that the antenna has the potential of multi-layer structure

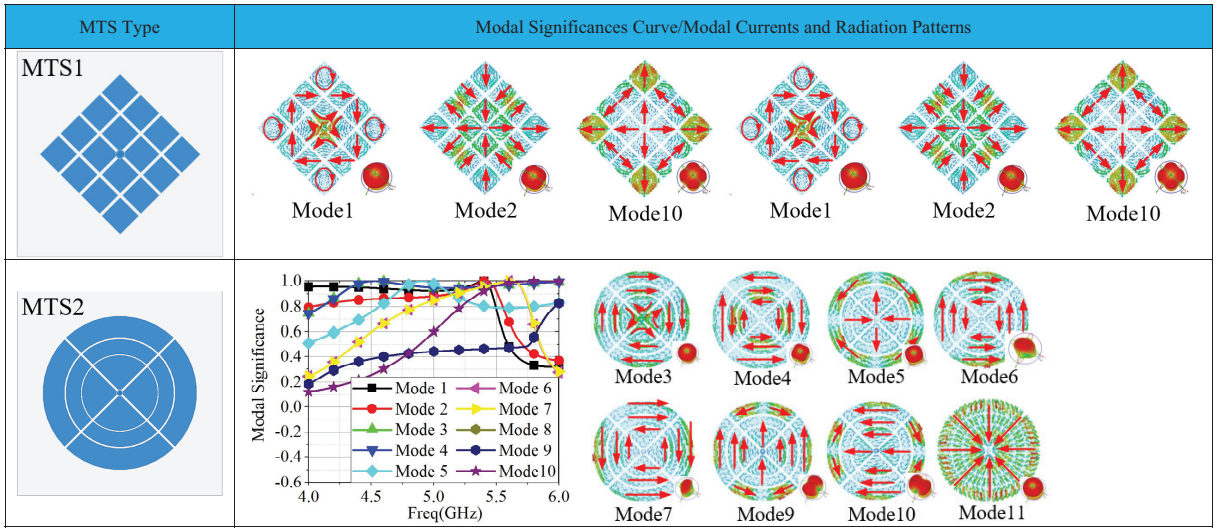


Fig. 1. 4×4 rectangular MTS (MTS1), circular MTS (MTS2), and the MS curve, modal currents, and radiation patterns of MTS1 and MTS2.

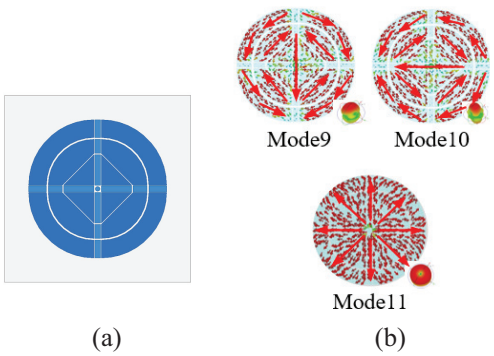


Fig. 2. (a) Optimized circular MTS. (b) Current distribution and radiation patterns of optimized MTS at 4 GHz.

design, the annular rectangular microstrip structure is introduced, so the antenna can achieve wide-beam radiation. At the same time, the coupled feed is used to excite the omnidirectional radiation in another frequency band of the MTS. To increase the isolation from the central coaxial line, the H-shaped coupling groove is etched in the corresponding coupling position in the ground layer. In addition, by etching four circular grooves in the ground layer and changing the electromagnetic field structure between the top radiation patch and the ground, the omnidirectional radiation irregularity can be optimized.

B. Antenna model

Based on the above analysis, a three-port common aperture antenna is proposed. The antenna structure diagram is shown in Fig. 3. The 1st and 2nd substrate layers of the antenna are composed of FR4 ($\varepsilon_r = 4.4$ and $\tan\delta = 0.02$). MTS and ring patches are printed on the 1st and the 2nd substrate layers, respectively, to generate omnidirectional and wide-beam radiation. The metal microstrips on both sides of the 3rd substrate layer (Rogers5880 with $\varepsilon_r = 2.2$ and $\tan\delta = 0.0009$) constitute the ground and feed structure, respectively. The ground has four H-shaped slots and four arc-shaped slots etched on it. On the reverse side of the feeding layer, a hybrid Wilkinson T-type power divider is adopted to uniformly excite the metasurface, which guarantees identical phase responses across all antenna ports and realizes a 1-to-4 power division function.

The dimensions of the antenna are shown in Table 1.

III. EXPERIMENTAL RESULTS

The fabricated prototypes of the three-port antenna are shown in Fig. 4. The simulation is conducted using HFSS. Figure 5 depicts the simulated and measured normalized radiation patterns of the antenna. The antenna achieves omnidirectional radiation beams of less than 2

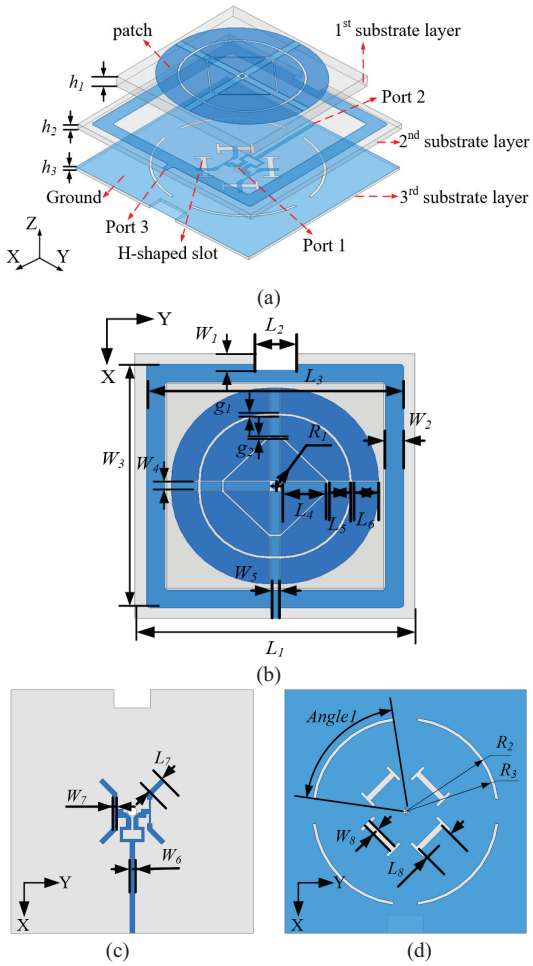


Fig. 3. Structure view of the proposed three-port common aperture antenna. (a) 3D view, (b) top view, (c) bottom view, and (d) ground layer.

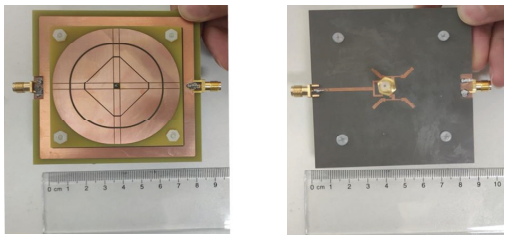
Table 1: Dimensions of the proposed three-port antenna (units: mm)

Symbol	Value	Symbol	Value	Symbol	Value
L_1	80	L_2	12	L_3	73
L_4	13	L_5	6	L_6	7.6
L_7	6	W_1	5	W_2	5.5
W_3	73.2	W_4	2.6	W_5	2
W_6	1.58	W_7	0.46	W_8	2
L_8	11	g_1	0.8	g_2	0.6
R_1	0.5	R_2	31	R_3	30
h_1	4	h_2	2	h_3	1
Angle	74.3°				

dB pattern roundness and 100° wide-beam radiation, and the difference between the main and cross polarization is greater than 10 dB. The measured and simulated S-parameters of each port are shown in Fig. 6. The peak

gain curve of each port is shown in Fig. 7 (a), and the simulation efficiency is shown in Fig. 7 (b). For omni-directional mode, $|S_{11}|$ and $|S_{22}| < -10$ dB bandwidths of 5.3% (2.92–3.08 GHz) and 13.2% (4.11–4.69 GHz), respectively. The simulation efficiency of in-band radiation is higher than 60% and 80%, respectively. For wide-beam radiation mode, the $|S_{33}| < -10$ dB bandwidth is 7.2% (1.74–1.87 GHz). In-band simulation radiation efficiency is higher than 60%. The isolation between any two ports is higher than 22 dB, indicating low mutual coupling and sufficient port independence for multi-port operation.

The simulation and measurement curves are generally consistent, showing that the designed three-port common aperture antenna meets the expected radiation performance. The discrepancy between simulated and measured results is mainly attributed to welding errors, substrate gaps, and measurement environmental errors.



(a) (b)

Fig. 4. Photographs of the fabricated three-port antenna. (a) Front view and (b) back view.

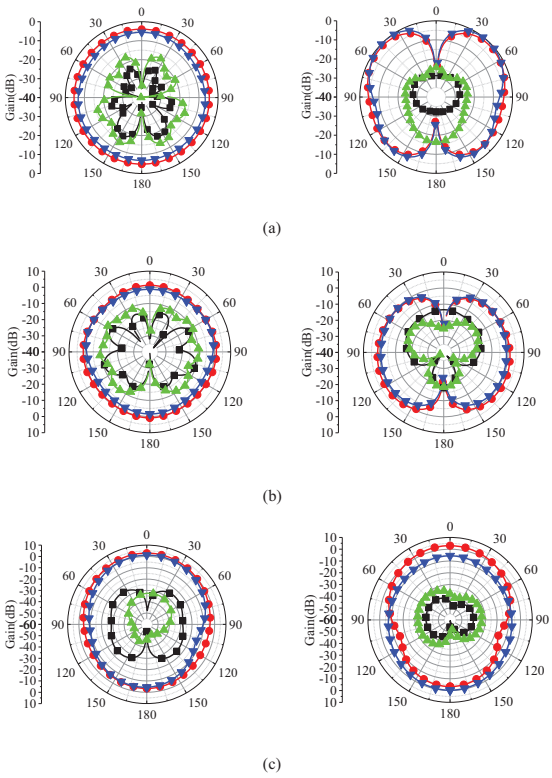


Fig. 5. Measured directional pattern of the proposed three-port antenna E plane (left) and H plane (right). (a) Radiation pattern of port 1 at 3 GHz, (b) radiation pattern of port 2 at 4.3 GHz, and (c) radiation pattern of port 3 at 1.8 GHz.

Table 2 compares the proposed antenna with existing three-port antennas in bandwidth, size, and isolation. Unlike [9, 19–22] in single continuous bands, the proposed antenna has different radiation patterns across its three bands. Its isolation is better than [19, 22], comparable to [9, 20], and worse than [21]. Its profile is lower than [20, 22]. Compared with [6], it provides band-specific patterns and higher isolation.

Table 2: Comparison with other three-port antennas

Ref.	Basic Structure	Working Frequency (GHz)	Size (λ_{min})	Iso. (dB)
[6]	Slot structure; Rectangular loop	0.77–0.93 1.53–1.83 2.4–2.64	$0.97 \times 0.64 \times 0.012$	>19
[9]	MTS	3.26–3.84	$1.02 \times 1.02 \times 0.06$	>22
[19]	Dielectric resonator antenna	5.58–6.17	$0.3 \times 0.3 \times 0.13$	>17
[20]	Dipoles, loop arrays	3.5–5.4	$1.0 \times 1.0 \times 0.12$	>22
[21]	Single patch	3.3–3.68	$1.35 \times 1.35 \times 0.1$	>35
[22]	Circular and ring patches	2.98–4.75	$1.09 \times 1.09 \times 0.125$	>15.3
Proposed	**MTS**	**1.74–1.87** **2.92–3.08** **4.1–4.69**	$\mathbf{1.25 \times 1.25 \times 0.1}$	**>22**

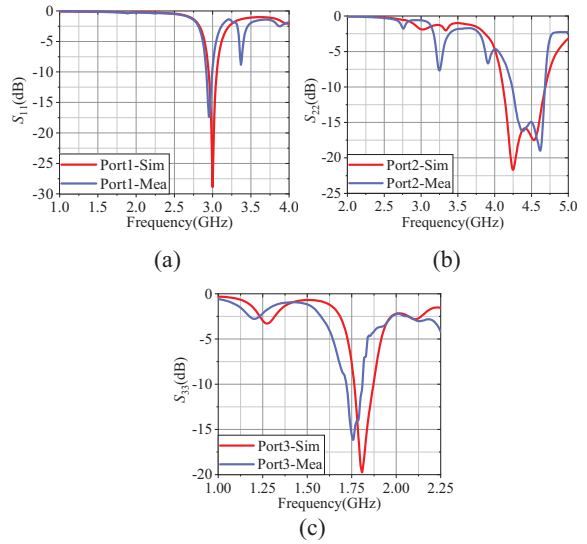


Fig. 6. Measured and simulated S-parameters of the proposed three-port antenna. (a) Port 1, (b) port 2, and (c) port 3.

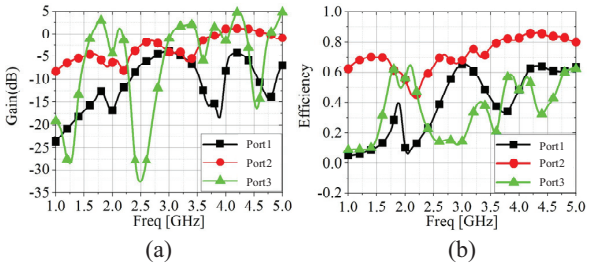


Fig. 7. (a) Peak gain curve of the proposed three-port antenna. (b) Radiation efficiency curve of the proposed three-port antenna.

IV. CONCLUSION

In this work, a three-port common aperture antenna based on MTS is designed and fabricated. The power divider coupling feed stimulates omnidirectional radiation performance at high frequency by feeding at different positions of the circular microstrip structure. At the same time, an annular microstrip patch structure is introduced in different outer layers of the MTS so that the antenna can generate wide-beam radiation. The antenna can generate omnidirectional radiation in the 2.92–3.08 GHz low frequency band and 4.11–4.69 GHz high frequency band, respectively, and wide-beam radiation in the 1.74–1.87 GHz low frequency band. The antenna presented in this paper has dual-frequency omnidirectional radiation and low-frequency wide-beam radiation. The antenna achieves high isolation between any two ports while maintaining high radiation efficiency within the operating bands. The antenna design scheme can be used for reference when scarce space resources and antenna integration requirements are high.

ACKNOWLEDGMENT

This work was supported by fund of Anhui Natural Science Foundation (No. 2208085MF161, No. 2208085QF185), Hefei Municipal Natural Science Foundation under Grant HZR2403, the Fundamental Research Funds (W2025JSKF0089, W2024JSKF0854).

REFERENCES

[1] B. Yang, Y. Xu, J. Tong, Y. Zhang, Y. Feng, and Y. Hu, "Tri-port antenna with shared radiator and self-decoupling characteristic for 5G smartphone application," *IEEE Trans. Antennas Propag.*, vol. 70, no. 6, pp. 4836–4841, June 2022.

[2] F. Qin, S. Gao, Q. Luo, C. X. Mao, C. Gu, G. Wei, J. Xu, J. Li, C. Wu, K. Zheng, and S. Zheng, "A simple low-cost common aperture dual-band dual-polarized high-gain antenna for synthetic aperture radars," *IEEE Trans. Antennas Propag.*, vol. 64, no. 7, pp. 2914–2922, July 2016.

[3] J. Ran, Y. Wu, C. Jin, P. Zhang, and W. Wang, "Dual-band multipolarized aperture-shared antenna array for Ku-/Ka-band satellite communication," *IEEE Trans. Antennas Propag.*, vol. 71, no. 5, pp. 3882–3893, May 2023.

[4] X. Li, R. Ma, H. Cai, Y.-M. Pan, and X. Y. Zhang, "High-gain dual-band aperture-shared CP patch antenna with wide AR beamwidth for satellite navigation system," *IEEE Antennas Wireless Propag. Lett.*, vol. 22, no. 8, pp. 1888–1891, Aug. 2023.

[5] Z. Wang, Y. Ning, and Y. Dong, "Hybrid metamaterial-TL-based, low-profile, dual-polarized omnidirectional antenna for 5G indoor application," *IEEE Trans. Antennas Propag.*, vol. 70, no. 4, pp. 2561–2570, Apr. 2022.

[6] P. Cheong, K.-F. Chang, W.-W. Choi, and K.-W. Tam, "A highly integrated antenna-triplexer with simultaneous three-port isolations based on multi-mode excitation," *IEEE Trans. Antennas Propag.*, vol. 63, no. 1, pp. 363–368, Jan. 2015.

[7] G. P. Gao, C. Yang, B. Hu, R. F. Zhang, and S. F. Wang, "A wearable PIFA with an all-textile MTS for 5 GHz WBAN applications," *IEEE Antennas Wireless Propag. Lett.*, vol. 18, no. 2, pp. 288–292, Feb. 2019.

[8] S. Liu, D. Yang, Y. Chen, K. Sun, X. Zhang, and Y. Xiang, "Low-profile broadband metasurface antenna under multimode resonance," *IEEE Antennas Wireless Propag. Lett.*, vol. 20, no. 9, pp. 1696–1700, Sep. 2021.

[9] Z. Wang, S. Liu, and Y. Dong, "Low-profile metasurface-based antenna with tripolarization for 5G applications," *IEEE Trans. Antennas Propag.*, vol. 69, no. 9, pp. 5437–5445, Sep. 2021.

[10] W. Yang, Q. Meng, W. Che, L. Gu, and Q. Xue, "Low-profile wideband dual-circularly polarized metasurface antenna array with large beamwidth," *IEEE Antennas Wireless Propag. Lett.*, vol. 17, no. 9, pp. 1613–1616, Sep. 2018.

[11] C. L. Holloway, E. F. Kuester, J. A. Gordon, J. O'Hara, J. Booth, and D. R. Smith, "An overview of the theory and applications of MTSs: The two-dimensional equivalents of metamaterials," *IEEE Antennas Propag. Mag.*, vol. 54, no. 2, pp. 10–35, Apr. 2012.

[12] S. Liu, D. Yang, Y. Chen, K. Sun, X. Zhang, and Y. Xiang, "Low-profile broadband metasurface antenna under multimode resonance," *IEEE Antennas Wireless Propag. Lett.*, vol. 20, no. 9, pp. 1696–1700, Sep. 2021.

[13] W. E. I. Liu, Z. N. Chen, and X. Qing, "Miniature wide-band non-uniform metasurface antenna using equivalent circuit model," *IEEE Trans. Antennas Propag.*, vol. 68, no. 7, pp. 5652–5657, July 2020.

[14] J. F. Wang, H. Wong, Z. Q. Ji, and Y. L. Wu, "Broadband CPW-fed aperture coupled MTS antenna," *IEEE Antennas Wireless Propag. Lett.*, vol. 18, no. 3, pp. 517–520, Mar. 2019.

[15] Z. Jiang, S. Meng, L. Nie, J. Qi, and F. Ji, "A low-profile tri-port multimode metasurface-based antenna using characteristic mode analysis," *IEEE Antennas Wireless Propag. Lett.*, vol. 24, no. 5, pp. 1119–1123, May 2025.

[16] G. Gao, R. F. Zhang, W. F. Geng, H. J. Meng, and B. Hu, "Characteristic mode analysis of a nonuniform metasurface antenna for wearable applications," *IEEE Antennas Wireless Propag. Lett.*, vol. 19, no. 8, pp. 1355–1359, Aug. 2020.

[17] Y.-H. Lv, R. Wang, B.-Z. Wang, and Z. N. Chen, "Anisotropic complementary metantenna for low sidelobe radiation and low in-band co-polarized scattering using characteristic mode analysis," *IEEE Trans. Antennas Propag.*, vol. 70, no. 11, pp. 10177–10186, Nov. 2022.

[18] T. Li and Z. N. Chen, "A dual-band MTS antenna using characteristic mode analysis," *IEEE Trans. Antennas Propag.*, vol. 66, no. 10, pp. 5620–5624, Oct. 2018.

[19] B. Zhang, J. Ren, T. Yang, Y.-T. Liu, Z. Zhao, and J. Zhao, "Three-port pattern- and polarization-diversity rectangular dielectric resonator antenna," *IEEE Trans. Antennas Propag.*, vol. 71, no. 6, pp. 5392–5397, June 2023.

[20] J. Han, R. Lian, D. Wu, M. Qin, and J. Zhang, "Design of a wideband tripolarized antenna with high isolation and diverse patterns," *IEEE Antennas Wireless Propag. Lett.*, vol. 23, no. 1, pp. 114–118, Jan. 2024.

[21] L. Y. Nie, B. K. Lau, H. Aliakbari, S. Xiang, B. Wang, and X. Q. Lin, "A low-profile wideband dual-resonance tri-port MIMO antenna," *IEEE Trans. Antennas Propag.*, vol. 70, no. 6, pp. 4866–4871, June 2022.

[22] Y. Yang, J. Ren, B. Zhang, J. Liu, H. Wang, and D. Song, "Wideband tripolarized MIMO antenna with pattern diversity for 5G application," *IEEE Antennas Wireless Propag. Lett.*, vol. 23, no. 1, pp. 349–353, Jan. 2024.



Z. N. Jiang was born in Lianyungang, Jiangsu, China. He received the Ph.D. degree from Nangjing University of Science and Technology, Nanjing, in 2012. Since 2013, he has been engaged in research on numerical methods for computational electromagnetism. He is currently a Professor at Hefei University of Technology and a Distinguished Professor at Anhui Institute of Information Technology. He has authored or co-authored more than 100 papers in prestigious international journals and conferences, and has served as a Program Committee Member for several international conferences. His current research interests include antennas and microwave devices.



L. Wu, a native of Bozhou, Anhui Province, China, is currently pursuing the M.S. degree at Hefei University of Technology. He has been engaged in the research of microwave antenna design since 2024.



B. Z. Sun, a native of Huaibei, Anhui Province, China, is currently pursuing the M.S. degree at Hefei University of Technology. He has been engaged in the research of microwave antenna design since 2024.



L. L. Yu, native of Yuexi County, Anhui Province, China. He obtained his Master of Business Administration from the School of Management, Hefei University of Technology, in 2012. His professional endeavors focus on the management and research of information security and artificial intelligence applications. Currently, he serves as Deputy Director of the Office of Informationization Construction and

Management at Hefei University of Technology. He is the author of several scholarly works, including Full-Stack Application and Migration of Domestic Operating Systems and Fundamentals and Applications of Artificial Intelligence. His current research interests encompass the integrated application of computer science and artificial intelligence technologies across diverse scenarios.

A Bear-Shaped UWB MIMO Antenna Based on Characteristic Mode Analysis

Xiaoyan Wei[1], Zhonggen Wang[1*], Wenyan Nie[2], Chenlu Li[3], and Zhengting Zhang[1]

[1]School of Electrical and Information Engineering
Anhui University of Science and Technology, Huainan 232001, China
xywei1216@163.com, zgwang@ahu.edu.cn,ztzhang818@163.com

[2]School of Mechanical and Electrical Engineering
Huainan Normal University, Huainan 232001, China
wynie5240@163.com

[3]School of Electrical and Information Engineering
Hefei Normal University, Hefei 230061, China
chenluli@hfnu.edu.cn
*Corresponding author

Abstract **–** This paper proposes a compact four-port ultra-wideband (UWB) multiple-input multiple-output (MIMO) antenna with bear-shaped patches based on characteristic mode analysis (CMA). The antenna measures $62 \times 62 \times 1$ mm^3, comprising orthogonally arranged bear-shaped radiating elements on the top layer, a cross-shaped hollowed-out decoupling structure on the bottom layer, and defected ground structures (DGS) with corner cuts and grooves at the four corners. Notably, the bear-shaped radiating elements are not just a morphological innovation; compared with traditional rectangular/circular elements, their irregular outline enriches equivalent current path diversity and increases excited resonant modes. Each antenna is optimized with etched slots, corner cuts and a T-shaped feeder, ensuring simultaneous excitation of five characteristic modes for UWB performance. For the MIMO configuration, mutual coupling is suppressed via orthogonal arrangement, the decoupling structure and DGS, with isolation over 20 dB. Simulations and measurements confirm the antenna operates in the 3.36–21.91 GHz band, featuring S11 < -10 dB and ECC < 0.005 across the band, a diversity gain approaching 9.9999 dB, 75–95% radiation efficiency, 7 dBi peak gain and a group delay less than 1 ns. This design outperforms existing designs in bandwidth, isolation and miniaturization, suited for advanced wireless communication scenarios requiring wide bandwidth, high isolation and a compact form factor.

Index Terms **–** Characteristic mode theory, defected ground structures, MIMO antenna, T-shaped feeder, ultra-wideband antenna.

I. INTRODUCTION

With advances in wireless communication technologies, demand for bandwidth capacity and data transmission rates has grown exponentially [1]. Ultra-wideband (UWB) technology offers unique advantages including ultra-wide bandwidth, high temporal resolution enabled by nanosecond pulses and low power consumption. It is well suited for short-range high-speed data transmission [2, 3] and precise positioning, and holds broad application potential in radar, Internet of Things (IoT) and vehicle-to-everything (V2X) [4]. Despite these merits, UWB faces multipath fading. Multiple-input multiple-output (MIMO) technology addresses this challenge via multi-antenna spatial diversity and multiplexing [5, 6], which enhances system capacity and reliability. Integrating UWB and MIMO has yielded devices that boost wireless communication capacity and transmission rates while mitigating multipath effects.

For MIMO systems, isolation stands as a paramount indicator of diversity performance and, to tackle the coupling issue between antenna elements, researchers have elaborated various decoupling techniques such as decoupling stubs [7], defected ground structures (DGS) [8, 9], and electromagnetic bandgaps (EBG) [10].

Submitted On: December 23, 2025
Accepted On: July 23, 2026

1054-4887 © ACES

https://doi.org/10.13052/2026.ACES.J.410703

Among these, a neutralization line composed of a disk and metal strips is applied to antenna elements to effectively enhance isolation [11], while a square decoupling structure is placed between antenna elements to mitigate mutual coupling [12]. For bandwidth enhancement, slotting microstrip lines improves impedance matching and broadens the operating band [13]. An improved embedded feed combined with a slotted ground plane is used to extend the bandwidth without compromising radiation performance [14]. By utilizing two distinct UWB antenna elements to excite different resonant modes, a bandwidth of 2.6–11 GHz is achieved while maintaining high isolation [15]. UWB performance is attained by slotting the antenna radiating patch and engineering a defected ground plane [16]. Extending circular elements with a backplane and truncating rectangular elements expands the operating bandwidth while preserving stable radiation characteristics [17]. Finally, a planar low-profile microstrip patch antenna sandwiched between a finite ground plane and a surface is presented, achieving an impedance bandwidth of 2–11.2 GHz [18].

Although various technologies have been applied to the design of UWB MIMO antennas, many existing designs still rely on the trial-and-error method, often lacking sufficient theoretical guidance and physical insight. Characteristic mode analysis (CMA), on the other hand, enables targeted structural optimization by revealing modal characteristics. It has been shown to facilitate performance improvements in a range of antenna designs [19–22], as exemplified below. For instance, a low-profile wideband circularly polarized antenna is presented in [19], where four linearly polarized modes are adjusted to the target frequency band via CMA. A probe-fed grounded antenna with a sandwich structure is proposed in [20]; CMA reveals that this configuration excites the TM_{01} and TM_{02} modes, resulting in a monopole-like radiation pattern with low cross-polarization. A tri-band circularly polarized metasurface antenna is developed in [21] using CMA, where the metasurface unit structure is modified to suppress reverse currents and excite desired resonant modes. Furthermore, a compact wideband dual-polarized antenna with high isolation is reported in [22]; CMA is utilized to narrow the patch center and introduce a U-shaped slot into the L-shaped probe, effectively suppressing higher-order modes.

In summary, this paper proposes a compact UWB MIMO antenna consisting of four bear-shaped radiating elements and four DGS. Bandwidth and isolation are improved by introducing a cross-shaped decoupling structure, adding L-shaped branches to the stubs, and etching rectangular slots and triangular slots on the DGS. The antenna operates in the frequency band of 3.36–21.91 GHz, covering the UWB range. It achieves an isolation of more than 20 dB across the entire band and a peak gain of 7 dBi, with excellent radiation performance and diversity performance. In addition, the design evolution of the antenna is guided by CMA. By analyzing the modal current and electric field distributions, the feeding points of the rectangular microstrip lines for the radiating elements are determined. This ensures the simultaneous excitation of five characteristic modes, effectively achieving UWB operation.

II. ANTENNA DESIGN

A. Antenna structure

Figure 1 illustrates the overall geometric structure of the four-port MIMO antenna. The antenna has an overall size of $62 \times 62 \times 1$ mm and is printed on an FR4 dielectric substrate with a relative permittivity (ε_r) of 4.4 and a loss tangent ($\tan\delta$) of 0.02, employing a 50 Ω microstrip line for feeding. Table 1 presents the detailed optimized parameter values. The antenna's radiating elements are bear-shaped patches, which are arranged orthogonally on the top layer of the dielectric substrate in a compact configuration to maximize utilization of the substrate space. On the bottom layer of the dielectric substrate, the four corners of the ground plane incorporate cut-angle and groove structures, which optimize grounding performance and further enhance isolation between elements. Moreover, a cross-intersecting microstrip line structure is positioned

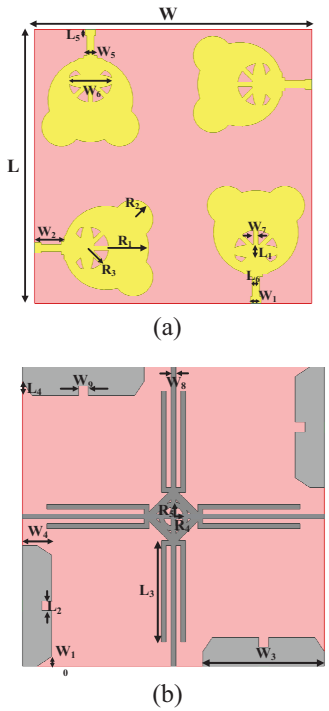


Fig. 1. UWB MIMO antenna structure: (a) top-side antenna structure, (b) bottom-side antenna structure.

Table 1: Parameter dimensions of the antenna

Parameter	L	L1	L2	L3	L4	L5
Value (mm)	62	3.12	2	21	3	1.51
Parameter	L6	W	W1	W2	W3	W4
Value (mm)	1.6	62	2.3	6.02	25	6
Parameter	W5	W6	W7	W8	W9	W10
Value (mm)	3	10.92	1	1	2	2
Parameter	R1	R2	R3	R4	R5	
Value (mm)	9.5	4.4	4.8	2	3	

in the central area. This cross-intersecting structure consists of multiple microstrip lines intersecting in a cross pattern with hollow geometric patterns in the middle, and it mitigates electromagnetic coupling between antenna elements by regulating the current distribution. Collectively, the bottom-layer structures work in conjunction with the top-layer radiating elements, enabling the MIMO antenna to achieve wideband operation and high isolation characteristics.

B. Design and analysis of a single antenna based on characteristic mode

To systematically optimize the UWB performance of the proposed bear-shaped structure, CMA is employed as the core theoretical guidance throughout the antenna design process. Based on the Method of Moments (MoM), CMA solves the generalized eigenvalue equation $[X]J_{\mathrm{n}} = \lambda_n[R]J_{\mathrm{n}}$, extracting the inherent characteristic modes of the structure. These modes are independent of any specific excitation source. Each mode is characterized by a Modal Significance (MS) value indicating its excitability and a Characteristic Angle (CA) reflecting its resonant state, with the corresponding modal current distribution revealing the spatial locations of strong currents on the conductor surface. In the proposed design, CMA first identifies the candidate characteristic modes and evaluates their excitation feasibility by examining whether their current distributions are concentrated near the feeding port, which reveals that only three of the five candidate modes are initially excitable. CMA then guides the subsequent structural modifications, including the radial slot, ground plane truncations, rectangular slot, and T-shaped feeder, to adjust the modal current distributions of the remaining modes to overlap with the feeding region and shift their resonant frequencies into the target band to collectively cover a continuous ultra-wide bandwidth. Through this iterative CMA-guided optimization, all five characteristic modes are eventually excited simultaneously, achieving continuous UWB operation. The effectiveness of this approach is validated through the structural evolution from Antenna 1 to Antenna 3, supported by MS, CA, and modal current distribution analyses presented below.

Figure 2 illustrates the structural evolution process of the single antenna, and Fig. 3 presents the corresponding simulated S-parameters. The single antenna is fabricated on an FR4 substrate with dimensions of $37 \times 25 \times 1$ mm. The evolved structure is modeled and subjected to CMA using the commercial CST (Computer Simulation Technology) software. Figure 4 shows the MS and CA of Antenna 1, and Fig. 5 presents the modal current distributions at resonance. MS indicates the contribution degree of each mode within a specific frequency range. A value close to 1 means the mode is more likely to be excited under appropriate excitation, while a value below 0.707 indicates a low probability of resonance. CA reflects the resonant characteristics of the mode. A value close to 180° indicates a stronger resonant condition.

As shown in Fig. 4, among the 12 characteristic modes, modes 1, 2, 4, 5, and 11 can theoretically be excited under appropriate excitation. However, as illustrated in Fig. 5, the currents of modes 4 and 11 are primarily distributed on the edge of the bear-shaped patch and the middle section of the feeder as well as the upper edge of the ground plane, respectively. Since these strong-current regions are distant from the feeding port and mode 4 further exhibits low current intensity, their contribution to the antenna's bandwidth is limited; in contrast, modes 1, 2, and 5 exhibit intense current concentration in the feeder and adjacent ground regions, facilitating their effective excitation. Nevertheless, the combined bandwidth supported by these three modes remains inadequate to satisfy UWB requirements. The S-parameter curve of Antenna 1 (Fig. 3) reveals that its dual operating bands span 3.47–8.75 GHz and 10.39–16.79 GHz, neither of which complies with UWB standards. Accordingly, optimization of the antenna structure is necessitated, with the optimized structure presented in Fig. 2 (b).

As shown in Fig. 2 (b), compared with Antenna 1, Antenna 2 has a radial slot etched into the circular section of its patch, and isosceles right triangles are truncated from both the left and right sides of the ground plane. The radial slot disrupts the continuous current flow on the circular head region, effectively lengthening the current path for modes whose currents are concentrated on this region, which shifts their resonant frequencies downward. Meanwhile, the truncated isosceles right triangles remove ground plane area near the edges, modifying the ground current return paths and enhancing current density on the remaining ground surface, which promotes the excitation of higher-order modes and extends the highfrequency band by approximately 2 GHz.

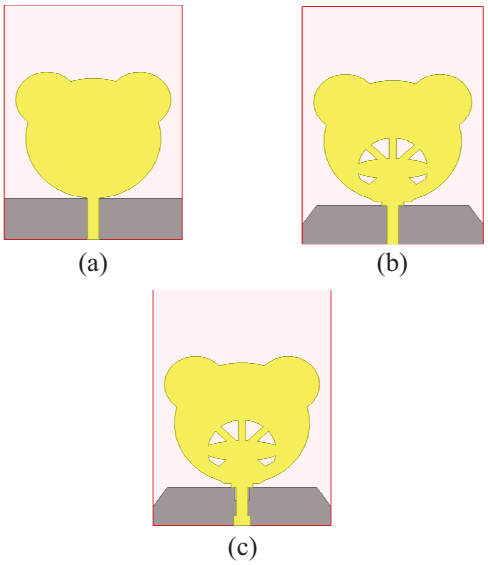


Fig. 2. Evolutionary process of antenna structure: (a) Antenna 1, (b) Antenna 2, and (c) Antenna 3.

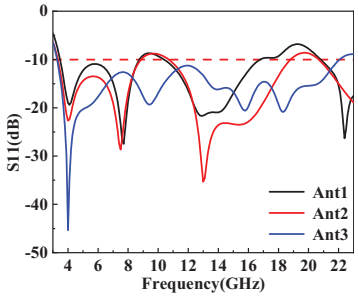


Fig. 3. Simulated S-parameter plot of the antenna.

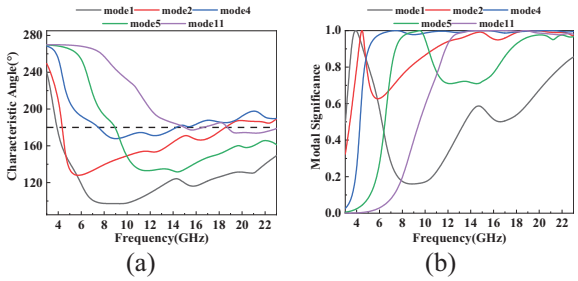


Fig. 4. Simulated results of mode analysis of Antenna 1: (a) Modal Significance and (b) Characteristic Angle.

Figure 6 presents the MS and CA of Antenna 2, and Fig. 7 illustrates the corresponding modal current distributions. In contrast to Antenna 1, Antenna 2 exhibits altered characteristic mode configurations and extended effective bandwidth. The resonant frequency of mode 4 decreases slightly due to the lengthened current path introduced by the radial slot. However, its current is predominantly concentrated above the bear-shaped

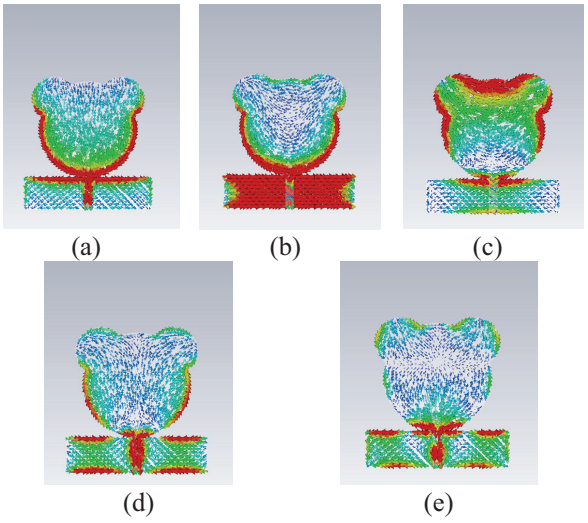


Fig. 5. Simulated mode current distribution of Antenna 1: (a) mode 1 at 3.89 GHz, (b) mode 2 at 4.35 GHz, (c) mode 4 at 7.49 GHz, (d) mode 5 at 8.95 GHz, (e) mode 11 at 15.01 GHz.

patch and distant from the feeding port, so it cannot be excited. The resonant frequencies of modes 1, 2, and 5 exhibit a slight upward shift, as the triangular ground truncations redirect their current distributions toward the ground plane edges, shortening the effective current return path for these modes. As depicted in Fig. 7, they can be effectively excited owing to their strong localized distribution in the vicinity of the feeding port. The resonant frequency of mode 11 is reduced by approximately 0.2 GHz, as the radial slot also disrupts the high-frequency current paths on the upper part of the patch. The S-parameter curve in Fig. 3 indicates that the high-frequency band of Antenna 2 is extended by 2 GHz, reducing the bandwidth gap to 9.5–10.2 GHz. However, impedance matching in the 9–11 GHz range is still not fully satisfactory, so further optimization of Antenna 2's structure is required.

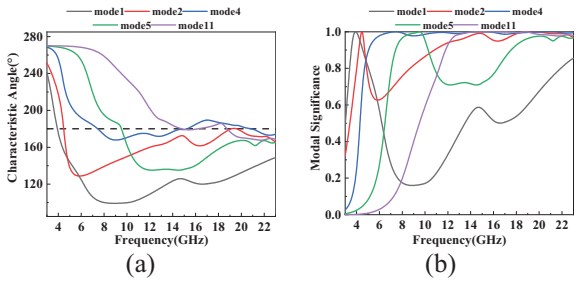


Fig. 6. Simulated results of mode analysis of Antenna 2: (a) Modal Significance and (b) Characteristic Angle.

To shift the characteristic modes toward lower frequencies and ensure their excitation, as shown in

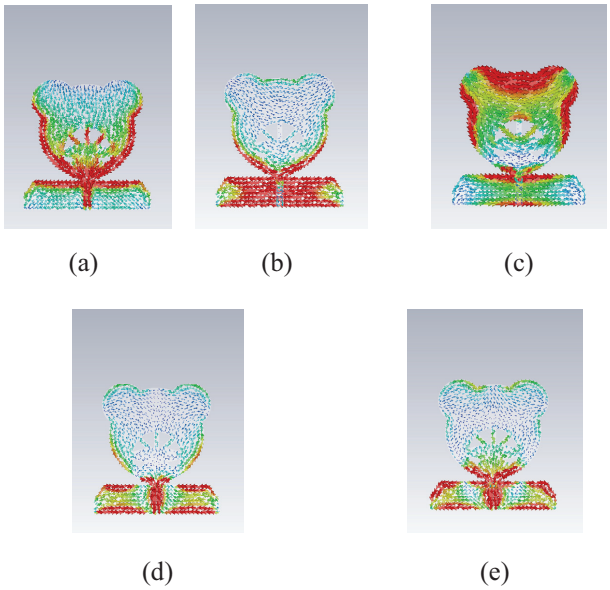


Fig. 7. Simulated mode current distribution of Antenna 2: (a) mode 1 at 3.91 GHz, (b) mode 2 at 4.47 GHz, (c) mode 4 at 7.45 GHz, (d) mode 5 at 9.51 GHz, (e) mode 11 at 14.81 GHz.

Fig. 2 (c), Antenna 3 has a rectangular slot etched into the ground plane and adopts a T-shaped feeder. The rectangular slot introduces an additional current discontinuity in the ground plane, which redirects the surface current of mode 4 (previously concentrated far from the feeding port) toward the feeding region. The T-shaped feeder provides broader capacitive coupling to the radiating patch compared with the original microstrip line, improving impedance matching across multiple resonant frequencies simultaneously. These modifications collectively redirect current concentrations toward the feeding port, enabling the simultaneous excitation of five modes and extending the effective bandwidth to cover the majority of the UWB range.

Figure 8 presents the MS and CA of Antenna 3. Figure 9 illustrates the modal current distributions at resonance. A comparison of Figs. 9 and 7 reveals key changes. As predicted by the mechanism discussed above, mode 4 becomes excitable in Antenna 3, which broadens the bandwidth. The resonant frequencies of modes 1, 2, 4, and 5 shift downward, attributable to the increased effective current path lengths caused by the ground plane slot and the modified coupling characteristics of the T-shaped feeder. The resonant frequency of mode 11 shifts upward by 4 GHz, which is consistent with the altered current distribution at higher frequencies due to the combined effect of the ground plane modification and the feeder redesign. As shown in Fig. 9, the current for each mode is strengthened and concentrated near the feeding port, confirming that the structural modifications successfully reshape the modal current distributions to facilitate their effective excitation. Figure 8 further indicates the combined bandwidth of these modes, fully covering the 3.28–22.01 GHz range. S-parameter results in Fig. 3 confirm that the simulated operating frequency band of Antenna 3 is 3.28–22.01 GHz, which is consistent with the measured result of 3.36–21.91 GHz presented in section III. To further verify the radiation performance of the optimized single antenna across the entire UWB, its radiation patterns at three representative frequencies are analyzed below.

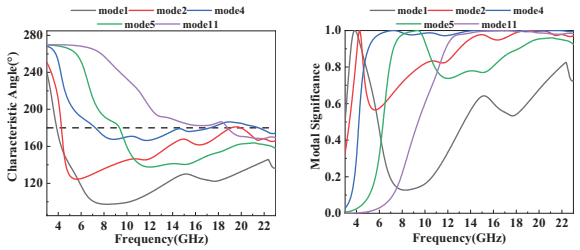


Fig. 8. Simulated results of mode analysis of Antenna 3: (a) Modal Significance and (b) Characteristic Angle.

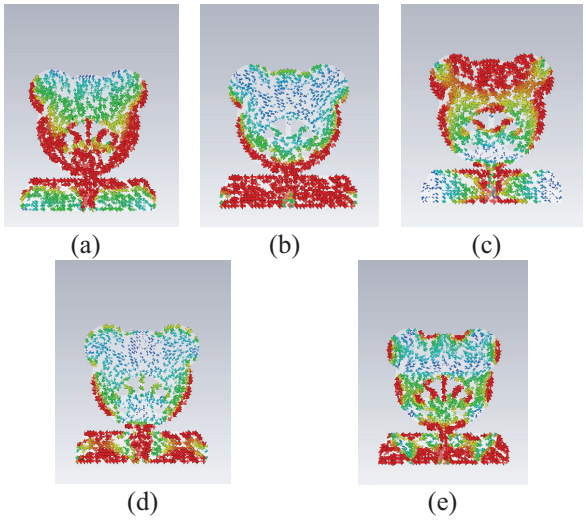


Fig. 9. Simulated mode current distribution of Antenna 3: (a) mode 1 at 3.85 GHz, (b) mode 2 at 4.27 GHz, (c) mode 4 at 7.23 GHz, (d) mode 5 at 9.35 GHz, (e) mode 11 at 18.81 GHz.

The CMA results presented above can be further interpreted in terms of the physical role of each geometric feature. Conventional rectangular or circular patches exhibit relatively uniform current path lengths, which limits the number of distinct resonant modes that can be effectively excited. The bear-shaped geometry

overcomes this limitation through its irregular bionic outline. Specifically, the circular head region provides current paths analogous to those on circular patches, supporting lower-order modes (modes 1 and 2) in the 3–5 GHz range, as confirmed by the modal current distributions in Figs. 5, 7, and 9. The protruding ear structures introduce current path segments with shorter effective lengths, contributing to higher-order mode excitation at mid-band frequencies. Meanwhile, the tapered body section and the concave transitions between the ears and the face create geometric discontinuities that redistribute surface current density, increasing the frequency separation between adjacent modes and reducing modal overlap. While the bear-shaped patch inherently supports five significant characteristic modes within the 3.28–22.01 GHz band, only three of these modes (modes 1, 2, and 5) are initially excitable, as the currents of modes 4 and 11 are concentrated far from the feeding port. These geometric features collectively provide the rich modal diversity that, combined with the structural optimizations described above, enables the simultaneous excitation of all five characteristic modes for continuous UWB operation.

Figure 10 presents the simulated co-polarization (solid lines) and cross-polarization (dashed lines) normalized radiation patterns of the optimized single antenna (Antenna 3) at three representative frequencies, 4.6 GHz, 15.4 GHz, and 18.5 GHz, covering the low-, mid-, and high-frequency regions of the UWB operating band. At 4.6 GHz, the antenna exhibits a typical dipole-like radiation characteristic, with the E-plane ($\varphi = 0^\circ$) showing a standard figure-of-eight pattern and the H-plane ($\varphi = 90^\circ$) presenting quasi-omnidirectional radiation behavior. The cross-polarization level is approximately 15–20 dB below the co-polarized component in the main radiation direction, indicating good polarization purity. At 15.4 GHz, the increased electrical size of the antenna leads to slight multi-lobing and pattern fluctuations; nevertheless, the dominant radiation characteristics are preserved and the cross-polarization component remains significantly below the co-polarized field over most angular regions. At 18.5 GHz, the radiation pattern exhibits more pronounced multi-lobed characteristics due to higher-order mode excitation, while the overall quasi-omnidirectional behavior is maintained. Although the cross-polarization level increases slightly at certain angles, it remains sufficiently below the co-polarized component, confirming acceptable polarization performance across the operating band. Overall, the single antenna maintains stable radiation characteristics and good polarization purity throughout the UWB band, supporting the implementation of the subsequent four-port MIMO antenna configuration.

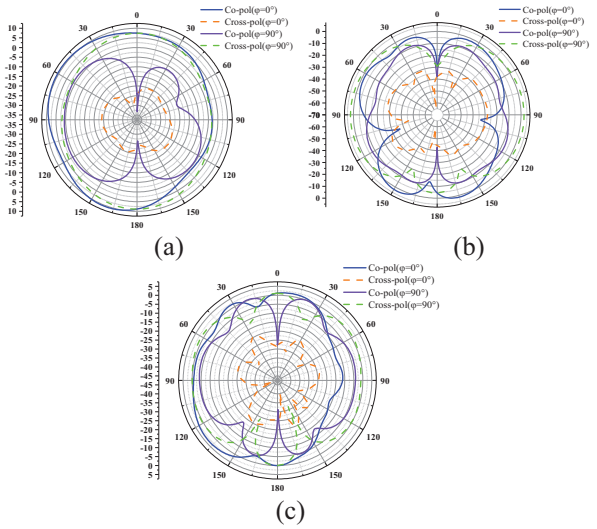


Fig. 10. Simulated radiation patterns of the optimized single antenna (Antenna 3) at three representative frequencies: (a) 4.6 GHz, (b) 15.4 GHz, (c) 18.5 GHz. Solid lines: co-polarization; dashed lines: cross-polarization.

C. MIMO antenna design and analysis

The designed single antenna is rotated symmetrically around the center to form a four-element MIMO antenna configuration, as shown in Fig. 11 (a) (referred to as Antenna Model 4). To further reduce mutual coupling, an isolation structure consisting of a cross-shaped decoupling structure with hollow patterns and eight L-shaped branches is introduced between the antenna elements, as shown in Fig. 11 (b) (referred to as Antenna Model 5). In both configurations, the current distributions are obtained by exciting Port 1 while terminating Ports 2, 3, and 4 with matched 50 Ω loads.

Figure 12 presents the simulated S-parameters of Antenna Model 4 and Antenna Model 5, including the reflection coefficient (S11) and transmission coefficient (S12) curves for both configurations. For the reflection coefficient characteristics, without the isolation structure (Antenna Model 4), the resonant frequency shifts slightly due to mutual interference and impedance mismatch caused by the rotational replication of radiating elements. With the isolation structure added (Antenna Model 5), the resonant frequency is restored and the operating bandwidth remains essentially unchanged. For the isolation performance, without the isolation branches, the isolation between certain port pairs falls below 20 dB in some frequency bands. Although the DGS blocks most of the surface current, residual coupling still exists between the antenna elements. With the isolation structure added, the residual coupling current is further suppressed and the isolation is significantly improved to above 20 dB across the

entire 3.36–21.91 GHz operating band. The effectiveness of this isolation structure is further confirmed by the measured S-parameter results of the fabricated MIMO antenna prototype presented in section A (Fig. 15), where S12 remains below −20 dB across the full operating band. The introduction of the isolation structure not only enhances isolation and reduces crosstalk, but also improves signal transmission capacity and spectrum utilization of the MIMO system.

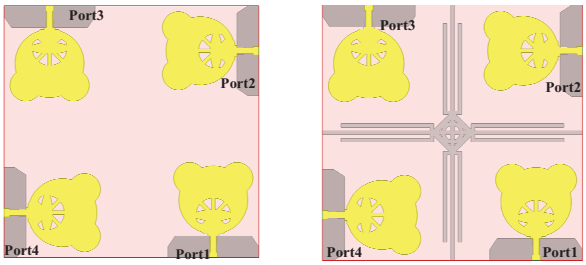


Fig. 11. MIMO antenna design: (a) Antenna Model 4 and (b) Antenna Model 5.

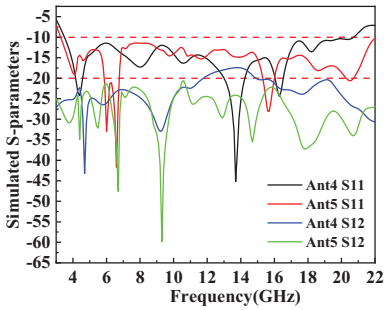


Fig. 12. Simulated S-parameters before and after adding an isolated branch.

D. Antenna parameter analysis

During the antenna optimization process, the single-parameter scanning method was employed. By considering the positions of parameters within the antenna, the influence of each parameter on the return loss S11 was analyzed. Figure 13 illustrates the optimization results.

The first group consists of width-related parameters for the radiation patch. These parameters directly affect the resonant characteristics of the radiating element by altering its equivalent electrical length and reactance distribution. With W9 as an example, when the length increases from 1.5 mm to 2 mm, the resonant frequency of the low frequency band shifts slightly downward as the equivalent electrical length increases, and the S11 value within this band remains consistently below −10 dB. Meanwhile, due to the more balanced reactance distribution in the mid-frequency band, the fluctuation amplitude of S11 is significantly reduced. However, if the width is further increased to 3.5–4.0 mm, the resonant mode of the high-frequency band will be disturbed, causing a shift in resonant frequency. The matching performance degrades accordingly, with S11 rising above −10 dB. Accordingly, for balancing multi-band resonance and matching, the optimal width is identified as W9 = 2 mm.

The second group comprises length-related parameters for the ground plane/isolation structure. These parameters indirectly influence antenna performance by regulating the current return path and resonant mode. With L6 as an example, when the length is less than 1.6 mm, the matching performance in the low-frequency band is excellent. However, the resonant mode in the mid-frequency band becomes unstable, leading to severe fluctuations in S11. When the length is set to 1.6 mm, the continuity between the resonant frequencies of the mid-frequency band and the low-frequency band is significantly improved, and the S11 value across the entire frequency band remains stably below −10 dB. If the length is further increased to more than 2.0 mm, changes in the current path will cause the resonant frequency of the high-frequency band to shift upward, which in turn leads to a noticeable rise in the S11 value. Hence, the optimal value for balancing resonance continuity and S11 performance is identified as L6 = 1.6 mm.

The third group refers to width-related parameters at the interface between the radiation patch and the isolation structure. These parameters affect both the current distribution of the radiating element and the electromagnetic coupling between elements, thereby influencing resonance and matching. With W4 as an example, when the width ranges from 3 mm to 5 mm, the resonant frequency in the low-frequency band achieves good matching; however, due to coupling imbalance in the mid-to-high frequency band, the resonant frequencies are scattered and S11 fluctuates drastically. When the width is increased to 6 mm, the coupling in the mid-to-high frequency band tends to stabilize, the coverage range of resonant frequencies expands, and the S11 value within this range drops to below −10 dB. If the width is further increased to 7–8 mm, excessive coupling will cause a shift in the resonant mode of the high-frequency band, leading to an upward shift of the resonant frequency and a subsequent rise in the S11 value. Consequently, the optimal value for achieving multi-band resonance coverage and low S11 performance is confirmed as W4 = 6 mm.

III. RESULTS AND DISCUSSION

A. S-parameters

The MIMO antenna was simulated using Ansys Electronics Desktop 2021 R2. To verify the antenna's

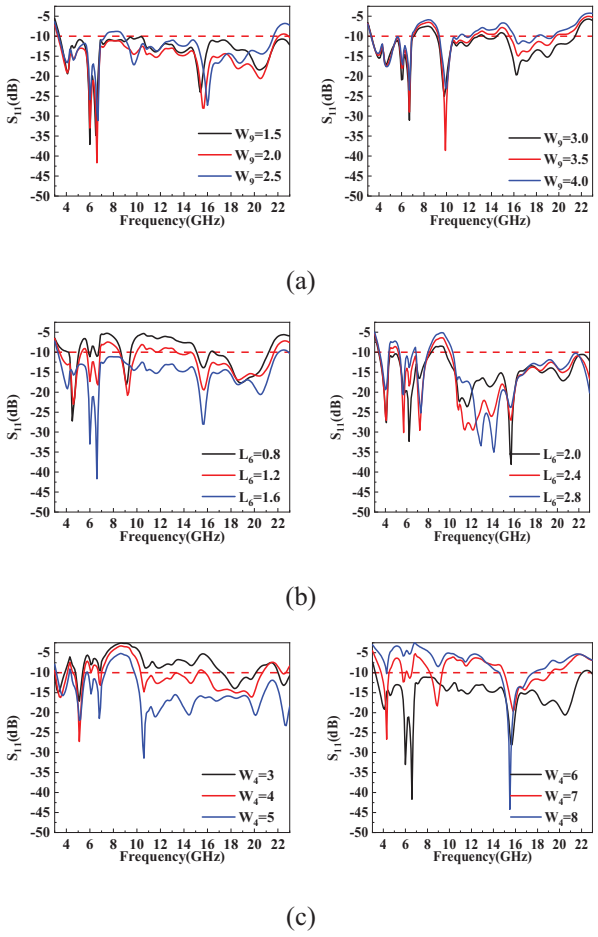


Fig. 13. Effect of adjusted parameters on S_{11} parameters: (a) W_9, (b) L_6, and (c) W_4.

practical performance, the optimized model was fabricated into a prototype, with the finished prototype shown in Fig. 14 (a). The prototype was then measured using an Agilent N52235A vector network analyzer, and the measurement setup is illustrated in Fig. 14 (b). Owing to the structural symmetry of the orthogonal arrangement, ideally the reflection coefficients (S11 = S22 = S33 = S44) are identical across all ports, and the radiation patterns of all elements share the same shape with successive 90° rotation. For the coupling parameters, S12 and S13 are presented to represent the adjacent and diagonal coupling paths, respectively. Therefore, only the S-parameter results measured from Port 1 (S11, S12, and S13) are shown for brevity. Figure 15 shows that the antenna operates over a frequency range of 3.36–21.91 GHz, thereby achieving wide bandwidth coverage. Furthermore, within the UWB frequency band, both the S12 and S13 parameters remain consistently below −20 dB, indicating excellent isolation performance. While minor discrepancies are observed between the measured and simulated S11, S12, and S13 results, their overall trends are highly consistent, confirming stable wideband performance. These discrepancies are primarily attributed to the frequency-dependent insertion loss of the SMA connectors, fabrication tolerances in fine structural features such as the narrow slots and ear details of the bear-shaped patch, and the frequency-dependent dielectric properties of the FR4 substrate, which deviate from the nominal simulation value at higher frequencies.

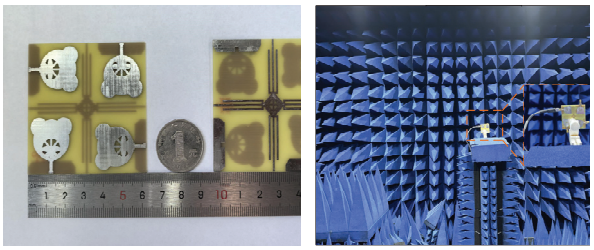


Fig. 14. Proposed antenna: (a) antenna object and (b) antenna microwave darkroom measurement environment.

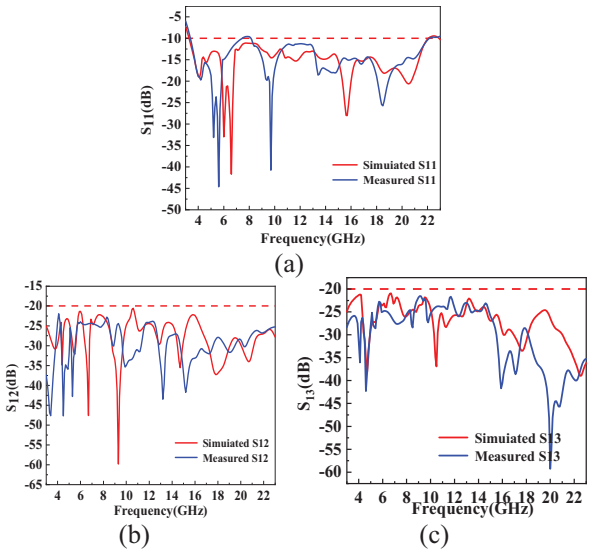


Fig. 15. Simulated and measured S-parameters of the MIMO antenna: (a) S11, (b) S12, (c) S13.

B. Radiation properties

Figure 16 presents the measured 2-D radiation patterns of the proposed four-port UWB MIMO antenna at three representative frequencies (6.6 GHz, 15.4 GHz, and 20.5 GHz), covering the entire operating band. The measurements were carried out in a far-field anechoic chamber using a standard far-field measurement setup. During the measurement, one port was excited while the other three ports were terminated with 50 Ω

matched loads. The gain distributions were recorded in the E-plane ($\varphi = 0°$, XOZ plane) and H-plane ($\varphi = 90°$, YOZ plane) over the angular range $0-180°$.

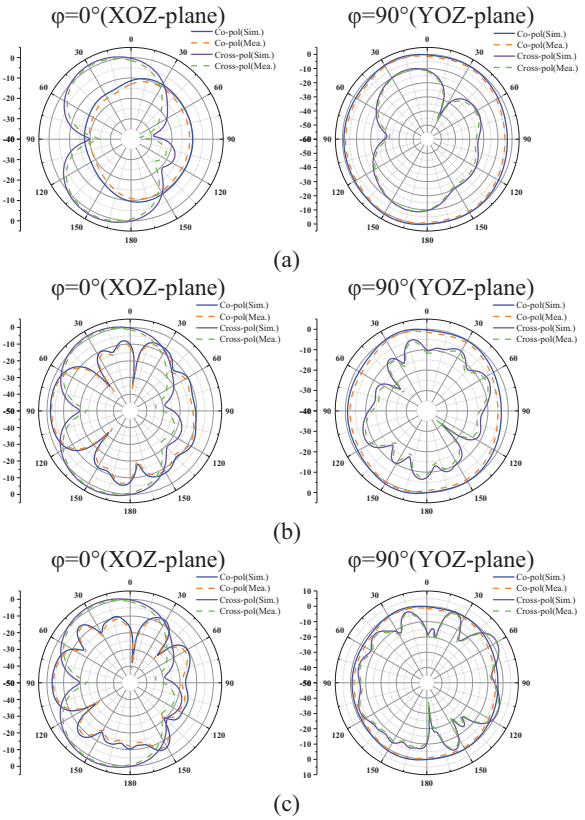


Fig. 16. Modeled and measured radiation characteristics: (a) 6.6 GHz, (b) 15.4 GHz, and (c) 20.5 GHz.

At the low frequency of 6.6 GHz, the E-plane exhibits a typical dipole-like figure-of-eight pattern with main lobes directed at 0° and 180°, while the H-plane shows good quasi-omnidirectional characteristics, which are beneficial for wide-angle radiation coverage. As the frequency increases to 15.4 GHz, due to the increased electrical size of the antenna at higher frequencies, the E-plane pattern exhibits noticeable ripples and subsidiary lobes, although the main radiation directions remain stable. The H-plane generally retains its quasi-omnidirectional behavior with slightly increased fluctuations. At 20.5 GHz, higher-order modes are excited, resulting in multi-lobed patterns with stronger angular variations. Nevertheless, the antenna still maintains stable radiation characteristics.

Regarding polarization purity, the antenna exhibits good cross-polarization suppression across the entire operating band. At 6.6 GHz, the cross-polarization level is below -15 dB in the main radiation directions, while at 15.4 GHz it remains below -18 dB. At 20.5 GHz, the cross-polarization level increases slightly but is still significantly lower than the co-polarized component, with a difference of approximately 15–20 dB in the main radiation directions. These results indicate good polarization discrimination throughout the operating band. Furthermore, at all measured frequencies, the simulated and measured co-polarization and cross-polarization patterns agree well, validating the effectiveness and practical radiation performance of the proposed antenna.

Figure 17 presents the peak gain and radiation efficiency of the optimized single antenna (Antenna 3) and the proposed four-port MIMO antenna (Antenna Model 5) across the operating band. As shown in Fig. 17 (a), the simulated peak gain of Antenna 3 ranges from 2.5 to 7.8 dBi, while that of Antenna Model 5 reaches 4.0–7.0 dBi with a maximum value of approximately 7.0 dBi. The measured peak gain of Antenna Model 5 generally follows the same trend as the simulation, with slight deviations attributed to fabrication tolerances and measurement uncertainties. The gain fluctuation at higher frequencies is mainly due to the excitation of higher-order modes and the increased electrical size of the antenna. As shown in Fig. 17 (b), the simulated radiation efficiency of both antennas remains above 72% throughout the entire operating band, with most frequencies maintaining efficiency above 80%. For Antenna Model 5, the measured radiation efficiency stays consistently above 78% across the operating band, matching the simulated trend well. The comparable efficiency between the single antenna and the MIMO antenna demonstrates that the proposed decoupling structures introduce only marginal additional conduction or dielectric losses. Overall, the measured gain results are in good agreement with the simulated data, validating the effectiveness of the proposed design.

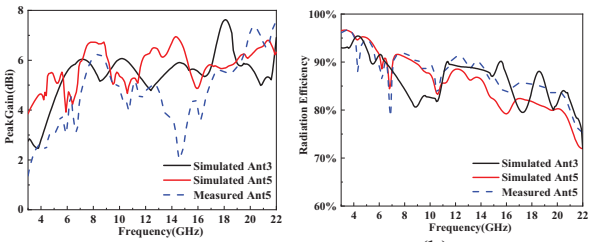


Fig. 17. (a) Peak gain and (b) radiation efficiency of the optimized single antenna (Ant3) and MIMO Antenna (Ant5).

C. MIMO antenna performance

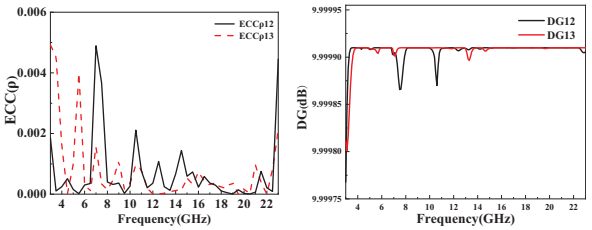
C.1. DG and ECC

The diversity characteristics and mutual coupling performance of MIMO antennas can be characterized

by the envelope correlation coefficient (ECC). The ECC quantifies the spatial correlation between the far-field radiation patterns of different antenna elements, with lower values indicating better independence among the elements. The radiation pattern-based ECC is calculated using both the θ and φ components of the far-field electric field over the entire 4π solid angle, assuming an isotropic propagation environment, as shown in equation (1) [4]. Diversity gain (DG) is a key metric that characterizes the degree of signal amplification or attenuation in MIMO systems, determined by equation (2) [4]. Typically, the ECC of MIMO antennas is required to be below 0.5 to meet the specifications for S-parameters (dB), radiation efficiency (%), and peak gain (dBi); furthermore, the closer the DG value is to 10, the more excellent the performance of the MIMO antenna. As illustrated in Fig. 18, the ECC of the proposed antenna is consistently below 0.005, and the DG approaches 10, demonstrating that it meets the requirements for communication applications within the 3.36–21.91 GHz band.

$$\rho_{e,ij} = \frac{\left| \iint_{4\pi} (\vec{E}_i(\theta,\phi) \cdot \vec{E}_j^*(\theta,\phi)) d\Omega \right|^2}{\iint_{4\pi} |\vec{E}_i(\theta,\phi)|^2 d\Omega \cdot \iint_{4\pi} |\vec{E}_j^*(\theta,\phi)|^2 d\Omega}, \quad (1)$$

$$DG = 10 \times \sqrt{1 - |ECC|}. \quad (2)$$



(a) (b)

Fig. 18. (a) ECC and (b) DG of the proposed antenna.

C.2. TARC

The total active reflection coefficient (TARC) is a metric used to evaluate the overall reflection performance of MIMO antennas, which comprehensively takes into account the reflected signals at all ports and the mutual coupling effects between antenna elements. Its core idea is to reflect the overall impedance matching efficiency of the antenna and the coupling degree between ports by quantifying the total reflection characteristics of the system under all-port excitation. Ideally, TARC should approach zero, which indicates that the antenna can efficiently absorb incident power and reduce reflection and mutual coupling interference. The TARC of this MIMO system can be calculated by the following equation [4]:

$$TARC = \frac{\sqrt{\sum_{i=1}^{4} \left| S_{i1} + \sum_{n=2}^{4} S_{in} e^{j\theta n-1} \right|^2}}{2}. \quad (3)$$

As shown in Fig. 19, in the frequency range of 3.36–21.91 GHz, the curves of TARC12 and TARC13 mostly remain at a relatively low decibel level. Among these, a large number of frequency bands are below −10 dB, and the performance in some regions is even better. This indicates that the reflection and mutual coupling effects between the ports of the proposed MIMO antenna are weak. It can not only absorb incident power more efficiently and reduce reflection loss, but also ensure different ports have good independence, which is conducive to improving the communication capacity and reliability of the MIMO system.

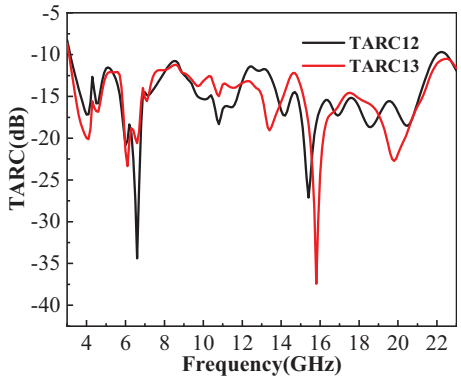


Fig. 19. Simulation results of the TARC of the proposed antenna.

C.3. CCL

Channel capacity loss (CCL) is a key metric for evaluating the effective data transmission performance of MIMO communication systems, which quantifies the capacity degradation caused by mutual coupling between antenna elements. Its core idea is to reflect the impact of inter-port coupling on the system's transmission efficiency by measuring the loss of available channel capacity. Ideally, the CCL should be as small as possible, which indicates that the antenna's coupling effect has little influence on the channel capacity, thus ensuring efficient data transmission. The CCL of this MIMO system can be calculated by the following equation [4]:

$$CCL = -\log_2(\Psi^R), \quad (4)$$

where Ψ^R denotes the receiver's correlation matrix, expressed as:

$$\Psi^R = \begin{bmatrix} \Psi_{11} & \Psi_{12} \\ \Psi_{21} & \Psi_{22} \end{bmatrix}.$$

The elements of the matrix are defined as:

$$\Psi_{11} = 1 - (|S_{12}|^2 + |S_{13}|^2)$$
$$\Psi_{12} = -(S_{11} + S_{12} + S_{13} + S_{14})$$
$$\Psi_{13} = (S_{22} + S_{23} + S_{24} + S_{21})$$
$$\Psi_{14} = 1 - (|S_{21}|^2 + |S_{23}|^2).$$

As shown in Fig. 20, within the operating frequency range of 3.36–21.91 GHz, the curves of CCL12 and CCL13 mostly maintain a relatively low level. Most frequency bands have CCL values below 0.1 bps/Hz, and some regions even approach −0.1 bps/Hz, which is far less than the reliable value of 0.4 bps/Hz. This result indicates that the mutual coupling between the ports of the proposed MIMO antenna has a minimal impact on the channel capacity, effectively reducing capacity loss. It not only enables the system to transmit data more efficiently but also enhances the communication reliability of the MIMO system, which is conducive to the practical application of the antenna in UWB communication scenarios.

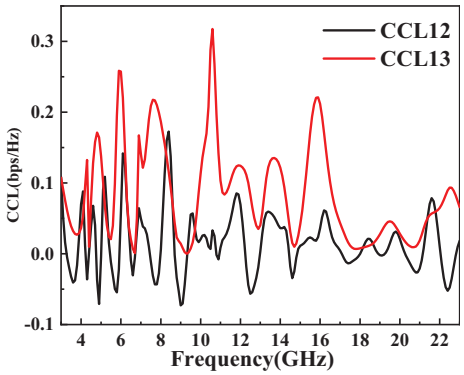
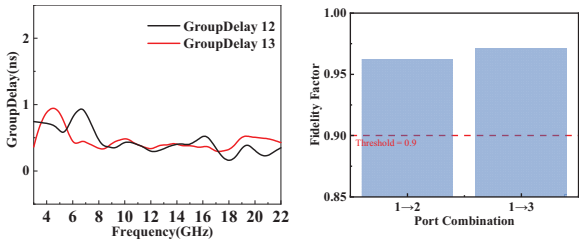


Fig. 20. Simulation results of the CCL of the proposed antenna.

C.4. Pulse fidelity and group delay characteristics

Figure 21 (a) shows the group delay characteristics of the proposed four-element UWB MIMO antenna, corresponding to the transmission paths between Port 1 and Port 2 (Group Delay 12) as well as Port 1 and Port 3 (Group Delay 13). Both curves exhibit stable and flat performance across the entire operating band of 3.36–21.91 GHz, with group delay values ranging from approximately 0.2 to 1.0 ns and only minor, gradual fluctuations. No pronounced abrupt changes or severe oscillations are observed throughout the frequency range. To further quantify the impact of these characteristics on pulse distortion, the fidelity factor (FF) is calculated for the two paths, as shown in Fig. 21 (b). The FF, which measures the similarity between the input and output pulses, is a critical metric for UWB systems, with a minimum acceptable threshold of 0.9. Both paths exhibit FF values significantly above this threshold: the FF for the 1→2 path is approximately 0.962, while the FF for the 1→3 path reaches approximately 0.971. These results confirm that the flat group delay performance effectively mitigates frequency dispersion, avoiding excessive delay differences that would otherwise cause pulse broadening and signal distortion. The excellent time-domain performance ensures reliable signal integrity for UWB impulse-based communication and ranging applications.



(a) (b)

Fig. 21. Time-domain performance of the proposed antenna: (a) group delay and (b) fidelity factor.

C.5. Comparative study

Table 2 provides a comparative analysis of the proposed antenna against existing designs with respect to key performance metrics, including size, operating bandwidth, isolation, number of ports, and ECC. Firstly, the proposed antenna achieves an operating bandwidth of 3.36–21.91 GHz, which exceeds that of most referenced designs (2.1–20 GHz [25] and 4.4–11.1 GHz [20]), enabling full coverage of the C/X/Ku bands. Secondly, its 62×62 mm^2 four-port configuration is more compact than larger four-port counterparts such as [24] and [25] (80×80 mm^2) and, unlike two-port schemes [20], it does not compromise multi-stream transmission capability. Meanwhile, the antenna maintains full-band isolation greater than 20 dB, outperforming [26] (>18 dB) and [27] (>17 dB), and matching the isolation level of [28] while offering a wider bandwidth. The high isolation (>25 dB) of [24] and [25] comes at the cost of a larger footprint. Finally, with an ECC of less than 0.006, the proposed antenna outperforms most designs [20, 24, 25], and is only slightly higher than that of [29] (<0.004) while featuring a more compact size. Thus, the proposed antenna essentially achieves balanced optimization of various performance metrics, resolves common tradeoffs in existing designs, and meets the typical requirements for UWB MIMO antennas.

Table 2: Performance comparison of the proposed MIMO antenna with other works

Ref.	Size (mm^2)	Bandwidth (GHz)	Isolation (dB)	Port	ECC
[8]	$0.25 \times 0.35\lambda_0$	3–11	>25	2	<0.004
[16]	$0.48 \times 0.97\lambda_0$	3.1–10.6	>31	2	<0.035
[19]	$0.35 \times 0.43\lambda_0$	3–10.7	>25	2	≤0.01
[20]	$0.91 \times 0.91\lambda_0$	3.4–8.25	>25	4	<0.01
[21]	$0.56 \times 0.56\lambda_0$	2.1–20	>25	4	<0.02
[22]	$0.67 \times 0.67\lambda_0$	2.8–13.3	>18	4	<0.06
[23]	$0.35 \times 0.35\lambda_0$	2.96–11.25	>17	4	<0.012
[24]	$0.60 \times 0.60\lambda_0$	3–11	>20	4	<0.02
[25]	$0.55 \times 0.55\lambda_0$	1–20	>20	4	<0.004
This Work	$0.69 \times 0.69\lambda_0$	3.36–21.91	>20	4	<0.005

IV. CONCLUSION

This paper presents an innovative bear-shaped radiating element antenna for the miniaturization, high isolation, and wide bandwidth requirements of UWB MIMO antennas, where the radiating element is not merely a morphological innovation. Its irregular outline enriches the diversity of equivalent current paths, facilitates the cooperative excitation of multiple characteristic modes, and lays a structural foundation for UWB performance. Meanwhile, with CMA as the core theoretical guidance, the proposed configuration integrates DGS, a cross-shaped hollowed-out decoupling structure, and eight L-shaped matching stubs to form a systematic decoupling scheme, suppressing mutual coupling between elements from the perspective of physical mechanisms and overcoming the limitations of traditional trial-and-error approaches. Through the in-depth integration of structural optimization and theoretical guidance, the antenna achieves wideband coverage of 3.36–21.91 GHz with isolation exceeding 20 dB, and comprehensive advantages of high radiation efficiency and low ECC. It thereby provides an efficient and reliable antenna solution for advanced wireless communication scenarios with stringent requirements on bandwidth, isolation, and volume, such as V2X, autonomous driving positioning, and industrial IoT. Future work will focus on further miniaturizing the antenna without losing core performance to adapt to more compact terminal devices, and replacing traditional FR4 substrates with flexible substrates to expand its application potential in wearable devices.

ACKNOWLEDGMENT

This work was supported in part by the Natural Science Research Project of Anhui Educational Committee under Grant no. 2025AHGXZK31006, in part by The Research Foundation of Jiangsu Engineering Research Center for Bionics Control Technology and Equipment under No. FSKZ202503, and in part by the Fund of Anhui Mining Machinery and Electrical Equipment Coordination Innovation Center (Anhui University of Science and Technology) under grant No. KSJD202406.

REFERENCES

[1] K. S. Muttair, A. Z. G. Zahid, O. A. S. Al-Ani, A. M. Q. Al-Asadi, and M. F. Mosleh, "Antennas performance comparison of multi-bands for optimal outdoor and indoor environments wireless coverage," *Indonesian Journal of Electrical Engineering and Informatics (IJEEI)*, vol. 9, no. 4, pp. 846–858, 2021.

[2] B. Wu, X.-Y. Sun, H.-R. Zu, H.-H. Zhang, and T. Su, "Transparent ultrawideband halved coplanar Vivaldi antenna with metal mesh film," *IEEE Antennas Wireless Propag. Lett.*, vol. 21, pp. 2532–2536, 2022.

[3] J. F. Li, Q. X. Chu, Z. H. Li, and X. X. Xia, "Compact dual band-notched UWB MIMO antenna with high isolation," *IEEE Trans. Antennas Propag.*, vol. 61, pp. 4759–4766, 2013.

[4] M. S. Sharawi, "Printed multi-band MIMO antenna systems and their performance metrics [wireless corner]," *IEEE Antennas Propag. Mag.*, vol. 55, no. 5, pp. 218–232, 2013.

[5] S. Kim, E. Visotsky, P. Moorut, K. Bechta, A. Ghosh, and C. Dietrich, "Coexistence of 5G with the incumbents in the 28 and 70 GHz bands," *IEEE J. Sel. Areas Commun.*, vol. 35, no. 6, pp. 1254–1268, 2017.

[6] J. H. Lee, J. S. Choi, and S. C. Kim, "Cell coverage analysis of 28 GHz millimeter wave in urban microcell environment using 3-D ray tracing," *IEEE Trans. Antennas Propag.*, vol. 66, no. 3, pp. 1479–1487, 2018.

[7] H. Ullah, S. Ur Rahman, Q. Cao, I. Khan, and H. Ullah, "Design of SWB MIMO antenna with extremely wideband isolation," *Electronics*, vol. 9, no. 1, p. 194, 2020.

[8] L. Wang, Z. Du, H. Yang, R. Ma, Y. Zhao, X. Cui, and X. Xi, "Compact UWB MIMO antenna with high isolation using fence-type decoupling structure," *IEEE Antennas Wireless Propag. Lett.*, vol. 18, pp. 1641–1645, 2019.

[9] A. Fitri, U. Umaisaroh, and M. Alaydrus, "A novel parasitic EBG structure to enhance mutual coupling for 2.45 GHz MIMO antenna," in *2022 International Conference on Radar, Antenna, Microwave, Electronics, and Telecommunications (ICRAMET)*, pp. 253–257, 2022.

[10] A. R. Vilenskiy, V. I. Litun, and K. V. Lyulyukin, "Wideband beam steering antenna array of printed cavity-backed elements with integrated EBG structure," *IEEE Antennas Wireless Propag. Lett.*, vol. 18, no. 2, pp. 245–249, Feb. 2019.

[11] S. Zhang and G. F. Pedersen, "Mutual coupling reduction for UWB MIMO antennas with a wideband neutralization line," *IEEE Antennas Wireless Propag. Lett.*, vol. 15, pp. 166–169, 2016.

[12] R. K. Garg, S. Singhal, M. V. Nair, and R. Tomar, "Wideband planar UWB MIMO antenna design with a leaf-shaped four-port," *IEEE Antennas Wireless Propag. Lett.*, vol. 13, pp. 1663–1666, 2014.

[13] H. C. Ye, C. Mao, L. L. Dai, and X. Y. Zhang, "Dual-band dual-polarized antenna and array with enhanced bandwidth for 5G millimeter-wave applications," *IEEE Antennas Wireless Propag. Lett.*, vol. 24, no. 7, pp. 1829–1833, July 2025.

[14] T. Vijetha and D. R. Krishna, "Dual band notch antenna for ultra wide band applications," in *2022 IEEE Microwaves, Antennas, and Propagation Conference (MAPCON)*, pp. 1961–1965, 2022.

[15] S. Jayant, G. Srivastava, and S. Kumar, "Pattern diversity and isolation enhancement of UWB MIMO antenna based on characteristic modes for mobile terminals," *International Journal of Microwave and Wireless Technologies*, pp. 793–804, 2023.

[16] S. Zhang and G. F. Pedersen, "Mutual coupling reduction for UWB MIMO antennas with a wideband neutralization line," *IEEE Antennas Wireless Propag. Lett.*, vol. 15, pp. 166–169, 2016.

[17] M. V. Yadav and S. Baudha, "A miniaturized printed antenna with extended circular patch and partial ground plane for UWB applications," *Wireless Personal Communications*, vol. 116, no. 1, pp. 311–323, 2020.

[18] R. I. Nawar, A. M. Abdelhady, and A. Y. Hassan, "High performance circularly polarized quad-elements for 5G wireless communications," *Arabian Journal for Science and Engineering*, pp. 1–18, 2025.

[19] W. H. Chen, L. H. Ye, K. Ding, F. Jiang, and D.-L. Wu, "A broadband circularly polarized antenna using characteristic mode analysis," *IEEE Trans. Antennas Propag.*, vol. 72, no. 12, pp. 9143–9151, 2024.

[20] C. Fu, C. Feng, W. Chu, Y. Yue, X. Zhu, and W. Gu, "Design of a broadband high-gain omnidirectional antenna with low cross polarization based on characteristic mode theory," *IEEE Antennas Wireless Propag. Lett.*, vol. 21, no. 9, pp. 1747–1751, 2022.

[21] M. Ren, J. Li, H. Zhao, and C. Xia, "A novel triband circularly polarized metasurface antenna based on characteristic mode analysis," *IEEE Antennas Wireless Propag. Lett.*, vol. 23, no. 11, pp. 3817–3821, 2024.

[22] Z. Zhan, W. Huang, R. Deng, and B. Li, "Compact dual polarized antenna with wide band and high isolation using characteristic mode analysis," *Progress in Electromagnetics Research C*, vol. 142, pp. 95–106, 2024.

[23] S. Modak and T. Khan, "A slotted UWB-MIMO antenna with quadruple band-notch characteristics using mushroom EBG structure," *AEU–International Journal of Electronics and Communications*, vol. 134, p. 153673, 2021.

[24] A. Ghosh, A. Ghosh, and J. Kumar, "Circularly polarized wideband quad-element MIMO antenna with improved axial ratio bandwidth and mutual coupling," *IEEE Antennas Wireless Propag. Lett.*, vol. 23, pp. 4718–4722, 2024.

[25] V. S. D. Rekha, P. Pardhasaradhi, B. T. P. Madhav, and Y. U. Devi, "Dual band notched orthogonal 4-element MIMO antenna with isolation for UWB applications," *IEEE Access*, vol. 8, pp. 145871–145880, 2020.

[26] S. Kumar, G. H. Lee, D. H. Kim, W. Mohyuddin, H. C. Choi, and K. W. Kim, "Multiple-input-multiple-output/diversity antenna with dual band-notched characteristics for ultra-wideband applications," *Microwave Opt. Technol. Lett.*, vol. 62, no. 1, pp. 336–345, 2020.

[27] X. Lu, S. Linghu, F. Pang, and T. Zhang, "A miniaturized ultra-wideband MIMO antenna design with dual-band notched characteristics," *Progress in Electromagnetics Research M*, vol. 115, pp. 45–58, 2023.

[28] S. S. Ahmed, B. Khan, M. Manzoor, M. Souri, M. Alibakhshikenari, M. F. Darsinos, and E. Falcone, "A compact CPW-fed ultra-wideband multi-input-multi-output (MIMO) antenna for wireless communication networks," *IEEE Access*, vol. 10, pp. 25278–25289, 2022.

[29] Y. Yao, Y. Shao, J. Zhang, and J. Zhang, "A transparent antenna using metal mesh for UWB MIMO applications," *IEEE Trans. Antennas Propag.*, vol. 71, pp. 3836–3844, 2023.



Xiaoyan Wei received the B.E. degree from Anhui University of Science and Technology, China, in 2024. She is currently pursuing the M.S. degree at Anhui University of Science and Technology. Her current research interests include the theory and design of UWB MIMO antenna based on characteristic mode analysis.



Zhonggen Wang received the Ph.D. degree in electromagnetic field and microwave technique from the Anhui University of China (AHU), Hefei, P. R. China, in 2014. Since 2014, he has been with the School of Electrical and Information Engineering, Anhui University of Science and Technology. His research interests include computational electromagnetics, array antennas, and reflect arrays.



Wenyan Nie is a professor at Huainan Normal University, China. She received the B.S. and M.S degrees from Anhui University of Science and Technology in 2007 and 2012, respectively. Her research interests include computational electromagnetic methods, antenna theory and design.



Chenlu Li received the Ph.D. degree from Anhui University, China, in 2017. She is currently working at Hefei Normal University. Her research interests include electromagnetic scattering analysis of targets and filtering antenna design.



Zhengting Zhang received the B.E. degree from Anhui University of Science and Technology, China, in 2024. He is currently pursuing the M.S degree at Anhui University of Science and Technology. His current research interests include the design and research of miniaturized antennas for 5G Sub-6 GHz applications.

A Deep Learning and NSGA-II Based Multi-Objective Optimization Framework for SAR-Aware AMC-Backed Wearable Antenna Design

Muthukumaravel K[1] and Suganthi Santhanam[2]

[1]Department of Electronics and Communication Engineering, Meenakshi Ramaswamy Engineering College, Thathanur, Ariyalur, Tamil Nadu, India
muthu.kadhir@gmail.com

[2]Department of Electronics and Communication Engineering, K.Ramakrishnan College of Technology, Samayapuram, Trichy, Tamil Nadu, India
suganthis.ece@krct.ac.in

Abstract – This paper presents a SAR-aware machine-learning framework for optimizing an AMC-backed triple-band wearable antenna based on a two-iteration Sierpinski carpet radiator operating at 1.82, 2.42, and 5.00 GHz. A 600-sample full-wave CST dataset varies feed length, AMC-to-antenna gap, fractal scale, and AMC inter-cell gap. A multi-task DNN maps four normalized inputs to twelve outputs: gain, resonance-frequency deviation, SAR1g, and SAR10g across all bands. NSGA-II then identifies Pareto-optimal gain–SAR trade-offs, while SHAP indicates feed length and AMC gap dominate SAR. The optimized design achieves gains of 4.12/4.25/4.38 dBi and SAR of 0.082/0.075 W/kg, satisfying IEEE C95.1 and ICNIRP limits and improving over 2.6–2.9 dBi standalone gain values.

Index Terms – 5G sub-6 GHz, artificial magnetic conductor (AMC), deep learning, fractal geometry, machine learning, NSGA-II, SAR-aware design, wearable antenna.

I. INTRODUCTION

Wearable and mobile communication systems require compact antennas that can operate near the human body without degrading radiation performance or exceeding Specific Absorption Rate (SAR) limits. In body-centric operation, biological tissues behave as lossy dielectric media, causing electromagnetic absorption, bandwidth variation, gain reduction, and efficiency loss. This issue is critical for sub-6 GHz 5G and healthcare devices, where SAR reduction must be achieved without sacrificing antenna performance.

Fractal geometries, including the Sierpinski carpet, are widely used for compact multiband antennas because they increase the effective current path within a small radiator area. However, fractal radiators alone can produce localized near-field concentration around the feed and fractal edges. When placed close to lossy tissue, this effect may increase backward radiation, reduce radiation efficiency, and raise SAR. Hence, compact multiband operation must be supported by a structure that controls body-directed radiation.

Artificial magnetic conductors (AMCs) mitigate the performance degradation caused by the close proximity of wearable antennas to the human body by providing an approximately in-phase reflection response within their operating band. When positioned behind the radiating element, AMC surfaces can reduce body-directed radiation, enhance forward gain, and support lower specific absorption rate (SAR). These benefits have been demonstrated using AMC-integrated cavity-backed substrate-integrated waveguide antennas, dual-band low-SAR MIMO configurations, 2.4-GHz wearable antennas, fabric-based body-centric antennas, conformal dual-band structures, textile antennas, and compact biomedical wearable platforms [1–8]. Recent data-driven antenna studies have also progressed from comprehensive ML and deep-learning reviews to hybrid electromagnetic modelling of UWB MIMO antennas, convolutional-neural-network-based near-field prediction, incremental variable-fidelity multiobjective optimization, and ML-assisted synthesis of dielectric-filled slotted-waveguide antennas with prescribed sidelobe levels [9–13]. These developments demonstrate the increasing importance of computationally efficient and performance-aware optimization in complex antenna systems.

Fractal geometries have been employed to obtain compact and low-profile wearable antennas, including on-body WBAN radiators, flexible dual-band tree-fractal structures, and hybrid fractal antennas optimized using artificial neural networks and firefly algorithms.

Submitted On: February 22, 2026
Accepted On: June 30, 2026

1054-4887 © ACES

https://doi.org/10.13052/2026.ACES.J.410704

Wideband AMC loading has additionally been used to enhance the gain and off-body communication performance of low-profile monopole antennas [14–17]. A low-profile all-textile UWB antenna incorporating an AMC was subsequently developed for WBAN applications [18]. Curvature-adaptive triple-band metamaterial and uniplanar compact electromagnetic-bandgap loading has been investigated for wearable wireless and medical body-area networks [19]. A breathable triple-band EBG-loaded fractal antenna has also been proposed for WBAN operation [20], while a metamaterial-inspired dual-band antenna has been examined for body-area communication applications [21]. Although these studies demonstrate the benefits of fractal, AMC, EBG, and metamaterial loading, the simultaneous optimization of gain, radiation efficiency, resonance stability, and SAR within a unified and interpretable design framework remains insufficiently explored.

Machine learning has increasingly been applied to antenna modelling and optimization because it can represent nonlinear relationships between geometrical parameters and electromagnetic responses. Data augmentation has been incorporated into ML-assisted antenna optimization to improve prediction using limited training samples [22]. Data-driven models have also been developed to predict the resonant frequency and directivity of UMTS/LTE quasi-Yagi antennas [23], while established ML techniques have been employed to optimize double T-shaped monopole antennas [24]. An efficient modified K-nearest-neighbour method has been introduced for antenna optimization and design [25]. Neural-network-assisted optimization has further been investigated for electromagnetic applications [26], and a deep-reinforcement-learning framework has been developed for automated antenna optimization [27]. A compact triband antenna employing an AMC reflector has also demonstrated the suitability of AMC-backed configurations for WBAN communication [28]. Motivated by these developments, the present study combines AMC loading and fractal geometry with a deep-neural-network surrogate model, NSGA-II-based multiobjective optimization, and SHapley Additive exPlanations interpretation to achieve simultaneous multiband gain enhancement and SAR reduction.

A. Motivation and contribution

This work presents a SAR-aware ML-assisted optimization framework for a compact AMC-backed triple-band wearable antenna operating at 1.82, 2.42, and 5.00 GHz. The radiator uses a two-iteration Sierpinski carpet fractal geometry. A 600-sample CST dataset is generated by varying feed length, AMC-to-antenna gap, fractal scale factor, and AMC inter-cell gap to model gain, resonance stability, SAR_{1g}, and SAR_{10g}. A DNN surrogate predicts realized gain, resonance-frequency deviation, SAR_{1g}, and SAR_{10g} across the three bands and is coupled with NSGA-II for gain maximization and SAR minimization. SHAP analysis identifies the dominant design variables controlling gain and SAR. Compared with the authors' previous work [28], which reported the baseline fractal AMC-backed antenna, this study adds SAR-aware DNN modeling, NSGA-II multi-objective optimization, SHAP-based interpretation, and gain–SAR trade-off analysis. The optimized design improves realized gain from 2.6–2.9 dBi to 4.12–4.38 dBi, while reducing SAR to 0.082 W/kg for 1 g tissue and 0.075 W/kg for 10 g tissue, satisfying IEEE C95.1 and ICNIRP limits.

II. BASELINE ANTENNA OVERVIEW

The baseline antenna geometry is adopted from the authors' earlier work [28], where a compact triple-band fractal antenna with AMC backing was conventionally characterized. In the present work, the same geometry is used only as the starting platform for SAR-aware ML optimization. The DNN training, NSGA-II optimization, SHAP interpretation, gain–SAR trade-off analysis, and SAR-constrained design selection are newly developed in this study. The reference antenna consists of a two-iteration hybrid Sierpinski–Koch fractal radiator on a flexible FR4 substrate with thickness 1.82 mm, relative permittivity $\varepsilon_r = 4.4$, and loss tangent 0.02. The antenna has a compact footprint of $23 \times 30\,\text{mm}^2$. A coplanar waveguide (CPW) feed excites the planar radiator, while the etched fractal slots increase the effective electrical length and support multiband resonance without increasing the antenna size.

Figure 1 shows the standalone fractal antenna, and Fig. 2 presents its simulated reflection coefficient. The antenna resonates at 1.82 GHz, 2.42 GHz, and 5.0 GHz, covering ISM, WLAN, and sub-6 GHz 5G bands. The corresponding realized gains are 2.6 dBi, 2.72 dBi, and 2.9 dBi. However, without reflective backing, backward radiation and surface-wave propagation reduce forward gain and radiation efficiency. SAR simulations also indicate increased tissue absorption during on-body operation. These limitations motivate AMC integration and ML-assisted gain–SAR optimization in the following sections.

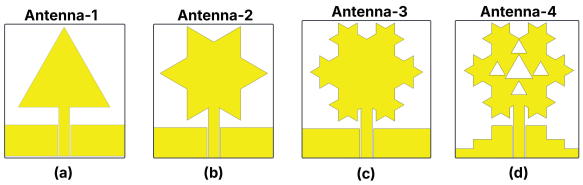


Fig. 1. Geometry of the standalone fractal antenna.

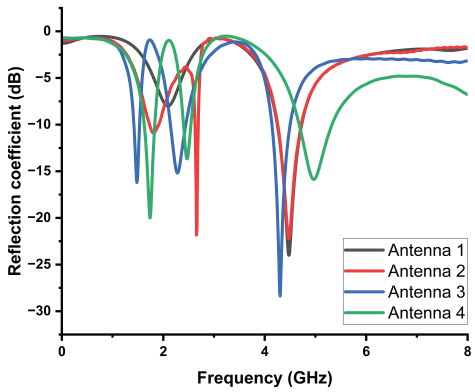


Fig. 2. Simulated reflection coefficient (S_{11}) for the baseline antenna.

III. AMC DESIGN AND CHARACTERIZATION FOR SAR REDUCTION AND GAIN ENHANCEMENT

The AMC backing is introduced to reduce SAR and improve forward gain in near-body operation by reflecting backward-directed fields in phase. This reduces body-directed radiation, which is critical for wearable antennas placed close to lossy tissue.

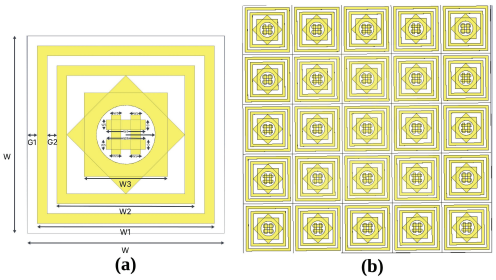


Fig. 3. (a) AMC unit cell geometry; (b) 5×5 AMC array layout.

A. AMC unit cell design

The AMC unit cell in Fig. 3 uses three concentric square-ring resonators tuned to 1.82, 2.42, and 5.00 GHz. A central grid patch provides capacitive coupling for miniaturization and high surface impedance. The unit cell is designed on a 1.82 mm FR4 substrate with $\varepsilon_r = 4.4$, $\tan\delta = 0.02$, a 35 μm copper layer, and a continuous ground plane. The dimensions are listed in Table 1.

The AMC unit-cell outer dimension is 9.00 mm, denoted by W_1. The 0.5 mm value is not the unit-cell periodicity; it represents the AMC inter-cell gap g_c between adjacent cells in the 5×5 array. Including this gap, the effective array pitch is approximately 9.5 mm. This distinction avoids confusion among unit-cell size, array pitch, and inter-cell spacing.

Table 1: Geometrical dimensions of the AMC unit cell

Parameter	Value (mm)
W_1	9.00
W_2	7.00
W_3	4.24
W_4	3.00
W_5	0.50
G_1	0.50
G_2	0.50
R	3.00

B. Operating principle, reflection phase, and bandwidth

The AMC operates as an equivalent parallel LC network, where the square rings provide inductance and the inter-ring gaps provide capacitance. Its resonance frequency is approximated by

$$f_{\text{res}} = \frac{1}{2\pi\sqrt{LC}}. \tag{1}$$

Unlike a PEC surface, which introduces a 180° phase shift, the AMC provides near-zero reflection phase at resonance and prevents destructive interference with the radiator.

Full-wave simulations under normal plane-wave incidence with periodic boundary conditions confirm triband AMC behavior. Figure 4 shows zero-phase crossings at 1.8 GHz, 2.42 GHz, and 5 GHz. The 2.42 GHz ISM band provides an usable bandwidth of approximately 327 MHz, supporting stable wearable biomedical and communication operation.

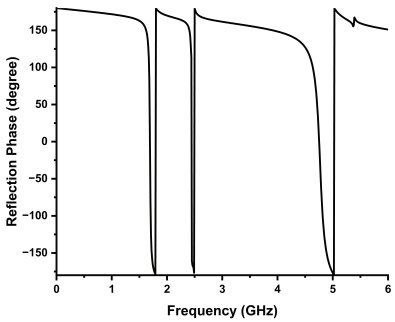


Fig. 4. Reflection phase response of AMC unit cell.

IV. INTEGRATION OF AMC WITH ANTENNA

The triple-band fractal antenna was integrated with the AMC array and first evaluated under free-space conditions to isolate the effect of AMC backing before human-body loading. At the operating bands, the AMC

reflects backward-directed fields in phase, suppresses body-facing radiation, improves forward gain, and supports SAR reduction.

A. Antenna fabrication and AMC array configuration

The AMC backing was realized as a 5×5 array of tri-band AMC unit cells resonating at 1.82, 2.42, and 5.00 GHz. The inter-cell spacing is denoted as $g_c = 0.5$ mm, which is not the unit-cell periodicity. Each unit cell has an outer lateral dimension of 9.0 mm, giving an effective array pitch of approximately 9.5 mm when g_c is included.

The AMC layer was fabricated on a 1.6 mm FR4 substrate with $\varepsilon_r = 4.4$ and loss tangent 0.02. The fractal antenna was fabricated on an identical FR4 substrate and excited through a CPW feed. An optimized AMC-to-antenna air gap of $g_a = 3$ mm was maintained using low-loss dielectric spacers. This vertical separation was selected from the NSGA-II-optimized design to balance forward-gain enhancement, SAR reduction, and compact profile.

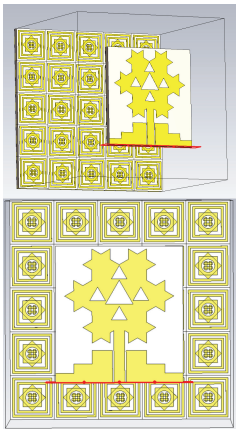


Fig. 5. 3D model of the AMC-integrated antenna, highlighting the optimized AMC-to-antenna air gap $g_a = 3$ mm.

Figure 5 shows the 3D AMC-integrated antenna and highlights the optimized air gap. Figure 6 presents the fabricated prototype and measurement arrangement, where the radiator and AMC layer are assembled with $g_a = 3$ mm.

The reflection coefficient was measured using a vector network analyzer after standard SOLT calibration at the SMA connector reference plane. The standalone and AMC-backed antennas were measured under identical calibration conditions. For the AMC-backed case, the radiator and AMC layer were kept parallel, and $g_a = 3$ mm was maintained during measurement. Gain and

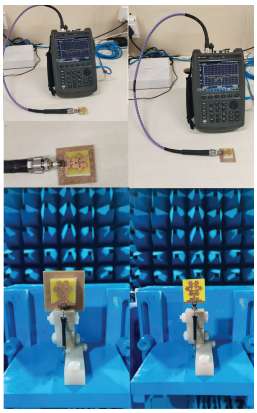


Fig. 6. Fabricated AMC-backed triple-band fractal antenna prototype and measurement arrangement, showing the assembled radiator–AMC configuration with the optimized AMC-to-antenna air gap $g_a = 3$ mm.

radiation patterns were measured using a calibrated reference antenna in a standard far-field setup. The antenna under test was placed on a low-reflection support, and patterns were recorded at 1.82, 2.42, and 5.00 GHz. Minor differences between simulated and measured results are attributed to fabrication tolerance, FR4-property variation, SMA soldering, conductor roughness, cable and connector losses, air-gap misalignment, and residual environmental reflections. Nevertheless, the measured trends confirm gain enhancement, improved forward radiation, and higher radiation efficiency with AMC backing.

B. Reflection coefficient comparison

The measured reflection coefficient ($|S_{11}|$) of the standalone and AMC-backed antennas is shown in Figs. 7 and 8. The standalone antenna exhibits resonance dips of -20 dB, -14.7 dB, and -15 dB at 1.82, 2.42, and 5.00 GHz, confirming triple-band operation. With AMC backing, the dips improve to -21 dB, -16 dB, and -15.6 dB, with a broader -10 dB bandwidth of about 820 MHz near 2.42 GHz. The improvement is due to AMC in-phase reflection, which stabilizes impedance

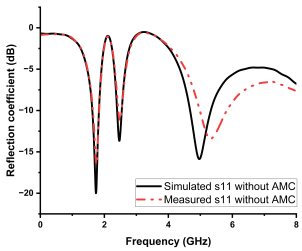


Fig. 7. Simulated and measured $|S_{11}|$ of the standalone antenna at 1.82, 2.42, and 5.00 GHz.

matching and suppresses backward radiation. Minor simulation–measurement shifts arise from fabrication tolerances.

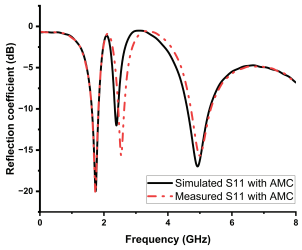


Fig. 8. Simulated and measured $|S_{11}|$ of the AMC-backed antenna at 1.82, 2.42, and 5.00 GHz.

C. Gain analysis

Figure 9 compares the realized gain of the standalone and AMC-backed antennas. At 1.82, 2.42, and 5.00 GHz, the gain increases from 2.60, 2.72, and 2.90 dBi to 4.12, 4.25, and 4.38 dBi, respectively. This enhancement results from improved impedance matching, higher radiation efficiency, reduced body-directed radiation, and constructive AMC reflection toward the forward hemisphere.

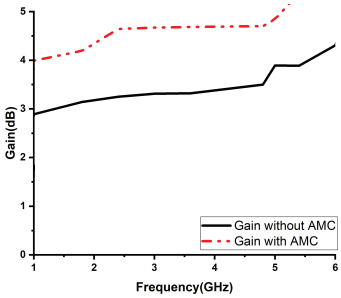


Fig. 9. Gain comparison of the standalone and AMC-backed antenna configurations over the operating frequency range.

D. Radiation pattern and efficiency evaluation

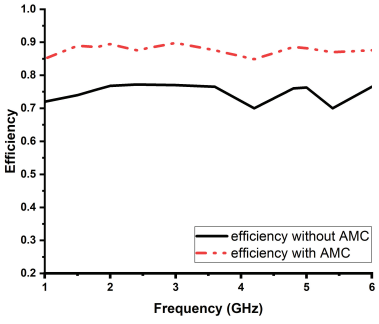


Fig. 10. Simulated and measured total radiation efficiency of the AMC-backed antenna at 1.82, 2.42, and 5.00 GHz.

Figure 10 shows the total radiation efficiency. The standalone antenna achieves 72–78%, whereas the AMC-backed design exceeds 85% across all operating bands. This confirms reduced substrate-mode loss and surface-wave propagation after AMC integration. The gain improvement is therefore due to both higher accepted-power radiation and improved forward directivity.

The E-plane and H-plane radiation patterns in Figs. 11 (a)–(f) show stronger forward radiation and suppressed back lobes after AMC integration. This behavior

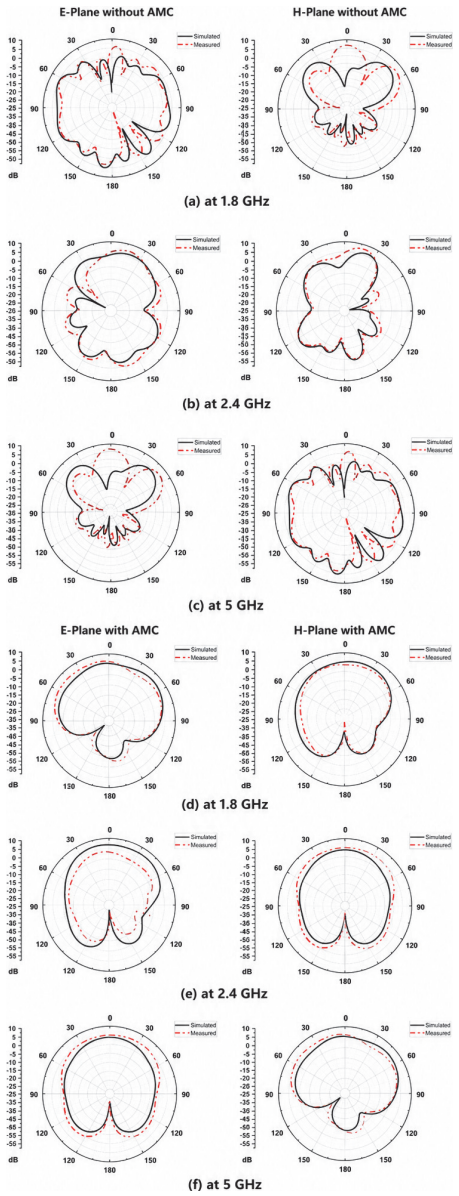


Fig. 11. Simulated and measured radiation patterns at (a) 1.82 GHz, (b) 2.42 GHz, and (c) 5 GHz without AMC, and (d) 1.82 GHz, (e) 2.42 GHz, and (f) 5 GHz with AMC.

supports stable wearable links and reduces user-directed electromagnetic exposure.

E. Wearable applicability and practical stability considerations

For wearable operation, bending, body proximity, wearing position, and deformation can affect impedance matching, radiation pattern, and SAR distribution. The AMC backing therefore acts not only as a gain-enhancement layer but also as an electromagnetic isolation layer between the radiator and lossy tissue. Bending modifies the effective current path of the fractal radiator and the spacing between the radiator and AMC surface, which may cause small resonance shifts and impedance variation. The AMC-backed structure is expected to be more stable than the standalone radiator because it suppresses backward radiation and reduces near-field coupling into the body. The optimized AMC-to-antenna air gap $g_a = 3$ mm further maintains controlled radiator–AMC coupling.

Antenna response may also vary with placement on the arm, chest, shoulder, or wrist due to differences in curvature, tissue thickness, and dielectric loading. Strongly curved regions can introduce larger detuning than flatter regions, while closer body contact may slightly reduce radiation efficiency. The AMC reduces these effects by redirecting radiation away from the body-facing side and limiting field penetration into tissue. From the SAR perspective, the AMC suppresses backward-directed fields and reduces tissue absorption. Thus, the optimized AMC-backed antenna is expected to maintain lower SAR than the standalone antenna under close-body operation, as discussed in the SAR analysis section. Although the present work verifies SAR reduction, gain enhancement, and stable radiation behavior through simulation and measurement, complete garment-level validation is beyond its scope. Future work will include repeated bending cycles, different bending radii, and multi-position body measurements. Therefore, the claim is limited to SAR-aware, AMC-backed wearable-oriented operation.

V. SAR-AWARE MACHINE LEARNING-BASED OPTIMIZATION FRAMEWORK

A. Motivation and problem formulation

Wearable and body-centric antennas require compact, efficient, and SAR-compliant operation. Conventional optimization mainly targets gain, impedance bandwidth, and radiation efficiency, but neglecting SAR in close-body use may violate international safety limits. Therefore, this work integrates SAR directly into an ML-assisted optimization loop for the AMC-backed triple-band fractal antenna operating at 1.82, 2.42, and 5.00 GHz.

The framework combines CST full-wave simulation, supervised learning, and evolutionary optimization. A dataset of 600 antenna geometries was generated by varying four design variables: feed length L_f, which controls input impedance, CPW-fed current distribution, and local electric-field concentration; AMC-to-antenna air gap g_a, which defines the vertical separation between the radiator and AMC surface and affects coupling, in-phase reflection, forward gain, and SAR; fractal scale factor η, which tunes effective current-path length and resonance positions; and AMC inter-cell gap g_c, which controls coupling between adjacent AMC cells in the 5×5 array, reflection-phase stability, field confinement, and surface-wave suppression.

The same variables are used for dataset generation, DNN surrogate training, NSGA-II optimization, and SHAP analysis. Here, g_c denotes the AMC inter-cell gap, not the AMC unit-cell periodicity; the optimized value of 0.5 mm represents the spacing between adjacent AMC cells. Similarly, g_a denotes the vertical AMC-to-antenna air gap.

For each geometry, realized gain, radiation efficiency, resonance-frequency deviation, SAR_{1g}, and SAR_{10g} were extracted at each operating band. Figure 12 summarizes the complete pipeline: CST-based dataset generation, DNN surrogate modeling, NSGA-II-based multi-objective gain–SAR optimization, and SHAP-based interpretation of parameter influence.

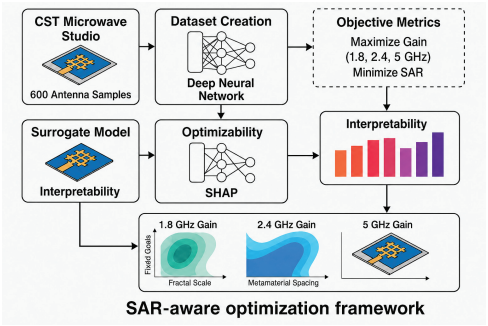


Fig. 12. SAR-aware optimization framework integrating CST-driven dataset generation, DNN-based surrogate modeling, SHAP interpretability, and NSGA-II optimization for gain–SAR trade-offs across 1.82, 2.42, and 5.00 GHz.

B. Definition of optimization variables and sampling strategy

The four geometrical variables used for dataset generation, DNN training, and NSGA-II optimization are defined in Table 2: feed length L_f, AMC-to-antenna air gap g_a, fractal scale factor η, and AMC inter-cell gap g_c.

Table 2: Optimization variables for DNN–NSGA-II training

Var.	Sym.	Physical Role	Range	Opt.
Feed length	L_f	Controls CPW current path, impedance matching, and feed-region electric-field concentration	8.5–10.5 mm	9.6 mm
AMC air gap	g_a	Radiator–AMC spacing; controls in-phase reflection, coupling, forward gain, and SAR	2.5–4.5 mm	3 mm
Fractal scale	η	Controls effective radiator length and tunes 1.82, 2.42, and 5.00 GHz resonances	1.6–2.4	2.0
AMC cell gap	g_c	Gap between adjacent AMC cells in the 5×5 array; controls coupling and reflection-phase stability	0.3–0.7 mm	0.5 mm

All variables were sampled using Latin hypercube sampling. Here, g_c is the AMC inter-cell gap, not the AMC unit-cell periodicity.

These variables govern impedance matching, resonance tuning, near-field coupling, backward-radiation suppression, realized gain, and SAR distribution. Here, g_c denotes the spacing between adjacent AMC cells in the 5×5 array, not the AMC unit-cell periodicity. The vertical separation between the radiator and AMC is denoted as g_a.

A total of 600 full-wave CST samples were generated within the bounds in Table 2 using Latin hypercube sampling. The ranges include the nominal geometry and fabrication-tolerant variations. For each sample, resonant frequency, realized gain, radiation efficiency, resonance-frequency deviation, SAR_{1g}, and SAR_{10g} were extracted at 1.82, 2.42, and 5.00 GHz for surrogate modeling and multi-objective optimization.

C. Dataset generation

Each CST sample was arranged as an input–output pair. The input vector is

$$\mathbf{x} = [L_f,\ g_a,\ \eta,\ g_c]^T, \tag{2}$$

where the variables follow the definitions in Table 2. For each operating band, the target outputs were realized gain, resonance-frequency deviation, SAR_{1g}, and SAR_{10g}; hence, each sample had a twelve-component output vector across 1.82, 2.42, and 5.00 GHz. Radiation efficiency was also retained for performance evaluation.

The dataset was balanced across the selected design space to reduce bias and overfitting. SAR extraction used the same phantom model, antenna-to-phantom distance, input-power normalization, tissue properties, and mesh settings for all samples. This ensured consistent SAR labels for DNN training and NSGA-II optimization.

1. Deep neural network (DNN) architecture

A fully connected multi-task DNN was used as a surrogate model to predict gain, resonance stability, and SAR from antenna geometry at 1.82, 2.42, and 5.00 GHz. A single model was trained for all three bands, as shown in Fig. 13. The normalized input vector is defined as

$$\mathbf{x} = [L_f,\ g_a,\ \eta,\ g_c]^T, \tag{3}$$

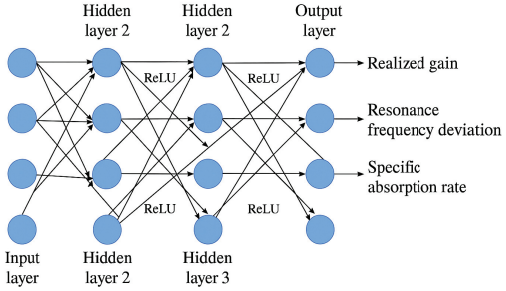


Fig. 13. DNN architecture with four geometrical input variables and twelve linear output nodes for predicting realized gain, resonance-frequency deviation, SAR_{1g}, and SAR_{10g} at 1.82, 2.42, and 5.00 GHz.

where L_f, g_a, η, and g_c denote feed length, AMC-to-antenna air gap, fractal scale factor, and AMC inter-cell gap, respectively.

To avoid a long single-column equation, the output vector is defined frequency-wise as

$$\mathbf{y} = [\mathbf{y}_{1.82}^T, \mathbf{y}_{2.42}^T, \mathbf{y}_{5.00}^T]^T, \tag{4}$$

where

$$\mathbf{y}_f = [G_f,\ \Delta f_f,\ SAR_f^{1g},\ SAR_f^{10g}]^T. \tag{5}$$

Here, G_f, Δf_f, SAR_f^{1g}, and SAR_f^{10g} represent realized gain, resonance-frequency deviation, 1 g SAR, and 10 g SAR at frequency f, respectively, where $f \in \{1.82, 2.42, 5.00\}$ GHz. The resonance-frequency deviation is calculated as

$$\Delta f_f = |f_r - f_t|, \tag{6}$$

where f_r is obtained from the simulated reflection coefficient and f_t is the target frequency.

The DNN consists of four input neurons, three fully connected hidden layers with 128, 64, and 32 ReLU neurons, and twelve linear output neurons. Training used the Adam optimizer with an initial learning rate of 1×10^{-3}, batch size of 32, maximum 500 epochs, early stopping with 30-epoch patience, and an 80:20 training–validation split. All variables were normalized

during training and converted back to physical units after prediction.

A weighted multi-task MAE loss was used to prioritize SAR prediction. For compact notation, the error terms at each frequency f are defined as

$$\begin{aligned} e_G(f) &= \mathrm{MAE}(\hat{G}_f, G_f), \\ e_{\Delta f}(f) &= \mathrm{MAE}(\widehat{\Delta f}_f, \Delta f_f), \\ e_{1g}(f) &= \mathrm{MAE}(\widehat{SAR}_f^{1g}, SAR_f^{1g}), \\ e_{10g}(f) &= \mathrm{MAE}(\widehat{SAR}_f^{10g}, SAR_f^{10g}). \end{aligned} \tag{7}$$

The total weighted loss is then written as

$$\begin{aligned} \mathscr{L}_{\mathrm{total}} = \frac{1}{3} \sum_{f \in \mathscr{F}} \big[& w_G e_G(f) + w_{\Delta f} e_{\Delta f}(f) \\ & + w_{1g} e_{1g}(f) + w_{10g} e_{10g}(f) \big], \end{aligned} \tag{8}$$

where $\mathscr{F} = \{1.82, 2.42, 5.00\}$ GHz. The loss weights are

$$\begin{aligned} w_G = 1, \quad w_{\Delta f} = 1, \\ w_{1g} = 3, \quad w_{10g} = 3. \end{aligned} \tag{9}$$

The higher SAR weights emphasize biological safety while preserving gain and resonance-deviation accuracy.

Model accuracy was evaluated using RMSE and R^2:

$$\mathrm{RMSE} = \sqrt{\frac{1}{N} \sum_{i=1}^{N} (y_i - \hat{y}_i)^2}, \tag{10}$$

$$R^2 = 1 - \frac{\sum_{i=1}^{N} (y_i - \hat{y}_i)^2}{\sum_{i=1}^{N} (y_i - \bar{y})^2}. \tag{11}$$

The trained DNN achieved $R^2 > 0.92$ for frequency-dependent gain and SAR prediction. During optimization, SAR_{1g} and SAR_{10g} were predicted at each band, and the worst-case SAR across the three bands was used for safety-constrained design selection.

2. NSGA-II multi-Objective genetic algorithm

The trained DNN was coupled with NSGA-II to search for antenna geometries that balance gain, resonance stability, and SAR at 1.82, 2.42, and 5.00 GHz. The design variables were L_f, g_a, η, and g_c, with the same bounds used during CST dataset generation. For each candidate geometry, the DNN predicted realized gain, resonance-frequency deviation, SAR_{1g}, and SAR_{10g} at all bands.

The optimization maximized realized gain and minimized resonance-frequency deviation, SAR_{1g}, and SAR_{10g}. The worst-case SAR across the three bands was used for constraint handling. Table 3 lists the NSGA-II settings, including binary tournament selection, simulated binary crossover, polynomial mutation, and penalty-based feasibility ranking.

Table 3: NSGA-II settings for SAR-aware optimization

Parameter	Value/Method
Design variables	4
Population size	100
Generations	50
Parent selection	Binary tournament
Crossover	Simulated binary crossover; probability = 0.90; distribution index = 20
Mutation	Polynomial mutation; probability = 0.25; distribution index = 20
Constraint handling	Penalty-based feasibility ranking
Stopping criterion	Maximum generations or negligible Pareto-front spread improvement

Candidate solutions exceeding $\mathrm{SAR}_{1g} = 0.09$ W/kg or $\mathrm{SAR}_{10g} = 0.083$ W/kg were penalized. Designs with large resonance deviation were also ranked lower to avoid low-SAR but mismatched solutions. The Pareto plots in 18, and 19 are two-dimensional projections of the higher-dimensional solution space. Final selection used the full multi-frequency DNN output, including gain, resonance deviation, SAR_{1g}, and SAR_{10g} at 1.82, 2.42, and 5.00 GHz. The selected feasible non-dominated design achieved realized gains of 4.12, 4.25, and 4.38 dBi at 1.82, 2.42, and 5.00 GHz, respectively, while maintaining $\mathrm{SAR}_{1g} = 0.082$ W/kg and $\mathrm{SAR}_{10g} = 0.075$ W/kg.

D. SHAP and interpretability analysis

SHAP were used to interpret the DNN predictions and relate the learned trends to antenna physics. This step is important because the proposed framework targets high realized gain while maintaining SAR below the imposed limits of $\mathrm{SAR}_{1g} < 0.09$ W/kg and $\mathrm{SAR}_{10g} < 0.083$ W/kg.

Figure 14 shows the SHAP feature importance for SAR_{1g} and SAR_{10g}. Feed length L_f and AMC-to-antenna air gap g_a have the strongest influence on SAR, followed by AMC inter-cell gap g_c, while the fractal scale factor η has the lowest SAR contribution. This trend is physically consistent. The feed length modifies the CPW-fed current distribution and local electric-field hotspots, whereas g_a controls near-field coupling,

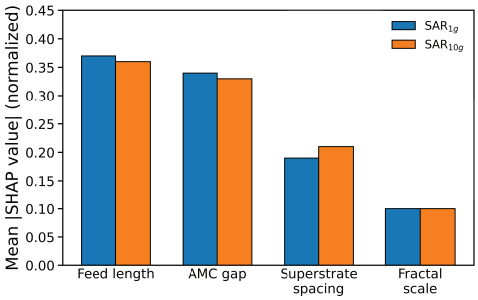


Fig. 14. SHAP feature importance for SAR_{1g} and SAR_{10g} highlighting the dominant influence of feed length L_f and AMC-to-antenna air gap g_a.

backward-radiation suppression, and body-facing field penetration. The inter-cell gap g_c affects AMC coupling and reflection-phase stability, while η mainly governs resonance tuning and gain. Thus, SHAP confirms that the gain–SAR optimization is physically meaningful and not only data-driven.

E. Optimization results and analysis

1. Model performance comparison

The proposed SAR-aware framework was evaluated by comparing a standalone DNN predictor with the hybrid NSGA-II + DNN approach. The comparison considered realized gain at 1.82, 2.42, and 5 GHz, SAR_{1g}, SAR_{10g}, and total radiation efficiency, as summarized in Table 4.

Table 4: Comparison of ML optimization strategies

Model	Gain† (dBi)	SAR_{1g} (W/kg)	SAR_{10g}/Eff. (W/kg/%)
DNN-only	4.05/4.18/4.28	0.088	0.081 / 88.2
NSGA-II+DNN	4.12/4.25/4.38	0.082	0.075 / 87.6

†Gain values are reported at 1.82/2.42/5.00 GHz.

The DNN-only model gives competitive gain values of 4.05 / 4.18 / 4.28 dBi, but its SAR values remain higher at 0.088 W/kg for SAR_{1g} and 0.081 W/kg for SAR_{10g}. The NSGA-II + DNN approach improves the gain–SAR balance, achieving 4.12 / 4.25 / 4.38 dBi at 1.82 / 2.42 / 5 GHz while reducing SAR_{1g} to 0.082 W/kg and SAR_{10g} to 0.075 W/kg. Both methods maintain efficiency above 87%, indicating that SAR reduction is not obtained through excessive radiation loss.

Figure 15 further shows that the NSGA-II + DNN solutions cluster in a lower-SAR region while retaining higher gain. This confirms the benefit of including SAR as an explicit optimization objective for wearable antenna design.

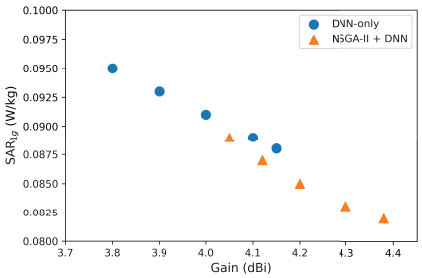


Fig. 15. Comparison of DNN-only and NSGA-II-augmented optimization results showing gain–SAR_{1g} clustering behaviour.

2. NSGA-II convergence behavior

The convergence of NSGA-II was evaluated over 50 generations to verify stable gain–SAR optimization. Figure 16 shows the SAR_{1g} and gain evolution. During early generations, SAR fluctuates due to broad design-space exploration. After nearly 30 generations, the search converges to SAR_{1g} near 0.082 W/kg, while gain approaches the optimized upper range of approximately 4.38 dBi. This confirms that NSGA-II can reduce SAR while maintaining high realized gain under the imposed safety constraints.

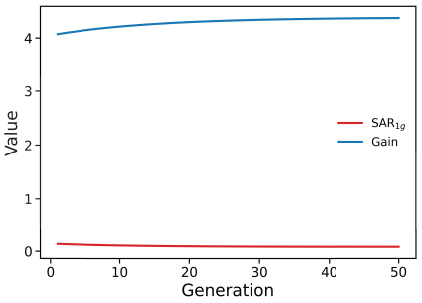


Fig. 16. NSGA-II convergence behavior showing the evolution of SAR_{1g} and gain over 50 generations.

Figure 17 shows a similar trend for SAR_{10g}. The convergence is more gradual because 10 g averaging smooths local field variations. The final population approaches SAR_{10g} values close to 0.075 W/kg while

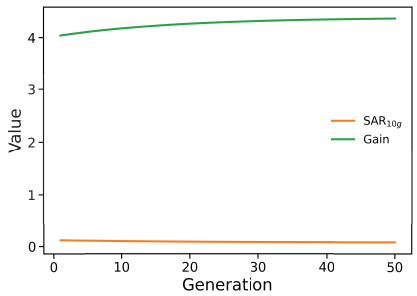


Fig. 17. NSGA-II convergence trend for SAR_{10g} and gain across 50 generations.

retaining a stable high-gain response. Thus, the convergence results confirm that the optimized designs satisfy both electromagnetic and biological safety requirements at 1.82, 2.42, and 5 GHz.

3. Pareto fronts and trade-Off plots

Pareto fronts were analyzed to evaluate the trade-off between realized gain and SAR across 1.82, 2.42, and 5 GHz. Figure 18 shows the SAR_{1g}–gain Pareto front. Across the three bands, higher-gain solutions show a moderate SAR increase; however, SAR_{1g} remains confined to approximately 0.076–0.086 W/kg, while realized gain reaches 4.38 dBi. This indicates that the SAR-aware constraints limit tissue exposure without preventing high-gain operation.

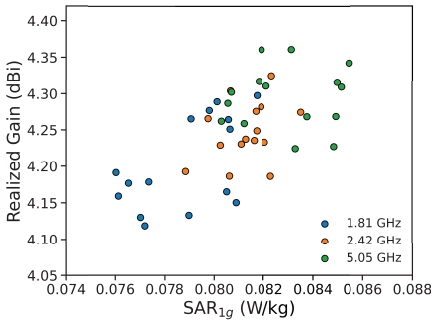


Fig. 18. Pareto front for SAR_{1g} versus realized gain across 1.82, 2.42, and 5 GHz.

Figure 19 presents the corresponding SAR_{10g}–gain Pareto front. Due to volumetric averaging, SAR_{10g} remains lower, within approximately 0.069–0.079 W/kg. A slight SAR_{10g} increase occurs at higher gain levels, but all values remain below the conservative safety threshold. These Pareto fronts support selection of antenna geometries that balance gain enhancement and SAR compliance for wearable operation.

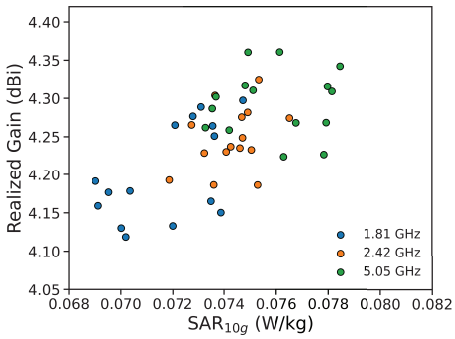


Fig. 19. Pareto front for SAR_{10g} versus realized gain across 1.82, 2.42, and 5 GHz.

4. Surface and contour analysis

Surface plots from the trained DNN surrogate were used to examine the effect of coupled design variables on gain and SAR at 1.82, 2.42, and 5.00 GHz. Here, g_a denotes the vertical AMC-to-antenna air gap, while g_c denotes the AMC inter-cell gap.

Figure 20 shows gain surfaces as functions of fractal scale factor η and g_a. At 5.00 GHz, gain is strongly affected by η, indicating the role of current-path shaping at the upper band. At 1.82 and 2.42 GHz, gain depends on both η and g_a, showing the combined effect of fractal tuning, field confinement, and AMC in-phase reflection. In all cases, gain remains below 4.38 dBi, consistent with the NSGA-II results.

Figure 21 maps SAR_{1g} and SAR_{10g} as functions of feed length L_f and g_a. Shorter feed lengths and smaller air gaps increase SAR due to stronger near-field coupling and localized current concentration. Moderate L_f values with optimized g_a form low-SAR regions, where SAR_{1g} remains below approximately 0.086 W/kg and SAR_{10g} remains below 0.079 W/kg without reducing gain. These maps provide direct design guidance for selecting safe high-gain geometries.

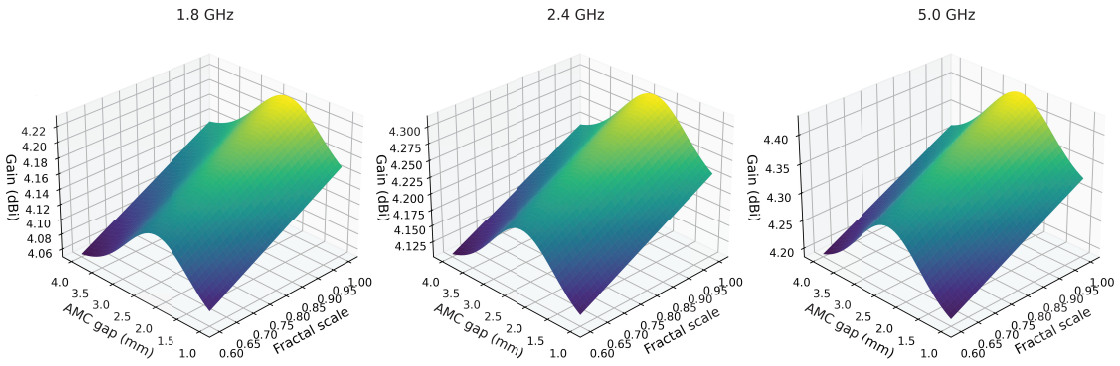


Fig. 20. Gain surface plots as functions of fractal scale factor η and AMC-to-antenna air gap g_a at (a) 1.82 GHz, (b) 2.42 GHz, and (c) 5.00 GHz.

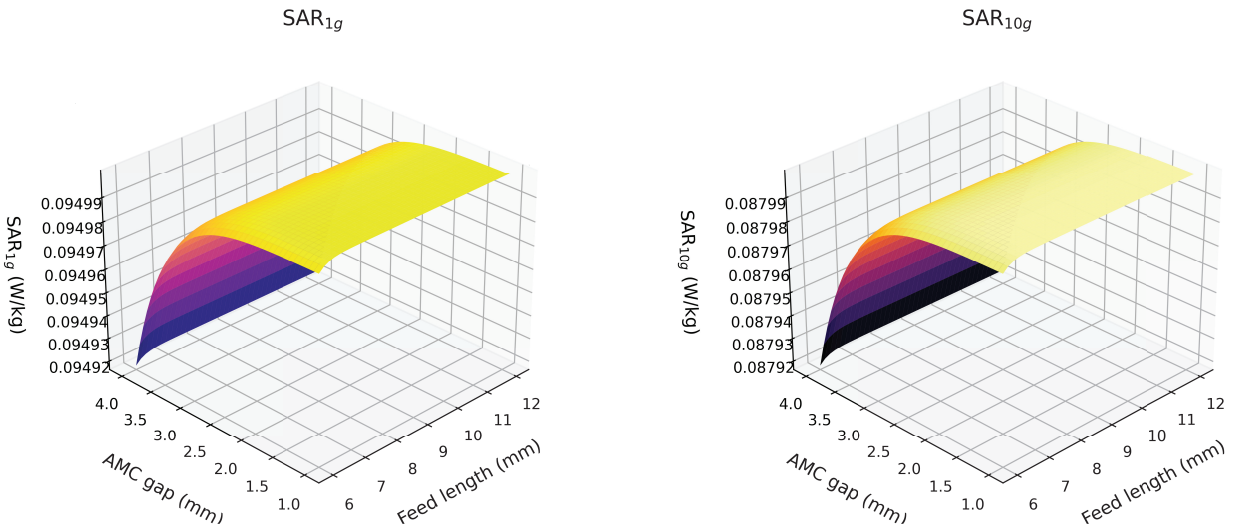


Fig. 21. Surface plots of SAR_{1g} and SAR_{10g} as functions of feed length L_f and AMC-to-antenna air gap g_a.

F. Optimized design parameters

The final NSGA-II + DNN design was selected to balance gain, resonance stability, and SAR compliance. It achieves a maximum realized gain of approximately 4.38 dBi, with $SAR_{1g} = 0.082$ W/kg and $SAR_{10g} = 0.075$ W/kg. These values are below IEEE C95.1 and ICNIRP exposure limits. The optimized geometry is listed in Table 5, with parameter roles supported by SHAP analysis and DNN surface responses.

Table 5: Optimized SAR-constrained geometry

Parameter	Opt.	Design Role
Fractal scale η	2.0	Sets current path and triple-band resonance; dominant gain tuning at 5.00 GHz
Feed length L_f	9.6 mm	Controls CPW current, matching, and feed-region SAR hotspots
AMC cell gap g_c	0.5 mm	Gap between 5×5 AMC cells; affects coupling, phase stability, surface-wave suppression, and isolation
AMC air gap g_a	3 mm	Radiator–AMC spacing; controls in-phase reflection, gain–SAR trade-off, and radiation efficiency

The selected values were obtained through the closed-loop CST–DNN–NSGA-II process, not through isolated tuning. The final antenna supports SAR-compliant operation at 1.82, 2.42, and 5 GHz for LTE, ISM, and sub-6 GHz 5G bands. Table 6 summarizes the main components of the SAR-aware optimization framework.

Table 6: Summary of the SAR-aware ML framework

Component	Compact description
Objective	Maximize gain at 1.82, 2.42, and 5.00 GHz; minimize Δf, SAR_{1g}, and SAR_{10g}
Variables	L_f, g_a, η, g_c; g_a: radiator–AMC gap; $g_c = 0.5$ mm: AMC inter-cell gap, not periodicity
Dataset	600 CST full-wave samples generated from the four-variable design space
DNN surrogate	Four inputs; hidden layers of 128/64/32 neurons; twelve outputs; ReLU hidden activation; linear output; SAR-weighted MAE loss
Outputs	Gain, Δf, SAR_{1g}, and SAR_{10g} at 1.82, 2.42, and 5.00 GHz
Optimizer	NSGA-II: population 100, 50 generations, binary tournament, SBX crossover, polynomial mutation, SAR-penalty ranking
Interpretability	SHAP-based parameter ranking and physical interpretation
Validation	Pareto fronts, convergence plots, surface maps, and final CST verification
Best result	Gain up to 4.38 dBi; $SAR_{1g} \approx 0.082$ W/kg; $SAR_{10g} \approx 0.075$ W/kg

Overall, the framework embeds SAR constraints into ML-based antenna optimization and supports physically interpretable design selection using SHAP and surface mapping. It maintains high gain while satisfying SAR limits across 1.82, 2.42, and 5 GHz.

VI. SAR ANALYSIS AND RESULTS

The SAR performance of the proposed antenna was evaluated to verify the SAR-aware ML optimization

framework discussed in the previous section. Unlike conventional AMC-backed designs that reduce SAR mainly through shielding, this work includes SAR as a constrained objective in the DNN–NSGA-II optimization loop. Thus, the reported SAR values result from simultaneous gain maximization and localized absorption minimization. Table 7 compares the standalone antenna and the optimized AMC-backed configuration.

Table 7: Standalone and optimized AMC-backed antenna performance

Metric	Standalone	AMC opt.
Gain @ 1.82 GHz	2.60 dBi	4.12 dBi
Gain @ 2.42 GHz	2.72 dBi	4.25 dBi
Gain @ 5.00 GHz	2.90 dBi	4.38 dBi
Efficiency	72–78%	$> 87\%$
Back radiation	High	Suppressed
SAR_{1g}	0.71 W/kg	0.082 W/kg
SAR_{10g}	0.21 W/kg	0.075 W/kg

A. SAR simulation setup and evaluation protocol

SAR was evaluated in CST Microwave Studio using the same finite-integration full-wave setup for both standalone and optimized AMC-backed antennas. The antenna was placed parallel to a planar multilayer human-body phantom consisting of skin, fat, and muscle. The phantom size was $120 \times 120 \times 60$ mm^3, with 2 mm skin, 5 mm fat, and the remaining depth modeled as muscle. The lower antenna surface was kept 5 mm above the top skin layer for both configurations. For the AMC-backed case, the AMC layer was placed between the radiator and phantom, with the optimized AMC-to-antenna air gap $g_a = 3$ mm.

SAR values were normalized to 1 W accepted input power. Both SAR_{1g} and SAR_{10g} were extracted at 1.82, 2.42, and 5.00 GHz using identical tissue properties, mesh settings, input normalization, and averaging methods. SAR_{1g} was compared with IEEE C95.1, while SAR_{10g} was compared with ICNIRP guidelines. The simulation conditions and tissue dielectric properties are summarized in Tables 8 and 9, respectively. These same settings were also used for the CST dataset applied in DNN training and NSGA-II optimization.

B. SAR distribution analysis (1 g and 10 g)

Figure 22 shows the simulated SAR distributions of the standalone and optimized AMC-backed antennas at 1.82, 2.42, and 5.00 GHz for 1 g and 10 g averaging models. Under 1 W accepted input power normalization, the standalone antenna exhibits localized SAR hotspots near the feed and fractal-radiator edges due to strong near-field coupling and direct backward field penetration into tissue. The peak SAR values reach 0.71 W/kg for SAR_{1g} and 0.21 W/kg for SAR_{10g}, as listed in Table 7.

With AMC backing, the SAR distribution is reduced and more confined. The AMC suppresses backward radiation and redirects energy toward the forward hemisphere through in-phase reflection, thereby limiting tissue penetration. The optimized design reduces SAR_{1g} to 0.082 W/kg and SAR_{10g} to 0.075 W/kg across the operating bands. These values remain below IEEE C95.1 and

Table 8: SAR simulation setup

Parameter	Setting
Tool	CST Microwave Studio full-wave solver
Phantom	Planar skin–fat–muscle model
Size	$120 \times 120 \times 60$ mm^3
Layer thickness	Skin: 2 mm; fat: 5 mm; muscle: remaining depth
Antenna–phantom gap	5 mm from lower antenna surface to skin
AMC air gap	$g_a = 3$ mm for optimized AMC-backed case
Power norm.	1 W accepted input power at antenna port
SAR averaging	1 g and 10 g tissue models
Safety limits	IEEE C95.1 for SAR_{1g}; ICNIRP for SAR_{10g}
Frequencies	1.82, 2.42, and 5.00 GHz
Mesh	Adaptive refinement near feed, AMC gaps, edges, and tissue interface
Convergence	Stable S-parameter and SAR response

Table 9: Dielectric properties of tissue phantom

f	Tissue	ε_r	σ (S/m)
1.82 GHz	Skin	38.5	1.18
	Fat	5.3	0.10
	Muscle	54.0	1.35
2.42 GHz	Skin	37.3	1.48
	Fat	5.2	0.11
	Muscle	52.7	1.73
5.00 GHz	Skin	35.0	3.70
	Fat	5.0	0.24
	Muscle	49.6	4.05

Tissue density ρ: skin = 1109 kg/m^3, fat = 911 kg/m^3, muscle = 1090 kg/m^3.

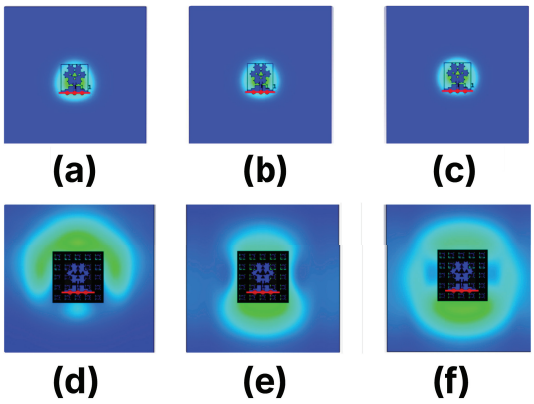


Fig. 22. Simulated SAR distributions for the standalone and optimized AMC-backed antenna configurations under 1 W accepted input power normalization: (a)–(c) SAR_{1g} at 1.82, 2.42, and 5.00 GHz; (d)–(f) SAR_{10g} at the corresponding frequencies.

ICNIRP limits, confirming the safety of the optimized wearable configuration.

C. Gain-SAR trade-Off validation

The gain–SAR trade-off is validated using Table 7 and Fig. 23. The optimized AMC-backed antenna achieves realized gains of 4.12, 4.25, and 4.38 dBi at 1.82, 2.42, and 5.00 GHz, respectively, exceeding the standalone antenna response. This gain improvement is obtained while reducing SAR by nearly one order of magnitude for both 1 g and 10 g averaging models. Thus, the ML-assisted optimization identifies geometries that improve forward radiation while satisfying SAR constraints.

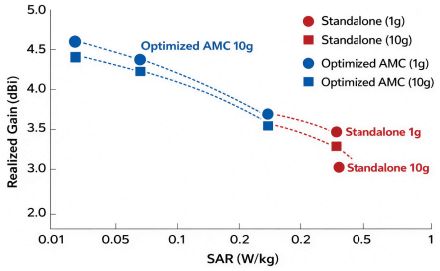


Fig. 23. Gain–SAR trade-off comparison between the standalone and optimized AMC-backed antenna configurations for 1 g and 10 g tissue models.

D. Discussion of the optimized design

The SAR and radiation results confirm the benefit of combining AMC backing with SAR-aware ML optimization. The AMC reduces surface-wave propagation and backward radiation, while the optimized feed length and AMC-to-antenna air gap regulate near-field current distribution and field confinement. These effects reduce localized SAR hotspots without degrading radiation performance. The optimized AMC-backed antenna maintains radiation efficiency above 87%, showing that SAR reduction is achieved through field redistribution rather than added dissipative loss. Compared with the standalone antenna, the optimized design provides higher gain, improved efficiency, suppressed back radiation, and SAR values below international exposure limits. The present work focuses on SAR-aware AMC-backed antenna optimization using DNN surrogate modeling, NSGA-II optimization, and SHAP interpretation. Detailed bending-cycle tests, multi-position on-body measurements, and long-term motion stability are reserved for future work. Therefore, the wearable claim is limited to SAR-aware, wearable-oriented operation rather than complete garment-level validation.

VII. PERFORMANCE COMPARISON

Table 10 compares the proposed antenna with reported AMC-based SAR-reduction designs. Most prior works achieve SAR below 0.4 W/kg but are mainly single- or dual-band and do not include ML-based optimization. In contrast, the proposed design combines a triple-band response at 1.82, 2.42, and 5 GHz with DNN–NSGA-II-based SAR optimization. It achieves SAR values of 0.082 W/kg for 1 g tissue and 0.075 W/kg for 10 g tissue while maintaining a peak realized gain of 4.38 dBi. These results confirm that the ML-optimized MTM-AMC structure improves the gain–SAR trade-off and satisfies IEEE C95.1 and ICNIRP safety limits.

Table 10: Performance comparison of AMC-based wearable antennas with SAR mitigation

Ref.	Overall Size	Freq. (GHz)	SAR	SAR_{1g} (W/kg)	SAR_{10g} (W/kg)	ML	Gain (dBi)	AMC Type
[2]	76.5×76.5 mm^2	2.45, 5.8	Yes	NR	0.1175/0.1697	No	3.34/7.48	3×3 dual-band annular AMC
[4]	$0.55\lambda_0 \times 0.55\lambda_0 \times 0.016\lambda_0$	2.45	Yes	0.759	0.389	No	5.23/$\geq$ 4.11	2×2 square-loop AMC
[6]	NR	2.45	Yes	NR	NR	No	1.65 with 75% increase	3×3 textile AMC
[7]	$66 \times 40 \times 4$ mm^3	2.45, 5.8	Yes	0.035/0.014	0.018/0.032	No	8.5/9.2	3×2 dual-hexagonal textile AMC
[8]	$36 \times 36 \times 3.8$ mm^3	5.8	Yes	0.0117	0.00244	No	7.5–7.9	6×6 fractal AMC
[17]	NR	6.5, 8.15	Yes	0.223/0.324	NR	No	9.7 maximum	2×2 wideband AMC reflector
[29]	$40.5 \times 40.5 \times 6$ mm^3	5.8	Yes	4.8	NR	No	7.47	5×5 square-patch/square-ring AMC
[30]	$0.72\lambda_0 \times 0.72\lambda_0 \times 0.15\lambda_0$	2.45, 5.4	Yes	0.58/1.04	NR	No	7.2/4.0	4×4 dual-band circular-slotted AMC
Proposed	**60×50 mm^2**	**1.82, 2.42, 5.00**	**Yes**	**0.082**	**0.075**	**Yes**	**4.38 maximum**	**ML-optimized MTM–AMC**

VIII. CONCLUSION

This work presented a SAR-aware DNN–NSGA-II framework for optimizing an AMC-backed triple-band Sierpinski carpet wearable antenna at 1.82, 2.42, and 5.00 GHz. A 600-sample CST dataset was used to model the relation between geometry, gain, and SAR. The DNN enabled fast prediction, NSGA-II selected Pareto-optimal gain–SAR designs, and SHAP identified feed length and AMC gap as dominant SAR factors, while fractal scaling mainly affected high-frequency gain. The optimized antenna achieved 4.38 dBi peak gain and SAR values of 0.082 W/kg (1 g) and 0.075 W/kg (10 g), satisfying IEEE C95.1 and ICNIRP limits. Future work will study bending, body placement, and deformation stability.

REFERENCES

[1] Y. Thangavelu, B. Thangaraju, and R. Maheswar, "Design and SAR analysis of an AMC-integrated wearable cavity-backed SIW antenna," *Micromachines*, vol. 15, no. 12, p. 1530, 2024.

[2] C. Du, L.-R. Pei, J. Zhang, and C.-X. Shi, "A gain enhanced dual-band low SAR AMC-based MIMO antenna for WBAN and WLAN applications," *Progress in Electromagnetics Research M*, vol. 115, pp. 21–34, 2023.

[3] A. Flórez Berdasco, M. E. de Cos Gómez, J. Laviada, and F. Las-Heras, "AMC-backed twin arrow antenna for wearable electronic travel aid system at 24 GHz," *IEEE Antennas and Wireless Propagation Letters*, vol. 23, no. 11, pp. 3337–3341, 2024.

[4] U. Ali, S. Ullah, A. Basir, B. Kamal, L. Matekovits, and H. Yoo, "Design and SAR analysis of AMC-based fabric antenna for body-centric communication," *IEEE Access*, vol. 11, pp. 73894–73911, 2023.

[5] S. Wang and H. Gao, "A dual-band wearable conformal antenna based on artificial magnetic conductor," *International Journal of Antennas and Propagation*, vol. 2022, p. 9970477, 2022.

[6] O. M. Youssef, M. El Atrash, and M. A. Abdalla, "A compact fully fabric I-shaped antenna supported with textile-based AMC for low SAR 2.45 GHz wearable applications," *Microwave and Optical Technology Letters*, vol. 65, no. 7, pp. 2021–2030, 2023.

[7] W. Bouamra, I. Sfar, A. Mersani, L. Osman, and J.-M. Ribero, "Dual-band textile AMC antenna for WLAN/WBAN applications on the human arm," *International Journal of Electronics and Telecommunications*, vol. 68, no. 2, pp. 209–216, 2022.

[8] M. Yadav, M. Ali, and R. P. Yadav, "A compact and economical AMC backed antenna solution for wearable biomedical applications," *International Journal of Microwave and Wireless Technologies*, vol. 15, no. 9, pp. 1514–1523, 2023.

[9] N. Sarker, P. Podder, M. R. H. Mondal, S. S. Shafin, and J. Kamruzzaman, "Applications of machine learning and deep learning in antenna design, optimization, and selection: A review," *IEEE Access*, vol. 11, pp. 103890–103915, 2023.

[10] D. Sarkar, T. Khan, Jayadeva, and A. A. Kishk, "Machine learning assisted hybrid electromagnetic modeling framework and its applications to UWB MIMO antennas," *IEEE Access*, vol. 11, pp. 19645–19656, 2023.

[11] M. R. Khan, C. L. Zekios, S. Bhardwaj, and S. V. Georgakopoulos, "A deep learning convolutional neural network for antenna near-field prediction and surrogate modeling," *IEEE Access*, vol. 12, pp. 39737–39747, 2024.

[12] W. Chen, Q. Wu, B. Han, C. Yu, H. Wang, and W. Hong, "Efficient incremental variable-fidelity machine-learning-assisted hybrid optimization and its application to multiobjective antenna design," *IEEE Transactions on Antennas and Propagation*, vol. 72, no. 12, pp. 9347–9354, 2024.

[13] T. Naous, A. Al Merie, S. K. Al Khatib, M. Al-Husseini, R. M. Shubair, and H. M. El Misilmani, "Machine learning-aided design of dielectric-filled slotted waveguide antennas with specified sidelobe levels," *IEEE Access*, vol. 10, pp. 30583–30595, 2022.

[14] A. Arif, M. Zubair, M. Ali, M. U. Khan, and M. Q. Mehmood, "A compact, low-profile fractal antenna for wearable on-body WBAN applications," *IEEE Antennas and Wireless Propagation Letters*, vol. 18, no. 5, pp. 981–985, 2019.

[15] A. N. Alkhafaji, S. M. Abdulsatar, and J. K. Ali, "Design of flexible dual-band tree fractal antenna for wearable applications," *Progress in Electromagnetics Research C*, vol. 125, pp. 51–66, 2022.

[16] M. Kaur and J. S. Sivia, "ANN and FA based design of hybrid fractal antenna for ISM band applications," *Progress in Electromagnetics Research C*, vol. 98, pp. 127–140, 2020.

[17] B. Hazarika, B. Basu, and A. Nandi, "A wideband, compact, high gain, low-profile, monopole antenna using wideband artificial magnetic conductor for off-body communications," *International Journal of Microwave and Wireless Technologies*, vol. 14, no. 2, pp. 194–203, 2022.

[18] W. Thaiwirot, J. Ardhan, S. Prengsri, P. Akkaraekthalin, and S. Chalermwisutkul, "The low-profile all-textile UWB antenna with AMC for WBAN applications," *EURASIP Journal on Wireless Communications and Networking*, vol. 2025, no. 1, p. 56, 2025.

[19] T. Messatfa, S. Berhab, F. Chebbara, and M. S. Soliman, "Curvature-adaptive compact triple-band metamaterial uniplanar compact electromagnetic

bandgap-based printed antenna for wearable wireless and medical body area network applications," *Processes*, vol. 12, no. 7, p. 1380, 2024.

[20] M. Sandhya and L. Anjaneyulu, "Improved wearable, breathable, triple-band electromagnetic bandgap-loaded fractal antenna for wireless body area network applications," *ETRI Journal*, vol. 46, no. 4, pp. 571–580, 2024.

[21] U. Ali, S. Ullah, A. Basir, S. Yan, H. Ren, B. Kamal, and L. Matekovits, "Design and performance investigation of metamaterial-inspired dual band antenna for WBAN applications," *PLOS ONE*, vol. 19, no. 8, p. e0306737, 2024.

[22] J. Zhang, J. Xu, Q. Chen, and H. Li, "Machine-learning-assisted antenna optimization with data augmentation," *IEEE Antennas and Wireless Propagation Letters*, vol. 22, no. 8, pp. 1932–1936, 2023.

[23] M. A. Haque, D. Saha, S. S. Al-Bawri, L. C. Paul, M. A. Rahman, F. Alshanketi, A. Alhazmi, A. H. Rambe, M. A. Zakariya, and S. S. Ba Hashwan, "Machine learning-based technique for resonance and directivity prediction of UMTS LTE band quasi-Yagi antenna," *Heliyon*, vol. 9, no. 9, p. e19548, 2023.

[24] Y. Sharma, H. H. Zhang, and H. Xin, "Machine learning techniques for optimizing design of double T-shaped monopole antenna," *IEEE Transactions on Antennas and Propagation*, vol. 68, no. 7, pp. 5658–5663, 2020.

[25] L. Cui, Y. Zhang, R. Zhang, and Q. H. Liu, "A modified efficient KNN method for antenna optimization and design," *IEEE Transactions on Antennas and Propagation*, vol. 68, no. 10, pp. 6858–6866, 2020.

[26] A. Papathanasopoulos, P. A. Apostolopoulos, and Y. Rahmat-Samii, "Optimization assisted by neural network-based machine learning in electromagnetic applications," *IEEE Transactions on Antennas and Propagation*, vol. 72, no. 1, pp. 160–173, 2024.

[27] F. Peng and X. Chen, "An antenna optimization framework based on deep reinforcement learning," *IEEE Transactions on Antennas and Propagation*, vol. 72, no. 10, pp. 7594–7605, 2024.

[28] K. Muthukumaravel and S. Santhanam, "Design and optimization of a triple-band fractal antenna with AMC-backing for wearable sub-6 GHz applications," *IETE Journal of Research*, 2026.

[29] P. Saha, D. Mitra, and S. K. Parui, "Control of gain and SAR for wearable antenna using AMC structure," *Radioengineering*, vol. 30, no. 1, pp. 81–88, 2021.

[30] V. Rajavel and D. Ghoshal, "AMC-based low-profile dual-band slotted patch antenna for IoT devices in the healthcare system," *Iranian Journal of Science and Technology, Transactions of Electrical Engineering*, vol. 47, no. 2, pp. 437–450, 2023.



Muthukumaravel K received the Bachelor of Engineering degree in Electronics and Communication Engineering from Annamalai University, Chidambaram, Tamil Nadu, India, and the Master of Engineering degree in Applied Electronics from Anna University, Chennai, Tamil Nadu, India. He has more than 12 years of academic experience and is currently serving as an Assistant Professor in the Department of Electronics and Communication Engineering at Meenakshi Ramaswamy Engineering College, Thathanur, Ariyalur, Tamil Nadu, India. His research interests include antenna design and related RF communication systems. He has actively participated in several faculty development programs and completed multiple NPTEL courses.



Suganthi Santhanam received the Bachelor of Engineering degree in Electronics and Communication Engineering from Bharathidasan University, Tiruchirappalli, Tamil Nadu, India, the Master of Engineering degree in Computer and Communication Engineering from Anna University, Chennai, Tamil Nadu, India, and the Ph.D. degree in RF MEMS from Anna University, Chennai. She has more than 25 years of academic experience and is currently serving as a Professor in the Department of Electronics and Communication Engineering at K. Ramakrishnan College of Technology, Tamil Nadu, India. Her research interests include artificial neural networks, digital signal processing, MATLAB-based modeling, computer-aided design of VLSI circuits, and microwave modeling methodologies. She has published more than 30 research articles in SCI- and Scopus-indexed journals and has received research funding from AICTE and ICMR. She has actively participated in and organized several faculty development programs, including Anna University-sponsored FDPs. She is currently guiding research scholars in the areas of wireless sensor networks, image processing, RF device design, photonic networks, and VLSI design.

Deep Learning Enhanced Hybrid BEM-rMLNCA Method for Efficient Power Cable Crosstalk Prediction

Abdul Mueed, Weiqiang Tang*, and Rui Ma

School of Automation and Electrical Engineering
Lanzhou University of Technology, Lanzhou, Gansu 730050, China
twqzjh@163.com
*Corresponding Author

Abstract **–** This paper presents a deep learning-assisted hybrid Boundary Element Method (BEM)-recompressed Multilevel Nested Cross Approximation (rMLNCA) algorithm for efficient and accurate crosstalk prediction. This hybrid approach aims to combine the physics-based precision of BEM with the compression efficiency of rMLNCA and the nonlinear learning capability of deep neural networks (DNN) for high-fidelity modeling with reduced computational requirements. Under this proposed method, three parameters are predicted for crosstalk: Near-End Crosstalk (NEXT), Far-End Crosstalk (FEXT), and Common-Mode Current (CMC) measurement. The impedance and coupling parameters are computed using BEM, while rMLNCA decomposes and recompresses the far-field matrices into low-rank admissible blocks, reducing both memory and time significantly. It improves predictive accuracy further by learning nonlinear relationships among geometric, material, and frequency-dependent features using an optimized deep neural network architecture. The suggested model has high predictive consistency with the 5-fold cross-validation R^2 of 0.9736 ± 0.0053. Final evaluation results showed that there is strong accuracy, as depicted by R^2 and MAPE values for NEXT, FEXT, and CMC of 0.9707/15.10%, 0.9602/11.11%, and 0.9750/8.19%, respectively, validating generalization performance.

Index Terms **–** Boundary element method, deep neural network, far-end crosstalk, near-end crosstalk, power cable, recompressed multilevel nested cross approximation.

I. INTRODUCTION

Crosstalk parameter estimation plays a critical role in electromagnetic compatibility. If the interference of neighbor cables degrades signal quality, it also generates difficult-to-remove Far-End Crosstalk (FEXT) in high-speed data transmission [1, 2]. In particular, cables like LIFY and AWG23 have been designed to be resistant against electromagnetic interference for control and data systems [3]. However, compared to the extensive studies done on external interference, internal crosstalk within twisted pairs remains limited [4].

Impedance matrices dealing with crosstalk and current distribution are mostly derived by analytical methods which are then numerically accelerated by sophisticated numerical techniques like integral equation-fast Fourier transform [5] and adaptive integral method [6]. The methods mentioned improve calculation efficiency, however, they remain limited in terms of nonlinear memory computations. Advanced numerical techniques, including finite difference method [7], and method of moments (MoM) [8], have significantly improved the accuracy of crosstalk analysis compared to earlier methods. Conductor partitioning-based approaches [9], volumetric finite element method [10], and Boundary Element Method (BEM) [11] have very high computational burdens, whereas MoM remains the most efficient among the methods dealing with a complex geometry. The adaptive cross approximation (ACA) technique efficiently reduces the computational cost of singular value decomposition through low-rank compression, thus proving ideal for large-scale electromagnetic and multiconductor transmission line (MTL) analyses [12].

Low-rank approximations of far-field impedance matrix interactions are effectively compressed with controlled error tolerance. Methods such as ACA [13] and Hybrid Cross Approximation [14] enhance stability but are without hierarchical organization, limiting the reduction in complexity. Exploiting the nesting property of Lagrange polynomials allows the construction of hierarchical H^2-matrices [15] that further improve computational efficiency. Further advances in fast algorithms by kernel-independence and nesting have resulted in direct H^2-matrix formulations with reduced conversion complexity from $O(N \log N)$ [16]. Notably, two kernel-independent methods (nested equivalent source

Submitted On: November 18, 2025
Accepted On: July 07, 2026

1054-4887 © ACES

https://doi.org/10.13052/2026.ACES.J.410705

approximation and nested skeletonization) achieve this by using multilevel equivalent sources and proxy surface sampling, respectively [17].

Nested cross approximation (NCA) is an algebraic method that constructs hierarchical low-rank bases with near-linear memory and computational cost using only a few matrix samples [18]. However, the existing algebraic fill strategies rely on globally nested bases; as the problem size increases, the far-field blocks grow fast and, hence, the strategy becomes inefficient. On this account, a deep learning-assisted approach is developed by recursively performing the recompression on the local admissible blocks so that this approach scales better for electrically large problems.

The present study describes a deep learning-assisted hybrid method that incorporates a DNN with BEM and Multilevel Nested Cross Approximation (rMLNCA) for efficient and accurate crosstalk prediction in power cables. DNN enhances the rMLNCA process in computational efficiency, stability, and scalability for crosstalk analysis. With its pattern recognition capability, it refines the numerical compression kernel to achieve high-fidelity modeling of complex coupling behavior. This approach yields a hybrid DNN-BEM-rMLNCA with near-linear computational complexity, significantly reducing the computational burden compared with traditional approaches. The model makes effective predictions of Near-End Crosstalk (NEXT), Far-End Crosstalk (FEXT), and Common-Mode Current (CMC). Validation was performed against the conventional nested cross approximation and the transmission line matrix method.

The paper is organized thus: Theoretical background and simulation setup for single- and multiwire crosstalk are presented in section II, while section III describes the hybrid DNN-assisted model. Section IV presents the results and analysis, and section V concludes the study.

II. PROPOSED MODEL DESCRIPTION

A. Numerical model

A.1. Single-to-single cable

This research is based on single-to-single-line parameter estimation for crosstalk analysis of an AWG23 single-core cable. One wire is used as an aggressor and the other as a victim. Both NEXT and FEXT crosstalk on the victim line are calculated and confirmed. Table 1 provides the cable parameters while Fig. 1 represents the cross-sectional model and the circuit schematic where P_1-P_2 are NEXT ports and P_3-P_4 are FEXT ports.

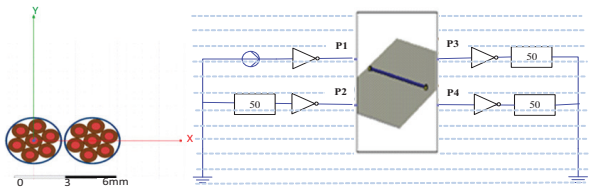


Fig. 1. Single-line crosstalk simulation model.

Table 1: Single wire parameter (AWG)

Parameter	Value
Relative distance between cables d	5 mm
Height above the ground h	50 mm
Single core conductor radius r_1	0.286 mm
Insulation thickness of single core wire t_1	0.19 mm (PE)
Termination resistance	50 Ω
Line length 1	1 m

A.2. Single cable to twisted pair

The analysis in this part is focused on the parametric study of the twisted LIFY cable. The cables are multistrand, multicore composite and, for crosstalk analysis, a singlecore wire is considered as the aggressor and the twisted pair as the victim. The parameters to be varied are presented in Table 2, and the cable model is depicted in Fig. 2. Ports P_1-P_3 illustrate NEXT on lines 1–3, and P_4-P_6 refer to FEXT on the same lines.

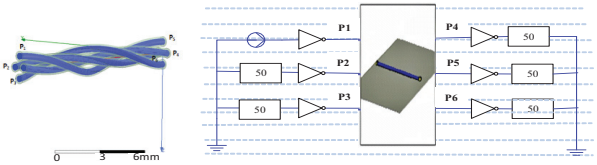


Fig. 2. Simulation of twisted pair crosstalk.

Table 2: Twisted wire constraints (LIFY)

Parameter	Value
Relative distance between cables d	5 mm
Height over the ground h	50 mm
Single core conductor radius r_1	0.286 mm
Insulation thickness of single core wire t_1	0.19 mm (PE)
Twisted pair radius r_2	0.50 mm
Insulation thickness of twisted pair t_2	1.0 mm (PE)
Termination resistance	50 Ω
Line length 1	1 m

B. Deep learning model

This paper proposes a hybrid algorithm aided by deep learning to predict power cable crosstalk with high accuracy. The hybrid model (Fig. 3) integrates a 100-layer deep neural network with the BEM-rMLNCA numerical method. It utilizes the shape and material properties to predict NEXT and FEXT. The model, which was trained on 1000 samples and stabilized with batch normalization and dropout, achieved a speed-up of the calculation time by 97.2%, a reduction of the operational complexity by 87.5%, and the total time for the analysis of only 2.8 s, about 35 times faster than conventional methods.

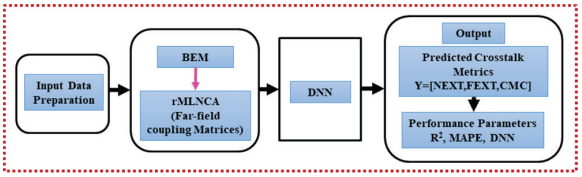


Fig. 3. DNN proposed method.

III. DNN ASSISTED BEM-RMLNCA ALGORITHM FOR POWER CABLE CROSSTALK

A. Implementation of DNN-BEM-rMLNCA algorithm for power cable crosstalk

BEM discretizes only boundaries, not the full domain. To handle dense matrices in complex problems, we introduce a hybrid rMLNCA for cable crosstalk that has a low-rank approach using minimal entries to approximate full information. A low-rank matrix S is represented by

$$S \in (UV^T)^{p\times q}. \tag{1}$$

The basis function is discretized by MoM for cable crosstalk interference parameters. The main purpose of the basis function is to discretize the number of segments (wires) in the MTL accordingly. The total number of wires is the sum of $N^{(r)}$, where $r = 1,2\ldots$M and $N =$ number of wires. The basis function for cable crosstalk based on rMLNCA is:

$$E_z(r) = \sum_{i=1}^{M}\sum_{r=1}^{N^{(r)}} \alpha_r g_r(r), \tag{2}$$

$$[S]^{p\times q} = [\widetilde{S}]^{p\times q} = [U]^{p\times r}[V]^{r\times q}. \tag{3}$$

The test functions are chosen within a weighted residual-Galerkin function to meet boundary requirements and linear independence, and use the same basis functions to approximate the solution to ensure numerical stability and weighted residual minimization convergence. The testing function w_j for the M-conductor cable crosstalk is:

$$\langle W_j, E\rangle = \sum \langle W_j, f_e(J_r, g_r)\rangle; \quad J = 1,2,\ldots,M. \tag{4}$$

The testing function based on the rMLNCA becomes:

$$[E_r] = [S_{pq}][I_r] = [U_{pr}][V_{rq}][I_r]. \tag{5}$$

Near-end crosstalk: Crosstalk occurs at the near end of the aggressor line closest to the driver. NEXT in terms of voltage is given by:

$$E_{Near} = \sum_{i=1}^{M}\sum_{r=1}^{N^{(r)}} U_{pr}^{(i)} S_r^{(i)} (V_{rq}^{(i)})^T \cdot I_{agg}(t-\tau_{Near}). \tag{6}$$

Far-end crosstalk: FEXT occurs at the end of the victim line opposite to the aggressor driver. The rMLNCA based approximation is:

$$E_{Far} = \sum_{i=1}^{M}\sum_{r=1}^{N^{(r)}} U_{pr}^{(i)} S_r^{(i)} (V_{rq}^{(i)})^T \cdot I_{agg}(t-\tau_{Far}). \tag{7}$$

The common mode measurement induced on a victim cable due to an aggressor's CM current is:

$$I_{CM} = \sum_{i=1}^{M}\sum_{r=1}^{N^{(r)}} U_{pr}^{(i)} \sum (V_{rq}^{(i)})^T \cdot I_{agg}(t-\tau_{CM}). \tag{8}$$

In equation (9), the convergence criterion epsilon ε is evaluated using the L_2 norm (Euclidean norm) of the residual vector. The convergence ε for the proposed solution is:

$$\|S - \tilde{S}\| \le \varepsilon. \tag{9}$$

Adaptive tree depth is determined by crosstalk convergence, with recursive subdivision terminating at Level 8 when successive changes fall below a predefined threshold. The resulting octa-level tree achieves a compression ratio of 1:775 and a basis function reduction factor of 0.612012. Tables 3 and 4 show the details.

Table 3: Average reduction order of matrix assembly

Matrix Assembly	Average Order
122575	1.386382
155996	1.371161
169755	1.355393
183034	1.334839
196787	1.319798
225281	1.297659
242185	1.289720
257994	1.282211
273871	1.275396
286440	1.269410

Table 4: Computation of basis function for power cable

Tetrahedra	Basis Function Order	Memory	Solution Time	Adaptive Passes
286440	0	299 MB	3 min	17
355596	1st	480 MB	9 min	13
293764	2nd	619 MB	10 min	12
122575	Mixed	0.765 KB	10 s	9

In the DNN method, the adjoined conditions limit the constraints of the far-field coupling matrix. The convergence is monitored for 50 epochs. Mean Absolute Error (MAE) decreases from ∼0.95 to less than 0.2 at around epoch 20 and remains at about 0.05 after 40 epochs, thus, the network can be considered effectively trained. The simultaneously training and validation error curves also suggest that the model generalizes well (Fig. 4).

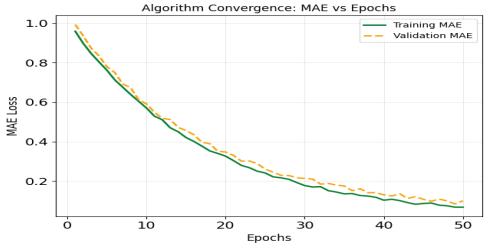


Fig. 4. MAE convergence of proposed algorithm.

Frobenius relative error between reference A_{gt} and predicted $\hat{A}$ along with the element-wise error $|\hat{A} - A_{gt}|$ of a rank- 816×16 far-field matrix is depicted in Fig. 5. The network accurately learns the lowrank features. On average, a ∼10% mean relative Frobenius error is achieved for 1000 test samples. The basic algorithmic flowchart is demonstrated in Fig. 6.

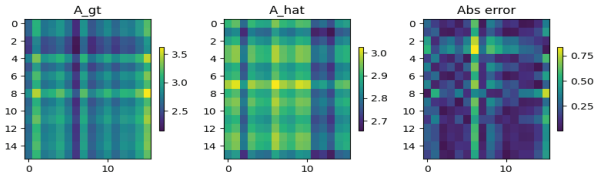


Fig. 5. Relative Frobenius error of proposed algorithm.

IV. RESULTS AND DISCUSSION

A. Power cable crosstalk analysis

In this section, a deep neural network prediction for power cable crosstalk analysis based on BEM-rMLNCA is presented. A HFSS-IE solver is used for the numerical solution of the proposed model layout of cables to build cable simulation models independently. The hybrid solver is used to compute the S-parameters from the computations of a low-rank matrix or rank deficient matrix. Simulated data is extracted, and then trained using dense DNN to predict the crosstalk in the power cable. Data normalization takes place.

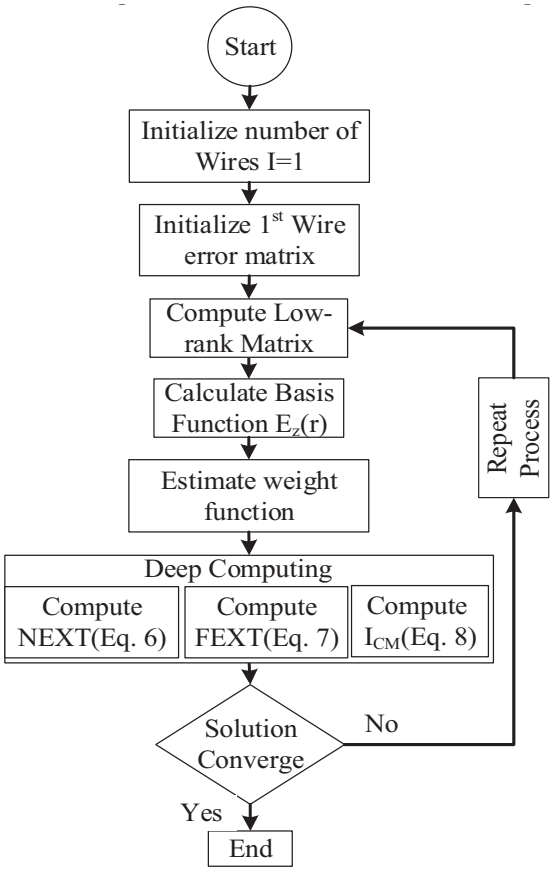


Fig. 6. Flowchart of DNN hybrid BEM-rMLNCA algorithm.

A.1. Near end crosstalk

Figure 7 presents the measured and predicted NEXT across 0.1–1 GHz. NEXT decreases with frequency, from approximately 0.7–0.9 dB at 0.1 GHz to 0.3–0.4 dB around 0.5 GHz, and down to about 0.05–0.2 dB at 1 GHz. The predicted values, shown as red crosses, trajectory well with the measured data, depicted as blue dots, except for minor deviations in the low-frequency region where NEXT is relatively high and more variable. The model accurately captures the frequency-dependent coupling behavior. The frequency-averaged relative error amounts to 0.032%, and the computational efficiency is 98%. Hence, the plot shows strong agreement between the predicted and actual NEXT, further confirming the reliability of the model over the operating band.

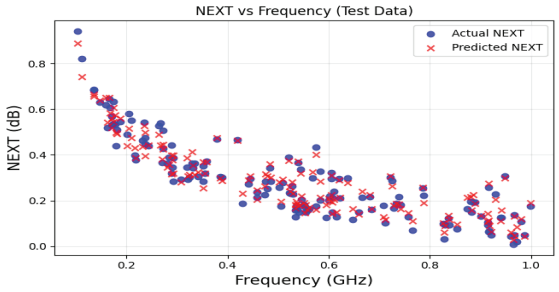


Fig. 7. Near-end crosstalk estimation.

A.2. Far end crosstalk

Figure 8 illustrates the variation of FEXT with frequency for a multiconductor power cable transmission system. Analysis covers frequencies from 0.1 to 1 GHz, where FEXT values range between 0.1 dB and 0.85 dB across 97 test cases. The results reveal an inverse relationship (FEXT decreases to around 0.25 dB as frequency rises), reflecting reduced electromagnetic coupling at higher frequencies. The comparison between predicted (red crosses) and measured (blue dots) values shows close alignment, with an average relative error 0.09%. Additionally, the matrix compression technique enhances computational efficiency by nearly 95%. This predicted computational efficiency gain demonstrates reduced runtime and increased solver throughput. Overall, the strong alignment between simulated and predicted results highlights the model's reliability and accuracy in estimating crosstalk within complex cable systems, achieving an effective balance between precision and computational speed.

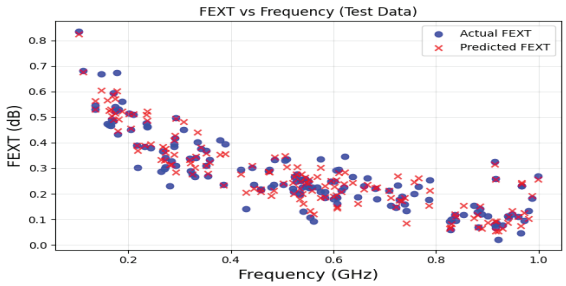


Fig. 8. Far-end crosstalk estimation.

A.3. Common mode current measurement

Figure 9 presents a comparison of the Common Mode Current test dataset values between 0 and 1 GHz that were both measured and predicted. Measured data (blue circles) and model predictions (red crosses) show the same rising trend with CMC increasing from about 0.05 A at 0.05 GHz to around 1 A at 1 GHz. The close matching indicates that the model performance is strong which is reflected by $R^2 = 0.9750$, root mean square error (RMSE) = 8.29%, and mean absolute percentage error (MAPE) = 8.19%. The RMSE is normalized by the mean absolute value of the reference crosstalk over the frequency band. These findings confirm the model's capability to grasp the nonlinear, frequency-dependent coupling behavior of the power cable. The minor differences at higher frequencies may be due to measurement uncertainty or boundary simplifications in the hybrid solver. The compressed matrix achieves 97% reduction with only ∼3% precision loss, thus the relative error is very small (0.05%) and the steady state behavior is stable. The steady-state behavior in this broadband frequency-domain analysis refers to the crosstalk and CMC's stabilized sinusoidal response at each frequency following the decay of all transient effects. Consequently, the measurements and predictions are in close agreement. Figure 10 shows the comparison of crosstalk based on DNN.

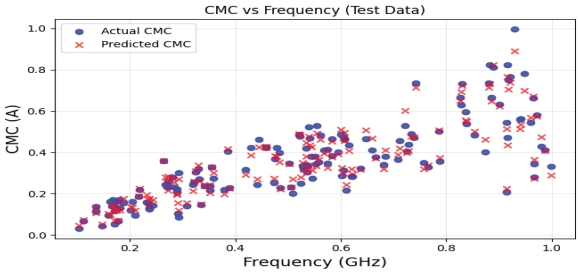


Fig. 9. Common mode current measurement for power cable.

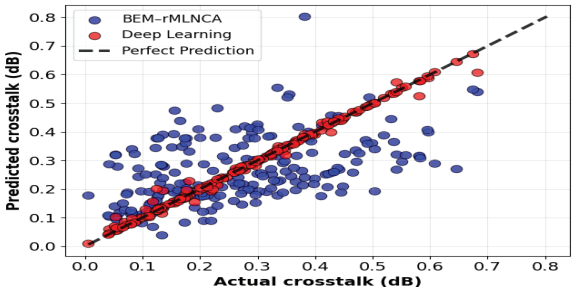


Fig. 10. Crosstalk comparison of the proposed algorithm.

B. Computing parameters

For the performance evaluation of the proposed algorithm, memory usage, CPU time, error, and accuracy were compared. Table 5 summarizes the memory and runtime performance, while Fig. 11 shows the error and accuracy plots. The combined analysis confirms strong predictive capability for key electromagnetic parameters. For NEXT, the model obtained $R^2 = 0.98$, while the errors are low: RMSE = 2.1%, MAPE = 3.5%. In the case of FEXT, it maintained reliable performance

Table 5: Computational parameters of proposed algorithm

Matrix	Hybrid Method		Traditional Method [20]		Transmission Line Matrix [19]	
Assembly	Memory (KB)	CPU Time	Memory (MB)	CPU Time	Memory (MB)	CPU Time
122575	1.36	2	135	11	135	14
155996	1.28	3	225	13	232	19
169755	0.990	3	296	22	299	27
183034	1.110	4	334	24	367	32
196787	1.1	4	488	26	498	38
225281	0.550	4	499	31	556	42
242185	1.29	5	545	39	667	46
257994	0.747	5	676	50	812	59
273871	0.875	6	787	54	987	67
286440	0.679	7	989	65	1089	80

with $R^2 = 0.94$, RMSE = 3.8%, MAPE = 5.2%, confirming that accuracy is consistent for both outputs.

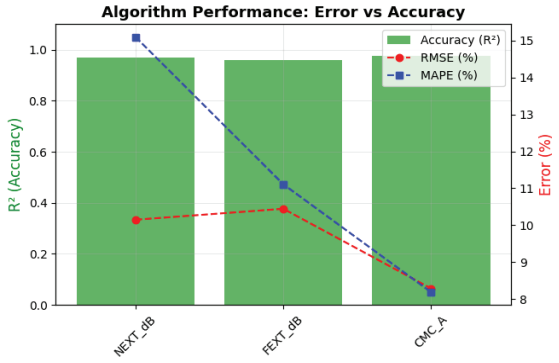


Fig. 11. Error vs Accuracy analysis of proposed algorithm.

V. CONCLUSION

In this paper, deep learning assisted hybrid BEM-rMLNCA is presented for complex electromagnetic coupling analysis to predict power cable crosstalk characteristics. The hybrid algorithm is a good approximation approach for far-field matrices entries. Numerical evaluations demonstrated excellent predictive performance achieving cross-validation R^2 values above 0.97 while maintaining low MAPE across the measurement parameters of NEXT, FEXT, and CMC current. Results identified that the hybrid algorithm's computational efficiency is about 97% and matrix compression order is 1:125, significantly reducing memory and processing requirements. These results thus confirm the capability of the model in capturing the complex coupling effects and frequency dependent behaviors in MTL. The DNN hybrid approach offers highly reliable, scalable, and efficient solutions for complex electromagnetic coupling analysis. The limitation of the proposed approach depend on data accuracy and error propagation from BEM-rMLNCA approximations and scalability issues for large multiconductor systems.

ACKNOWLEDGEMENT

This work was supported by the National Natural Science Foundation of China (Grant number 62463017), the Chinese Government Scholarship (Grant number 2024GSP000580), the Science and Technology Program of Gansu Province (Grant number 24CXGA039).

REFERENCES

[1] W. Zhang, S. Li, W. Yan, Z. Chen, and Y. Zhao, "Crosstalk prediction between single wire and non-uniform twisted-wire pair," *Electromagnetics*, vol. 41, no. 7, pp. 518–532, Oct. 2021.

[2] Z. Wu, Z. Yang, A. Mueed, S. Khan, B. Usman, and M. Asif, "Computational analysis of shielded twisted pair cable based on MoM-MLFMM algorithm," in *ICEET*, pp. 1–6, Oct. 2021.

[3] Z. Xi, T. Liang, Y. Z. Xie, and J. Guo, "Enhanced transmission model for predicting coupling between electromagnetic field and a twisted-wire pair of complex dielectric coatings," in *APEMC*, pp. 101–103, Sep. 2022.

[4] J. L. Rotgerink, R. Serra, and F. Leferink, "Multiconductor transmission line modeling of crosstalk between cables in the presence of composite ground planes," *IEEE Trans. Electromagn. Compat.*, vol. 63, no. 4, pp. 1231–1239, 2020.

[5] A. Mueed, Y. Zhao, W. Yan, S. Khan, Q. Q. Liu, and C. Huang, "Skin effect and proximity effect analysis of stranded conductor based on mixed order MoM with adaptive cross approximation algorithm," *Engineering Analysis with Boundary Elements*, vol. 120, pp. 52–58, 2020.

[6] M. Li, Y. Hu, R. Chen, and G. Vecchi, "Electromagnetic modeling of moving mixed conductive and dielectric BoRs with an effective domain decomposition method," *IEEE Trans. Antennas Propag.*, vol. 68, no. 12, pp. 7978–7985, 2020.

[7] Y. Liu and E. Michielssen, "Parallel fast time-domain integral-equation methods for transient electromagnetic analysis," *Parallel Algorithms in Computational Science and Engineering*, pp. 347–379, 2020.

[8] R. Jia, S. Zuo, X. Zhao, Z. Lin, Y. Zhang, and M. Yang, "A novel parallel direct solver using adaptive cross approximation for analysis of electromagnetic radiation problems with complex structures," *IEEE Trans. Antennas Propag.*, vol. 72, no. 3, pp. 2962–2967, 2024.

[9] P. F. Li, S. W. Qu, S. Yang, and J. Hu, "Fundamental relation between phased array radiation and scattering fields," *IEEE Trans. Microw. Theory Tech.*, vol. 71, no. 9, pp. 3797–3809, 2023.

[10] M. Nale, O. Chadebec, J. M. Guichon, O. Pinaud, B. Ramdane, V. Roche, M. Minola, and C. Göeau, "Transient modeling of corrosion protection systems with BEM-electrical circuit hybrid model," *IEEE Trans. Magn.*, vol. 59, no. 5, pp. 1–5, 2023.

[11] J. Tibaut, M. Schanz, and J. Ravnik, "Fast boundary-domain integral method with the H^2-matrix formulation for large scale numerical investigations," *Engineering Analysis with Boundary Elements*, vol. 138, pp. 1–12, 2024.

[12] V. A. Kandappan, V. Gujjula, and S. Ambikasaran, "HODLR2D: A new class of hierarchical matrices," *SIAM J. Sci. Comput.*, vol. 45, no. 5, pp. A2382–A2408, 2023.

[13] S. Börm, "Adaptive fast multiplication of $\mathscr{H}^2$-matrices," *Math. Comp.*, vol. 94, no. 352, pp. 825–852, 2025.

[14] M. Li and Y. Hu, "Simulation of surface enhanced Raman scattering from nanoparticles with wideband nested equivalence source approximation," *IEEE J. Multiscale Multiphysics Comput. Tech.*, vol. 7, pp. 1–8, 2022.

[15] C. Yang and D. Jiao, "Algebraic and fast nested construction method for generating rank-minimized H^2-matrix for solving electrically large surface integral equations," *IEEE J. Multiscale Multiphysics Comput. Tech.*, vol. 9, pp. 10–19, 2023.

[16] N. Lochner and M. N. Vouvakis, "On the H^2 representation of EFIE MoM," in *IEEE AP-S/USNC-URSI*, pp. 1930–1931, July 2022.

[17] M. Ancellin, P. Marchand, and F. Dias, "Towards high-performance linear potential flow BEM solver with low-rank compressions," *Energies*, vol. 17, no. 2, p. 372, 2024.

[18] L. Cong, H. Bin, H. Zongjun, and N. Zhongrong, "Analysis of 2-D orthotropic potential problems using fast multipole boundary element method with higher order elements," *Chin. J. Theor. Appl. Mech.*, vol. 53, no. 4, pp. 1038–1048, 2021.

[19] B. Yang, "Modeling and analysis of multiconductor transmission lines by distributed transfer function method," *Journal of Electronics*, 2024, doi:10.37256/jeee.3220245717.

[20] A. Mueed, Y. Zhao, Y. Wei, Z. B. Zhu, and Q. L. Liu, "Analysis of lossy multiconductor transmission lines (MTL) using adaptive cross approximation (ACA)," *Applied Computational Electromagnetics Society (ACES) Journal*, vol. 34, no. 11, pp. 1769–1776, 2019.



Abdul Mueed was born in Bhakkar, Pakistan. He received the Master's degree in Electrical Engineering from the University of Engineering and Technology, Taxila in 2015. From 2009 to 2017, he worked as a Lecturer in Electrical Engineering at the Dr. A. Q. Khan Institute of Technology, Mianwali. He is currently working as a Research Scholar at Lanzhou University of Technology, Lanzhou, China. His primary research interests include electromagnetic compatibility problems, computational electromagnetics, power system transients, EMC related application in biomedical engineering, and application of artificial intelligent in EMC.



Weiqiang Tang was born in Wuzhou, China. He received the B.S. degree in Automation from Lanzhou University of Technology, Lanzhou, in 2003, the M.S. degree in Control Theory and Control Engineering from Lanzhou University of Technology, Lanzhou, in 2008, and the D.S. degree in Control Science and Engineering from Xi'an Jiaotong University, Xi'an, in 2012. His research interests include advanced control theory and its application and robust control.



Rui Ma was born in Gansu, China. He received the master's degree in control theory and engineering from Lanzhou University of Technology, Lanzhou, in 2024. He is currently studying for his Ph.D. at Lanzhou University of Technology, majoring in pattern recognition and intelligent systems. His main research focus are intelligent control and motion control.

An Efficient Multi-GPU Accelerated IEDG-CBFM-SMWA Method for Electromagnetic Scattering Analysis

Ziang Shen[1], Xinlei Chen[1,2], and Zhuo Li[1]

[1]Key Laboratory of Radar Imaging and Microwave Photonics
College of Electronic and Information Engineering,
Nanjing University of Aeronautics and Astronautics, Nanjing 211106, China
shenziang@nuaa.edu.cn, chenxl@nuaa.edu.cn, lizhuo@nuaa.edu.cn

[2]Key Laboratory of Inlet and Exhaust System Technology
College of Energy and Power Engineering,
Nanjing University of Aeronautics and Astronautics, Nanjing 211106, China

Abstract – This paper presents a multiple graphics processing units (GPUs) accelerated direct solver for the method of moments (MoM). First, we integrate the characteristic basis function method-Sherman-Morrison-Woodbury formula-based algorithm (CBFM-SMWA) and the integral equation discontinuous Galerkin (IEDG) method. The IEDG can enforce current continuity across nonconformal meshes by employing hybrid RWG/half-RWG basis functions. Second, we develop a SMWA-centric multi-GPU parallelization strategy that fully exploits the intrinsic parallelism in compression and solution of hierarchical matrices, while CBFM serves to reduce the number of unknowns. The proposed multi-GPU IEDG-CBFM-SMWA achieves substantial computational acceleration over its CPU implementation while overcoming the memory limitations of conventional GPU-accelerated MoM. Numerical examples demonstrate that the proposed method offers excellent scalability across multiple GPUs, significant performance advantages and reliable accuracy for solving electrically large scattering problems.

Index Terms – Direct solver, method of moments (MoM), multiple graphics processing unit (multi-GPU).

I. INTRODUCTION

The method of moments (MoM) [1, 2] has been recognized as a powerful numerical method for solving electromagnetic problems due to its high computational accuracy, and various acceleration techniques have been developed to overcome its inherent high computational complexity, including the adaptive cross approximation (ACA) [3, 4] based method and the fast multipole algorithm (FMA) [5, 6] based method, which have significantly extended MoM's applicability for solving electrically large problems. Concurrently, with the rapid evolution of hardware, graphics processing units (GPUs) have become an important component in high-performance computing (HPC). GPUs offer exceptional parallel processing capabilities at a relatively low cost, making them ideal for accelerating computationally intensive algorithms. Therefore, there exists a promising research direction in developing GPU-accelerated high-performance numerical methods that leverage modern parallel architectures to achieve high efficiency for solving electromagnetic problems.

Filling and solving the impedance matrix represent the most computationally intensive stages in the MoM, typically consuming the majority of execution time. However, the inherent independence of matrix elements provides opportunities for parallel acceleration. The pioneering GPU implementations of MoM were demonstrated in [7–9], and subsequent research in [10, 11] investigated GPU's architectural characteristics to optimize program efficiency on GPUs. Despite these advances, the conventional MoM continues to present significant challenges due to the enormous memory requirements for storing the full impedance matrix, which often exceed the capacity of GPU devices. While out-of-core techniques proposed in [7, 12] addressed memory constraints by dividing the matrix into blocks and processing them sequentially, these approaches introduce data transfer overhead and require complex load balancing strategies. Consequently, the integration of fast methods and GPU acceleration represent a more practical solution approach. References [13–16] introduced GPU implementations of the FMA and multi-level FMA (MLFMA), achieving superior performance over CPU versions. Considering that iterative solvers employed in these methods may encounter convergence difficulties when facing ill-conditioned matrices, direct

Submitted On: January 14, 2026
Accepted On: June 08, 2026

1054-4887 © ACES

https://doi.org/10.13052/2026.ACES.J.410706

solvers not only circumvent convergence issues but also offer advantages for multi-excitation problems, such as monostatic radar cross-section (RCS) analysis. This has motivated GPU-accelerated implementations of direct solution methods, including the characteristic basis function method (CBFM) [17–20]. Nevertheless, for electrically large problems, the reduced matrix generated by the CBFM still consumes considerable resources which may exceed device memory capacity limitations.

This paper presents a high-performance direct solver leveraging the CBFM-Sherman-Morrison-Woodbury formula-based algorithm (CBFM-SMWA) [21], integral equation discontinuous Galerkin (IEDG) method [22, 23] and multi-GPU acceleration. The proposed method not only efficiently compresses and solves the conventional MoM matrix equation, but also can ensure current continuity at nonconformal meshes by employing a hybrid basis function scheme combining of Rao-Wilton-Glisson (RWG) and half-RWG basis functions. Furthermore, the multi-GPU acceleration can enhance the computational efficiency while maintaining high numerical accuracy.

II. THEORETICAL BACKGROUND

Conventional MoM typically requires conformal meshes, whereas the IEDG [22] relaxes this constraint by allowing nonconformal meshes between different structures. A half-RWG basis function is defined on a single triangle, as shown in Fig. 1, and current continuity is enforced through interior penalty terms rather than through mesh continuity. Specifically, RWG basis functions are retained within each conformal mesh region, while half-RWG basis functions are introduced at the boundaries of different structures where mesh are nonconformal. This hybrid RWG/half-RWG strategy preserves the modeling flexibility of independent meshing while maintaining the solution accuracy.

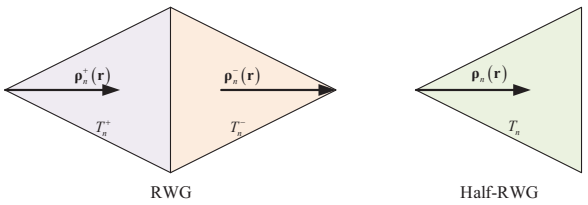


Fig. 1. Schematic diagram of RWG and half-RWG basis functions.

As a fast algorithm that can effectively reduce the number of unknowns, the CBFM [23, 24] partitions the target into several blocks and constructs characteristic basis functions (CBFs) for each block. This process transforms the original MoM matrix equation into a reduced version:

$$\mathbf{Z}^{CBF}\mathbf{I}^{CBF} = \mathbf{V}^{CBF}, \tag{1}$$

where $\mathbf{Z}^{CBF}$ represents the reduced impedance matrix, $\mathbf{V}^{CBF}$ is the reduced excitation coefficients vector, and $\mathbf{I}^{CBF}$ denotes the reduced current coefficient vector. The reduced impedance matrix between the i-th block and the j-th block can be expressed as:

$$\mathbf{Z}_{ij}^{CBF} = \mathbf{J}_i^T \mathbf{Z}_{ij}^{RWG} \mathbf{J}_j, \tag{2}$$

where $\mathbf{J}_i$ and $\mathbf{J}_j$ are the CBFs on the i-th and j-th block, respectively. $\mathbf{Z}_{ij}^{RWG}$ is the mutual impedance matrix of RWG/half-RWG between the i-th block and the j-th block. Since the number of CBFs is substantially smaller than the number of RWG basis functions, both the number of unknowns and the matrix dimension are substantially reduced.

The Sherman-Morrison-Woodbury formula-based algorithm (SMWA) provides an effective hierarchical decomposition strategy for further matrix compression and computational complexity reduction [21, 25]. Firstly, the SMWA employs a multilevel balanced binary tree to decompose the target. The reduced self-impedance matrix of leaf nodes can be directly solved and, for non-leaf nodes, its reduced matrix equation is partitioned as:

$$\begin{bmatrix} \mathbf{Z}_{11} & \mathbf{Z}_{12} \\ \mathbf{Z}_{21} & \mathbf{Z}_{22} \end{bmatrix} \begin{bmatrix} \mathbf{I}_1 \\ \mathbf{I}_2 \end{bmatrix} = \begin{bmatrix} \mathbf{V}_1 \\ \mathbf{V}_2 \end{bmatrix}, \tag{3}$$

where $\mathbf{Z}_{11}$ and $\mathbf{Z}_{22}$ is the self-impedance matrix of the two child nodes, $\mathbf{Z}_{12}$ and $\mathbf{Z}_{21}$ denote the reduced mutual impedance matrices between child nodes, $\mathbf{V}$ and $\mathbf{I}$ are the excitation and current vectors of the nodes. The mutual impedance matrices $\mathbf{Z}_{12}$ and $\mathbf{Z}_{21}$ can be efficiently decomposed by ACA [3, 21] as follows:

$$\begin{cases} \mathbf{Z}_{12} \approx \mathbf{U}_{12}\mathbf{V}_{12} \\ \mathbf{Z}_{21} \approx \mathbf{U}_{21}\mathbf{V}_{21} \end{cases}. \tag{4}$$

Multiplying both sides of (3) by the inverse matrix of

$$\begin{bmatrix} \mathbf{Z}_{11} & \mathbf{0} \\ \mathbf{0} & \mathbf{Z}_{22} \end{bmatrix}, \tag{5}$$

we have

$$\begin{bmatrix} \mathbf{1} & \mathbf{Z}_{11}^{-1}\mathbf{U}_{12}\mathbf{V}_{12} \\ \mathbf{Z}_{22}^{-1}\mathbf{U}_{21}\mathbf{V}_{21} & \mathbf{1} \end{bmatrix} \begin{bmatrix} \mathbf{I}_1 \\ \mathbf{I}_2 \end{bmatrix} = \begin{bmatrix} \mathbf{Z}_{11}^{-1}\mathbf{V}_1 \\ \mathbf{Z}_{22}^{-1}\mathbf{V}_2 \end{bmatrix}, \tag{6}$$

where $\mathbf{1}$ is identity matrix and $\mathbf{0}$ is zero matrix. The inverse matrix $\mathbf{Z}_{11}^{-1}$ and $\mathbf{Z}_{22}^{-1}$ can be obtained by direct inversion or recursively via the SMWA algorithm [21].

The solution of (6) can be efficiently obtained by using the SMW formula [21]:

$$(\mathbf{1}+\mathbf{UV})^{-1} = \mathbf{1}-\mathbf{U}(\mathbf{1}+\mathbf{VU})^{-1}\mathbf{V}. \tag{7}$$

Therefore, the computational complexity is remarkably reduced. More detailed solution steps can be found in [21].

As demonstrated throughout this section, a significant advantage of the SMWA is its independence from the underlying basis functions. This flexibility not only facilitates the incorporation of hybrid RWG/half-RWG basis functions for handling nonconformal meshes, but also enables the generation of CBFs at the leaf nodes of the SMWA's binary tree structure to reduce the size of the hierarchical matrix.

III. MULTI-GPU ACCELERATED IEDG-CBFM-SMWA IMPLEMENTATION

The GPU implementation of the IEDG-CBFM-SMWA leverages the parallelism inherent in GPU architectures to accelerate the generation of CBFs, decomposition and solution of hierarchical matrix. The compute unified device architecture (CUDA) developed by NVIDIA provides a mature GPU programming framework with highly optimized linear algebra libraries such as cuSOLVER and cuBLAS, making it the foundational platform for the GPU implementation discussed in this paper.

A. GPU-accelerated MoM functions

Before introducing the proposed multi-GPU accelerated method, we must first implement the GPU-MoM functions upon which its computation depends. As described in section I, the matrix filling process is inherently parallelizable as each element of impedance matrix or voltage vector can be computed independently. Following pre-processing on the host, the mesh data and basis function information are transferred to the device. After allocating sufficient memory space on the device, the host will launch GPU kernel functions that spawn thousands of concurrent threads, where each thread assigned to fill a single matrix element.

Although CUDA has minimized the complexity of GPU programming, effective GPU implementation requires more than a straightforward port of CPU code. It requires careful management of thousands of parallel threads and optimization strategies tailored to the GPU's architectural characteristics. For instance, thread blocks must be configured to align with 32 threads per warp to maximize hardware resource utilization, as shown in Fig. 2, and memory hierarchy optimizations such as texture memory or constant memory are used to accelerate frequent data operations. Consequently, achieving high-performance on the GPU entails considerable effort in kernel design and resource management.

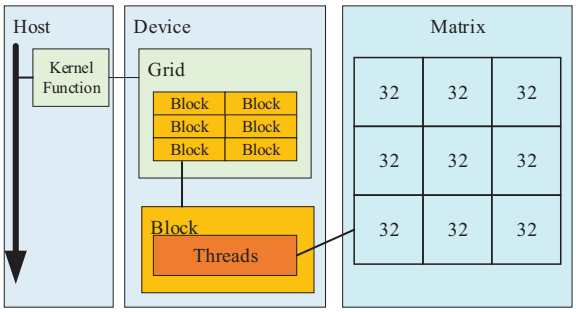


Fig. 2. Task allocation within a CUDA kernel function. A kernel function starts a grid containing multiple blocks, and each block contains multiple threads. Each thread is responsible for filling one element in the matrix. Elements are grouped into a warp of 32, with each thread warp performing the filling process concurrently for optimal efficiency.

Furthermore, once the impedance matrix and voltage vector have been completely assembled in GPU memory, the resulting dense linear system is solved directly using the highly optimized routines provided by the NVIDIA cuSOLVER library. This approach avoids the need for a hand-crafted GPU-based solver and ensures a robust, high-performance solution of the MoM system with minimal development overhead, allowing our efforts to remain focused on the multi-GPU acceleration strategies.

B. Multi-GPU IEDG-CBFM-SMWA

Having established the foundation of GPU-MoM, we now present the proposed SMWA-centric multi-GPU parallelization strategy, which restructures the solution phase to exploit hierarchical matrix parallelism across multiple devices. The steps follow.

B.1. Host-centric hierarchical matrix construction

The SMWA initiates with a recursive binary partitioning of basis functions. The CPU is responsible for constructing and managing the binary tree topology, while the computationally intensive task of filling the impedance matrix for each node is fully offloaded to the GPUs. To avoid write conflicts and to accommodate the hybrid RWG/half-RWG filling formulation, the matrix elements are computed using an edge-to-edge interaction scheme. Since the matrix filling processes for different nodes are mutually independent, they can be distributed across multiple GPUs for parallel execution. However, because the number of basis functions varies significantly across different levels of the tree, dynamic

workload distribution is required to prevent idle computing resources.

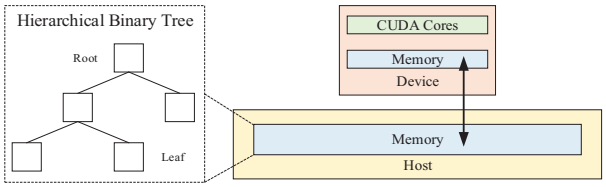


Fig. 3. SMWA's hierarchical binary tree is stored in the host memory. Matrices are only passed to the GPU memory when computation is needed, and retrieved after computation is complete.

The hierarchical matrix operations in the SMWA dictate a deliberate design choice regarding memory management. Unlike conventional GPU-accelerated MoM solvers that aim to retain the entire system matrix in device memory, our approach maintains the binary tree and all impedance submatrices in host memory, as illustrated in Fig. 3. This decision is motivated by the requirements of the SMWA. Specifically, during tree traversal, frequent manipulation of block submatrices within impedance matrices of parent nodes is required. Such operations are inefficient when implemented directly in device memory. Conversely, host memory offers the flexible random-access capabilities required for such manipulations, while also serving as a datasharing space accessible to all GPUs in a multi-GPU configuration.

Throughout the entire multi-GPU IEDG-CBFM-SMWA solution process, rather than just in this step, each GPU acts as a specialized computational accelerator. Relevant data will be transferred to GPU memory only when the host requires computationally intensive tasks, such as matrices multiplication or linear equations solution. Once the computation is complete, the results are returned to host memory, and the GPU memory is released to make room for subsequent tasks. This host-centric memory model, with GPUs dynamically invoked as co-processors, is specifically tailored to the hierarchical traversal pattern of the SMWA.

B.2. CBF generation and hierarchical matrix compression

When the hierarchical impedance matrix has been filled, the excitation-independent CBFs are generated at leaf nodes. In the present IEDG-CBFM-SMWA, a leaf node may contain both RWG and half-RWG basis functions. CBF generation therefore involves hybrid basis functions [23]. Since operations on individual leaf-nodes are strictly independent, they constitute an ideal workload for parallel dispatch. The host will allocate several threads corresponding to the number of leaf nodes in the binary tree, with each thread assigned to a GPU. Filling the impedance matrix and excitation vector leverage the same CUDA kernel functions as above, whereas matrix operations utilize routines from the cuBLAS and cuSOLVER libraries. Given that the number of leaf nodes typically exceeds the number of available GPU devices, multiple threads will be assigned to same GPU device. These threads exploit concurrent execution through dedicated CUDA streams, enabling overlapping data transfer operations and computation to minimize idle time and maximize hardware utilization, as shown in Fig. 4.

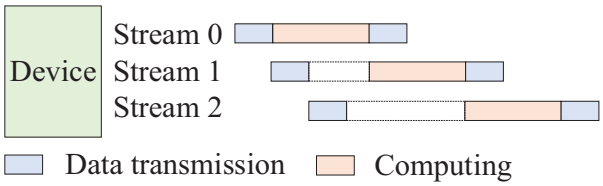


Fig. 4. Computation strategy based on multiple CUDA streams. This strategy overlaps device computation and data transmission to effectively hide data transmission time.

The generated CBF on the leaf nodes will be used to compress the hierarchical impedance matrix. Specifically, the compression phase propagates upward through the binary tree and, crucially, this process maintains node level parallelism. When multiple leaf nodes project their CBFs onto a shared parent node, their operations act on strictly disjoint impedance sub-blocks. This spatial separation inherently eliminates write-conflicts and allows concurrent compression across different branches of the tree without the need for any synchronization overhead. This conflict-free design maximizes GPU occupancy while completing the hierarchical reduction. This SMWA-driven compression strategy is absent in conventional GPU-CBFM implementations and constitutes a key of our multi-GPU acceleration framework.

B.3. SMWA-centric multi-GPU solver

The SMWA matrix factorization proceeds as a level-synchronous traversal of the hierarchical matrix, from the leaf nodes toward the root. Crucially, all nodes at a given level are mutually independent, with data dependencies existing only between different levels. This inherent level-wise independence provides the foundation for our multi-GPU parallelization strategy, as shown in Fig. 5. At the commencement of each level, the host dynamically allocates several threads corresponding to the number of nodes and each thread executes the

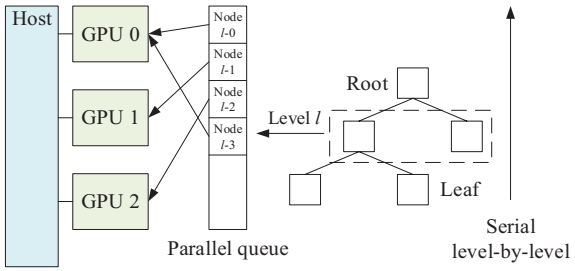


Fig. 5. Schematic diagram of parallel SMWA solution. In the hierarchical matrix, different levels are sequential, but all nodes at the same level are independent of each other.

complete SMWA computation sequence for its assigned node.

Hierarchical partitioning ensures that nodes at the same level possess a comparable number of basis functions. Consequently, the computational workload is intrinsically balanced. Moreover, to maximize hardware utilization, the mapping strategy adapts to the ratio of active nodes to available GPUs. When the number of GPU devices is insufficient relative to the node count, multiple threads will be assigned to the same GPU with task scheduling managed through different CUDA stream concurrency. Conversely, when GPU resources exceed node requirements, a one-to-one thread-to-device mapping is established to maximize parallel execution efficiency. The scenario where GPU resources exceed computational demands occurs exclusively near the root node, therefore, the resulting resource waste is negligible. This adaptive resource allocation strategy ensures optimal hardware utilization across varying problem scales while maintaining computational efficiency throughout the hierarchical solution process.

IV. NUMERICAL EXAMPLES

All examples in this paper were executed on a Dell Precision T7910 workstation. The platform comprises dual Intel Xeon E5-2690 v2 CPUs and three NVIDIA Quadro K6000 GPUs. The programs were compiled by NVIDIA nvcc 11.4 compiler. The CPU implementations utilize the Eigen for dense matrix operations, while the GPU implementations leverage linear algebra functions from the cuBLAS and cuSOLVER libraries.

To validate the accuracy of the proposed method, we computed the RCS of two canonical targets and compared the results with reference solutions obtained from the commercial solver Feko, as shown in Fig. 6. The two test cases are a cube with a side length of 1.0 m and a cylinder with a radius of 0.5 m and a height of 1.0 m. Both models are made of a perfect electric conductor (PEC) and discretized by non-conformal meshes and conformal meshes with an average edge length of $\lambda/10$ at a frequency of 2 GHz. The non-conformal mesh of the cube contains 56512 triangles, while the conformal mesh contains 54312 triangles. Similarly, for the cylinder, the non-conformal mesh contains 50944 triangles, while the conformal mesh contains 51058 triangles. The proposed GPU-accelerated IEDG-CBFM-SMWA uses non-conformal meshes and the Feko uses conformal meshes. As can be seen from Fig. 6, the results of the proposed method are in excellent agreement with those of Feko, confirming the accuracy of the proposed method.

To evaluate efficiency and memory usage, we compared the computational resources required by the single-GPU accelerated CBFM and the proposed method. Similarly, the proposed method uses non-conformal meshes and the GPU accelerated CBFM uses conformal meshes. The measured computation times are summarized in Tables 1 and 2. The “CBF Generation” step records the time required to generate CBFs, which operates on the partitioned blocks for CBFM, and on the leaf nodes of the binary tree for IEDG-CBFM-SMWA. The “Matrix Filling” step records the time to fill the reduced matrix of CBFM. The “Matrix Decomposition and Solution” step records the time for CBFM to solve the reduced matrix directly using the “cusolverDnCCgesv” routine in cuSOLVER, and for IEDG-CBFM-SMWA to decompose the hierarchical matrix via ACA and solve it. Tables 1 and 2 indicate that, although the matrix solving stage of GPU accelerated IEDG-CBFM-SMWA is slower than GPU-CBFM, it is still within an acceptable range.

For the cube model, the conventional MoM defines 85320 RWG / Half-RWG basis functions, and the IEDG-CBFM-SMWA compresses these unknowns into 11523 CBFs. Storing the reduced impedance matrix in single-precision complex format demands approximately 1 GB of GPU memory. In contrast, the hierarchical impedance matrix of the proposed IEDG-CBFM-SMWA requires a peak GPU memory of only 282 MB during the entire solution process. For the cylinder model, the corresponding memory usages are 0.8 GB versus 183 MB. These results demonstrate that the proposed method effectively exchanges a slight increase in solving hierarchical matrix time for a decisive reduction in memory usage. By keeping the peak memory usage well within the capacity of GPU memory, the method enables the direct solution of electrically large problems that would otherwise exceed the device memory limits. This substantial memory advantage combined with the parallel strategy constitutes the principal algorithmic benefit of the proposed method over GPU-CBFM approaches.

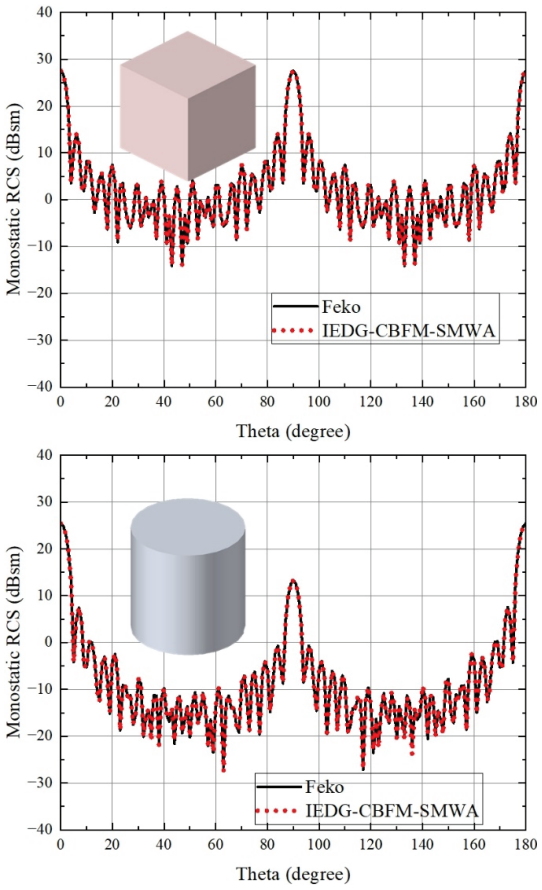


Fig. 6. Comparison of monostatic RCS results. The black curve represents the results of Feko, the red dot set represents the results of GPU-accelerated IEDG-CBFM-SMWA.

Table 1: Comparison of cube calculation times

Method	CBF Generation	Matrix Filling	Matrix Decomposition and Solution	Total
GPU-CBFM	45.8 s	1340 s	8.2 s	1390 s
GPU-IEDG-CBFM-SMWA	59.4 s	1520 s	16.5 s	1600 s

Table 2: Comparison of cylinder calculation times

Method	CBF Generation	Matrix Filling	Matrix Decomposition and Solution	Total
GPU-CBFM	56 s	1080 s	2.3 s	1140 s
GPU-IEDG-CBFM-SMWA	49.9 s	1192 s	15.4 s	1250 s

To further evaluate the proposed method on a complex, multiscale geometry, we constructed a drone model as shown in Fig. 7. The model measures 3.0 m in length, 8.3 m in wingspan, and was discretized into 38964 triangular elements. Owing to the geometric complexity of the wingtip assemblies, vertical stabilizer, and landing gear mechanisms, partial mesh refinement was applied in these regions, resulting in nonconformal mesh at the junctions with the primary airframe structures.

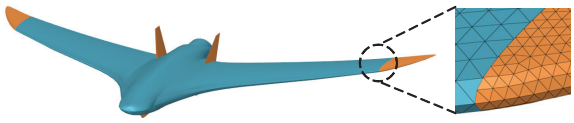


Fig. 7. Schematic of a drone model. The main structure is blue, and the detailed structure is orange. Because different structures use different mesh sizes, the meshes between the structures are nonconformal.

The monostatic RCS was computed at 750 MHz frequency. For reference, we also used Feko to calculate the results of the model being partitioned into a conformal mesh and compared the results with those of the proposed algorithm, as shown in Fig. 8. The results show that both IEDG-CBFM-SMWA achieve good agreement with Feko.

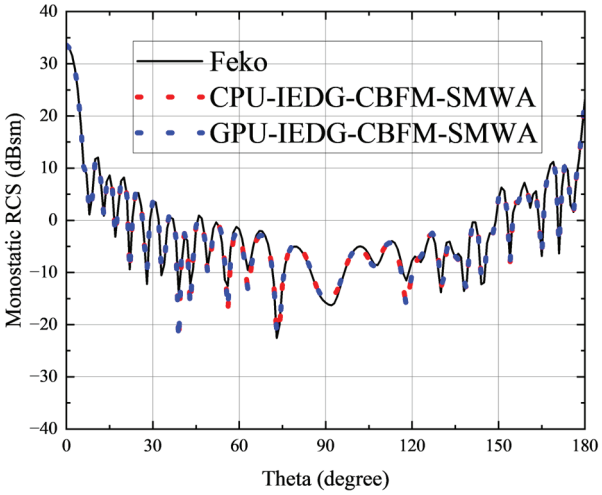


Fig. 8. Comparison of monostatic RCS results. Black curve represents the results of Feko, red dot set and blue dot set represent the results of CPU-based and GPU-based IEDG-CBFM-SMWA.

Table 3: Comparison of calculation times

Method	CBF Generation	Matrix Filling	Matrix Decomposition and Solution	Total
CPU-IEDG-CBFM-SMWA	1020 s	1401 s	21 s	2450 s
1 GPU-IEDG-CBFM-SMWA	48.8 s	662.9 s	11.6 s	724 s
3 GPU-IEDG-CBFM-SMWA	17.1 s	212.7 s	8.1 s	238 s

The computational efficiency of the IEDG-CBFM-SMWA was evaluated. The CPU version was parallelized via OpenMP with 20 CPU threads and the GPU versions were executed by single-GPU and three-GPU configurations. Table 3 shows a comparison of the solution time under different hardware. It can be seen that the multi-GPU accelerated IEDG-CBFM-SMWA achieved substantial computational speedup over the CPU version and demonstrated effective scaling from one to three GPUs.

V. CONCLUSION

This paper presents a multi-GPU accelerated IEDG-CBFM-SMWA. In our implementation, the integration of hierarchical matrix compression, direct solution techniques, and multi-GPU acceleration achieves substantially efficient electromagnetic scattering calculation. It requires less memory than the conventional GPU-accelerated CBFM, thus enabling the solution of larger electromagnetic scattering problems.

ACKNOWLEDGMENT

This work was supported in part by the National Nature Science Foundation of China under Grant 62371228, in part by Key Laboratory of Inlet and Exhaust System Technology, Ministry of Education, under Grant CEPE2024012, and in part by the Project of Key Laboratory of Radar Imaging and Microwave Photonics (Nanjing University of Aeronautics and Astronautics), Ministry of Education under Grant NJ20240005.

REFERENCES

[1] R. F. Harrington, *Field Computation by Moment Methods*. New York: MacMillan, 1968.

[2] W. C. Gibson, *The Method of Moments in Electromagnetics*. Boca Raton: CRC Press, 2007.

[3] K. Zhao, M. N. Vouvakis, and J. F. Lee, "The adaptive cross approximation algorithm for accelerated method of moments computations of EMC," *IEEE Trans. Electromagn. Compat.*, vol. 47, no. 4, pp. 763–773, 2005.

[4] J. M. Tamayo, A. Heldring, and J. M. Rius, "Multilevel adaptive cross approximation (MLACA)," *IEEE Trans. Antennas Propag.*, vol. 59, no. 12, pp. 4600–4608, 2011.

[5] R. Coifman, V. Rokhlin, and S. Wandzura, "The fast multipole method for the wave equation: A pedestrian prescription," *IEEE Antennas Propag. Mag.*, vol. 53, no. 3, pp. 7–12, 1993.

[6] J. Song, C. C. Lu, and W. C. Chew, "Multilevel fast multipole algorithm for electromagnetic scattering by large complex objects," *IEEE Trans. Antennas Propag.*, vol. 45, no. 10, pp. 1488–1493, 1997.

[7] S. X. Peng and Z. P. Nie, "Acceleration of the method of moments calculations by using graphics processing units," *IEEE Trans. Antennas Propag.*, vol. 56, no. 7, pp. 2130–2133, 2008.

[8] D. D. Donno, A. Esposito, G. Monti, and L. Tarricone, "Parallel efficient method of moments exploiting graphics processing units," *Microw. Opt. Technol. Lett.*, vol. 52, no. 11, pp. 2568–2572, 2010.

[9] E. Lezar and D. B. Davidson, "GPU-accelerated method of moments by example: Monostatic scattering," *IEEE Antennas Propag. Mag.*, vol. 52, no. 6, pp. 120–135, 2011.

[10] T. Topa, A. Karwowski, and A. Noga, "Using GPU with CUDA to accelerate MoM-based electromagnetic simulation of wire-grid models," *IEEE Antennas Wireless Propag. Lett.*, vol. 10, pp. 342–345, 2011.

[11] T. Topa, A. Noga, and A. Karwowski, "Adapting MoM with RWG basis functions to GPU technology using CUDA," *IEEE Antennas Wireless Propag. Lett.*, vol. 10, pp. 480–483, 2011.

[12] T. Topa, "Load-balanced Fortran-based out-of-GPU memory implementation of the method of moments," *IEEE Antennas Wireless Propag. Lett.*, vol. 16, pp. 813–816, 2017.

[13] M. Cwikla, J. Aronsson, and V. Okhmatovski, "Low-frequency MLFMA on graphics processors," *IEEE Antennas Wireless Propag. Lett.*, vol. 9, pp. 8–11, 2010.

[14] Q. M. Nguyen, V. Dang, O. Kilic, and E. El-Araby, "Parallelizing fast multipole method for large-scale electromagnetic problems using GPU clusters," *IEEE Antennas Wireless Propag. Lett.*, vol. 12, pp. 868–871, 2013.

[15] J. Guan, S. Yan, and J. M. Jin, "An OpenMP-CUDA implementation of multilevel fast multipole algorithm for electromagnetic simulation on multi-GPU computing systems," *IEEE Trans. Antennas Propag.*, vol. 61, no. 7, pp. 3607–3616, 2013.

[16] W. J. He, Z. Yang, X. W. Huang, W. Wang, M. L. Yang, and X. Q. Sheng, "Solving electromagnetic scattering problems with tens of billions of unknowns using GPU accelerated massively parallel MLFMA," *IEEE Trans. Antennas Propag.*, vol. 70, no. 7, pp. 5672–5682, 2022.

[17] J. I. Perez, E. García, J. A. de Frutos, J. R. Almagro, and M. F. Cátedra, "Application of GPU computing to the characteristic basis function method," in *2012 6th European Conference on Antennas and Propagation (EuCAP)*, Prague, Czech Republic, pp. 1003–1006, 2012.

[18] J. Zhang and Y. Sun, "Parallel SVD-CBFM based on GPU acceleration," in *2019 Cross Strait*

Quad-Regional Radio Science and Wireless Technology Conference (CSQRWC), Taiyuan, China, pp. 1–3, 2019.

[19] Y. Su and R. Mittra, "GPU-acceleration of characteristic basis function method (CBFM) for efficient analysis of complex platforms involving layered media," in *2019 USNC-URSI Radio Science Meeting*, Atlanta, GA, USA, pp. 43–44, 2019.

[20] R. Mittra, T. Marinovic, O. Ozgun, S. Liu, and R. K. Arya, "Novel strategies for efficient computational electromagnetic (CEM) simulation of microstrip circuits, antennas, arrays, and metamaterials part-II: Characteristic basis function method, perfectly matched layer, GPU acceleration," *Applied Computational Electromagnetics Society (ACES) Journal*, vol. 40, no. 06, pp. 471–498, 2025.

[21] X. Chen, C. Gu, Z. Li, and Z. Niu, "Accelerated direct solution of electromagnetic scattering via characteristic basis function method with Sherman-Morrison-Woodbury formula-based algorithm," *IEEE Trans. Antennas Propag.*, vol. 64, no. 10, pp. 4482–4486, 2016.

[22] Z. Peng, K. H. Lim, and J. F. Lee, "A discontinuous Galerkin surface integral equation method for electromagnetic wave scattering from nonpenetrable targets," *IEEE Trans. Antennas Propag.*, vol. 61, no. 7, pp. 3617–3628, 2013.

[23] Y. Su, R. Mittra, and W. Sheng, "Analysis of scattering from multi-scale and multiple targets using characteristic basis function (CBFM) and integral equation discontinuous Galerkin (IEDG) methods," *J. Electromagn. Waves Applicat.*, vol. 31, no. 10, pp. 969–980, 2017.

[24] E. Lucente, A. Monorchio, and R. Mittra, "An iteration-free MoM approach based on excitation independent characteristic basis functions for solving large multiscale electromagnetic scattering problems," *IEEE Trans. Antennas Propag.*, vol. 56, no. 4, pp. 999–1007, 2008.

[25] X. Fang, Q. Cao, Y. Zhou, and Y. Wang, "Multiscale compressed and spliced Sherman-Morrison-Woodbury algorithm with characteristic basis function method," *IEEE Trans. Electromagn. Compat.*, vol. 60, no. 3, pp. 716–724, 2018.



Ziang Shen received his Bachelor's degree in 2017 and his Master's degree in 2020 from Nanjing University of Aeronautics and Astronautics, China, and is presently pursuing the Ph.D. degree. His research focuses on high-performance computational electromagnetics, specifically frequency-domain, time-domain, and high-frequency asymptotic algorithms.



Xinlei Chen received the Ph.D. degree from Nanjing University of Aeronautics and Astronautics, China, in 2015. Currently, he is an Associate Professor at Nanjing University of Aeronautics and Astronautics. He has published over 80 papers in journals and conferences, including *IEEE Transactions on Antennas and Propagation* and *IEEE Antennas Wireless Propagation Letters*. His research interests include integral equation methods in electromagnetic problems.



Zhuo Li received the B.Sc. degree in electronic engineering and the M.E. degree in electromagnetic fields and microwave techniques from Nanjing University of Aeronautics and Astronautics (NUAA), Nanjing, China, in 2001 and 2004, respectively, and the Ph.D. degree in radio engineering from the State Key Laboratory of Millimeter Waves, Southeast University, Nanjing, in 2009. From 2015 to 2016, he was a Visiting Scholar with the Department of Physics, Arizona State University, Tempe, AZ, USA. He is currently a Full Professor with the College of Electronic and Information Engineering in NUAA. He has authored or co-authored over 160 papers in refereed journals and conference proceedings, including *Advanced Science, Advanced Optical Materials, Nano Letters, Physical Review Applied, IEEE Transactions on Microwave Theory and Techniques, IEEE Transactions on Antennas and Propagation*, and *IEEE Transactions on Electromagnetic Compatibility*. He has filed more than 30 patents. His current research interests include plasmonic metamaterials, MHz-through-THz technologies and transceivers for wireless sensors and biomedical applications, electromagnetic compatibility in avionics system and auto electrical system. He is also interested in the modeling and design of microwave and terahertz photonic circuits and systems.

Li is a Senior Member of the Chinese Institute of Electronics and a Committee Member of the Antenna Branch of the Chinese Institute of Electronics. He received the Second Prize in Natural Science of the China Institute of Electronics in 2019 and the NUAA Outstanding Undergraduate Teaching Promotion Award in 2019. He is on the Advisory Board for *Journal of Physics D: Applied Physics* and on the Review Board for many international journals including *Advanced Materials, ACS Photonics, Nanotechnology, Nano-Micro Letters, IEEE T-MTT, IEEE T-AP*, and *IEEE T-EMC*. He has served as the Invited Speaker and Session Chair in many international conferences and workshops.

Ant Colony Algorithm Optimized Method for Electromagnetic Interference Suppression of Power Line Inspection UAVs

Jian Chen, Yuxuan Huang*, and Ziheng Wan

Zhuhai Power Supply Bureau
Guangdong Power Grid Co. Ltd., Zhuhai 519000, China
chenjian_986@163.com, huangyx1996@igit.ac.cn, wanziheng999@163.com
*Corresponding author

Abstract **–** Power inspection drones face severe electromagnetic interference issues in complex electromagnetic environments. Methods such as wavelet transform, matched filtering, and traditional support vector machines (SVM) have been applied in the field of interference suppression, however, the transient characteristics of interference are highly random and bursty. Existing methods have significant deficiencies in extracting key information in the time-frequency domain, making it difficult to accurately characterize interference features. This leads to large deviations in the peak values of frequency-domain amplitude characteristics and fails to achieve the desired suppression performance. To effectively suppress electromagnetic interference, an ant colony algorithm-optimized electromagnetic interference suppression method for power inspection drones is proposed. Wavelet decomposition transform is used to optimize the signal waveform of power inspection drones, thereby improving signal quality. By combining discrete Fourier transform processing and matched filtering transform, transient time-frequency domain features of interference are extracted based on the optimized drone signal waveform. Using the transient time-frequency domain features, a SVM trained with a linear kernel function is employed to detect high-density integrated electromagnetic interference. A filter is adopted to suppress electromagnetic interference by adjusting its coefficients, and the ant colony algorithm is utilized to adaptively optimize these coefficients, achieving high-density integrated electromagnetic interference suppression for power inspection drones. Experimental results show that the optimized signal waveform is smoother and more stable. The error between the frequency-domain amplitude characteristic peak of electromagnetic interference signals extracted by this method and the actual interference peak is less than 5 dB. After applying the proposed suppression method, the electromagnetic interference intensity is reduced to below 1 $\mathrm{W/cm^2}$, and the signal-to-noise ratio (SNR) of the suppressed signal is relatively high.

Index Terms **–** Ant colony optimization, high-density integrated electromagnetic interference, interference suppression.

I. INTRODUCTION

As the scale of power systems continues to expand and their level of intelligence steadily improves, unmanned aerial vehicle (UAV) power inspection technology, leveraging its advantages of high efficiency and flexibility, has become an important means of ensuring the safe operation of power grids. However, the electromagnetic environment in areas with dense power equipment is relatively complex, and there are high-intensity and broad-spectrum electromagnetic interference sources in typical scenarios such as substations and high-voltage transmission corridors, which pose a serious challenge to the reliability of UAV inspection systems. Traditional decentralized electromagnetic compatibility designs often struggle to address mutual interference among sensors, communication modules, and flight control systems within highly integrated UAV platforms, especially when multiple mission payloads work collaboratively. The coupling effect of electromagnetic interference [1] can lead to chain reactions such as UAV signal distortion, positioning drift, and even control system failure. Such interference not only affects the accuracy of inspection data but may also cause safety hazards such as UAV loss of control, directly threatening the stable operation of power facilities. Therefore, interference suppression under high-density integration conditions is of great significance for promoting the development of intelligent inspection technology and ensuring power grid safety.

In the process of continuously expanding the application of drone technology, electromagnetic interference has become increasingly prominent and has become a key factor affecting its performance and reliability. Cheng et al. [2] used adaptive beamforming to suppress high-density integrated electromagnetic

Submitted On: February 11, 2026
Accepted On: May 27, 2026

1054-4887 © ACES

https://doi.org/10.13052/2026.ACES.J.410707

interference in UAV remote communication, and optimized beam direction through phase compensation to deal with frequency hopping. Yang and Li [3] used wavelet threshold denoising and magnetic disturbance compensation models to realize the anti-electromagnetic interference of substation patrol UAV, and responded to strong interference by controlling the transmission power. Li et al. [4] established the electromagnetic field effect model of EHV transmission lines and defined the minimum anti-interference distance to avoid the influence of field strength. Meng et al. [5] used microwave ferrite birefringence effects and adaptive variable polarization controls to make antenna radiation and interference wave form polarization orthogonal to realize anti-interference.

The existing methods mostly focus on the single link of interference suppression, lack the whole link collaborative design from signal waveform optimization $\rightarrow$ feature extraction $\rightarrow$ intelligent detection $\rightarrow$ adaptive suppression, and do not use the intelligent optimization algorithm to globally optimize the filter parameters, resulting in obvious deficiencies in the suppression effect and robustness in the complex multi-interference superposition scene. Therefore, an ant colony algorithm optimization method for electromagnetic interference suppression of Power Patrol UAV is proposed.

II. HIGH-DENSITY INTEGRATED ELECTROMAGNETIC INTERFERENCE SUPPRESSION FOR POWER INSPECTION UAVs

This section focuses on the problem of high-density integrated electromagnetic interference of Power Patrol UAVs in complex electromagnetic environments, and carries out systematic research from four aspects (signal waveform optimization, interference time-frequency domain feature extraction, interference detection, interference suppression) and proposes a complete set of interference suppression method processes.

Based on wavelet decomposition as the signal front-end de-noising foundation, using discrete Fourier transform as the time-frequency domain bridge, using matched filtering to capture transient weak anomaly characteristics, using a support vector machine (SVM) to complete interference classification detection, and finally using an ant colony algorithm to adaptively optimize the filter coefficient to realize interference suppression, these five methods constitute a complete technical link from signal preprocessing $\rightarrow$ feature extraction $\rightarrow$ intelligent detection $\rightarrow$ adaptive suppression, and each link is collaborative and complementary, breaking through the limitations of the traditional single method in the complex electromagnetic environment.

A. Optimization of signal waveform for unmanned aerial vehicles in power inspection

The electromagnetic interference coupling effect [6, 7] exists between the external environment of the Power Patrol UAV and the airborne equipment, and the signal quality directly affects the interference suppression effect. Therefore, the wavelet decomposition method is used to reconstruct and optimize the signal waveform before interference suppression, so as to improve the signal quality and prevent the suppression process from reducing signal stability. The dual optimization strategy of wavelet decomposition wavelet transform adopted in this section is different from the traditional single wavelet de-noising method. The refined separation of signal and noise is achieved by introducing binary wavelet transform, which provides a high-quality signal base for subsequent time-frequency feature extraction.

Based on the Nyquist sampling theorem, the sampling rate should be at least twice the highest frequency of the signal to avoid signal aliasing on the same frequency. Assuming the continuous time of the power inspection drone signal is $x(t)$, where t represents the time variable. In order to convert the continuous signal of the power inspection drone into a discrete signal, it is necessary to sample at a fixed sampling interval T_s on the time axis. The discrete signal of the sampled power inspection drone and the discrete data sequence of the power inspection drone signal collected by the sensor are:

$$X = x(t)nT_s, \tag{1}$$

where n represents the index of the sampling point, which represents the position of the sampling point.

By combining wavelet transform operations, X is transformed into a series of approximate coefficients and detail coefficients. Assuming that j represents the level of decomposition, the specific expression for wavelet decomposition is:

$$X = (A_1, B_1) + (A_2, B_2) + \cdots + (A_j, B_j), \tag{2}$$

where A_j represents the approximation coefficient of the j-th layer, and B_j represents the detail coefficient of the j-th layer. Combined with threshold processing, wavelet coefficients are denoised, and differentiation threshold is set based on signal characteristics and noise level. Low-frequency signals use lower threshold to retain the main components [8–10], and high-frequency signals use higher threshold to remove noise. The approximate coefficients and detail coefficients of each layer are used to reconstruct layer by layer through inverse wavelet transform from top to bottom. The approximate coefficients of the highest layer are used as the initial

signal, and the detail coefficients of the current layer are fused step by step. After completing all levels of transformation, the preliminary reconstructed signal is obtained:

$$X' = p_{j-1}X(A'_j, B'_j), \tag{3}$$

where p_{j-1} represents the intermediate signal generated during the inverse wavelet transform process, and X' represents the discrete signal of the reconstructed power inspection drone signal.

The interference signal is separated into different frequency components by wavelet decomposition. The high-frequency noise is denoised by threshold and the key low-frequency components are retained. The original waveform is reconstructed layer by layer by inverse wavelet transform. On this basis, wavelet transform is introduced to realize signal-to-noise separation. The environmental interference and UAV signals are effectively divided, and the echo signals are summarized to form the observation sequence.

Using the idea of wavelet transform, the interference observation sequence is transformed to obtain the first wavelet transform result. Perform binary discretization processing on scale parameters to generate binary wavelet transform results:

$$\begin{cases} X_J = \dfrac{1}{J}\displaystyle\int_{-\infty}^{+\infty} \vartheta(X')\chi\left(\dfrac{X'-\omega}{H}\right)d\omega \\ X'_J = \dfrac{1}{2^J}\displaystyle\int_{-\infty}^{+\infty} X_J\bar{\chi}\left(\dfrac{X_J-\omega}{2^J}\right)d\omega \end{cases}, \tag{4}$$

where J represents the scale parameter of wavelet transform, χ represents the mother wave function, ω represents the duration of pulse continuity, H represents the absorption coefficient of electromagnetic wave interference, $\bar{\chi}$ represents the mother wave function in Fourier transform form, and ϑ represents the integral operation function.

The original interference signal is converted into two wavelet signals by binary wavelet transform, and the transformation coefficients are obtained. The signal points satisfying the noise characteristics in the decomposed signal are searched and set to 0. All kinds of noise are projected into different wavelet spaces, and the denoised signal waveform optimization results are generated after traversing all wavelet signal points:

$$X'' = \begin{cases} \lambda(\sigma_J)(|\sigma_J| - (l\rho)^{1/2})_J & |\sigma_J| \geq \eta \\ 0 & |\sigma_J| < \eta \end{cases}, \tag{5}$$

where σ represents the signal variance, λ represents the sign function, η represents the noise threshold, l represents the logarithmic function, and ρ represents the length of the electromagnetic wave interference signal sequence. Use the optimized waveform of the power inspection drone signal as the subsequent electromagnetic interference suppression result.

B. Extraction of interference transient time-frequency domain features based on optimized UAV signal waveform

To conduct in-depth research on the electromagnetic interference of power inspection drone signals, the transient frequency domain characteristics of the optimized power inspection drone signals in the previous section were extracted. Based on the time-frequency domain analysis of the conventional discrete Fourier transform, the matched filter transform is further introduced to capture the transient weak abnormal interference signal, which makes up for the deficiency of the pure Fourier transform in the transient feature capture. At the same time, the inverse gamma distribution aggregation is used to determine the anomaly discrimination threshold, and the refined extraction of time-frequency domain features is realized. This feature extraction process is directly linked to the waveform optimization results in section A, ensuring that feature extraction is based on high-quality signals.

The transient radiation field of the units in a row and b column of the power inspection drone signal array can be expressed as:

$$C_{ab} = \frac{sIe^{-\mu l_{ab}} f(\varphi)X''}{l_{ab}}, \tag{6}$$

where l_{ab} represents the distance between the signal array of the power inspection drone in a row and b column and the field point, and μ represents the wave number of the electromagnetic wave of the power inspection drone signal during the fluctuation process, $\mu = 2\pi/\lambda$, λ represents the electromagnetic wavelength, φ represents the azimuth angle, $f(\varphi)$ represents the directional diagram function of the signal array unit of the power inspection drone, s represents the total number of units in the signal array of the power inspection drone, and I represents the high-density integrated signal value of the transient power inspection drone.

Through superposition calculation, the total transient radiation field strength of the signal array of the electric power inspection UAV is obtained, which is expressed as:

$$C_n = sIf(\varphi)\sum_{a=1}^{n}\sum_{b=1}^{n} c_{ab}. \tag{7}$$

The transient total field strength data of the power inspection UAV signal array obtained by discrete Fourier transform processing is used to convert the initial

transient field strength data into frequency domain information, and the time domain continuous curve representation is:

$$\beta(C_n) = \upsilon + \sum_{g=1}^{n} \left[\frac{u_g \cos(g\pi C_n) + v_g \sin(g\pi C_n)}{T} \right], \quad (8)$$

where υ is the bias, u_g and v_g are the Fourier coefficients of the g-th electromagnetic interference process, and T represents the duration of the transient total field strength data of the power inspection UAV signal.

The time-domain characteristics of transient total field strength of power inspection UAV signal array are transformed into transient frequency-domain characteristics of power inspection UAV signal, which is expressed as:

$$P(C_n) = \sum_{n=0}^{N-1} \beta(C_n) e^{-2\pi n/N}, \quad (9)$$

where N represents the frequency domain feature length of the transient total field strength of the power inspection UAV signal array.

In the complex electromagnetic environment of power inspection, the communication signal of UAVs will experience attenuation. The time-frequency domain features are conventional time-frequency domain features, which are prone to missing transient weak interference abnormal signals. Therefore, matched filtering transformation is used to capture the time-frequency characteristics of transient abnormal signals.

Under electromagnetic interference [11], assuming the Doppler frequency deviation of the actual received UAV communication signal is f_d, $b(n)$ represents the pseudo code of the abnormal signal, and the optimized signal waveform is filtered again, expressed as:

$$L_i = \sum_{i=0}^{M-1} X'' b(n) e^{-(2\pi f_d i T + \varphi)}, \quad (10)$$

where M represents the length of the communication signal processing filter, φ represents the initial phase value of the communication signal, and i represents the i-th matched filter. According to the autocorrelation characteristics of pseudocode, the frequency difference value of the n-th filter output under Doppler frequency shift is the effective compensation frequency difference value of matched filter transformation. Using the normalized frequency response of the i-th matched filter, the time-frequency domain feature extraction of interference transient is completed:

$$Z_i = \sin(\pi f_d \beta(C_n) P(C_n)) \times \left(\sum_{i=0}^{N-1} L_i e^{-(2\pi f_d i)} \right) \times \left(\sum_{i=0}^{N-1} L_i e^{-(2\pi f_d n)} \xi \right) \Big/ M, \quad (11)$$

where ξ represents the compensation coefficient. The normalized frequency response of the i-th matched filter [12, 13] is obtained by multiplying the frequency response of the fast Fourier transform with the frequency response of the partially matched filter.

When matching filter is used to extract the transient time-frequency domain characteristics, each frequency point corresponds to a group of samples, the UAV signal is crest, and abnormal interference leads to the change of energy superposition characteristics. According to this, the maximum operator is used to set the threshold to extract the abnormal characteristics, and the discrimination threshold of abnormal interference acquisition is determined according to the inverse gamma distribution aggregation normalized frequency.

C. High-density integrated electromagnetic interference detection based on transient time-frequency domain features of interference

The high-density integrated electromagnetic interference sources of power inspection drones are diverse, including natural electromagnetic phenomena, anthropogenic electromagnetic radiation, and enemy electronic countermeasures. These interference signals may exist in the form of continuous waves or pulse waves, causing varying degrees of interference to the communication link of UAVs. Therefore, in order to effectively suppress high-density integrated electromagnetic interference [14, 15], it is necessary to accurately detect high-density integrated electromagnetic interference from UAV communication signals based on the transient time-frequency domain characteristics of interference.

A convolutional neural network support vector machine (CNN-SVM) detection model with convolution pooling structure is constructed. The multidimensional transient time-frequency domain features extracted in section B are used as input, and the local spatial correlation of features is automatically extracted through convolution layer. The pooling layer reduces the feature dimension and enhances the noise resistance. Finally, SVM completes the nonlinear classification decision. Compared with the traditional SVM which directly inputs the original features, the CNN-SVM structure significantly improves the recognition accuracy of complex electromagnetic interference patterns, and provides reliable interference localization and classification results for the adaptive suppression in section D.

SVM is a widely used machine learning method for classification problems. The basic principle is to find the optimal linear classifier that maximizes the boundary distance on the training dataset, thereby achieving maximum stability of the classifier. For nonlinear problems, SVM maps the input space to a high-dimensional feature space by introducing a kernel function, making the originally linearly inseparable problem linearly separable [16, 17]. In the high-density integrated electromagnetic interference detection of UAVs, SVM is used as a classifier to distinguish between normal communication signals and high-density integrated electromagnetic interference. Input the extracted interference transient time-frequency domain feature parameters into the SVM model, and use a labeled training dataset (including feature parameter samples of normal communication signals and electromagnetic interference) to train the SVM model. This SVM model adds multiple convolutional and pooling layers before the fully connected layer to enhance the detection performance of electromagnetic interference signals [18, 19]. Considering the attenuation of wireless communication network signals due to diffusion loss and path loss during transmission, a linear kernel function is selected to train the detection capability of SVM:

$$S_i = \sum_{i=1}^{M} \alpha_i y_i (Z_i) + b, \tag{12}$$

where α_i and y_i represent the Lagrange multiplier and label of the i-th electromagnetic interference feature sample in the SVM model, respectively, M represents the number of training samples, and b represents the bias term.

The SVM model is mapped to the signal type label. Through the classifier algorithm, the probability distribution corresponding to each signal type can be calculated:

$$\rho(S_i \mid M) = \frac{e^{W_i S_i + b_i}}{\sum_{i=1}^{M} e^{W_i S_i + b_i}}, \tag{13}$$

where W_i and b_i represent the weight and bias of the classifier, respectively.

According to the principle of maximum posterior probability, the SVM model is trained to find the learning ability of maximum probability:

$$\rho_{\max} = \arg\max \frac{\rho(S_i \mid M)\rho(M \mid \lambda)}{\sum_{i=1}^{M} \rho(S_i \mid M)\rho(M \mid \lambda)}, \tag{14}$$

where λ represents the prior probability parameter of the training sample. After the training is completed, the decision function of high-density integrated electromagnetic interference classification detection based on SVM model is [20]:

$$F = \text{sign}\left(\sum_{i=1}^{n} c_i y_i B(Z_i, b) + \beta \right), \tag{15}$$

where $B(b_i, b)$ is the sigmoid kernel function, which is characterized by its ability to implicitly map input data to a high-dimensional space and achieve nonlinear separability of data in this high-dimensional space, c_i is the category label of normal drone signal characteristics, β is the intercept term, b_i is the feature vector corresponding to the electromagnetic interference training sample i of the power inspection drone, b is the feature vector corresponding to all test samples.

The classification of SVM model is used to complete the detection of high-density integrated electromagnetic interference, and the detected interference signals are taken as the object of subsequent suppression.

D. Implementation of high-density integrated electromagnetic interference suppression based on ant colony algorithm

In response to the detected high-density integrated electromagnetic interference signal, a filter is used to filter out the electromagnetic interference from the drone signal by adjusting the filtering coefficient, generating a series of steady-state drone communication signals to achieve automatic suppression of high-density integrated electromagnetic interference. The innovation of this section is that the ant colony algorithm is used to globally optimize the adaptive correction feedback coefficient of the filter, and the interference category information of CNN-SVM detection output in section C is used as the optimization constraint to construct the closed-loop framework of detection guidance suppression. Compared with the fixed coefficient filter or the traditional gradient optimization method, the swarm intelligence search mechanism of an ant colony algorithm can effectively avoid falling into local optimization, realize the global optimal configuration of filter parameters in the complex multi-interference superposition scene, and minimize signal loss. The ant colony algorithm is a meta heuristic optimization algorithm based on swarm intelligence, which can effectively explore different regions of the solution space, find the global optimal solution, and have good flexibility and fast convergence advantages [21, 22]. Therefore, this paper uses the ant colony algorithm to adaptively optimize the coefficients of the filter and improve the suppression effect.

The electromagnetic interference component will generate a leading phase in a specific section of the high-density integrated signal of the power inspection drone. The signal expression of the n superimposed electromagnetic interference components in the d-th

phase interval of the high-density integrated signal of the power inspection drone is:

$$I_d = \frac{F_c(F)\eta_k n' \sqrt{\varsigma^2 \times \lambda^2}}{d}, \tag{16}$$

where ς and λ represent the sampling period and amplitude of the electromagnetic interference observation values, respectively, η_k represents the high-density integrated signal quantity injected into the power inspection UAV, F_c represents the superposition scale function.

Thus, the high-density integrated signal of the power inspection drone is divided into interference containing signals and interference-free interval signals. However, the high-density integrated signal of the power inspection drone exhibits second-order oscillation characteristics. This characteristic is manifested as a distinct electromagnetic peak on the Bode plot, and the frequency corresponding to the peak is the electromagnetic interference frequency. When the communication signal of UAVs contains signal components with frequencies similar to electromagnetic interference, it will affect the suppression effect and signal continuity, resulting in high signal loss costs for interference suppression and limiting its effectiveness in practical engineering applications. Therefore, this paper dynamically adjusts the output of the filter by monitoring and providing feedback on changes in electromagnetic interference in real time, in order to reduce signal loss. By adaptively adjusting the feedback coefficient to continuously increase the damping ratio, the goal of electromagnetic interference suppression can be achieved [23].

In order to enhance the suppression capability of the filter when dealing with key electromagnetic interference components, it is necessary to optimize its design to ensure that its output response within the main electromagnetic interference frequency range is maximally suppressed, and the electromagnetic interference components in the suppressed signal meet the requirement of being below the preset threshold, thereby improving signal quality. The mathematical model for optimizing the suppression target of the constructed filter is:

$$\min W = \min\left(\frac{\int_{\omega_\delta}^{\omega_\chi} W_g(I_d) dI_d}{F(\omega_\chi - \omega_\delta)}\right), \tag{17}$$

where ω_χ and ω_δ are the upper and lower frequency limits of the main electromagnetic interference segment, W_g is the adaptive correction feedback coefficient.

The ant colony algorithm is employed for adaptive optimization of filter correction feedback coefficients. During the optimization process, the ants' positions are treated as parameters to be optimized. To ensure successful optimization, ants must navigate through migration by employing core strategies: optimal direction identification and preference-based movement. The optimal direction identification strategy is implemented through:

$$M_s(W_g) = \phi(P_s(t) - P_s(t-1)), \tag{18}$$

$$\phi = W_g^2 r_d, \tag{19}$$

where ϕ represents the dynamic adjustment coefficient used to balance the search behavior of the ant colony. A larger value may make the ant colony more inclined towards global search, while a smaller value may promote local fine search. When $P_s(t)$ is t iterations, the optimal position searched by the ant colony population is the best solution among all ant colony positions, r_d represents a random number with a value range of $(0,1)$, which increases the randomness and diversity of the search.

The convergent mobility strategy is defined by:

$$G_s = |F_s + M_s|, \tag{20}$$

where G_s represents the adjusted ant colony position and F_s represents the radius of particle motion.

Each individual ant colony adopts a movement pattern to move. The optimization process of filter parameters based on an ant colony algorithm is as follows.

Step 1: randomly generate a certain number of ant colony individuals, each of which represents a set of filter parameters. At the same time, the interference category information output from section C CNN-SVM detection is encoded into the initial pheromone distribution of ant colony search, so that the search direction is biased towards the identified interference frequency region.

Step 2: update the position of the ant colony according to the optimal direction identification strategy and the preferential movement strategy of the ant colony algorithm. In each iteration, the pheromone volatilization rate is dynamically adjusted by using the interference category label output by the detection module. When multiple types of composite interference are detected, the pheromone volatilization rate is reduced to enhance the global search ability. When a single interference is detected, the pheromone volatilization rate is increased to accelerate the local convergence.

Step 3: simulate the optimization behavior of ant colony and conduct local search in the solution space to find a better combination of filter parameters. At the same time, the signal quality feedback mechanism after interference suppression is introduced, and the SNR after interference suppression is used as the fitness evaluation index to reverse modify the pheromone update rule.

Step 4: repeat steps 2 to 3 until the upper limit of the number of iterations is reached or the SNR does not increase significantly after 10 consecutive iterations.

Step 5: after the iteration, output the ant colony position with the best performance, that is, the optimal parameters of the filter. At the same time, the final optimized parameters and the detection category information are stored in the parameter library for the rapid initialization of interference suppression in the next inspection task.

The optimal parameters are input into (17) to complete the filter optimization, and the original UAV signal is input into the filter to complete the high-density integrated electromagnetic interference suppression of Power Patrol UAV. The whole suppression process forms a closed-loop control process of detection → parameter initialization → optimization → suppression → feedback.

III. EXPERIMENT AND ANALYSIS

In order to verify the effectiveness and superiority of the proposed method in the suppression of high-density integrated electromagnetic interference of Power Patrol UAV, this section designs a comparative experiment covering a variety of interference types and different interference intensities, and systematically analyzes the experimental results from the four dimensions of waveform optimization, feature extraction, interference detection, and interference suppression.

A. Experimental setup

In order to verify the performance of the high-density integrated electromagnetic interference suppression method for power inspection UAVs based on an ant colony algorithm studied in this paper, experimental tests are designed. The experimental object is a power inspection UAV system operated by Zhuhai Power Supply Bureau of Guangdong Power Grid Co. Ltd, equipped with an EM-Sense 6050 high-density integrated electromagnetic sensor module (frequency response range of 10 Hz–6 GHz), used to collect electromagnetic interference signals in the transmission line corridor. The experimental scenario is a real electromagnetic interference environment (as shown in Fig. 1). The UAV inspection path within a 3-kilometer radius of the 500 kV high-voltage substation in the area where the power company is located includes typical interference sources such as wire corona discharge, partial discharge of insulators, and interference from adjacent communication base stations. Based on the real electromagnetic interference environment, a simulation platform was constructed using Keysight N9021B MXA signal analyzer and R&S SMW200A vector signal generator to generate composite electromagnetic interference signals that comply with IEEE C63.30-2021 standards (including six types: sweep frequency interference, noise frequency modulation interference, narrowband aiming interference, comb multi tone interference, frequency band noise interference, pulse noise interference). The raw electromagnetic signal collected by the UAV inspection system has a sampling rate of 1 GS/s and a resolution of 12 bits. There are a total of 12 inspection tasks, each lasting 30 minutes, with a total data volume of about 2.4 TB. Gaussian white noise (SNR $= 5-20$ dB) and modulation interference (carrier frequency 1–500 MHz, bandwidth 10 kHz–5 MHz) are added to generate 1000 sets of samples, each lasting for 10 ms. The data is divided into training set, validation set, and testing set in a ratio of 70:15:15.



Fig. 1. Experimental environment.

Based on the experimental subjects and data scale, the experimental hardware environment is set up as shown in Table 1.

Table 1: Hardware settings of experimental environment

Hardware	Deploy
Drone platform	DJI Matrice 300 RTK (RTK positioning accuracy ±1 cm)
Electromagnetic transducer	EM-Sense 6050 (6 GHz bandwidth, 16 channel synchronization)
Signal simulator	R&S SMW200A (20 GHz RF bandwidth)
Computing servers	Dell PowerEdge R750 (2× Intel Xeon Gold 6348, 512 GB DDR4, 4× NVIDIA A100 80 GB)
Memory system	Huawei OceanStor 6800 (total capacity 1 PB)
Network equipment	Cisco Catalyst 9400

The software environment for running the research method program is shown in Table 2.

Based on the above experimental software and hardware environment, run the wavelet transform, matched filter transform, SVM, and ant colony algorithm applied in this paper. The algorithm settings are shown in Table 3.

Table 2: Experimental software environment settings

Software Environment	Allocation
Monitor system	Ubuntu 20.04 LTS (Linux kernel 5.15)
Programming language	Python 3.8
Simulation platform	MATLAB 2023a
Machine learning framework	SciPy 1.10.1
Signal processing tools	PyTorch 1.12.1

Table 3: Algorithm parameter settings

Method	Parameter Item	Set Value
Wavelet Transform	Basis Function	Daubechies 4
	Decomposition Layers	6 layers
Support Vector Machine	Kernel Function	Radial Basis Function (RBF)
	Grid Search Validation Step	0.01
Matched Filtering	Typical Interference Pulse Width	50 ns
	Rising Edge	20 ns
	Threshold Setting	$3 \times \sigma$ (noise standard deviation)
Ant Colony Algorithm (ACO)	Ant Count	50
	Pheromone Factor (α)	1
	Heuristic Factor (β)	2
	Pheromone Volatilization Rate (ρ)	0.1
	Number of Iterations	200

Under the same environmental and data conditions mentioned above, the methods of adaptive beamforming technology [2] and wavelet threshold denoising and magnetic interference compensation model [3] will be used as comparison methods to conduct comparative tests with the method proposed in this paper.

B. Analysis of experimental results

B.1. Optimization results of power inspection UAV signal waveform

This paper uses wavelet decomposition transform to reconstruct and optimize the waveform of the power inspection drone signal before interference suppression, in order to improve signal quality. The waveform optimization results of the power inspection drone signal obtained by this method are shown in Fig. 2.

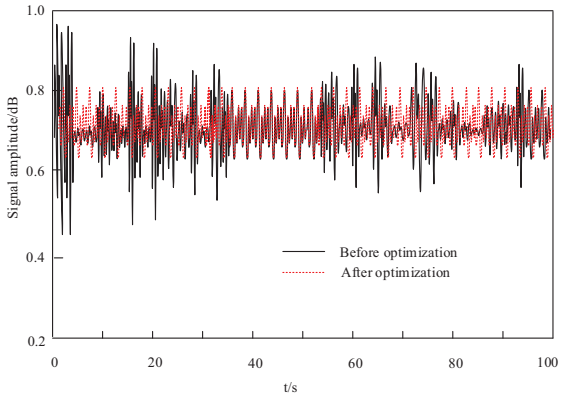


Fig. 2. Optimization results of signal waveform for unmanned aerial vehicle for power inspection.

From the experimental results in Fig. 2, it can be seen that the optimized signal waveform exhibits significant optimization effects compared to the original signal. The high-frequency noise and interference components have been effectively decomposed, resulting in smoother and more stable signal waveforms. At the same time, the amplitude and phase information of the drone signal were accurately preserved without any significant distortion or distortion.

B.2. Extraction results of interference transient time-frequency domain features

Based on the transient radiation total field strength of the drone signal array, the discrete Fourier transform is used to extract the transient frequency domain features of the optimized power inspection drone signal at different frequencies. The extraction results are shown in Fig. 3.

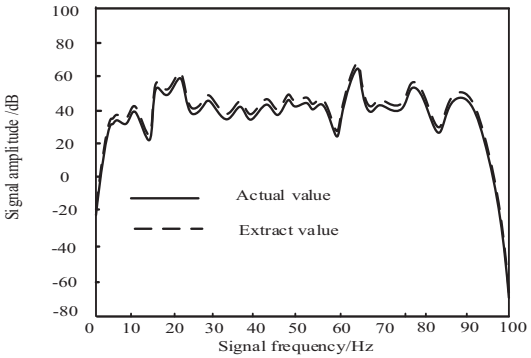


Fig. 3. Extraction results of time-frequency domain features of interference transient.

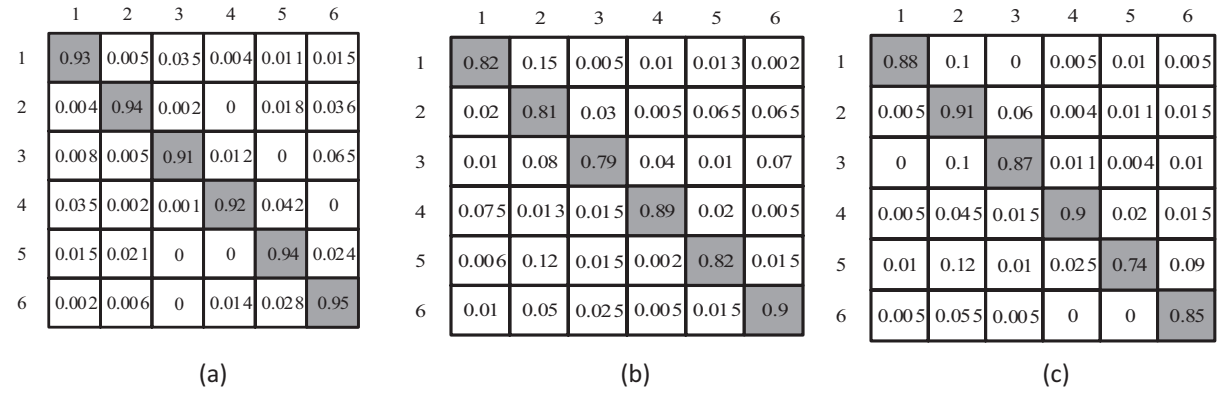


Fig. 4. Comparison of the accuracy of high-density integrated electromagnetic interference detection: (a) approach of the present study, (b) methodology of adaptive beamforming technology, and (c) methodology of wavelet threshold denoising and magnetic interference compensation model.

Table 4: Comparison of electromagnetic interference detection performance of different methods

Method	Average Accuracy (%)	Average Recall Rate (%)	Average F1 Score	Average Detection Time (ms)
Proposed Adaptive beamforming technology	96.4	95.7	96.0	12.3
Wavelet threshold denoising and magnetic	82.1	79.3	80.7	18.7
interference compensation model	85.6	83.2	84.4	15.9

As shown in Fig. 3, the method proposed in this paper extracts the frequency domain amplitude characteristic peak values of electromagnetic interference signals from UAV signal arrays through discrete Fourier transform, which are basically consistent with the actual interference peak values, with an error of less than 5 dB, meeting the requirements of signal feature extraction. Based on the frequency domain amplitude characteristic peak, interference signals can be effectively detected.

B.3. High density integrated electromagnetic interference detection effect

This method is based on the time-frequency domain characteristics of interference transients, and runs a SVM algorithm with set parameters to detect high-density integrated electromagnetic interference from power inspection drones in drone communication signals. Compare the accuracy of three methods for detecting six types of electromagnetic interference: sweep frequency interference, noise frequency modulation interference, narrowband aiming interference, comb shaped multi tone interference, frequency band noise interference, and pulse noise interference. Use a confusion matrix to characterize the detection results, as shown in Fig. 4.

From Fig. 4, it can be seen that the proposed method has a much higher accuracy rate in detecting high-density integrated electromagnetic interference than the other two methods, indicating that the proposed method can more accurately classify different types of electromagnetic interference signals into corresponding categories, reducing false positives and false negatives, and has advantages in detection accuracy.

In order to further quantify the detection performance, this paper calculates the average accuracy, recall, and F1 scores of each method on the test set, as well as the average time-consuming of a single detection (ms). The results are shown in Table 4. It can be seen from Table 4 that the accuracy rate, recall rate, and F1 score of this method are significantly better than those in adaptive beamforming technology and wavelet threshold denoising and magnetic interference compensation model, which are at least 10.8, 12.4, and 11.6 percentage points higher. This shows that the proposed method has lower risk of false detection and missed detection in interference detection.

In terms of computational efficiency, due to the CNN-SVM structure, the convolution layer and pooling layer can extract features in parallel, and the average time-consuming of a single detection is only 12.3 ms, 34% less than the method in adaptive beamforming technology and 23% less than the method in wavelet threshold denoising and magnetic interference compensation model, which can meet the requirements of UAV real-time processing. It is worth discussing that the method in adaptive beamforming technology relies on traditional SVM to directly input the original features,

which has a weak ability to distinguish complex interference patterns, resulting in a low recall rate. Although the method in wavelet threshold denoising and magnetic interference compensation model uses the depth network, it is not optimized for the time-frequency domain features, and the features are easy to be confused under low SNR, so the accuracy rate is lower than that of this method. In this paper, the weak transient characteristics are enhanced by matched filter transform and, combined with CNN-SVM structure, the high-precision and high-efficiency interference detection is realized.

B.4. Suppression effect of high-density integrated electromagnetic interference for power inspection UAVs

The electromagnetic interference suppression method proposed in this paper is applied to suppress the high-density integrated electromagnetic radiation interference of power inspection drones. The amplitude spectrum of electromagnetic interference before and after suppression is shown in Fig. 5.

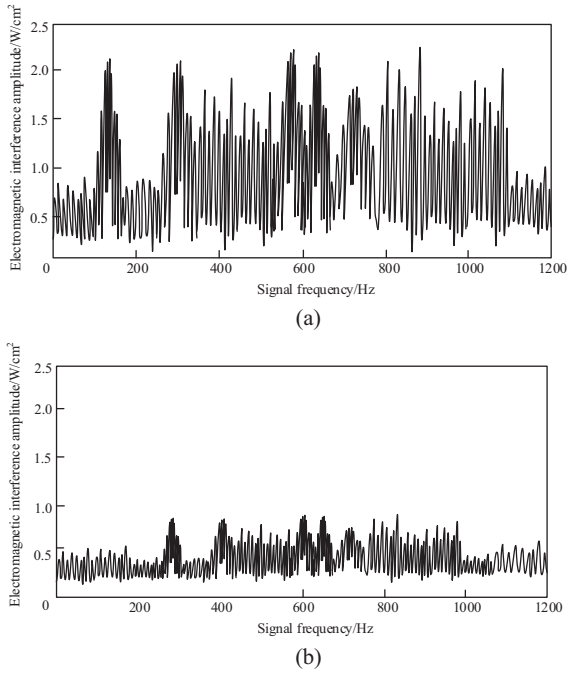


Fig. 5. Electromagnetic interference amplitude (a) before and (b) after suppression.

From Fig. 5 it can be seen that, before electromagnetic interference suppression, the electromagnetic amplitude of the drone signal can reach over 2.0 W/cm^2. After applying the method described in this paper for suppression, the electromagnetic interference intensity was significantly reduced, and the electromagnetic amplitude change tended to stabilize, controlled at a level below 1 W/cm^2. This result indicates that the suppression method proposed in this paper has significant effectiveness in practical applications.

In order to quantitatively demonstrate the suppression effect of the method proposed in this paper, SNR was selected as the evaluation index. The larger the SNR, the better the electromagnetic interference suppression effect, making the communication signal of the drone clearer. The signal-to-noise of high-density integrated electromagnetic interference suppression for power inspection drones using three comparative methods is shown in Fig. 6.

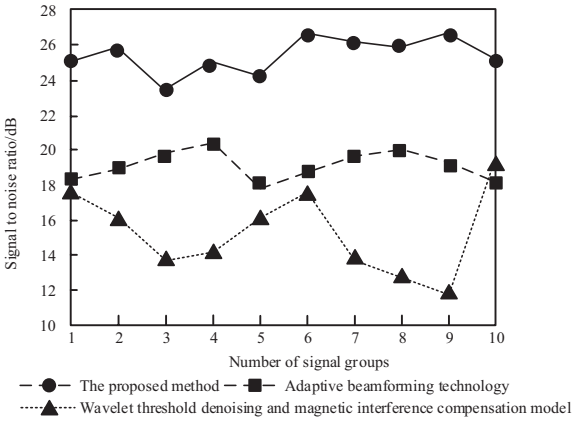


Fig. 6. Signal-to-noise ratio for electromagnetic interference suppression.

From Fig. 6 it can be seen that, as the number of signal groups increases, the SNR of our method fluctuates but, overall, it remains above 22 dB and consistently higher than the other two methods, proof that the proposed method has the best electromagnetic interference suppression effect, which can better preserve useful signals while suppressing electromagnetic interference, thereby improving signal quality.

In order to further verify the robustness of this method under different interference intensities, the electromagnetic interference suppression performance of this method, adaptive beamforming technology method, and wavelet threshold denoising and magnetic interference compensation model method are compared in four scenarios with SNRs of 5 dB, 10 dB, 15 dB, and 20 dB. At the same time, in order to investigate the comprehensive suppression ability of the method under the condition of superposition of multiple types of interference, two groups of composite interference scenarios, i.e., frequency sweep interference and narrowband aiming interference, impulse noise interference and frequency band noise interference, were set for testing. The SNR results of each method after suppression in different scenes are shown in Table 5. It can be seen

Table 5: Comparison of signal-to-noise ratio after suppression by various methods in different scenarios

Scenario/Method	Proposed Method	Adaptive Beamforming Technology	Wavelet Threshold Denoising and Magnetic Interference Compensation Model
SNR = 5 dB	18.6	12.3	14.1
SNR = 10 dB	21.4	15.8	17.2
SNR = 15 dB	24.7	19.5	20.8
SNR = 20 dB	27.3	22.1	23.6
frequency+narrowb and composite interference	19.2	13.5	15.8
Pulse+band composite interference	17.8	11.7	13.9

from Table 5 that under the four single interference intensity scenarios, the SNR after suppression of this method is significantly better than that of adaptive beamforming technology and wavelet threshold denoising and magnetic interference compensation model, especially under the condition of strong interference with low SNR (5 dB). The SNR of this method is 6.3 dB higher than that of adaptive beamforming technology and 4.5 dB higher than that of wavelet threshold denoising and magnetic interference compensation model, reflecting the stronger anti-interference ability of this method in the strong interference environment.

In the complex interference scenario, the proposed method also maintains the highest SNR after suppression, which shows that the filter parameters optimized by an ant colony algorithm can adaptively cope with the complex situation of multi type interference superposition and has good robustness. The method in Cheng et al. [2] relies on adaptive beamforming, which reduces the accuracy of beam pointing control when multiple interference sources exist at the same time, resulting in the deterioration of the suppression effect. The wavelet threshold de-noising method in Yang and Li [3] has the problem of confusion between high-frequency useful signals and interference components in the face of composite interference, and the improvement of SNR after suppression is limited. To sum up, this method shows the optimal suppression performance and the strongest robustness under the conditions of different interference intensity and multiple types of interference superposition, and can effectively ensure the communication reliability of Power Patrol UAV in complex electromagnetic environment.

IV. CONCLUSION

The paper studies the high-density integrated electromagnetic interference suppression method for power inspection unmanned aerial vehicles based on an ant colony algorithm. Using wavelet decomposition transform to optimize the signal waveform of power inspection unmanned aerial vehicles, combined with discrete Fourier transform processing and matched filtering transform, extracting the time-frequency domain characteristics of interference transients, and using an ant colony algorithm to achieve high-density integrated electromagnetic interference suppression of power inspection unmanned aerial vehicles. The test results show that the frequency domain amplitude characteristic peak of the electromagnetic interference signal extracted by this method has a low error compared to the actual interference peak, effectively reducing the intensity of electromagnetic interference and improving the signal-to-noise ratio and quality of the signal.

REFERENCES

[1] J. H. Kim, G. J. Kim, and Y. M. S. Ju, "A review of the effectiveness of shielding curtains for improving radiation safety management of electromagnetic radiation in diagnostic X-ray rooms," *J. Magn.*, vol. 28, no. 4, pp. 438–442, 2023.

[2] J. M. Cheng, Y. Li, and G. F. Zhu, "High density integrated electromagnetic interference suppression technology for unmanned aerial vehicle remote communication," *Mod. Electr. Tech.*, vol. 47, no. 12, pp. 96–100, 2024.

[3] J. Yang and B. Li, "Anti-electromagnetic interference design of unmanned aerial vehicle automatic inspection system in substation," *Mach. Des. Manuf. Eng.*, vol. 53, no. 3, pp. 83–86, 2024.

[4] N. Li, K. Cao, B. Li, J. Yang, and X. Zhang, "Research on anti-electromagnetic interference technology of transmission line inspection based on multi-rotor UAV," *Manuf. Autom.*, vol. 45, no. 10, pp. 29–33, 2023.

[5] Q. Meng, B. Zhang, W. L. Yao, H. Yin, Y. Zhou, and X. K. Ge, "A study on adaptive variable polarization anti-jamming antenna of UAV," *Mod. Radar*, vol. 46, no. 6, pp. 61–66, 2024.

[6] H. Akbari, S. Taeb, and A. A. H. Adibzadeh, "Nonionizing electromagnetic irradiations; biological interactions, human safety," *Shiraz Univ. Med. Sci.*, vol. 13, no. 4, pp. 299–308, 2023.

[7] R. Ramirez-Vazquez, I. Escobar, and V. E. Arribas, "Personal exposure to radiofrequency electromagnetic fields: A comparative analysis of international, national, and regional guidelines," *Env. Res. Section A*, vol. 246, no. 4, pp. 11812401–11812411, 2024.

[8] C. Osman, K. Baha, and Y. S. Cagri, "Assessment of occupational exposure levels of cleaning product manufacturing factory workers to electromagnetic fields," *Radiat. Prot. Dosimetry*, vol. 198, no. 4, pp. 197–207, 2022.

[9] E. V. Styazhkina, Y. R. Akhmadullina, Y. V. Gainetdinova, E. A. Payalova, and E. A. Pryakhin, "Mutagenic effect during combined exposure to ionizing and non-ionizing electromagnetic radiation," *Bull. Exp. Biol. Med.*, vol. 176, no. 5, pp. 645–648, 2024.

[10] I. Ruiz, G. Vizkelethy, A. E. E. Mcdonald, S. W. Howell, P. M. Thelen, M. D. Goldflam, and T. E. Beechem, "Detection of high energy ionizing radiation using deeply depleted grapheme-oxide-semiconductor junctions," *J. Appl. Phys.*, vol. 132, no. 18, pp. 1845031–1845038, 2022.

[11] M. Vaughan, W. Michailow, M. Tan, M. Salih, L. Li, H. Beere, D. A. Ritchie, E. H. Linfield, A. G. Davies, and J. E. Cunningham, "Enhanced delivery and detection of terahertz frequency radiation from a quantum cascade laser within dilution refrigerator," *J. Low Temp. Phys.*, vol. 213, no. 5/6, pp. 306–316, 2023.

[12] G. Xiao, R. Gu, N. Sun, and Y. Zhang, "Research on feature matching optimization algorithm for automotive panoramic surround view system," *Comput. Syst. Sci. Eng.*, vol. 48, no. 5, pp. 1329–1348, 2024.

[13] T. Joseph, T. Fischer, and M. Milford, "Matched filtering-based LiDAR place recognition for urban and natural environments," *IEEE Robot. Autom. Lett.*, vol. 10, no. 3, pp. 2566–2573, 2025.

[14] S. Uechi and K. Shiba, "Effects of electromagnetic fields generated from transcutaneous transformer: Analysis of internal electric field when the number of transmitting and receiving coil layers is changed," *J. Japan Soc. Appl. Electr. Mech.*, vol. 30, no. 2, pp. 222–229, 2022.

[15] I. Collado, A. Vazquez-Lopez, S. Heredia, J. Vega, A. Jiménez-Suárez, D. Maestre, and S. G. Prolongo, "Electromagnetic interference shielding of a sequential dual-curing thiol-epoxy system reinforced with GNPs with high shape memory," *ACS Appl. Mater. Interf.*, vol. 17, no. 12, pp. 18954–18970, 2025.

[16] M. M. Vijay, S. G. Kumar, R. S. Subramanian, M. Karthikeyan, G. Krishnaraj, and N. Manikanda Prabu, "Light spectrum optimization based Adaboost SVM for the secured communication in vehicular Ad Hoc network," *AIP Conf. Proc.*, vol. 3204, no. 1, p. 020019, 2025.

[17] S. Bayrak, "Unveiling intrusions: Explainable SVM approaches for addressing encrypted Wi-Fi traffic in UAV networks," *Knowl. Inform. Syst.*, vol. 66, no. 11, pp. 6675–6695, 2024.

[18] U. K. Lilhore, S. Dalal, and S. Simaiya, "A cognitive security framework for detecting intrusions in IoT and 5G utilizing deep learning," *Comput. Secur.*, vol. 136, pp. 10356001–10356022, 2024.

[19] B. Panda and P. Singh, "A deep convolutional-GRU-SVM-based hybrid approach for signal detection of uplink NOMA system," *Wirel. Pers. Commun.*, vol. 138, no. 2, pp. 861–878, 2024.

[20] C. Guo, L. You, X. Li, G. Hu, S. Wang, and C. Cao, "A novel biometric authentication scheme with privacy protection based on SVM and ZKP," *Comput. Secur.*, vol. 144, pp. 10399501–10399512, 2024.

[21] M. J. Alam, R. Chugh, S. Azad, and R. Hossain, "Ant colony optimization-based solution to optimize load balancing and throughput for 5G and beyond heterogeneous networks," *J. Wirel. Commun. Network.*, vol. 2024, no. 1, p. 44, 2024.

[22] X. Jia, C. Tang, and X. L. J. Zhang, "Research on dual robot collaboration method based on improved double ant colony algorithm," *Ind. Robot*, vol. 51, no. 3, pp. 424–435, 2024.

[23] Y. Huang, J. Zhao, and J. G. Chen, "Anti-interference method of electronic communication signal in complex electromagnetic environment," *Comput. Simul.*, vol. 40, no. 8, pp. 159–163, 2023.



Jian Chen, male, born August 1986, of Han ethnicity, Qingyuan, Guangdong, China. He graduated with a bachelor's degree in Automation from Guangdong University of Technology in 2009 and earned a master's degree in Electrical Engineering from South China University of Technology in 2015. His research focuses on power communication and network security. From 2009 to present, he has served as a senior engineer at Zhuhai Power Supply Bureau, Guangdong Power Grid Co. Ltd.



Yuxuan Huang, born February 1996, male, native of Zhuhai, Guangdong, China, Han ethnicity, graduated with a bachelor's degree in Electronic Information Science and Technology from Guangdong University of Technology in 2018. His research focus is electronic communication. From 2018 to present, he has served as an

engineer at Zhuhai Power Supply Bureau, Guangdong Power Grid Co. Ltd.



Ziheng Wan, born May 1999, male, from Foshan, Guangdong, China, Han ethnicity. He graduated with a bachelor's degree in Automation from Guangdong University of Technology, in 2022. His research focuses on power emergency response and satellite communication systems. From 2022 to present, he has worked as an engineer at the Zhuhai Power Supply Bureau of Guangdong Power Grid Co. Ltd.

A Hybrid Triangle–Voxel Model with Local Voxelization for Resolving Diffraction Edge Deficiency in Ray Tracing

Baolai Zhang[1], Dan Shi[1,*], Jinyu Song[1], Xiaoyong Liu[1], Hongbo Tao[2,*], Huichun Yang[3], Zhonghua Xin[4], and Yuhao Jia[4]

[1]School of Electronic Engineering Beijing University of Posts and Telecommunications, Beijing 100876, China
2024140409@bupt.edu.cn, shidan@bupt.edu.cn, 438182694@qq.com, liuxiaoyong@srtc.org.cn

[2]State Radio Monitoring Center Testing Center, Beijing 102609, China
taohongbo@srtc.org.cn

[3]School of Automation Beijing Information Science and Technology University, Beijing 100192, China
52009222@qq.com

[4]China Coal Research Institute, Beijing 101320, China
en55015@hotmail.com, jiayuhaobuaa@163.com

*Corresponding Authors

Abstract – Accurate diffraction modeling is essential for ray-tracing-based wireless propagation prediction. The geometric representation of objects in the simulation scene greatly affects diffraction prediction accuracy. Conventional triangular meshes lack the explicit edge information required for diffraction modeling, while global voxelization introduces geometric distortion and substantial computational overhead. This paper presents a hybrid triangle–voxel model that performs local voxelization only within potential diffraction regions (PDR) determined by the first Fresnel zone. The proposed method reconstructs diffraction paths that cannot be captured by pure triangular meshes while preserving triangular facets for direct and reflected rays. Compared with a commercial ray-tracing tool, it achieves an average ray–surface intersection error of 246.4 mm and average path loss, delay, and phase errors of 0.35 dB, 0.12 ns, and 42.0°, respectively. It also reduces the voxel count and computation time by 60% and 25%. The results show that the proposed model balances diffraction-path recoverability, geometric fidelity, and computational efficiency.

Index Terms – Diffraction modeling, hybrid triangle–voxel model, potential diffraction region, ray tracing.

I. INTRODUCTION

As wireless communication systems evolve and the need for reliable radio coverage in complex environments increases [1], accurate modeling of radio frequency propagation has become increasingly important. Diffraction plays a crucial role in non-line-of-sight (NLOS) scenarios, imposing stringent requirements on the physical accuracy and environmental adaptability of wireless propagation models [2, 3].

Among various propagation modeling methods, ray tracing has long been a core technology of wireless propagation prediction [4–6]. Its theoretical foundations are rooted in geometric optics (GO), geometric diffraction theory (GTD), and uniform diffraction theory (UTD) [7–9]. Ray tracing approximates the propagation of electromagnetic waves from the transmitter to the receiver as optical rays characterizing multipath components.

Diffraction is essential for accurately characterizing the field strength in NLOS regions [10]. However, the prediction accuracy of UTD-based diffraction strongly depends on well-defined edges in the geometric model [11–13]. Triangular mesh models are widely used to represent complex surfaces due to their geometric fidelity and storage efficiency. Nevertheless, such smooth triangular surfaces cannot naturally provide the sharp edge structures required for UTD-based diffraction modeling [14]. Degli-Esposti et al. [15] proposed several acceleration techniques for ray-tracing field prediction models, including Fresnel-zone-based spatial filtering that limits intersection calculations to geometrically relevant regions. Fresnel-zone concepts have also been used in UTD-based propagation models to improve the efficiency and accuracy of multiple-diffraction prediction [16]. While such approaches effectively reduce the number of candidate facets involved

Submitted On: March 29, 2026
Accepted On: July 21, 2026

1054-4887 © ACES

https://doi.org/10.13052/2026.ACES.J.410708

in ray tracing, they primarily aim at improving computational efficiency on existing geometric models and do not address a fundamental limitation of triangular meshes in diffraction modeling: smooth triangular surfaces reconstructed from real scenes usually lack the explicit sharp edges required by UTD diffraction formulations. Sun et al. [17] proposed a triangular mesh-based edge extraction method using local normal variations and geodesic neighborhoods to segment and preserve sharp features. Bærentzen [18] explored mesh optimization strategies to preserve sharp features. However, these methods are computationally expensive and impractical when dealing with dense, large-scale, or highly irregular realistic models.

In contrast, voxel-based models are well-suited for diffraction modeling using UTD or similar theories because their inherent mesh structure naturally introduces discrete edge and angular features [19]. Amanatides and Woo [20] proposed a fast voxel traversal algorithm that significantly reduces the cost of ray-voxel cross-testing. Díez et al. [21] optimized the surface voxelization of triangular meshes by detecting gaps and enforcing isometric scan lines, thereby achieving higher fidelity voxel surfaces. Despite these advancements, global voxelization of an entire environment still introduces substantial geometric distortion and incurs sharp increases in memory usage and runtime, which limits its applicability to high-precision wireless propagation modeling.

In this paper, a new hybrid triangle-voxel model is proposed that enables efficient diffraction path calculations in ray tracing while maintaining high geometric accuracy. Based on the first Fresnel region, potential diffraction region (PDR) between the transmitter and receiver are identified, and voxelization is performed only within these localized regions. In this way, the proposed representation preserves the surface fidelity required for direct and reflected paths and, at the same time, introduces localized discrete geometric features that are beneficial for diffraction path search. The proposed method yields results highly consistent with those of Wireless InSite (WI) in identifying valid diffraction paths, while reducing the voxelization count by approximately 60% and computation time by approximately 25% compared with global voxelization.

II. HYBRID TRIANGLE-VOXEL MODELING METHODOLOGY

A. Triangular mesh model reconstruction

The propagation scenario considered in this study involves a sculpture model surrounded by four transmitters and four receivers. To accurately model the realistic propagation environment, a multi-view 3D reconstruction approach was employed. Specifically, as shown in Fig. 1 (a), multi-view photographs of the sculpture reconstructed using Structure-from-Motion (SfM) and Multi-View Stereo (MVS) techniques in COLMAP, resulting in the point cloud model presented in Fig. 1 (b) [22, 23]. Subsequently, Poisson surface reconstruction was used to convert the point clouds into a digital model suitable for ray tracing simulation. The resulting digital model is composed of a large number of triangular surfaces. Figure 1 (c) shows the triangular model of the sculpture.

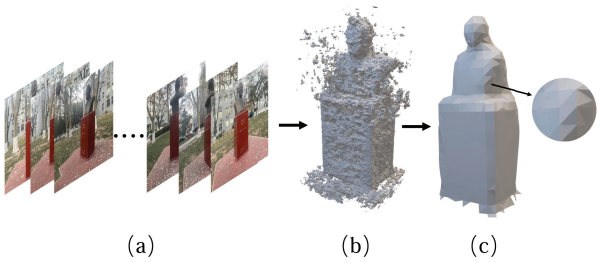


Fig. 1. Generation of sculpture triangle mesh model. (a) Dataset. (b) Point cloud model. (c) Triangle mesh model.

As the geometric basis of ray tracing simulation, the reconstructed triangular mesh model not only represents the environment geometry with high accuracy, but also offers efficient storage, making it suited for modeling direct and reflected propagation. However, due to the absence of well-defined diffraction edges, conventional triangular meshes cannot accurately characterize diffraction mechanism in ray tracing.

B. Fresnel-guided potential diffraction region selection

In order to accurately describe the diffraction mechanism in ray tracing, it is necessary to identify the regions where diffraction may occur. According to the UTD, diffraction can occur only along shape edges or wedge structures in the propagation environment [24]. However, in the triangular mesh model reconstructed from the real scene, the surfaces are geometrically continuous and lack explicit edges that serve as diffraction boundaries. This makes it difficult for traditional ray tracing algorithm to detect and trace diffraction paths.

To overcome this limitation, a hybrid triangle-voxel model is proposed, which performs local voxelization only in regions where diffraction may occur. These regions, referred to as PDR, are determined based on the first Fresnel region between each transmitter (TX) and receiver (RX) pair [25]. For each triangular surface of the sculpture model, its centroid is denoted as P_i, and the distances from P_i to the TX and RX are defined

as follows:

- $d_1 = |P_i - TX|$: the distance from P_i to the transmitter.
- $d_2 = |P_i - RX|$: the distance from P_i to the receiver.

The radius R of the first Fresnel zone at point P_i is given by:

$$R = \sqrt{\frac{\lambda d_1 d_2}{d_1 + d_2}}, \tag{1}$$

where λ is the wavelength. To provide a flexible PDR selection criterion, a Fresnel-zone threshold factor α is introduced. If the shortest distance from the centroid P_i to the line connecting the transmitter and receiver is less than or equal to αR, the triangular facet is classified as part of the PDR:

$$d(P_i, \overline{TXRX}) \leq \alpha R, \tag{2}$$

where $d(P_i, \overline{TXRX})$ denotes the shortest distance from P_i to the TX–RX connecting line, and α controls the size of the selected PDR. When α is smaller than 1, the PDR becomes more compact, which reduces the number of facets to be voxelized but may miss potential diffraction regions near the Fresnel-zone boundary. When α is larger than 1, more surrounding facets are included, which improves the robustness of diffraction-edge recovery but increases the voxelization cost. Unless otherwise specified, $\alpha = 1$ is used in this work, corresponding to the standard first Fresnel-zone selection. Figure 2 illustrates the potential diffraction zones detected in the statue scene with four transceivers when $\alpha = 1$, and displays the Fresnel zone ellipsoids for each TX-RX pair represented as ellipses in both horizontal and vertical directions. This criterion ensures that diffraction calculations are restricted to the geometrically effective area, thereby avoiding unnecessary global voxelization and reducing computational overhead.

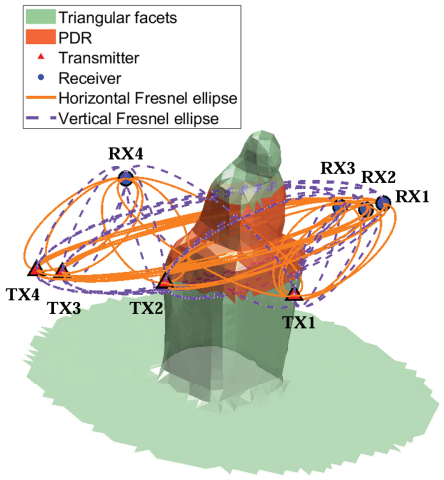


Fig. 2. Sculpture model with highlighted PDR regions.

C. Local voxelization in PDR

After identifying the PDR, a local voxelization algorithm is applied to convert the corresponding triangular facets into voxel representations. The voxel size is denoted by Δ. A smaller Δ provides finer geometric resolution and more accurate local diffraction edges, but it also increases the number of voxels and the computational cost. In contrast, a larger Δ reduces the voxel count but may introduce stronger staircase distortion and inaccurate edge positions. Therefore, the voxel size should be selected according to the wavelength and the required geometric accuracy. In this work, Δ is chosen to be approximately one-third of the wavelength, which provides a balance between diffraction-edge representation and computational efficiency.

For all vertices of the triangular facets within the PDR, an axis-aligned bounding box (AABB) is first calculated. To avoid boundary truncation during voxelization, the PDR bounding box is further expanded by n_m voxel layers, where n_m denotes the PDR margin layer number. The physical margin can be expressed as

$$m = n_m \Delta, \tag{3}$$

where Δ is the voxel size. A small margin may truncate potential diffraction edges near the PDR boundary, while an excessively large margin increases the local voxelization region and weakens the computational advantage of the proposed method. Therefore, a limited number of margin layers is used to ensure stable edge extraction without significantly increasing the voxel count.

The expanded bounding box is then divided into uniform voxel grids. For each triangular facet in the PDR, a local AABB is further calculated to restrict the range of candidate voxels. Each voxel in this subset is tested using its center point: if the center is within the bounding box of the triangle, the voxel is selected as part of the voxelized representation of the PDR. By traversing all candidate voxels, local voxelization of the PDR is completed, as illustrated in Fig. 3, resulting in a hybrid triangle–voxel representation [26].

These voxels provide well-defined edges and corners, which serve as the geometric singularities required for formulating diffraction in ray tracing. At the same time, voxelization is applied only to localized regions rather than the entire scene, and the remainder of the environment continues to be represented by triangular meshes. This hybrid representation preserves the geometric fidelity required for accurate direct and reflected ray interactions, while avoiding the substantial computational and memory overhead associated with globally voxelizing the entire model.

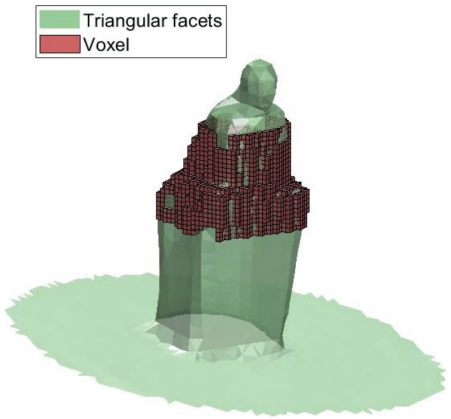


Fig. 3. A hybrid triangle-voxel model.

D. Diffraction treatment on voxel edges within the UTD framework

In the proposed hybrid triangle-voxel model, diffraction is calculated based on the UTD. After local voxelization is performed within the PDR, the intersection lines between adjacent voxel faces are extracted as candidate diffraction edges. Each voxel edge is regarded as an equivalent local wedge edge. For each TX-RX pair, only the voxel edges satisfying the visibility conditions from the transmitter to the edge and from the edge to the receiver are retained for diffraction calculation.

Let $\mathbf{r}_{\mathrm{T}}$, $\mathbf{r}_{\mathrm{R}}$, and $\mathbf{r}_{\mathrm{D}}$ denote the positions of the transmitter, receiver, and diffraction point on a valid voxel edge, respectively. The distances from the transmitter to the diffraction point and from the diffraction point to the receiver are expressed as:

$$s_1 = \|\mathbf{r}_{\mathrm{D}} - \mathbf{r}_{\mathrm{T}}\|, \tag{4}$$

$$s_2 = \|\mathbf{r}_{\mathrm{R}} - \mathbf{r}_{\mathrm{D}}\|. \tag{5}$$

The diffracted electric field at the receiver can be generally written as:

$$\mathbf{E}_d = \mathbf{E}_i(\mathbf{r}_{\mathrm{D}}) D_{\mathrm{UTD}} A(s_1, s_2) \exp[-jk(s_1 + s_2)], \tag{6}$$

where $\mathbf{E}_i(\mathbf{r}_{\mathrm{D}})$ is the incident electric field at the diffraction point, D_{UTD} is the UTD diffraction coefficient determined by the local wedge geometry, $A(s_1, s_2)$ is the spreading factor, and $k = 2\pi/\lambda$ is the wavenumber.

Therefore, the voxel edges introduced in the PDR provide the geometric singularities required for UTD-based diffraction modeling. The remaining triangular facets outside the PDR are still used for direct and reflected rays. In this way, the proposed model enables diffraction-path calculation while avoiding the geometric distortion and computational overhead caused by global voxelization.

III. SIMULATION AND ANALYSIS

A. Ray-tracing results with the proposed model

In this section, the pure triangular mesh model, the global voxelization model, and the proposed hybrid triangle-voxel model are applied and evaluated on our UTD-Based Ray-Tracing Solver (URTS). Meanwhile, the proposed hybrid model is also implemented on the commercial Wireless InSite platform to further validate its accuracy. The evaluation scenario includes a 3.28-meter-high sculpture placed on a ground plane, with a modeled ground region of 1.5 m in radius, which is mainly composed of three materials: concrete, marble, and gypsum, each modeled with different thicknesses. There are four transmitters and four receivers around the sculpture. As shown in Table 1, the number of PDR facets decreases as the frequency increases because of the reduced Fresnel-zone size, whereas the number of voxels increases significantly when the voxel size is scaled with the wavelength. Considering PDR visibility, diffraction edge resolution, and voxelization cost, the carrier frequency is set to 1 GHz, corresponding to a wavelength of approximately 0.3 m. The voxel size is selected as 0.1 m, which is approximately one-third of the wavelength.

Table 1: Voxelization characteristics under different frequencies

Freq.	λ (m)	Voxel Size (m)	PDR Facets	Voxels
0.8 GHz	0.375	0.125	638	186
1.0 GHz	0.300	0.100	568	360
1.5 GHz	0.200	0.0667	448	882
2.4 GHz	0.125	0.0417	332	2533

Figure 4 (a) shows the ray tracing results using the pure triangular mesh representation, where only six direct paths and seven reflected paths are observed. This is because, in the UTD method, diffraction can only occur at explicitly defined geometric edges, which are used to locate diffraction points, compute diffraction coefficients, and characterize the diffracted rays. However, the pure triangular mesh approximates the sculpture with smooth, continuously connected surfaces, making it impossible to locate valid diffraction edges and therefore yielding no diffraction paths. Figure 4 (b) shows the results obtained with full voxelization. Because each voxel provides well-defined boundaries and sharp edges, three diffraction paths are successfully detected. However, full voxelization produces faceted, staircase surfaces, which generate additional non-physical reflection paths due to the discretized geometry. Figure 4 (c) illustrates the results of the proposed local voxelization scheme, which preserves

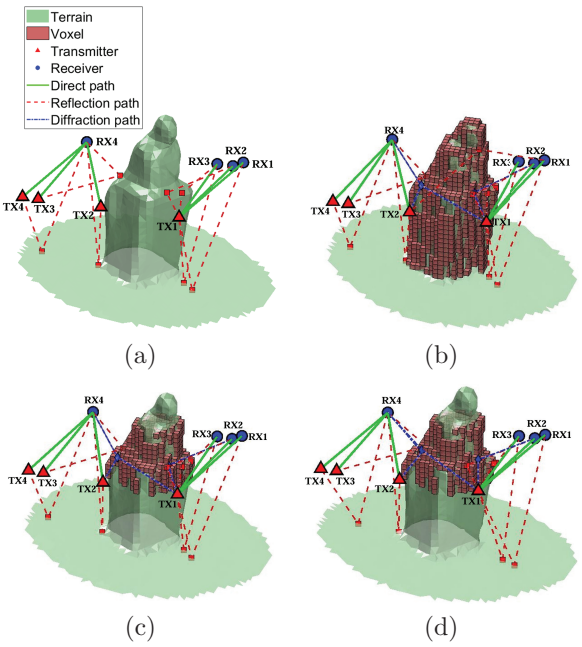


Fig. 4. Comparison of URTS and WI ray tracing results under different geometric modeling schemes. (a) URTS simulation using a pure triangular mesh model. (b) URTS simulation using global voxelization model. (c) URTS simulation using a hybrid triangle-voxel model. (d) WI simulation using a hybrid triangle-voxel model.

the geometric continuity of most surfaces while still providing discrete edges in the diffractive regions. Consequently, the physically valid diffraction paths are retained, and the spurious reflections introduced by full voxelization are effectively eliminated. Finally, Fig. 4 (d) presents the results obtained using the WI platform under the same local voxelization configuration, which closely match the URTS results in both path count and spatial distribution, demonstrating that the proposed hybrid modeling approach is applicable to different ray-tracing platforms and yields consistent propagation behavior across them.

B. Model accuracy analysis

The geometric distortion of the model surface directly affects the accuracy of ray–surface intersection prediction, which is critical for reliable ray tracing computation. To quantitatively assess the geometric fidelity of the proposed hybrid triangle-voxel representation, the root mean square surface distance (RMSD) between the voxelized model and the original triangular mesh is evaluated using the pure triangular surface model as the reference. The RMSD is defined as:

$$RMSD = \sqrt{\frac{1}{N}\sum_{i=1}^{N} d_i^2}, \tag{7}$$

where N denotes the number of sampling points uniformly distributed on the surface of the original triangular mesh, and d_i represents the shortest distance from sampling point P_i to the surface of the voxelized model. A total of 10,000 sampling points are uniformly distributed over the mesh surface. For each sampling point P_i, the shortest distance d_i to the voxelized surface is computed. The mean squared distance (MSD) is then obtained by averaging all d_i^2 values, and its square root yields the root mean square deviation (RMSD), which quantifies the global surface deviation. A smaller RMSD indicates a closer match to the reference geometry and thus less geometric distortion.

Figure 5 shows a quantitative comparison of the mean distance, median distance, and RMSD between the global voxelized and the proposed hybrid triangle–voxel models. All evaluated error metrics of the hybrid model are lower than those of the global voxel model. In particular, the RMSD is reduced by approximately 7% compared to the global voxelization, indicating that local voxelization more accurately preserves the original surface geometry. The hybrid model effectively reduces local surface distortion, which in turn improves the accuracy of ray–surface intersection prediction in ray-tracing propagation simulations.

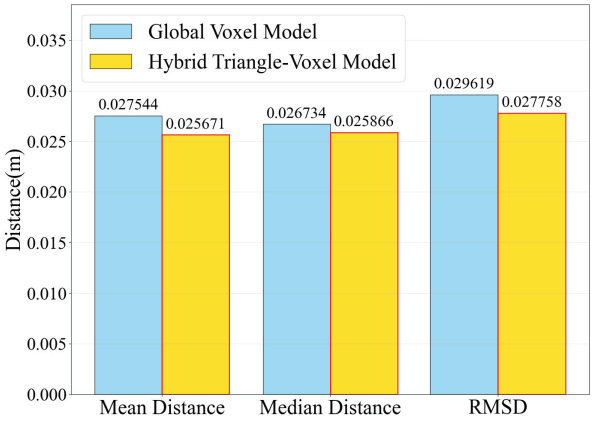


Fig. 5. Quantitative comparison of the mean distance, median distance, and RMSD between the global voxelization model and the hybrid triangle–voxel model.

In addition to geometric fidelity, the accuracy of the diffraction path generated by the application of the hybrid model is verified by comparing and analyzing the spatial deviation of ray-surface intersection points along the propagation paths obtained from URTS and WI. For each pair of corresponding intersection points along a propagation path, the 3D Euclidean distance e_i is calculated. These pointwise errors are then averaged to obtain the path-level mean error $\bar{e}_{path}$, expressed as:

$$\bar{e}_{path} = \frac{1}{N_p}\sum_{i=1}^{N_p} e_i, \tag{8}$$

where N_p is the number of intersections on the path. The overall average error is obtained by further averaging the path-level mean errors of all reflection and diffraction paths:

$$\bar{e}_{overall} = \frac{1}{N_{paths}} \sum_{k=1}^{N_{paths}} \bar{e}_k. \tag{9}$$

Figure 6 summarizes the results. The fifth reflection path exhibits the largest deviation of 402.7 mm due to its high sensitivity to geometric displacement, whereas the diffraction paths show smaller errors. Most path errors fall within ±1 standard deviation of the mean, as indicated by the red shaded area. The average intersection error between URTS and WI is 246.4 mm.

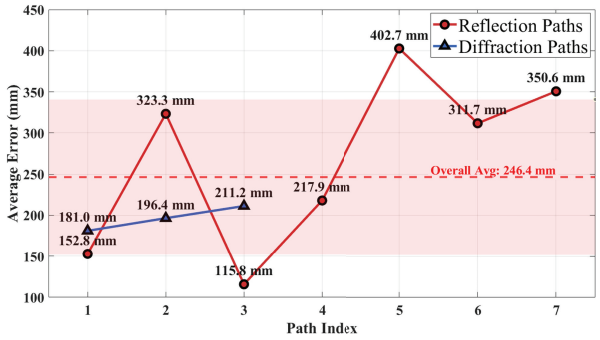


Fig. 6. Mean errors of ray–surface intersections for reflection and diffraction paths.

In addition, the path loss error, delay error, and phase error of the three dominant diffraction paths are calculated. The path loss error is defined as the absolute difference between the path losses predicted by URTS and WI. Since the same transmitted power and antenna configurations are used in both platforms, this metric is equivalent to the received-power deviation of the corresponding path. The delay error is obtained from the difference between the total propagation delays of the corresponding paths, while the phase error is calculated from the path-length difference normalized by the wavelength and wrapped into the range of -180° to 180°.

Table 2 summarizes the propagation-domain errors of the three dominant diffraction paths. The average path loss error is 0.35 dB, and the maximum path loss error is 0.52 dB. The average delay error is 0.12 ns, corresponding to a small path-length deviation of approximately 36 mm. The average phase error is 42.0°, and the maximum phase error is 57.6°. Since phase is highly sensitive to path-length differences at 1 GHz, these results are acceptable for diffraction-path validation. Overall, the proposed hybrid triangle–voxel model preserves the main spatial, power, delay, and phase characteristics of diffraction paths while maintaining high geometric fidelity, thereby demonstrating its physical reliability for diffraction modeling.

Table 2: Propagation-domain errors of diffraction paths

Path	Path Loss Error (dB)	Delay Error (ns)	Phase Error (deg)
D1	0.18	0.08	28.8
D2	0.34	0.11	39.6
D3	0.52	0.16	57.6
Mean	0.35	0.12	42.0

C. Computational efficiency and complexity analysis

To evaluate the computational efficiency of the proposed method, experiments were performed on a workstation equipped with an Intel (R) Core (TM) i9-14900K CPU @ 3.20 GHz and an NVIDIA GeForce RTX 3090 GPU. The sculptural model used in the experiments contains 3383 triangular faces. Table 3 summarizes the voxel counts, peak memory usage, and preprocessing time for both global and local voxelization schemes. Compared with the global voxelization (887 voxels), the local voxelization scheme uses only 360 voxels, achieving a 60% reduction in voxel count, a 25% decrease in computation time, and slightly lower peak memory consumption. Although the performance improvement may appear moderate due to the small-scale test scene, the acceleration is expected to be more significant in larger environments, where global voxelization would require substantially more voxels.

Table 3: Computational cost comparison of global and local voxelization

Model	Number of Voxels	Memory Usage (MB)	Computation Time (s)
Full Voxelization	887	34.9219	53
Local Voxelization	360	33.7891	40

IV. CONCLUSION

This paper presents a hybrid triangle–voxel model for efficient diffraction modeling in ray tracing. By identifying potential diffraction regions based on the first Fresnel-zone criterion and applying local voxelization only within these regions, the proposed method preserves geometric fidelity while reducing voxel count by 60% and computation time by 25%. Simulation results show close agreement with those from commercial software, with an average ray–surface intersection error of 246.4 mm. For the dominant diffraction paths, the average path loss error, delay error, and phase error are 0.35 dB, 0.12 ns, and 42.0°, respectively. These results demonstrate that the proposed model

preserves the main spatial, power, delay, and phase characteristics of diffraction paths while maintaining computational efficiency. The proposed model provides a physically interpretable approach for improving UTD-based diffraction prediction in reconstructed triangular-mesh scenarios. Future work will extend the validation to larger indoor and urban environments under different frequency bands.

ACKNOWLEDGMENT

This work was supported by the Beijing Municipal Natural Science Foundation (L233017), the National Key Laboratory of Intelligent Coal Mining and Strata Control (SKLIS202407), and the MIIT Key Laboratory of Radio Spectrum Monitoring Technology (SRTC-KFKT202501).

REFERENCES

[1] H. Jiang, M. Mukherjee, J. Zhou, and J. Lloret, "Channel modeling and characteristics for 6G wireless communications," *IEEE Network*, vol. 35, no. 1, pp. 296–303, Jan. 2021.

[2] G. Duggal, A. M. Kumar, R. M. Buehrer, H. S. Dhillon, N. Tripathi, and J. H. Reed, "Impact of frequency on diffraction-aided wireless positioning," in *2025 IEEE International Conference on Communications Workshops (ICC Workshops)*, pp. 1457–1463, 2025.

[3] F. Fuschini, E. M. Vitucci, M. Barbiroli, G. Falciasecca, and V. Degli-Esposti, "Ray tracing propagation modeling for future small-cell and indoor applications: A review of current techniques," *Radio Science*, vol. 50, no. 6, pp. 469–485, 2015.

[4] J. Zhang, J. Lin, P. Tang, W. Fan, Z. Yuan, X. Liu, H. Xu, Y. Lyu, L. Tian, and P. Zhang, "Deterministic ray tracing: A promising approach to THz channel modeling in 6G deployment scenarios," *IEEE Communications Magazine*, vol. 62, no. 2, pp. 48–54, 2024.

[5] D. Shi, N. Lv, N. Wang, and Y. Gao, "An improved shooting and bouncing ray method for outdoor wave propagation prediction," *Applied Computational Electromagnetics Society (ACES) Journal*, vol. 32, no. 7, pp. 581–585, July 2017.

[6] D. Shi, N. Lv, and Y. Gao, "A diffraction ray tracing method based on curved surface ray tube for complex environment," *Applied Computational Electromagnetics Society (ACES) Journal*, vol. 32, no. 7, pp. 608–613, July 2017.

[7] J. B. Keller, "Geometrical theory of diffraction," *Journal of the Optical Society of America*, vol. 52, no. 2, pp. 116–130, Feb. 1962.

[8] R. G. Kouyoumjian and P. H. Pathak, "A uniform geometrical theory of diffraction for an edge in a perfectly conducting surface," *Proceedings of the IEEE*, vol. 62, no. 11, pp. 1448–1461, Nov. 1974.

[9] F. Weinmann, "UTD shooting-and-bouncing extension to a PO/PTD ray tracing algorithm," *Applied Computational Electromagnetics Society (ACES) Journal*, vol. 24, no. 3, pp. 281–293, June 2009.

[10] S. Li, G. Cui, S. Guo, C. Jia, L. Kong, and X. Yang, "On the electromagnetic diffraction propagation model and applications," *IEEE Journal of Selected Topics in Applied Earth Observations and Remote Sensing*, vol. 13, pp. 884–889, 2020.

[11] K. W. Kim, M. D. Kim, J. Lee, J. J. Park, Y. K. Yoon, and Y. J. Chong, "Millimeter-wave diffraction-loss model based on over-rooftop propagation measurements," *ETRI Journal*, vol. 42, no. 6, pp. 827–836, 2020.

[12] S. Deng, G. R. MacCartney, and T. S. Rappaport, "Indoor and outdoor 5G diffraction measurements and models at 10, 20, and 26 GHz," in *2016 IEEE Global Communications Conference (GLOBECOM)*, pp. 1–7, 2016.

[13] J. Y. Lee, J. H. Lee, and S. C. Kim, "Improving the accuracy of millimeter-wave ray-tracing simulations by modeling roadside trees," *IEEE Antennas and Wireless Propagation Letters*, vol. 18, no. 1, pp. 162–166, 2019.

[14] R. Chen, M. Hua, S. He, Y. Zhang, and G. Zhu, "UTD solution for diffraction by anisotropic impedance wedge with arbitrary exterior wedge angle under arbitrary skew incidence," *IEEE Antennas and Wireless Propagation Letters*, pp. 1–5, 2025.

[15] V. Degli-Esposti, F. Fuschini, E. M. Vitucci, and G. Falciasecca, "Speed-up techniques for ray tracing field prediction models," *IEEE Transactions on Antennas and Propagation*, vol. 57, no. 5, pp. 1469–1480, 2009.

[16] M. B. Tabakcioglu, D. Ayberkin, and A. Cansiz, "Comparison and analyzing of propagation models with respect to material, environmental and wave properties," *Applied Computational Electromagnetics Society (ACES) Journal*, vol. 29, no. 6, pp. 486–491, June 2014.

[17] Y. Sun, D. L. Page, J. K. Paik, A. Koschan, and M. A. Abidi, "Triangle mesh-based edge detection and its application to surface segmentation and adaptive surface smoothing," in *Proceedings International Conference on Image Processing*, vol. 3, pp. 825–828, 2002.

[18] J. A. Bærentzen, "Optimizing 3D triangulations to recapture sharp edges," Tech. Rep. 11, IMM, DTU Compute, Lyngby, Denmark, 2006.

[19] I. Tropkina, A. Pyattaev, Y. Sadovaya, and S. Andreev, "Modeling of SHF/EHF radio-wave scattering for curved surfaces with voxel cone tracing," *IEEE Antennas and Wireless Propagation Letters*, vol. 21, no. 2, pp. 426–430, 2021.

[20] J. Amanatides and A. Woo, "A fast voxel traversal algorithm for ray tracing," *Proc. Eurographics '87*, pp. 3–10, 1987.

[21] S. D. Díez, C. C. Somolinos, and S. R. G. Palomo, "Optimizing surface voxelization for triangular meshes with equidistant scanlines and gap detection," *Computer Graphics Forum*, vol. 43, no. 6, p. e15195, 2024.

[22] J. L. Schonberger and J. M. Frahm, "Structure-from-motion revisited," in *Proceedings of the IEEE Conference on Computer Vision and Pattern Recognition*, pp. 4104–4113, 2016.

[23] J. L. Schönberger, E. Zheng, J. M. Frahm, and M. Pollefeys, "Pixelwise view selection for unstructured multi-view stereo," in *European Conference on Computer Vision*, pp. 501–518, 2016.

[24] T. Hashimoto, X. Zhang, and C. D. Sarris, "Heuristic UTD diffraction coefficient for three-dimensional dielectric wedges," *IEEE Transactions on Antennas and Propagation*, vol. 69, no. 8, pp. 4816–4826, 2021.

[25] T. S. Rappaport, "Wireless communications–principles and practice," *Microwave Journal*, vol. 45, no. 12, pp. 128–129, 2002.

[26] E. Eisemann and X. Décoret, "Fast scene voxelization and applications," in *Proceedings of the 2006 Symposium on Interactive 3D Graphics and Games*, pp. 71–78, 2006.



Baolai Zhang received the bachelor's degree in electronic information engineering from Civil Aviation University of China, Tianjin, China, in 2024. He is currently working toward the master's degree in new generation of electronic information technology with the Beijing University of Posts and Telecommunications, Beijing, China. His research interests include ray tracing and 3D reconstruction.



Dan Shi received the Ph.D. degree in electronic engineering from Beijing University of Posts and Telecommunications, Beijing, China, in 2008. She is a Professor with Beijing University of Posts and Telecommunications. Her research interests include electromagnetic compatibility, electromagnetic environment, and electromagnetic computation.



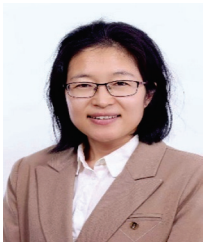
Jinyu Song received the bachelor's degree in electronic science and technology from Beijing University of Chemical Technology, Beijing, China, in 2024. He is currently working toward the master's degree in new generation of electronic information technology with Beijing University of Posts and Telecommunications, Beijing, China. His research interests include ray tracing, 3D reconstruction, and electromagnetic compatibility.



Xiaoyong Liu received the bachelor's degree in radio technology and information system from Tsinghua University, Beijing, China, in 2002. He is currently working toward the doctoral degree in electronic science and technology with the Beijing University of Posts and Telecommunications, Beijing, China. His research interests include electromagnetic compatibility, testing and measurement, and radio frequency spectrum technology.



Hongbo Tao received the Ph.D. degree in electronic engineering from Beijing University of Posts and Telecommunications, Beijing, China, in 2003. Currently, he works at the National Radio Monitoring Center. His research interests include radio detection technology, electromagnetic compatibility analysis, and specialized radio measuring instruments.



Huichun Yang received the Ph.D. degree in electronic engineering from Beijing University of Posts and Telecommunications, Beijing, China, in 2012. Her research interests include electromagnetic compatibility and antenna design.



Zhonghua Xin received the master's degree from Beijing Technology and Business University, Beijing, China, in 2002. She is a senior engineer with the Coal Science and Technology Research Institute. Her research interests include electromagnetic compatibility of mining electrical equipment and wireless equipment, and the electromagnetic environment of underground coal mines.



Yuhao Jia received the bachelor's degree in information and computing science from Beihang University, Beijing, China, in 2020, and the master's degree in electronic information engineering from City University of Hong Kong, Hong Kong, China, in 2023. He is currently a researcher with China Coal Research Institute (CCRI), Beijing, China. His research interests include intelligent detection technology and electromagnetic compatibility.

Numerical Modeling and Uncertainty Analysis of Downhole Low-Frequency Electromagnetic Transmission

Dongxiao Pang[1*], Huiyan Hou[2], Jinjun Bai[2], and Xiong Han[1]

[1]Drilling and Production Engineering Technology Research Institute
CNPC Chuanqing Drilling Engineering Co. Ltd., Guanghan, Sichuan 618300, China
dongxx_zyy@cnpc.com.cn, hanx_ccde@cnpc.com.cn

[2]Department of Electrical Engineering
Dalian Maritime University, Dalian 116026, China
hhy1120241357@dlmu.edu.cn, baijinjun@dlmu.edu.cn
*Corresponding author

Abstract – As oil and gas resource development extends into increasingly complex geological conditions, reliable downhole signal transmission has become a critical challenge in drilling and measurement-while-drilling (MWD) operations. In engineering practice, downhole low-frequency electromagnetic wave (LF-EM) transmission is widely used as an important means of downhole data telemetry because of its low dependence on drilling fluid. However, uncertainties in formation properties and fluctuations in geological parameters can significantly affect electromagnetic signal transmission, making it difficult for surface systems to stably receive downhole information in practical applications. To address this issue, a transmission channel model for downhole LF-EM is established based on FEKO. First, sensitivity analysis is performed to identify the key uncertainty parameters that have the most significant influence on signal attenuation. Then, the Kriging method and the Stochastic Collocation Method (SCM) are employed to conduct uncertainty analysis and to obtain the probability density function (PDF) of the received magnetic-field strength within the parameter fluctuation range. To compare the reliability and applicability of the two methods, Monte Carlo Method (MCM) simulation is adopted as the benchmark, and the Mean Equivalent Area Method (MEAM) is introduced for comprehensive evaluation. Results show that the SCM exhibits overall better fitting accuracy and computational stability than the Kriging method, making it more suitable for probabilistic prediction and risk assessment of downhole low-frequency electromagnetic transmission.

Index Terms – Downhole signal transmission, low-frequency electromagnetic waves, sensitivity analysis, uncertainty analysis.

I. INTRODUCTION

As oil and gas exploration and development continue to advance toward deep, ultra-deep, and more complex geological environments, the stable and efficient transmission of downhole signals has become a critical challenge in drilling and measurement-while-drilling (MWD) operations [1, 2]. Among various downhole wireless telemetry technologies, low-frequency electromagnetic wave communication, owing to its strong medium penetration capability and relatively long effective transmission distance, can overcome the limitations of conventional communication methods to a certain extent and provide important support for real-time data transmission and downhole condition monitoring [3, 4]. However, the diversity of formation media, together with the spatial heterogeneity of electromagnetic parameters such as electrical conductivity and permittivity, can lead to significant energy attenuation of low-frequency electromagnetic wave signals and even cause communication interruption [5–7], thereby reducing the reliability of this technology under complex formation conditions and limiting its engineering applicability. Therefore, this study focuses on the simulation and prediction of low-frequency electromagnetic wave propagation under geological multi-parameter uncertainty. By characterizing and predicting the statistical behavior of the received signals, the proposed framework provides quantitative support for engineering design and risk assessment.

To characterize the propagation process of downhole low-frequency electromagnetic wave (LF-EM), numerical electromagnetic simulation generally adopts mainstream numerical methods such as the finite-difference time-domain method (FDTD), the finite element method (FEM), and the Method of Moments (MoM), along with various improved and hybrid

Submitted On: April 01, 2026
Accepted On: July 24, 2026

1054-4887 © ACES

https://doi.org/10.13052/2026.ACES.J.410709

strategies derived from them [8]. For the downhole low-frequency propagation scenario considered in this paper, the electrical size of the model is relatively small, and the MoM provides a good balance between computational accuracy and efficiency. Previous studies have shown that Streich and Swidinsky established an electromagnetic source model with metallic wellbore coupling based on the MoM and analyzed the spatial distribution characteristics of electromagnetic fields in layered formations [9]. Wang et al. developed a propagation model for extremely low-frequency electromagnetic waves in wellbores and stratified formations, and verified its effectiveness through both simulations and experiments [10]. In recent years, [11] proposed a numerical model based on the two-dimensional MoM for low-frequency electromagnetic problems, systematically analyzing the effects of different discretization schemes on computational accuracy and numerical stability, thereby providing theoretical support for efficient simulation. Based on the above considerations, this paper adopts the MoM and performs the solution using the three-dimensional full-wave electromagnetic simulation platform FEKO. Its low-frequency stabilization technique can effectively alleviate the numerical instability of the conventional MoM at extremely low frequencies, thereby saving computational resources while maintaining computational accuracy.

Under this simulation framework, non-intrusive uncertainty quantification methods are adopted in this study to address the uncertainty of formation parameters, including Stochastic Reduced Order Models (SROM) [12], MoM [13], Monte Carlo Method (MCM) [14, 15], Kriging method [16], and Stochastic Collocation Method (SCM) [17]. Among these methods, both SROM and the MoM are computationally efficient, but their accuracy is usually limited. The MCM is widely regarded as a reliable benchmark, but its computational cost becomes significant when the cost of a single simulation is high. In contrast, the Kriging method and SCM offer better overall trade-offs between efficiency and accuracy, although they still face the problem of large computational scale in high-dimensional parameter spaces. In addition, the computational cost of a single FEKO simulation grows with the dimensionality of the random parameter space. To alleviate this issue, the sensitivity-analysis-based random variable reduction strategy proposed in [18] can be used to screen key random variables during the preprocessing stage, thereby effectively improving the computational efficiency of uncertainty analysis methods.

Based on the above methodology, this study investigates the uncertainty arising from random variations in formation conductivity and layer thickness within a FEKO-based low-frequency electromagnetic transmission model. First, sensitivity analysis is employed to identify the dominant uncertainty parameters and reduce the dimensionality of the random variable space. Subsequently, Kriging and SCM surrogate models are developed to characterize and predict the statistical response of the received magnetic field intensity under parameter uncertainty. MCM is adopted as a benchmark for evaluating the two approaches in terms of computational efficiency, probability density function (PDF) fitting performance, and errors in key statistical measures. Furthermore, to quantitatively assess the prediction accuracy, Mean Equivalent Area Method (MEAM) proposed in [19] is introduced. Combined with statistical indicators, including the mean, variance, relative error, and computational cost, a comprehensive evaluation of the predictive performance of different methods is conducted. The proposed framework provides an effective approach for uncertainty quantification of low-frequency electromagnetic wave propagation in downhole communication channels and offers quantitative support for engineering design and risk assessment.

The structure of this paper is as follows. Section II introduces the modeling process of the low-frequency electromagnetic transmission channel based on FEKO. Section III presents parameter preprocessing using sensitivity analysis. Section IV describes the procedures of uncertainty analysis based on the Kriging method and SCM, and comparatively evaluates the two methods. Section V concludes the paper.

II. LF-EM TRANSMISSION CHANNEL MODELING USING FEKO

In the downhole wireless direct-reading system (Fig. 1), the transmitting tool is lowered along the tubing to the target formation, where downhole production or environmental data are acquired and then transmitted

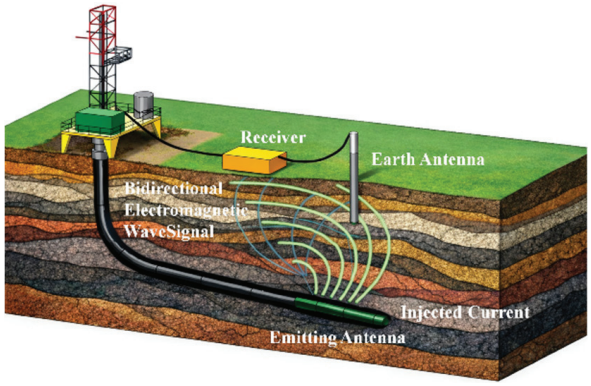


Fig. 1. Electromagnetic-wave-based downhole wireless direct-reading system.

to the surface through low-frequency electromagnetic waves. The surface receiver performs signal reception, demodulation, and decoding, thereby establishing a downhole-to-surface wireless transmission link [20]. However, due to the intricacy of the formation system, signal transmission may fail under complex formation conditions. The spatially non-uniform distribution of salinity, mineralization, and medium composition in the formation results in significant spatial variability and uncertainty in electromagnetic parameters, such as electrical conductivity and relative permittivity, at different depths. In addition, formation interfaces often appear as transition zones rather than clear boundaries, which leads to uncertainty in layer division and parameter assignment. Moreover, when constructing a continuous FEKO formation model from discrete data, assumptions are inevitably introduced. Therefore, statistically derived geometric parameters, such as formation thickness, are more appropriately characterized by interval estimation.

To achieve a balance between computational tractability and geological realism, this study is based on the measured formation data from the Yishan Slope of the Ordos Basin, and the formation layers are statistically grouped according to the ranges of electrical conductivity. For layers with stable lithology, small dispersion, and relatively weak influence on signal transmission, deterministic parameters are constructed using the weighted average method. For layers with strong heterogeneity, significant fluctuations, and dominant influence on transmission, the parameter intervals are retained to characterize their uncertainty.

As a result, the complex formation is equivalently represented by a nine-layer stratified FEKO medium model, and the electrical conductivity and layer thickness of each layer are listed in Table 1. The core of the transmitter is a loop antenna operating under a given working frequency and excitation current. To reduce the complexity of FEKO modeling, it is equivalently represented in this paper by a magnetic dipole source in the form of a current loop with a known time-varying current. The time-varying electromagnetic field excited by the magnetic dipole source induces eddy currents in the formation, which further radiate secondary magnetic fields. In this way, signal transmission along the wellbore direction is achieved through a continuous "magnetic-to-electric-to-magnetic" induction process. Finally, the received magnetic-field strength on the top plane of the FEKO model is taken as the signal reception value. The simulation flow for electromagnetic transmission channel modeling from the deepest downhole position to the wellhead is shown in Fig. 2.

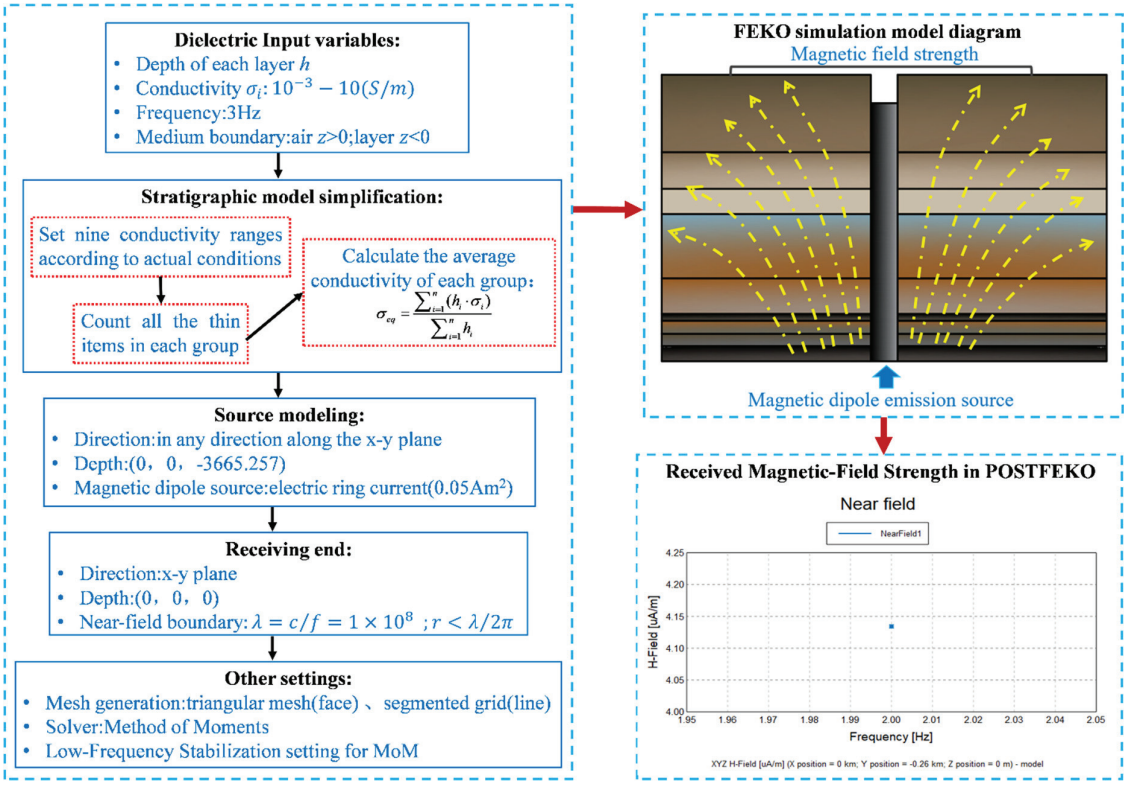


Fig. 2. FEKO-based simulation flowchart.

Table 1: Parameters of the nine-layer geological model in FEKO

Formation Group	**1**	**2**	**3**	**4**
Electrical Conductivity (S/m)	[5.5, 6.2]	[0.32, 0.8]	0.0865	[1, 2.1]
Layer Thickness (m)	[1017.5, 1296.5]	329.5	229	[1330, 1382]
5	**6**	**7**	**8**	**9**
0.015	0.0072	0.00385	[0.0007, 0.001]	0.00003
320.75	[47.25, 175.5]	23.5	112.5	50

$$
\begin{aligned}
IS_{pos}(i) = \frac{dy_\xi}{d\xi_i} &= 2 \times \frac{U_{FEKO}\left(\bar{\xi}_1, \ldots, \bar{\xi}_i + \frac{\delta_i}{2}, \ldots, \bar{\xi}_n\right) - U_{FEKO}\left(\bar{\xi}_1, \ldots, \bar{\xi}_i, \ldots, \bar{\xi}_n\right)}{\frac{\delta_i}{2}} \\
&- \frac{U_{FEKO}\left(\bar{\xi}_1, \ldots, \bar{\xi}_i + \delta_i, \ldots, \bar{\xi}_n\right) - U_{FEKO}\left(\bar{\xi}_1, \ldots, \bar{\xi}_i, \ldots, \bar{\xi}_n\right)}{\delta_i} + o(\delta_i) \\
IS_{neg}(i) = \frac{dy_\xi}{d\xi_i} &= 2 \times \frac{U_{FEKO}\left(\bar{\xi}_1, \ldots, \bar{\xi}_i - \frac{\delta_i}{2}, \ldots, \bar{\xi}_n\right) - U_{FEKO}\left(\bar{\xi}_1, \ldots, \bar{\xi}_i, \ldots, \bar{\xi}_n\right)}{\frac{\delta_i}{2}} \\
&- \frac{U_{FEKO}\left(\bar{\xi}_1, \ldots, \bar{\xi}_i - \delta_i, \ldots, \bar{\xi}_n\right) - U_{FEKO}\left(\bar{\xi}_1, \ldots, \bar{\xi}_i, \ldots, \bar{\xi}_n\right)}{\delta_i} + o(\delta_i).
\end{aligned} \tag{1}
$$

III. SENSITIVITY ANALYSIS AND RANDOM-VARIABLE REDUCTION

During the transmission of downhole LF-EM, uncertainties in formation, medium parameters can significantly affect signal propagation characteristics. Uncertainty analysis aims to characterize the response behavior of simulation outputs under perturbations in random input parameters. Since different input variables contribute unequally to the output response, the fast sensitivity analysis approach proposed in [18] is adopted to identify the relative importance of uncertain input variables. This method is based on a one-at-a-time (OAT) perturbation strategy, in which only a single input parameter is varied while all remaining parameters are maintained at their nominal values, thereby avoiding the high-dimensional combinatorial computations associated with simultaneous perturbations of all variables. Compared with direct uncertainty propagation involving the entire random parameter space, the OAT approach typically requires only local updates of model parameters, resulting in reduced geometric modifications, mesh reconstruction efforts, and computational costs. Consequently, sensitivity indices of the input parameters can be efficiently obtained at a relatively low computational expense. Subsequently, random variables with negligible sensitivity are replaced by their mean values, thereby achieving random variable reduction and reducing the dimensionality of the uncertainty space. The calculation procedure is described as shown in (1). After obtaining the sensitivity evaluation results under positive perturbation $IS_{pos}(i)$ and negative perturbation $IS_{neg}(i)$, the method constructs a comprehensive sensitivity index $IS(i)$ by averaging and combining the results from both sides:

$$IS(i) = |IS_{pos}(i)| + |IS_{neg}(i)|. \tag{2}$$

The relative contribution of each random variable to the output response can be obtained through normalization:

$$P(i) = \frac{IS(i)}{\sum_{i=1}^{N} IS(i)}, \tag{3}$$

where $\bar{\xi}_i$ is the mean of random variable ξ_i, and $U_{EFKO}(\bar{\xi}_1, \ldots, \bar{\xi}_i, \ldots, \bar{\xi}_n)$ is the received magnetic-field strength obtained from the FEKO simulation at the deterministic point $\{\bar{\xi}_1, \ldots, \bar{\xi}_i, \ldots, \bar{\xi}_n\}$. For the uncertainty parameter $k(\xi_i) = A + B \times \xi_i$, ξ_i denotes a uniformly distributed random variable over $[-1, 1]$, the mean and variance of the uncertain input parameter are k_M and k_σ, respectively, where $\begin{cases} k_M = A \\ k_\sigma = \frac{1}{3}B^2 \end{cases}$. Here, $\delta_i = \frac{\sqrt{3k_\sigma}}{k_M}$ is a small perturbation quantity. $S(i)$ denotes the sensitivity analysis result associated with random variable ξ_i, and $o(\delta_i)$ denotes the approximation error.

Based on the FEKO simulation model for downhole LF-EM transmission, seven groups of uncertain inputs exhibiting significant fluctuations in the measured data are selected in this study, as defined in (4), for sensitivity analysis. These include the electrical conductivity of the first layer $\sigma_1(\xi)$, second layer $\sigma_2(\xi)$, fourth layer $\sigma_4(\xi)$, and eighth layer $\sigma_8(\xi)$, as well as the thickness of the first layer $h_1(\xi)$, fourth layer $h_4(\xi)$, and

Table 2: Sensitivity analysis results for the seven groups of fluctuating parameters

Uncertainty Parameters	$\sigma_1(\xi)$	$\sigma_2(\xi)$	$\sigma_4(\xi)$	$\sigma_8(\xi)$	$h_1(\xi)$	$h_4(\xi)$	$h_6(\xi)$
Sensitivity Index	1.94%	1.81%	52.28%	0.07%	42.04%	1.26%	0.6%

sixth layer $h_6(\xi)$. The received magnetic-field strength obtained through POSTFEKO post-processing is then systematically evaluated.

$$\begin{aligned}
\sigma_1(\xi_1) &= 5.85 + 0.35 \times \xi_1 \text{ [s/m]} \\
\sigma_2(\xi_2) &= 0.56 + 0.24 \times \xi_2 \text{ [s/m]} \\
\sigma_4(\xi_3) &= 1.55 + 0.55 \times \xi_3 \text{ [s/m]} \\
\sigma_8(\xi_4) &= 0.00085 + 0.00015 \times \xi_4 \text{ [s/m]} \\
h_1(\xi_5) &= 1157 + 139.5 \times \xi_5 \text{ [m]} \\
h_4(\xi_6) &= 1356 + 26 \times \xi_6 \text{ [m]} \\
h_6(\xi_7) &= 111.375 + 64.125 \times \xi_7 \text{ [m]}
\end{aligned} \tag{4}$$

where $\xi_1, \xi_2, \xi_3, \xi_4, \xi_5, \xi_6$ and ξ_7 are uniformly distributed random variables over the interval $[-1, 1]$.

The sensitivity analysis results are presented in Table 2. The parameters $\sigma_1(\xi), \sigma_2(\xi), \sigma_8(\xi), h_4(\xi)$, and $h_6(\xi)$ account for less than 2% of the total weight, indicating that their effects on the output are negligible. Therefore, in the subsequent uncertainty analysis, they are equivalently replaced by their mean values according to (5).

$$\begin{aligned}
\sigma_1(\xi_1) &= 5.85 \\
\sigma_2(\xi_2) &= 0.56 \\
\sigma_8(\xi_4) &= 0.00085 \\
h_4(\xi_6) &= 1356 \\
h_6(\xi_7) &= 111.375.
\end{aligned} \tag{5}$$

In summary, the sensitivity analysis achieves random variable reduction during the preprocessing stage, accurately quantifies the influence of each formation parameter on the received magnetic-field strength obtained in POSTFEKO, and identifies the electrical conductivity of the fourth layer $\sigma_4(\xi)$ and the thickness of the first layer $h_1(\xi)$ as the dominant factors affecting electromagnetic wave signal attenuation. This provides clear guidance for surrogate model construction in the subsequent uncertainty analysis.

IV. UNCERTAINTY ANALYSIS USING KRIGING AND SCM

A. Kriging

The Kriging method is a surrogate modeling approach based on statistical learning. Its central idea is to generate multiple sets of deterministic parameters using Latin Hypercube Sampling (LHS), obtain the corresponding deterministic simulation results through numerical simulations, and then use these results to train and construct a surrogate model. The surrogate model is subsequently used as an approximate substitute for the complex original model in uncertainty analysis. The basic procedure is illustrated in Fig. 3. In this study, the high-sensitivity parameters identified by sensitivity analysis are selected as uncertain inputs. A twodimensional parameter space is constructed using the electrical conductivity of the fourth layer over the interval [1, 2.1] S/m and the thickness of the first layer over the interval [1017.5, 1296.5] m. LHS is then employed to generate nine training samples so as to cover representative regions of the parameter space, and the resulting sampling point vectors are given as shown in (6). A deterministic FEKO simulation in (7) is performed for each sample to obtain the corresponding received magnetic-field strength:

$$\begin{aligned}
S_{\text{Kriging}}(K) &= [X_1, X_2] \\
X_1 &= [1.47, 1.48, 1.854, 1.589, 2.049, 1.599, \\
&\quad 1.09, 1.403, 1.936]^T (s/m) \\
X_2 &= [1064.71, 1099.25, 1163.72, 1117, \\
&\quad 1030.24, 1291.8, 1140.64, 1158.12, \\
&\quad 1107.77]^T (m)
\end{aligned} \tag{6}$$

$$\begin{aligned}
Y_{FEKO} &= [9.08, 6.94, 2.688, 5.287, 5.73, 1.432, \\
&\quad 8.7, 4.97, 3.686] (mA/m),
\end{aligned} \tag{7}$$

where K denotes the sample index generated by Latin Hypercube Sampling. The training input matrix is $S \in \mathbb{R}^{9\times 2}$, and the corresponding output vector is $Y \in \mathbb{R}^9$. Each row of S corresponds to one LHS sample, and the associated entry of Y denotes the received magnetic-field strength obtained from the FEKO simulation.

The training set $\{S_{Kriging}(K), Y_{FEKO}\}$ for surrogate model construction is thus obtained. By selecting an appropriate fitting model, a surrogate model can be established to approximately represent the response surface of the FEKO model within the parameter space. Based on the trained surrogate model, a large number of prediction samples can be rapidly generated within the parameter fluctuation range (1600 samples in this

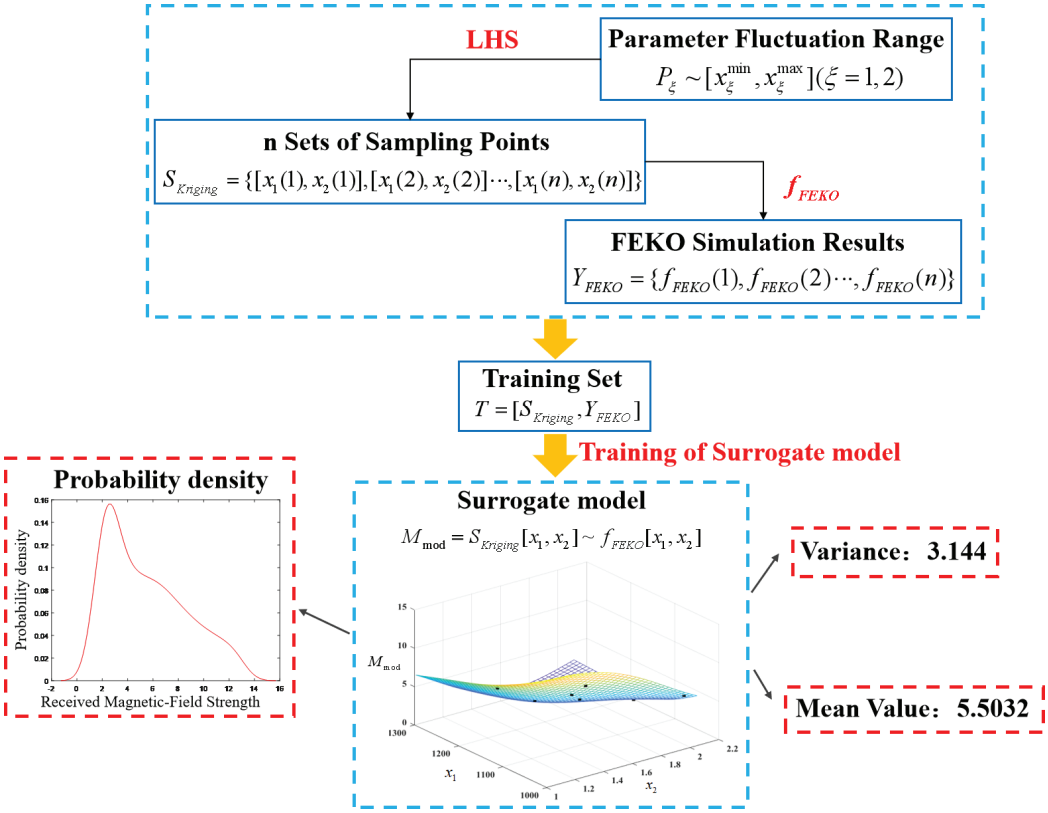


Fig. 3. Schematic illustration of the Kriging method (two-dimensional example).

study), from which the PDF of the received magnetic-field strength can be estimated. In this way, efficient statistical analysis and rapid prediction of the output distribution can be achieved.

B. SCM

SCM is an efficient uncertainty quantification approach based on Polynomial Chaos Expansion (PCE). Its central idea is to represent the output of a stochastic system as a polynomial function of the input random variables by means of orthogonal polynomial expansion. The specific procedure is illustrated in Fig. 4. For the two-dimensional uncertainty case, the random vector is defined as $X = \{X_1, X_2\}$. According to the generalized polynomial chaos theory, the zeros $\{z_1, \ldots, z_n\}$ of the chaos polynomial are then selected and combined in tensor-product form to generate the collocation points [17]. Let $X_1 = \{x_1^1, x_1^2, \ldots, x_1^9\}$ and $X_2 = \{x_2^1, x_2^2, \ldots, x_2^9\}$ denote the one-dimensional collocation nodes associated with the two uncertain variables. The two-dimensional collocation set is then constructed by their tensor product. Therefore, a total of $9 \times 9 = 81$ collocation points are obtained, as shown in (8).

By conducting multiple deterministic FEKO simulations at the collocation points $p(X)$ and then applying multidimensional Lagrange interpolation, the polynomial response with respect to the random variables can be obtained as shown in (8).

$$\begin{aligned} X_1 &= [1.124, 1.124, 1.124, 1.976, 1.976, 1.976, \\ &\quad 1.55, 1.55, 1.55](\text{s/m}) \\ X_2 &= [1048.9, 1261.5, 1157, 1048.9, 1261.5, \\ &\quad 1157, 1048.9, 1261.5, 1157](\text{m}), \\ p(X) &= X_1 \otimes X_2 = \{(x_1^i, x_2^j) \mid i, j = 1, \ldots, 9\} \end{aligned} \tag{8}$$

$$M_{FEKO}(X) = \sum_{i=0}^{n^2} \text{FEKO}[p_i(X)] L_i[p_i(X), p(X), X] \tag{9}$$

where $FEKO[p_i(X)]$ denotes the deterministic simulation result at collocation point $p_i(X)$, and $L_i[p_i(X), p(X), X]$ denotes the value of the multidimensional Lagrange interpolation polynomial evaluated at $p_i(X)$. Here, $M_{FEKO}(X)$ can be regarded as the trained surrogate model. By further substituting 5000 randomly sampled points within the fluctuation range into $M_{FEKO}(X)$, the uncertainty analysis results of the received magnetic-field strength can be efficiently obtained.

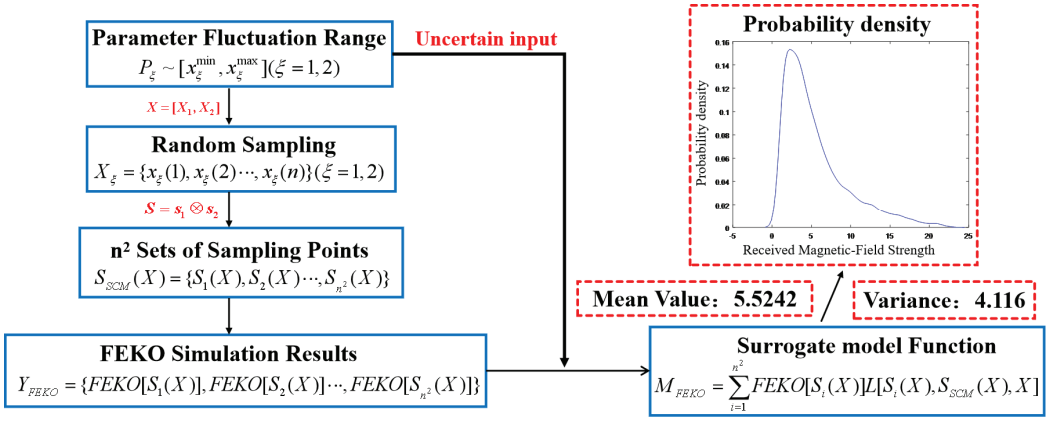


Fig. 4. Schematic illustration of the SCM (two-dimensional example).

C. Accuracy validation

Both surrogate models employed for uncertainty analysis were trained using the same set of nine sampling points. After model construction, 1600 prediction samples and 5000 prediction samples were generated for the Kriging and SCM models, respectively, to estimate PDF of the received magnetic field intensity. It should be noted that the difference in the number of prediction samples only affects the smoothness of the resulting PDF curves and does not influence the predictive accuracy of the surrogate models.

To evaluate the accuracy of the uncertainty analysis results obtained using the Kriging and SCM approaches, an additional set of 500 test samples was generated within the variation ranges of the high-sensitivity parameters using LHS. Corresponding outputs were obtained through FEKO simulations for each sample. Taking the PDF generated by MCM as the reference benchmark, the statistical predictions of the two surrogate-based approaches were compared and validated. The results indicate that the PDF curves predicted by both Kriging and SCM exhibit good agreement with the MCM benchmark within the principal probability region and capture the overall trend of the output distribution. This suggests that both surrogate models are capable of reproducing the uncertainty characteristics of the received magnetic field intensity. To further assess the reliability of the two uncertainty analysis approaches, PDF comparisons obtained using nine and 36 training samples are presented in Fig. 5. When only nine training samples are employed, the SCM prediction shows closer agreement with the MCM benchmark in terms of distribution width and the right-tail region, whereas the Kriging model still exhibits noticeable deviations. When the number of training samples is increased to 36, the PDFs predicted by both surrogate models become nearly indistinguishable from the MCM result. These observations indicate that SCM can achieve satisfactory prediction accuracy with relatively few training samples, whereas the performance of Kriging is more sensitive to the sample size.

Furthermore, quantitative comparisons of the mean, variance, and their relative errors (Table 3) reveal that the statistical measures predicted by SCM are consistently closer to the MCM benchmark and exhibit greater stability with increasing sample size. In contrast, Kriging shows larger errors under small-sample conditions and a relatively weaker capability to capture the complete characteristics of the probability distribution. Overall, under the conditions considered in this study, SCM demonstrates superior accuracy, robustness, and distribution-reconstruction capability compared with Kriging, particularly in the small-sample regime.

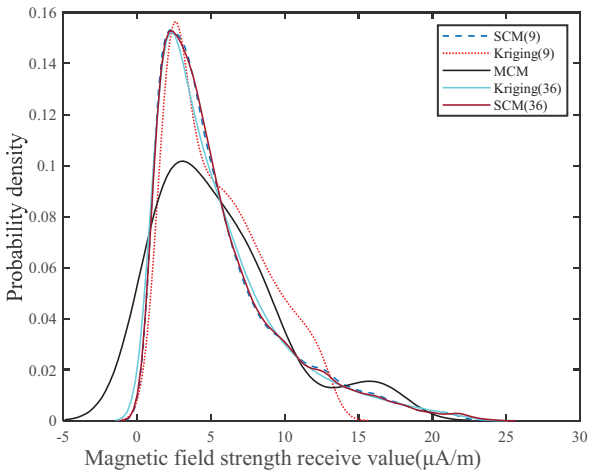


Fig. 5. Comparison of probability density functions.

To quantitatively assess the computational efficiency of the two uncertainty analysis methods, convergence studies were performed by progressively

Table 3: Comparison of statistical metrics

Statistical Metric	Mean Value	Variance	Relative Error of Mean Value	Relative Error of Variance
MCM	5.5326	4.1888	0	0
Kriging (9)	5.5032	3.1440	00.53%	24.94%
SCM (9)	5.5242	4.1160	00.15%	1.74%
Kriging (36)	5.4704	4.1390	1.12%	1.19%
SCM (36)	5.5254	4.1432	0.13%	1.09%

Table 4: Similarity to MCM versus number of training samples

Number of Sample Sets	9	16	25	36
Kriging-MCM Similarity	75.1%	84.56%	89.44%	92.96%
SCM-MCM Similarity	98.2%	98.65%	98.94%	99.05%

Table 5: Comparison of computational time

Analysis Method	Sensitivity Analysis Time (min)	Number of Model Evaluations	Total FEKO Simulation Time (min)	Algorithm Execution Time (min)	Total Computational Time (min)	Sensitivity Analysis Time Ratio
MCM	14.5	5000	2500	0.1	2514.6	0.58%
SCM	14.5	9	4.5	0.5	19.5	74.36%
Kriging	14.5	36	18	3.2	35.7	40.62%

increasing the number of training samples. MEAM was adopted to quantify the similarity between the predicted and reference distributions. Owing to the tensor-product construction of SCM, the number of collocation points in the two-dimensional parameter space is limited to perfect squares. Consequently, experiments were conducted using 9, 16, 25, and 36 training samples, and the corresponding similarity values are summarized in Table 4. Based on these results, the computational cost required to achieve a similarity level of 90% was further evaluated and compared.

As shown in Table 4, when only nine training samples were employed, the similarity between the SCM prediction and the MCM benchmark reached 98.2%, which was substantially higher than the 75.1% achieved by the Kriging model. When the number of training samples was increased to 36, the similarity between the Kriging prediction and the MCM benchmark also exceeded 90%, indicating that both surrogate models can achieve satisfactory prediction accuracy with sufficient training samples. The computational time of a single FEKO simulation was approximately 0.5 min. A total of $4 \times 7 + 1 = 29$ FEKO simulations were required for the sensitivity analysis procedure, corresponding to a computational cost of approximately 14.5 min. The total computational times of the different methods are summarized in Table 5. It can be observed that the computational cost of MCM is significantly higher than those of the surrogate-based uncertainty analysis approaches. Furthermore, SCM achieves higher similarity to the benchmark solution while requiring less computational effort than Kriging.

These results indicate that SCM provides a more favorable balance between prediction accuracy and computational cost. Therefore, for the low-frequency electromagnetic transmission uncertainty problem considered in this study, SCM exhibits superior predictive performance, computational efficiency, and numerical robustness.

V. CONCLUSION

This paper investigates the uncertainty of formation parameters in the low-frequency electromagnetic wave transmission system for downhole wireless direct-reading technology. Based on measured formation data, a refined nine-layer stratified geological model is established, and the downhole-to-surface transmission channel is modeled and solved using the FEKO electromagnetic simulation platform. First, preprocessing based on sensitivity analysis indicates that the electrical conductivity of the fourth layer and the thickness of the first layer are the key fluctuating parameters affecting electromagnetic wave signal attenuation. Subsequently, the Kriging method and the SCM are employed to obtain the PDF of the received magnetic-field strength under fluctuations of the high-sensitivity parameters. Compared with the MCM, the PDFs obtained by the two methods exhibit a high degree of agreement with

the MCM in terms of both the overall trend and the high-probability-density region, thereby verifying their statistical accuracy in uncertainty analysis. Finally, the MEAM is introduced to quantitatively evaluate the similarity between the predicted distributions and the reference distribution. The results demonstrate that SCM outperforms Kriging in terms of both distribution-fitting quality and computational efficiency. Furthermore, the predicted statistical measures, including the mean and variance, are in closer agreement with the benchmark solution. These findings indicate that SCM provides higher predictive accuracy and greater numerical robustness for the low-frequency electromagnetic transmission uncertainty problem investigated in this work.

ACKNOWLEDGEMENT

This paper is supported by the General Project of Liaoning Province, No. 2025-MS-092.

REFERENCES

[1] J. Sun, J. Yang, Y. Bai, K. Lyu, and F. Liu, "Research progress and development of deep and ultra-deep drilling fluid technology," *Petroleum Exploration and Development*, vol. 51, no. 4, pp. 1022–1034, 2024.

[2] A. E. Ibhaze, D. O. Akinola, A. L. Imoize, P. E. Orukpe, and F. O. Edeko, "A review of downhole communication technologies," *Journal of Telecommunication, Electronic and Computer Engineering*, vol. 14, no. 4, pp. 1–10, 2022.

[3] Y. Wu, F. Wang, J. Li, B. Wang, and D. Pang, "Wireless electromagnetic telemetry for metal cased wells: A novel approach with comprehensive channel analysis," *Geoenergy Science and Engineering*, vol. 233, no. 212573, 2024.

[4] Z. Li, J. Lin, S. Xing, X. Ji, M. Dang, and J. Wang, "A novel wireless electromagnetic wave transmission method applicable to water injection wells and analysis of the influence factors," *Scientific Reports*, vol. 15, no. 17230, 2025.

[5] C. Shao, L. Xu, X. Chen, Z. Chu, and B. Yang, "Factors affecting received signal intensity of electromagnetic measurement-while-drilling during underground in-seam horizontal drilling," *Journal of Natural Gas Science and Engineering*, vol. 56, pp. 212–221, 2018.

[6] Z. Wang, D. Jia, F. Sun, Z. Hao, and Q. Chen, "Network model and application in wellbore wireless communication of extremely low-frequency electromagnetic waves," *Journal of Geophysics and Engineering*, vol. 22, no. 3, pp. 672–681, 2025.

[7] H. Li, X. Chen, Y. Meng, Y. Chen, G. Li, and C. Xu, "A novel method for wireless telemetry during air drilling based on air pressure pulses," *Geoenergy Science and Engineering*, vol. 234, no. 212669, 2024.

[8] P. Sumithra and D. Thiripurasundari, "A review on computational electromagnetics methods," *Advanced Electromagnetics*, vol. 6, no. 1, pp. 42–55, 2017.

[9] R. Streich and A. Swidinsky, "On method-of-moments modelling of electromagnetic sources connected to metallic well casings," *Geophysical Journal International*, vol. 234, no. 2, pp. 1476–1483, 2023.

[10] Z. Wang, D. Jia, F. Sun, Q. Chen, S. Zhu, and Q. Wang, "Research on extremely low frequency electromagnetic wave model and simulation in wellbore communication," *Scientific Reports*, vol. 14, no. 20093, 2024.

[11] J. A. Luta, C. A. Castillo, D. C. Horvath, R. A. Howard, and S. D. Pekarek, "2-D method of moments formulations for nonlinear low-frequency electromagnetics," *Engineering Analysis with Boundary Elements*, vol. 179, no. 106383, 2025.

[12] Z. Fei, Y. Huang, J. Zhou, and Q. Xu, "Uncertainty quantification of crosstalk using stochastic reduced order models," *IEEE Transactions on Electromagnetic Compatibility*, vol. 59, no. 1, pp. 228–239, 2016.

[13] R. S. Edwards, A. C. Marvin, and S. J. Porter, "Uncertainty analyses in the finite-difference time-domain method," *IEEE Transactions on Electromagnetic Compatibility*, vol. 52, no. 1, pp. 155–163, 2010.

[14] S. A. Pignari, G. Spadacini, and F. Grassi, "Modeling field-to-wire coupling in random bundles of wires," *IEEE Electromagnetic Compatibility Magazine*, vol. 6, no. 3, pp. 85–90, 2017.

[15] H. Xie, J. F. Dawson, J. Yan, A. C. Marvin, and M. P. Robinson, "Numerical and analytical analysis of stochastic electromagnetic fields coupling to a printed circuit board trace," *IEEE Transactions on Electromagnetic Compatibility*, vol. 62, no. 4, pp. 1128–1135, 2020.

[16] H. You, M. Yang, D. Wang, and X. Jia, "Kriging model combined with Latin hypercube sampling for surrogate modeling of analog integrated circuit performance," in *Proc. 10th International Symposium on Quality Electronic Design (ISQED)*, San Jose, CA, USA, pp. 554–558, 2009.

[17] J. Bai, G. Zhang, D. Wang, A. P. Duffy, and L. Wang, "Performance comparison of the SGM and the SCM in EMC simulation," *IEEE Transactions on Electromagnetic Compatibility*, vol. 58, no. 6, pp. 1739–1746, 2016.

[18] J. Bai, Y. Wan, M. Li, G. Zhang, and X. He, "Reduction of random variables in EMC uncertainty simulation model," *Applied Computational Electromagnetics Society (ACES) Journal*, vol. 37, no. 9, pp. 941–947, 2022.

[19] J. Bai, L. Wang, D. Wang, A. P. Duffy, and G. Zhang, "Validity evaluation of the uncertain EMC

simulation results," *IEEE Transactions on Electromagnetic Compatibility*, vol. 59, no. 3, pp. 797–804, 2017.

[20] C. Zhang, H. Dong, J. Ge, and H. Liu, "Theoretical channel model and characteristics analysis of EM-MWD in the underground coal mine," *IEEE Access*, vol. 9, pp. 142644–142652, 2021.



Dongxiao Pang received his Ph.D. in Mechanical Engineering from Southwest Petroleum University, China, in 2007. He currently works as a senior engineer at Chuanqing Drilling Engineering Co. Ltd. He has long been engaged in research on downhole electromagnetic wireless transmission and measurement-while-drilling (MWD) technologies, and has received multiple Science and Technology Advancement Awards from CNPC.



Huiyan Hou received the B.Eng. degree in marine electrical and electronic engineering from Dalian Maritime University, China, in 2024. She is currently a graduate student in electrical engineering at Dalian Maritime University, where her research interests include electromagnetic wave propagation and uncertainty analysis methods.



Jinjun Bai received the B.Eng. degree in electrical engineering and automation in 2013 and Ph.D. degree in electrical engineering in 2019 from the Harbin Institute of Technology, Harbin, China. He is now a lecturer at Dalian Maritime University. His research interests include uncertainty analysis methods in EMC simulation, multi-physics field simulation methods.



Xiong Han, born in October 1985, is a senior engineer and deputy director of the Technology Research and Development Centre at the Drilling and Production Institute of China Petroleum Chuanqing Drilling Engineering Co. Ltd. He was selected for the second batch of the "Youth Science and Technology Talent Training Programme" by China National Petroleum Corporation. He mainly engages in research on oil and gas wellbore communication technology, has undertaken and participated in 20 national and provincial-level research projects, holds 21 authorized invention patents, has formulated one standard, published 25 papers, and authored two monographs.

Frequency-Selective Polarization Converter with Ultra-Wideband Linear-to-Circular Conversion and High Selectivity Based on Stair-Case Shape

Kun Liao[1*], Jie Shu[2], Ruquan Wen[1], Renxia Ning[3], and Zhiming Liu[2]

[1]School of Mechanical and Electronic Engineering
Pingxiang University, Pingxiang 337055, China
21010052@pxu.edu.cn, 1282479687@qq.com

[2]School of Information Engineering
Nanchang University, Nanchang 330031, China
2768177455@qq.com, lzmedu@foxmail.com

[3]School of Information Engineering
Huangshan University, Huangshan 245041, China
nrxxiner@163.com
*Corresponding author

Abstract – In this paper, an ultra-wideband and high-selectivity reflective polarization converter is presented, which is based on a simple stair-case shape. The simulation results indicate that the polarization converter achieves ultra-wideband linear-to-circular polarization conversion under linearly polarized incident wave. Its 3 dB axial ratio frequency band is 5.47–16.15 GHz, and its relative bandwidth is 98.8%; besides, linear-to-linear polarization conversion is realized on both sides of the circular polarization band from 4.57 to 5.30 GHz and 16.28 to 18.11 GHz when $S_{11} < -10$ dB. Therefore, multiple polarization functions are realized using a single simple structure. Moreover, the physical mechanism and surface current distributions of the polarization converter are analyzed. In addition, the sample is processed and tested, verifying the feasibility of our idea.

Index Terms – Reflective polarization converter, stair-case shape, tri-modal polarization conversion.

I. INTRODUCTION

Polarization is a basic characteristic of electromagnetic waves, and controlling polarization is of great significance in many application fields such as wireless communications, microwave radar, and optics [1–3]. The emergence of metasurfaces provide the new ideas for controlling the polarization of electromagnetic waves, and polarization converters based on metasurface have the characteristics of compact structure, low profile, and easier integration compared with traditional converters [4–6]. Therefore, the works of polarization control are investigated in depth based on metasurface polarization converters [7–9]. Among them, the main types of polarization control are linear-to-linear (LTL), linear-to-circular (LTC) and circular-to-circular (CTC) [10–12], for example, a triple-arrow resonant structure [13], which realizes the conversion from linear-polarized to cross-polarized in the range of 8.0–18.5 GHz. Reference [14] proposed a double V-shaped metasurface polarization converter to generate a broadband cross-polarized reflection band from 12.4 to 27.96 GHz. A metasurface polarization converter consists of an inner cross structure and outer double C-shaped ring was designed in [15], realizing the dual-band cross-polarized in the ranges of 9.38 to 13.36 GHz and 14.84 to 20.36 GHz. Zheng et al. presented a reflective polarization converter with two meander-lines and one metal-strip structure, which realizes low-frequency cross-polarized (fractional bandwidth of 59.6%) and high-frequency circular polarization conversion (fractional bandwidth of 13.0%) at linear-polarized incidence [16]. In addition, the transition band between two polarization bands has a bandwidth of 12.6%. A composite metasurface with metal strip and rectangular ring was proposed by Huang [17]. Results show that the cross-polarization conversion is achieved in two frequency bands. In our previous work, we designed a polarization converter based on inner cross structure and outer two pairs of serpentine lines structure to achieve polarization conversion in three frequency bands [9]. Based on the existing works, it is not difficult to find

Submitted On: July 08, 2025
Accepted On: June 15, 2026

1054-4887 © ACES

https://doi.org/10.13052/2026.ACES.J.410710

that metasurface polarization converters are easier to achieve linearly polarized than circularly polarized, and circular polarization conversion is difficult to achieve ultra-wideband control. Furthermore, the design method of using multi-structures to achieve multi-bands polarization control needs to be changed. Therefore, designing a single structure metasurface polarization converter to achieve multi-bands multi-polarization control is a great challenge.

A reflective polarization converter based on a single meander line ring is proposed in this paper, which achieves ultra-wideband LTC polarization conversion and cross polarization conversion on both sides of the circular polarization band. The innovations of this paper are as follows. A single structure polarization converter achieves three-frequency bands and two polarization controls, which is an advantage that the existing works do not have. The different polarization control frequency bands have high-selectivity for electromagnetic waves. In addition, the experiment results demonstrate the simulation data, and verify the feasibility of the design idea.

II. STRUCTURAL SIMULATION AND THEORETICAL ANALYSIS

A. Structural simulation

A schematic diagram of the unit cell for our polarization converter is represented in Fig. 1. The unit cell consists of a dielectric substrate F4BM220 ($\varepsilon_r = 2.2$, $\tan\delta = 0.001$) covered with a single stair-case shape metal structure and metal backplate, separated by an air layer of thickness $h = 4.5$ mm. The single stair-case shape is placed at an angle of 135° with respect to the horizontal. Physical parameters of the single stair-case shape are defined as $p = 15$ mm, $l_1 = 2.5$ mm, $l_2 = 2.9$ mm, $w = 0.3$ mm. Full-wave simulation software CST Microwave Studio is used to simulate the designed structure.

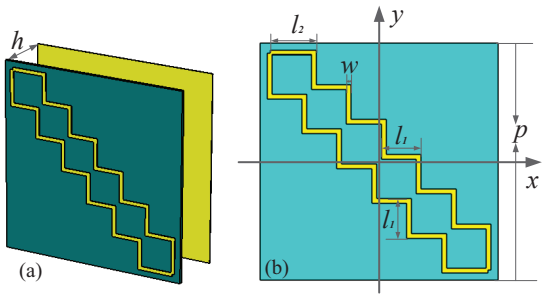


Fig. 1. Layout of the unit cell: (a) stereoscopic view and (b) front view.

Since a single stair-case shape is symmetrical about an oblique direction of 135°, the y-polarized incident wave is taken as the example. The reflection coefficients of the co- and cross-polarization are r_{yy} and r_{xy}, respectively. The phase difference between co- and cross-polarization reflection coefficients is $\Delta\varphi_{yx} = arg(r_{yy}) - arg(r_{xy})$. Polarization conversion ratio (PCR) and energy conversion ratio (ECR) are defined as $\mathrm{PCR} = r_{xy}^2/(r_{xy}^2 + r_{yy}^2)$ and $\mathrm{ECR} = r_{xy}^2 + r_{yy}^2$. Subsequently we simulated the reflection coefficients and phase difference of the polarization converter, as shown in Fig. 2.

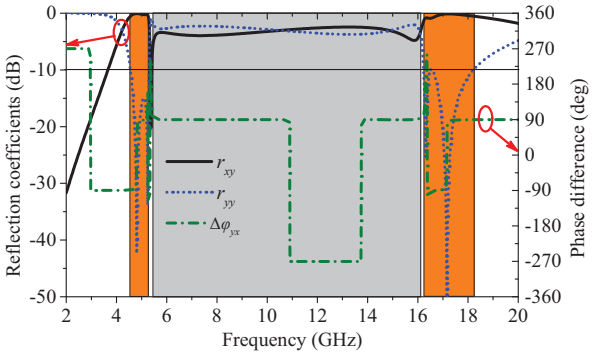


Fig. 2. Simulation results of reflection coefficients and phase difference.

Figure 2 describes that co- and cross-polarization reflection coefficients are almost equivalent in the gray areas, and phase difference is almost equal to 90° (the phase difference in some areas is −270°, which is also 90°). Hence, according to the standard of circularly polarized waves, the reflected waves in the gray areas are a left-handed circularly polarized wave. In addition, the cross-polarized reflection happened in the range of 4.57 to 5.30 GHz and 16.28 to 18.11 GHz when $S_{11} < -10$ dB in the two orange areas. Therefore, the designed polarization converter completes the polarization conversion in three-frequency bands using a single structure, which is one of the advantages of this work. Taking into account different incidence angles of the y-polarized wave, the simulation results were not satisfactory. The reason is that the increase in incident angle destroys polarization stability and leads to separation of polarization wave responses. High-order modes and gate lobes are excited in the high frequency band, resulting in impedance mismatch. Eventually, the electromagnetic characteristics significantly deteriorated, and the curve showed multiple peaks, depressions, and other phenomena. Therefore, this paper does not include an analysis of the incidence angles of the y-polarized wave.

Physical size values in the model are optimized during the design process. Changing any size can cause performance to deviate from intended goals. Therefore, only the final parameter values are given. Further, the results of PCR and ECR are calculated as described in Fig. 3.

According to Fig. 3, ECR is higher than 0.8 in three areas. Moreover, PCR has exceeded 0.9 in the range 4.57 to 5.30 GHz and 16.28 to 18.11 GHz, indicating that the polarization converter has high polarization efficiency.

Electromagnetic waves can be considered as circularly polarized waves when the axial ratio (AR) of the electromagnetic wave is less than 3.0 dB in practical engineering application. Equation (1) is used to calculate the AR of the reflected electromagnetic waves to determine the bandwidth of circular polarization.

$$\mathrm{AR} = \left(\frac{|r_{yy}|^2 + |r_{xy}|^2 + \sqrt{a}}{|r_{yy}|^2 + |r_{xy}|^2 - \sqrt{a}} \right)^{1/2}. \tag{1}$$

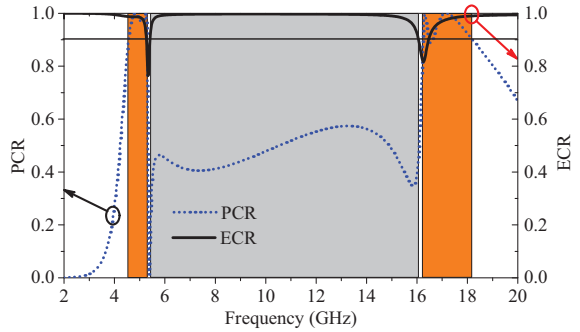


Fig. 3. Calculation results of PCR and ECR.

where $a = |r_{yy}|^4 + |r_{xy}|^4 + 2|r_{yy}|^2|r_{xy}|^2\cos(2\Delta\varphi_{yx})$. Figure 4 plots the calculation results of AR.

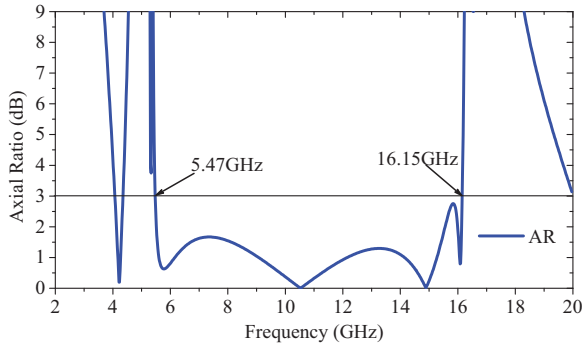


Fig. 4. AR vs frequency.

It can be seen from Fig. 4 that AR of the electromagnetic waves is within 3 dB in the frequency range 5.47–16.15 GHz, and relative bandwidth is 98.7%. Combined with the results in Fig. 2, the transition bands of the cross polarization and circular polarization bands are 5.30 to 5.47 GHz and 16.15 to 16.28 GHz, and the relative bandwidths corresponding to 3.1% and 0.8%, respectively. This illustrates that the designed polarization converter has high-selectivity for electromagnetic waves, which is very important in many applications. This is another advantage of this work.

B. Theoretical analysis

In order to deeply grasp the working mechanism of the polarization converter, a new coordinate system (uov) with u- and v-axis is defined. The coordinate axes are perpendicular to each other and deviate $\pm 45^\circ$ from the y-axis, as represented in Fig. 5.

According to the vector nature of the electric field, it can be decomposed into two component electric fields that are perpendicular to each other and have equal amplitude. Therefore, incident and reflected electric fields can be expressed as:

$$\overrightarrow{E_y^i} = \frac{\sqrt{2}}{2}|\overrightarrow{E_y^i}|(\overrightarrow{e_u} + \overrightarrow{e_v}), \tag{2}$$

$$\overrightarrow{E_y^r} = \frac{\sqrt{2}}{2}|\overrightarrow{E_y^i}|(r_{uu}\overrightarrow{e_u} + r_{vv}\overrightarrow{e_v}), \tag{3}$$

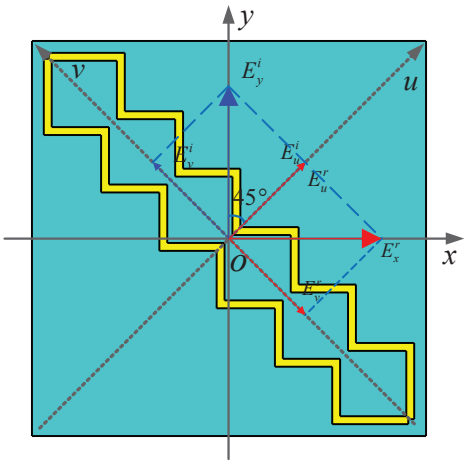


Fig. 5. New coordinate system and electric field decomposition.

where $\overrightarrow{e_u}$ and $\overrightarrow{e_v}$ represent the unit vector in the direction of the u- and v-axis, and r_{uu} and r_{vv} are regarded as the amplitude of co-polarized reflected wave under the u- and v-polarized incoming wave, respectively. In addition, the phase relationship of the co-polarized reflection coefficients r_{uu} and r_{vv} is: $\Delta\varphi_{uv} = \varphi_{uu} - \varphi_{vv}$. Hence, equation (3) can be written as:

$$\overrightarrow{E_y^r} = \frac{\sqrt{2}}{2} r_{uu}|\overrightarrow{E_y^i}|(\overrightarrow{e_u} + e^{-j\Delta\varphi_{uv}}\overrightarrow{e_v}). \tag{4}$$

Since the motion trajectory of the reflected electric fields vector is perpendicular to the propagation direction, the E_{ur} and E_{vr} components satisfy the following relationship:

$$E_{ur}^2 - 2E_{ur}E_{vr}\cos\Delta\varphi_{uv} + E_{vr}^2 = 0.5|E_{yi}|^2\sin^2\Delta\varphi_{uv}. \tag{5}$$

From the electric field decomposition in Fig. 5, $E_{xr} = \sqrt{2}(E_{ur} - E_{vr})/2$, $E_{yr} = \sqrt{2}(E_{ur} + E_{vr})/2$,

consequently, equation (5) can be described as:

$$\frac{2E_{xr}^2}{|E_{yi}|^2(1-\cos\Delta\varphi_{uv})}+\frac{2E_{yr}^2}{|E_{yi}|^2(1+\cos\Delta\varphi_{uv})}=1. \quad (6)$$

The x and y components of the reflected electric fields in equation (6) are:

$$|E_{xr}|=|E_x||_{E_{yr}=0}=\sqrt{2}|E_{yi}|\sqrt{(1-\cos\Delta\varphi_{uv})}/2$$
$$|E_{yr}|=|E_y||_{E_{xr}=0}=\sqrt{2}|E_{yi}|\sqrt{(1+\cos\Delta\varphi_{uv})}/2. \quad (7)$$

Therefore, the reflection coefficients of co- and cross-polarization can be obtained from equation (7) as:

$$r_{yy}=\sqrt{2}\cdot\sqrt{1+\cos\Delta\varphi_{uv}}/2$$
$$r_{xy}=\sqrt{2}\cdot\sqrt{1-\cos\Delta\varphi_{uv}}/2. \quad (8)$$

According to equation (8), the co- and cross-polarization reflection coefficients are $r_{yy}=1$, $r_{xy}=0$ when $\Delta\varphi_{uv}=0°$, and there is no polarization conversion. When $\Delta\varphi_{uv}=\pm180°$, the co- and cross-polarization reflection coefficients are $r_{yy}=0, r_{xy}=1$, and it has achieved a 90° linear polarization conversion.

However, the reflected wave is an elliptically polarized wave when $\Delta\varphi_{uv}\neq0°$ or $\Delta\varphi_{uv}\neq180°$. Hence, AR of the elliptically polarized wave can be written as:

$$\mathrm{AR}=\sqrt{(1\pm\cos\Delta\varphi_{uv})/(1\mp\cos\Delta\varphi_{uv})}. \quad (9)$$

When $\Delta\varphi_{uv}=\pm90°$, then AR = 1, and the linear polarization is converted to circular polarization. Based on the above research conclusions, the S-parameters at u- and v-polarized incidence are simulated, as depicted in Fig. 6.

As can be seen from Figs. 6 (a) and (b), the co-polarized reflection coefficients are basically identical under u- and v-polarized incident waves in the three frequency bands of 4.57–5.30 GHz, 5.47–16.15 GHz, and 16.28–18.11 GHz. Additionally, the co-polarized reflection phase difference is approximately −90° in the frequency range 5.47–16.15 GHz. According to the above theory, the circularly-polarized waves are realized in this frequency band. Finally, the AR values of equations (1) and (9) are calculated. From Fig. 6 (c), it can be seen that the AR values of the two paths are equal.

Furthermore, the surface current distributions of the polarization at different frequency points is analyzed to explain its working mechanism, as displayed in Fig. 7. Note that the induced current is distributed in different positions on the stair-case shape structure at different frequency points, and the current path length is different, which shows that this structure can achieve different polarization functions.

In Fig. 7 (a), the induced current path length at this frequency point occupies most of the structure,

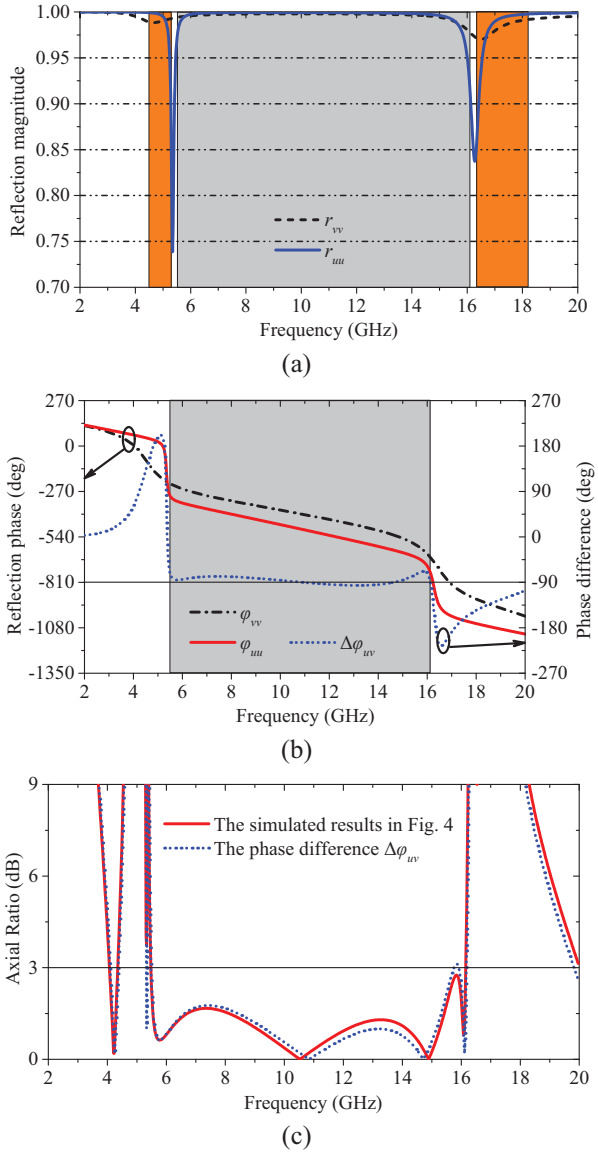


Fig. 6. (a) Refection magnitude of u- and v-polarized incoming wave, (b) reflection phase and phase differences, and (c) AR of the reflected wave.

which conforms to the principle of long current path and low resonance frequency point. In addition, the surface currents of the upper and lower metal layers are in opposite directions, forming a closed current loop and generating magnetic resonance, thus realizing cross-polarization conversion. At 11.0 GHz, the direction of the induced current in the upper and lower metal layers is perpendicular, indicating that the reflected wave is a circularly polarized wave. As can be seen in Fig. 7 (c), the induced current is concentrated on a short structural path, and the current directions of the upper and lower layers are in the same direction, which also achieves a 90° polarization conversion.

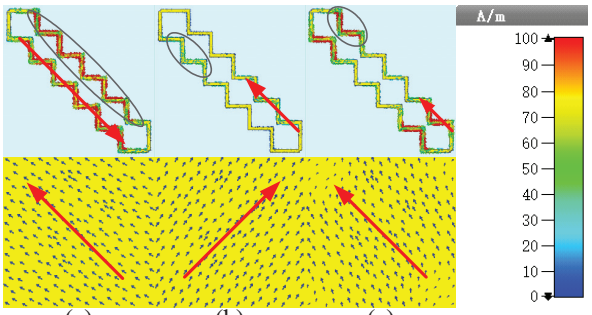


Fig. 7. Surface current distributions of upper and lower metal layers at frequency points (a) 5.0 GHz, (b) 11.0 GHz, and (c) 18.0 GHz.

III. PROCESSING AND MEASUREMENT

In order to demonstrate the conversion performance of the designed ultra-wideband polarization converter, the proposed polarization converter was fabricated and tested. The processed sample consists of 24×24 units with a size of 360×360 mm, as depicted in Fig. 8 (a). The metal structure is printed on a F4B dielectric substrate with relative dielectric constant of 2.2 using PCB printing technology, and the substrate thickness is 0.25 mm. Plastic nylon columns are used to support the whole structure. Figure 8 (b) shows the sample testing in a microwave darkroom environment. The sample is surrounded with absorbing materials to avoid diffraction interference of electromagnetic waves. The measurement equipment consists of a vector network analyzer and two standard broadband linearly polarized horns – one horn serving as a transmitting antenna and the other as a receiving antenna. Figure 8 (c) plots the test and simulation results of the designed polarization converter sample at vertical incidence.

It is not difficult to see from the results in Fig. 8 (c) that the experimental results are in good agreement with the simulation results, further demonstrating the feasibility and reliability of the design. Small deviations are allowed, taking into account factors such as machining accuracy, measurement tolerances, and background noise. In order to highlight the advantages of this work,

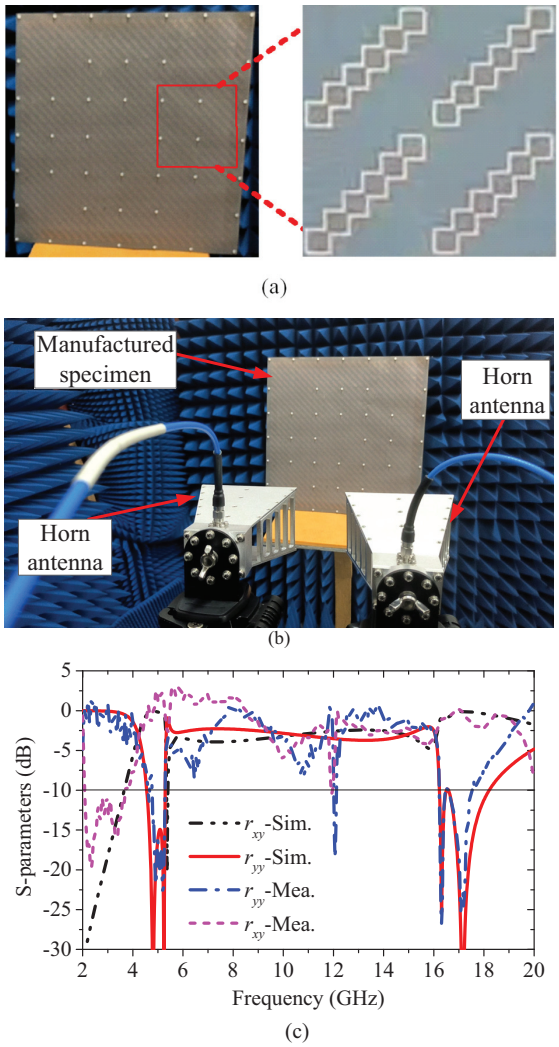


Fig. 8. (a) Fabricated sample, (b) measurement environment of the sample, and (c) measurement and simulation results at vertical incidence.

the characteristics of existing related articles are listed in Table 1.

According to Table 1, compared with existing polarization converters, the designed polarization converter has the characteristics of a single structure, multiple polarization modes and broadband operating bandwidth.

Table 1: Comparison with existing related articles

Ref.	Structural Diversity	Polarization Diversity	High-Selectivity	Polarization Bandwidth
[3]	Two	One	NO	49.1%
[18]	One	One	NO	91.2%
[9]	three	two	NO	82.2%
[15]	Two	One	NO	66.3%
[19]	Two	One	NO	31.7%
This Work	One	Two	3.1%, 0.8%	124.2%

IV. CONCLUSIONS

A metasurface polarization converter with a single structure is reported and has cross polarization – circular polarization – cross polarization frequency response characteristics. The simulation results denote that the LTC polarization conversion is realized in the range of 5.47–16.15 GHz (relative bandwidth of 98.8%). Furthermore, the relative transition bandwidths between linear polarization and circular polarization bands are 3.1% and 0.8%, respectively, indicating that the polarization converter has strong frequency selectivity. Theoretical analysis and experimental testing have demonstrated the reliability of the idea. So far, the polarization converter provides a certain theoretical foundation for multi-polarization control and polarized antenna design.

ACKNOWLEDGMENT

This work was supported by the National Natural Science Foundation of China (Grant No. 62201240, 62571224), the Natural Science Foundation of Jiangxi Province (Grant No. 2022BAB212005), the open research project of Engineering Research Center of Power Integrated Circuit AnHui Province (NO. ERCPZX202404), the Aeronautical Science Foundation of China (Grant No. 20230020052003, 20230000052035, 20230018052002).

REFERENCES

[1] A. K. Fahad, C. Ruan, R. Nazir, and B. Hassan, "Transmissive polarizer metasurfaces: From microwave to optical regimes," *Nanomaterials*, vol. 12, no. 10, p. 1705, 2022.

[2] S. Jorwal, A. Dubey, R. Gupta, and S. Agarwal, "A review: Advancement in metamaterial-based RF and microwave absorbers," *Sensors and Actuators A: Physical*, vol. 354, p. 114283, 2023.

[3] B. Hayat, J. Zhang, A. Majeed, M. Ishfaq, A. Khan, and S. Ahmad, "A low profile wideband linear to circular polarization converter metasurface with wide axial ratio and high ellipticity," *Electronics*, vol. 13, no. 2, p. 352, 2024.

[4] S. C. Jiang, X. Xiong, and Y. S. Hu, "Controlling the polarization state of light with a dispersion-free metastructure," *Physical Review X*, vol. 4, no. 2, p. 021026, 2014.

[5] Y. Zhao and A. Alù, "Manipulating light polarization with ultrathin plasmonic metasurfaces," *Physical Review B*, vol. 84, no. 20, p. 205428, 2015.

[6] G. Deng and Z. Kou, "Electrically controllable broadband reflective linear cross-polarization conversion based on liquid crystals," *Optics Express*, vol. 31, no. 17, pp. 27420–27432, 2023.

[7] X. Yuan, J. Chen, and J. Wu, "Graphene-based tunable linear and linear-to-circular polarization converters in the THz band," *Results in Physics*, vol. 37, p. 105571, 2022.

[8] X. Song, H. Lu, and S. Yang, "Ultra-wideband frequency selective surface with metal gratings for polarization conversion under arbitrary polarized angles," *Applied Computational Electromagnetics Society (ACES) Journal*, vol. 40, no. 10, pp. 1002–1009, 2025.

[9] K. Liao and S. Liu, "A polarization converter with single-band linear-to-linear and dual-band linear-to-circular based on single-layer reflective metasurface," *International Journal of RF and Microwave Computer-Aided Engineering*, vol. 32, no. 2, p. e22955, 2022.

[10] A. Ahmed, Q. Cao, and M. I. Khan, "An ultra-thin multifunctional chiral metasurface with asymmetric transmission, cross-polarization conversion, and circular dichroism for Ku- and K-band applications," *Journal of Physics D: Applied Physics*, vol. 57, no. 3, p. 035001, 2023.

[11] Z. Cui, Z. Xiao, and M. Chen, "A transmissive linear polarization and circular polarization cross polarization converter based on all-dielectric metasurface," *Journal of Electronic Materials*, vol. 50, no. 7, pp. 4207–4214, 2021.

[12] N. Pouyanfar, J. Nourinia, and C. Ghobadi, "Low-profile reflective surface for multi-band linear-to-linear and linear-to-circular polarization conversion," *IEEE Access*, vol. 11, pp. 135159–135165, 2023.

[13] A. Rashid, M. Murtaza, and S. A. A. Zaidi, "A single-layer, wideband and angularly stable metasurface based polarization converter for linear-to-linear cross-polarization conversion," *PLoS ONE*, vol. 18, no. 1, p. e0280469, 2023.

[14] X. Gao, X. Han, and W. P. Cao, "Ultrawideband and high-efficiency linear polarization converter based on double V-shaped metasurface," *IEEE Trans. Antennas Propag.*, vol. 63, no. 8, pp. 3522–3530, 2015.

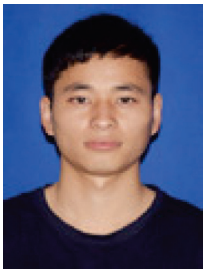
[15] C. Fu, Z. Sun, and L. Han, "Dual-bandwidth linear polarization converter based on anisotropic metasurface," *IEEE Photon. J.*, vol. 12, no. 2, pp. 1–11, 2020.

[16] Q. Zheng, C. Guo, and J. Ding, "Wideband metasurface-based reflective polarization converter for linear-to-linear and linear-to-circular polarization conversion," *IEEE Antennas Wireless Propag. Lett.*, vol. 17, no. 8, pp. 1459–1463, 2018.

[17] X. Huang, H. Yang, D. Zhang, and Y. Luo, "Ultra-thin dual-band metasurface polarization converter," *IEEE Trans. Antennas Propag.*, vol. 67, no. 7, pp. 4636–4641, 2019.

[18] J. L. Wu and B. Q. Lin, "Ultra-wideband reflective polarization converter based on anisotropic metasurface," *Chinese Physics B*, vol. 25, no. 8, p. 088101, 2016.

[19] A. Undrasi, D. Kundu, and K. K. Kamalesh, "A closely spaced dual-band dual-sense linear-to-circular polarization converter for X-band applications," *Optik-International Journal for Light and Electron Optics*, vol. 320, p. 172135, 2025.



Kun Liao received the Ph.D. degree in communication and information systems from Nanjing University of Aeronautics and Astronautics (NUAA), China, in 2023. He became a lecturer in Pingxiang University in 2024. His main research interests include antenna design, frequency selective surfaces and metasurfaces.



Jie Shu, born in 2004, is currently pursuing his Bachelor of Engineering degree in Communication Engineering at Nanchang University, China. His research interests include microwave filter design and antenna design.



Ruquan Wen, born in 1981, received a B.S. degree from Hunan University of Science and Technology, China, in 2004 and an M.S. degree from Lanzhou University of Technology in 2009. Her current research interests include signal processing and superconducting materials.



Renxia Ning, received a M.S. degree from Anhui University, China, in 2009. Her main research interests include metamaterials, terahertz, and micro-nano sensing devices, analog driver integrated circuits, and miniaturized RF antenna design.



Zhiming Liu, born in 1989, received a B.S degree from East China University of Technology, China, in 2012, a M.S. degree from Nanchang University in 2015, and a Ph.D. degree from Nanjing University of Aeronautics and Astronautics in 2019. His current research interests include electromagnetic metamaterial device design and application, microwave component and system design, and antenna design.